[Doctoral thesis] Precipitation in turbulent fluids

Original Citation:
Marchisio D.L. (2002). *Precipitation in turbulent fluids.* PhD thesis

Precipitation in Turbulent Fluids

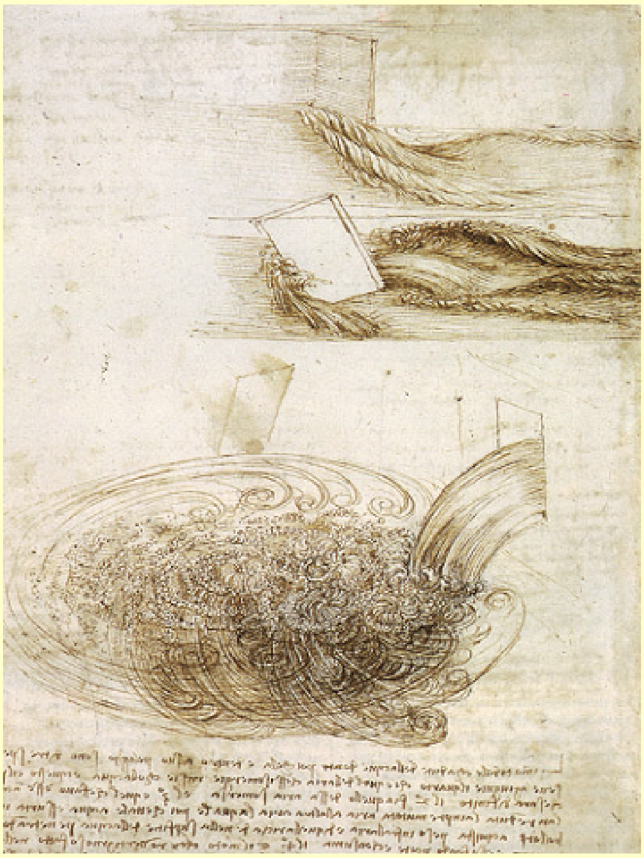

Daniele Marchisio

Politecnico di Torino

Dipartimento di Scienza dei Materiali ed Ingegneria Chimica

Dottorato di Ricerca in Ingegneria Chimica
XIV Ciclo (1998-2001)

Tesi:

Precipitazione in fluidi turbolenti

(Precipitation in turbulent fluids)

Candidato:
Daniele Marchisio

Relatori:
Antonello A. Barresi
Giancarlo Baldi

Coordinatore del Corso di Dottorato:
Giancarlo Baldi

Acknowledgments

I would like to express my gratitude to those people who helped me in these three years (besides my advisors.)

First of all I would like to thank Prof. Rodney O. Fox for having given me the opportunity to joint his group at Iowa State University (Ames, IA, USA) during my Ph.D. and for the financial support in that period.

I would like also to thank Prof. Laurent Falk for his help and collaboration during my permanence in his laboratory (Laboratoire des Sciences du Genie Chimique, Nancy, France.)

A special thank goes to Elise Fournier, who carried out the experimental flow field investigation for the Taylor-Couette reactor, and to Mirko Garbero and Daniela Bencivenga who also contributed to this work.

My gratitude goes also to Prof. Marco Vanni, who patiently solved the major part of my numerical and technical problems, and for having gotten angry only once in three years.

Contents

Introduction

Precipitation or reactive crystallization is an important unit operation in modern chemical industry. It is a fundamental step in the production of many catalysts, pigments, pharmaceutical products and also occurs during offshore oil drilling. Due to the complexity of the problem and the number of interacting phenomena a model can be conveniently used for reactor design and scale-up.

The main scope of this work is the development of a model for studying turbulent precipitation. Precipitation is a very complex process, in which solid particles are produced by a chemical reaction. This very fast chemical reaction generates supersaturation which is the actual driving force for nucleation and growth. Nucleation is the formation of the new solid phase, whereas crystal growth is the process of size enlargement due to solute molecules. Besides crystal growth there is another size-enlargement process, namely aggregation. During aggregation particles collide and possibly adhere, forming bigger particles. Particles may also undergo breakup processes and therefore reduce their size.

Study of precipitation has attracted much attention in the last two decades and experimental evidences showed that precipitation is strongly affected by mixing, since both the chemical reaction and the nucleation process are quasi-instantaneous. Mixing is thus responsible for the generation and the redistribution of the supersaturation, but plays also an important role during aggregation. As a consequence the precipitation model has to be based on a detailed description of mixing features of the reactor.

In this work the use of Computational Fluid Dynamics (CFD) for flow field and turbulence field predictions is extended to reacting scalar field predictions. In turbulent precipitation computations, CFD needs to be coupled with a micromixing model, for taking into account mixing at the molecular level, and the population balance for modeling solid phase evolution.

The work is divided into two parts: in the first part the fundamental aspects concerning precipitation and turbulent flow and mixing are presented and discussed. In the second part the model proposed in this work is presented and validated. The validation was carried out both by comparison with more sophisticated models and by comparison with experimental data. Barium sulfate precipitation, produced by aqueous solutions of barium chloride and sodium sulfate, was chosen as test reaction and was investigated in two chemical reactors: a Taylor-Couette reactor and a tubular reactor.

As concerns mixing at the molecular level the probability density function approach was used. In this work use of the finite-mode Probability Density Function is proposed for modeling precipitation. This part of the work was carried out in collaboration with Prof. Rodney O. Fox (Iowa State University.) As concerns the population balance the Standard Moment Method (SMM) was used but also a new method (Quadrature Method of Moment) was proposed and partially validated. Also this part of the work was carried out in collaboration with Prof. Rodney O. Fox.

The Taylor-Couette cell is made of two coaxial cylinders and the fluid is contained in the gap between the two. This reactor was chosen among the other possibilities (baffled and un-baffled stirred vessels) because it is quite easy to model it by using CFD codes. However no detailed validation in our operating conditions exists, and thus flow field and tracer dispersion predictions were validated through comparison with experimental data. Experiments were carried out by using laser techniques (Laser sheet visualization, Laser Doppler Anenometry, and Laser Induced Fluorescence.) This part of the work was carried out at the Laboratoires des Sciences du Genie Chimique (ENSIC, France) in collaboration with Prof. Laurent Falk and Dr. Elise Fournier (who carried out most of the experimental work of this part.) Moreover in order to investigate the mixing properties of the reactor, in the first part of the work, mixing efficiency has been evaluated by using a parallel reaction (iodide/iodate reaction.) As concers the tubular reactor the validation of flow field and tracer dispersion validation has been carried out in a previous work.

Another important issue concerns precipitation kinetics. A wide literature has been published in this field yielding different and sometimes contradictory results. However still now there exists a lack of information concerning kinetics, especially in particular conditions (e.g. excess of one of the two ions.) In this work also the effect of kinetic has been investigated, by comparing model predictions with different kinetic expressions for nucleation and growth. This part of the work was mainly carried out in the tubular reactor, since in this device mixing dynamic is simpler and already investigated in previous works.

Part I

Fundamentals

Chapter 1

Precipitation

Precipitation involves different steps, namely: nucleation, crystal growth, aggregation and breakage. Nucleation is the formation of nuclei of the solid phase, crystal growth and aggregation are two mechanisms responsible for size enlargement while breakage is responsible for size reduction of crystals. A detailed review of all these processes can be found in [1]. Here the discussion focuses on some particular aspects concerning barium sulfate precipitation[1].

1.1 Nucleation

Classical theories assume that solute molecules combine to produce embryos. For this transition it is possible to write the change in the Gibbs free energy in terms of two contributions, one due to the formation of the new volume and the other one due to the formation of the new surface:

$$\Delta G(L) = -\left(\frac{k_v L^3}{\nu}\right) k_B T \ln(S) + \gamma k_a L^2, \tag{1.1}$$

where k_v is the volume shape factor, k_a is the surface shape factor, L is the embryo size, ν is the embryo molecular volume, k_B is the Boltzmann constant, T is the absolute temperature, and γ is the surface energy. Shape factors are defined as follows

$$V = k_v L^3, \tag{1.2}$$

$$A = k_a L^2, \tag{1.3}$$

where V and A are the particle volume and surface, whereas the supersaturation ratio S is defined as:

$$S = \frac{c_{Ba} c_{SO_4}}{k_s}, \tag{1.4}$$

where c_{Ba} and c_{SO_4} are ion barium and ion sulphate concentration, k_s is the solubility product of barium sulphate (at room temperature k_s=1.14 × 10^{-4} mol^2/m^6), and the barium sulphate precipitation reaction is:

$$Ba^{++} + SO_4^{=} \rightarrow BaSO_{4(S)}. \tag{1.5}$$

---

[1] Notice that in this work breakup effects are not considered. This is supported by experimental evidences as it will be explained later.

When the supersaturation ratio, $S < 1$ the process is always non-spontaneous [i.e., $\Delta G(L) > 0$)], whereas when $S > 1$, $\Delta G(L)$ has a positive maximum. The height of this maximum in the free-energy curve is the activation energy for nucleation, and the value of L at which the maximum occurs is called critical nuclear size (L_c). Embryos larger than this size are stable nuclei and can grow to form macroscopic solid particles; embryos smaller than this size are unstable and are dissolved again in molecules. Given the free-energy of the transition it is possible to determine the number density of embryos:

$$N(L) = \left(\frac{1}{\nu_{sol}}\right) \exp\left(\frac{-\Delta G(L)}{k_B T}\right), \tag{1.6}$$

where $N(L)$ is the number density of embryos for unit volume of solution, and ν_{sol} is the molecular volume of the solvent. The rate at which stable embryos of size L_c (i.e., nuclei) are formed can be derived from the following reaction

$$molecules + embryo(L_c - molecules) \leftrightarrow nuclei \tag{1.7}$$

and the reaction rate can be expressed as:

$$\frac{dN(L_c)}{dt} = \left[k_1\left(\frac{1}{\nu_{sol}}\right) - k_2\right]\left(\frac{1}{\nu_{sol}}\right) \exp\left(-\frac{\Delta G(L_c)}{k_B T}\right), \tag{1.8}$$

where k_1 and k_2 are the kinetic constants for the direct and inverse reaction. Use of the Einstein theory to express the pre-exponential factor yields

$$J = \frac{dN(L_c)}{dt} = \frac{2D}{d^5} \exp\left(-\frac{\Delta G(L_c)}{k_B T}\right), \tag{1.9}$$

where D is the diffusion coefficient of the solute and d is the molecular diameter. The nucleation rate can be made dimensionless by dividing for the asymptotic value J_{max} at $S \rightarrow \infty$ for different values of the new parameter $A = (4k_a^3\gamma^3\nu^2/[27k_v^2 k_B T \ln(10)]^3)$. After this renormalization the nucleation rate becomes

$$\log\left(\frac{J}{J_{max}}\right) = -A[\log(S)]^{-2}. \tag{1.10}$$

This expression can be used to derive the nucleation rate by fitting the experimental data. This procedure was used by Nielsen [2] to determine barium sulfate nucleation rate and results are reported in Fig. 1.1.

In the generalized nucleation rate diagram two lines are presented, one for homogeneous nucleation, and one for heterogeneous nucleation. In the diagram the best-fit values for J_{max} and A are also reported. Homogeneous nucleation occurs in absence of a solid interface whereas heterogeneous nucleation occurs in the presence of a foreign solid interface. The two rates obey to the same functional form, but as the surface energy γ is different, two curves are obtained; in fact, for homogenous nucleation the surface energy refers to the solid/liquid interface, whereas for heterogeneous nucleation the surface energy refers to the solid/foreign interface. Using Nielsen's experimental data of barium sulfate precipitation [2] other expressions for the nucleation rate were found [3]:

$$J(c_{Ba}, c_{SO_4}) = \left\{ \begin{array}{c} 2.83 \times 10^{10} \Delta c^{1.775} \ \ (1/\mathrm{m}^3\mathrm{s}) \\ \text{for } \Delta c \leq 10 \ \mathrm{mol/m}^3 \\ 2.53 \times 10^{-3} \Delta c^{15} \ \ (1/\mathrm{m}^3\mathrm{s}) \\ \text{for } \Delta c > 10 \ \mathrm{mol/m}^3 \end{array} \right. \tag{1.11}$$

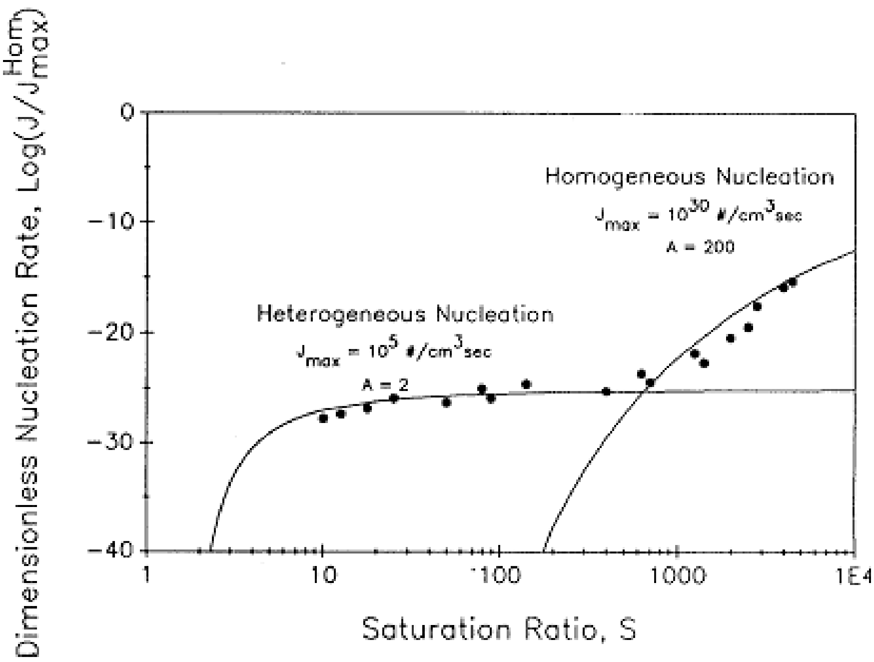

Figure 1.1: Dimensionless nucleation rate against supersaturation ratio.

where $\Delta c = \sqrt{c_{Ba}c_{SO_4}} - \sqrt{k_s}$ and again two expressions are given, for heterogeneous and homogeneous nucleation respectively.

This expression does not account for ion excess, that on the contrary was shown to have an effect on the final Crystal Size Distribution (CSD) [4, 5]. A detailed study of this effect on kinetics, and a review of a number of kinetic expressions available in literature can be found in [6]. The same authors in another work [7] derived an expression in terms of the reactant concentration ratio $R_0 = c_{Ba}/c_{SO_4}$ having the following form

$$\begin{aligned} J(c_{Ba}, c_{SO_4}) &= k \exp\left(\frac{-B}{[\ln\sqrt{c_{Ba}c_{SO_4}/k_s}]^2}\right) \\ B &= 14.9 + 67.57 \mid \log(R_0) \mid \\ k &= 2.5 \times 10^{11} R_0^{2.28} \quad \text{if} \quad R_0 > 1 \\ k &= 2.5 \times 10^{11} R_0^{-1.05} \quad \text{if} \quad R_0 < 1. \end{aligned} \tag{1.12}$$

Unfortunately their expressions were derived in a relatively small range of reactant concentration and thus are not applicable for a wide investigation.

The presented equations were derived by assuming ideal behavior of electrolytes in aqueous solutions. Wei and Garside [8] introduced activity coefficients in kinetic expressions by using a correlation available in literature [9]. The barium sulfate activity coefficient ($\gamma_\pm$) can be calculated as follows

$$\log(\gamma_\pm) = \frac{-2.044\sqrt{I}}{1+\sqrt{I}} + 0.5(F_1 + F_2), \tag{1.13}$$

where I is the ionic strength of the solution

$$I = 0.5(4c_{Ba} + 4c_{SO_4} + c_{Cl} + c_{Na}), \tag{1.14}$$

and F_1 and F_2 are defined as follows

$$\begin{aligned} F_1 &= 4B_{12}c_{Ba} + 2.25B_{14}c_{Cl}, \\ F_2 &= 4B_{12}c_{SO_4} + 2.25B_{32}c_{Na}, \end{aligned} \tag{1.15}$$

where B_{12},B_{14}, and B_{32} can be calculated as follows

$$\begin{aligned} B_{12} &= \frac{0.1512}{(1+0.375I)^2} - 0.037, \\ B_{14} &= \frac{0.1919208}{(1+0.75I)^2} - 0.059934, \\ B_{32} &= \frac{0.10656}{(1+0.75I)^2} - 0.0112. \end{aligned} \tag{1.16}$$

The correction of the driving force with the activity coefficient, as explained by Wei and Garside [8], results in the following expression for the nucleation rate [10]:

$$J(c_{Ba}, c_{SO_4}) = \left\{ \begin{array}{c} 6.61 \times 10^{10} \Delta c_{\pm}^{1.775} \quad (1/\mathrm{m}^3\mathrm{s}) \\ \text{for } \Delta c_{\pm} \leq 4.3 \text{ mol/m}^3 \\ 3.60 \times 10^{-4} \Delta c_{\pm}^{15} \quad (1/\mathrm{m}^3\mathrm{s}) \\ \text{for } \Delta c_{\pm} > 4.3 \text{ mol/m}^3 \end{array} \right. \tag{1.17}$$

where $\Delta c_{\pm} = \sqrt{c_{Ba}c_{SO_4}}\gamma_{\pm} - \sqrt{k_s}$ is the modified driving force.

1.2 Crystal growth

As concerns crystal growth several processes are involved, such as diffusion of solute from the bulk of the solution to the crystal surface, adsorption on crystal surface, diffusion over the surface, attachment to a step, diffusion along a step, and integration into a crystal kink site (see Fig. 1.2).

When the supersaturation ratio is very low, growth is controlled by a mononuclear process, in which a bunch of molecules, that form a single growth unit, attaches the old surface in only one point. This event can be seen as a superficial nucleation and consists in the formation of a growth site on crystal surfaces. Growth might be also controlled by a polynuclear process, in which the attachment of the old surface occurs in more than one point. When the time between two nucleation events is about 60% of the time needed to complete a single surface by diffusion along the surface itself, the two mechanisms are equally important. Whereas when the nucleation rate is less than 20% of the diffusion rate, the mononuclear process is predominant. These mechanisms play an important role in determining the final smoothness of the surface. At low supersaturation level also a screw dislocation growth was detected in several systems. This phenomenon is caused by the presence of a dislocation that offers a free site for growth, without surface nucleation. Increasing the supersaturation ratio nucleation events become more frequent and thus growth can be controlled by diffusion from the solution.

As explained by Dirksen and Ring [1] and Nielsen [11] different growth laws can be obtained, linear, parabolic, and exponential, if the controlling mechanism is respectively diffusion, surface spiral growth and surface nucleation (polynuclear). Concerning barium sulfate growth rate, Nielsen and Toft [12] by fitting experimental data proposed a parabolic expression with a kinetic constant (k_r) equal to 5.8×10^{-8} (m/s)/(mol/m^3)^2. In normal

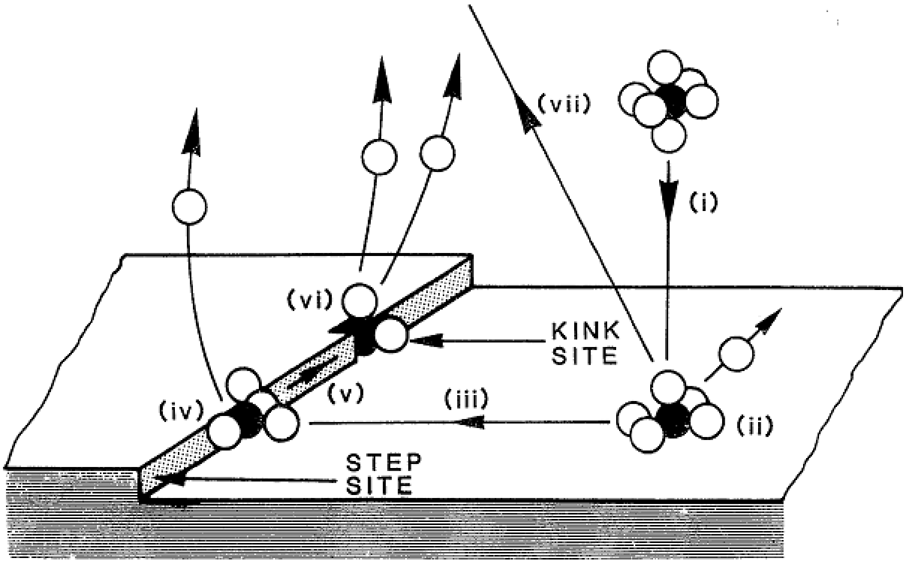

Figure 1.2: Schematic representation of the different steps involved in the growth of a face of a crystal.

applications barium sulfate growth is not controlled only by surface growth but also by diffusion. The final growth rate can be found as follows

$$\begin{aligned} G(c_{Ba}, c_{SO_4}) &= 5.8 \times 10^{-8} \Delta c_s^2 \\ &= k_d(c_{Ba} - c_{Ba}^*) \\ &= k_d(c_{SO_4} - c_{SO_4}^*) \quad (\mathrm{m/s}) \end{aligned} \tag{1.18}$$

where $\Delta c_s = \sqrt{c_{Ba}^* c_{SO_4}^*} - \sqrt{k_s}$, c_{Ba}^* and $c_{SO_4}^*$ are reactant concentrations on crystal surface and k_d is the mass transfer coefficient. The solution of this equation for given values of c_{Ba} and c_{SO_4} (bulk concentrations) can be found by using a simple Newton-Rapson method. Also in this case it is possible to introduce activity coefficients, and for this case Wei and Garside [8] found:

$$\begin{aligned} G(c_{Ba}, c_{SO_4}) &= 4.0 \times 10^{-7} \Delta c_s^{\pm 2} \\ &= k_d(c_{Ba} - c_{Ba}^*) \\ &= k_d(c_{SO_4} - c_{SO_4}^*) \end{aligned} \tag{1.19}$$

where $\Delta c_s^{\pm} = \sqrt{c_{Ba}^* c_{SO_4}^* \gamma_{\pm}} - \sqrt{k_s}$.

As concerns diffusion, Dirksen and Ring [1] showed that for particles smaller than 1 μm the slip velocity is very small, particles are entrapped in a microeddy, and growth is typically controlled by Brownian diffusion. In a recent work [13] a relationship for the Sherwood number for microparticles was proposed

$$Sh = \frac{\hat{k}_d L}{D} = 2 + 0.52 Re_p^{0.52} Sc^{1/3}, \tag{1.20}$$

where Re and Sc are the Reynolds and Schimdt numbers for microparticles

$$Re_p = \left(\frac{\varepsilon L^4}{\nu^3} \right)^{1/3}, \tag{1.21}$$

$$Sc = \frac{\nu}{D}, \tag{1.22}$$

and where ε is the turbulent dissipation rate, and ν is the kinematic viscosity of the fluid. This study is the first systematic experimental confirmation that the theoretical limit of Sherwood number equal to 2 is valid also for spherical microparticles in agitated systems. Using this expression in the limit of null slip velocity we find that

$$k_d = \frac{ShD}{L}\frac{M}{\rho} \approx \frac{2.0 \times 10^{-13}}{L}. \tag{1.23}$$

where D is the molecular diffusion coefficient, M is the molecular weight, and ρ is the crystal density. According to this equation k_d increases with decreasing particle dimension; this result seems to be in contradiction with another work [14], in which it was found that k_d is constant for particles smaller than 10 μm notwithstanding the difference in solute. However, given the limited number of experimental data used in achieving this conclusion, the use of a size-dependent growth rate (by using Eq. 1.18 coupled with Eq. 1.23) seems to be more appropriate.

Using a completely different approach other authors found different expressions for the growth rate. In order to take into account the effect of ion excess (R_0) the growth rate can be expressed as follows [7]:

$$\begin{aligned} G(c_A, c_B) &= k_g(c_{Ba} - \sqrt{k_s})^{1.15}(c_{SO_4} - \sqrt{k_s})^{0.95} \quad \text{(m/s)} \\ k_g &= 1.05 \times 10^{-5} 10^{-1.57/R_0} \quad \text{if} \quad R_0 > 1 \\ k_g &= 2.73 \times 10^{-5} 10^{-1.99 R_0} \quad \text{if} \quad R_0 < 1. \end{aligned} \tag{1.24}$$

1.3 Aggregation

Particle aggregation can be thought of as an extension of the concept of the diffusion-controlled growth theory, in fact, also in this case size enlargement is produced by the addition of a unit to the crystal, but in this case the growth unit is much larger than a molecule. Aggregation takes place in two steps. In the first one, particles must be brought into close proximity by a transport mechanism, producing what is usually called a collision. Then depending on the balance of the interparticle forces (i.e., attractive or repulsive) particles might adhere or not. Depending on the relative strength of each of the two contributions, the energy versus distance profile typically displays one of the following patterns (see Fig. 1.3):

(i) a deep minimum, called the primary minimum (PM), at close separation, followed by a maximum, called the energy barrier (EB), occurring at a larger distance

(ii) a deep (primary) minimum only

(iii) a large maximum (EB) but no significant secondary minimum.

The shape of the interaction profile has an important influence on aggregation kinetics. When there is a barrier, particles must overcome this, and if the height of the barrier is greater than $20k_BT$ the suspension is very stable. Lower values of the barrier height imply that a part of the particles have enough energy to surmount the barrier, and when the barrier is overcome, particles are held by the attractive forces in the primary minimum. When the energy barrier is not present the suspension is unstable and particles will aggregate quickly [15].

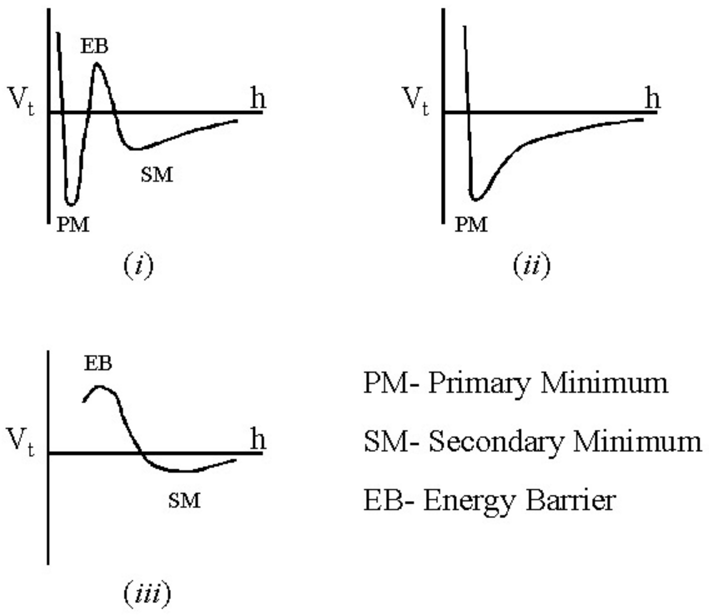

(*i*) (*ii*) (*iii*)

Figure 1.3: Schematic representations of total energy of interactions versus surface-to-surface separation distance profiles.

Attractive forces are caused by the short range Van der Waals forces, whereas repulsive forces are caused by double layer repulsions. The electrical double layer is due to the fact that particles have a surface charge, and because dispersions are electrically neutral, this charge must be balanced by an opposite charge in the solution. Several mechanisms determine the origin and the distribution of particle charge, such as ionization of surface groups, differential solution of ions from the ionic crystal surface, physical entrapment of charge inside the solid phase, and specific ion adsorption. An useful information on the dispersion stability can be obtained from the point of zero charge (PZC), that is the condition at which the surface charge is zero.

These considerations are useful in determining the colloid stability ratio (W), which is defined (for two spheres with radii a and b, separated by distance, R) as follows :

$$W = (a+b)\int_{a+b}^{\infty} \exp\left(\frac{V(R)}{k_B T}\right)\frac{dR}{R^2} \tag{1.25}$$

where $V(R)$ is the potential-energy function determined by the interaction potential of the two double layers. When crystals form an unstable colloidal supersaturated solution, W can reach values in the range from 1 to 1000, and crystals start to aggregate when their number density becomes sufficiently high. On the opposite when the colloidal system is stable W can range from 10^5 to 10^9. It is useful to highlight that quite often colloid stability is defined in terms of the collision efficiency (α), which is defined as the inverse of W.

Concerning aggregation kinetics, when particles are brought into close proximity by Brownian motions, the process is known as perikinetic aggregation. When particle motion is controlled by mean fluid flow or fluid velocity fluctuations the process is known as orthokinetic aggregation. Eventually particles may aggregate because of their inertia or as a consequence of external forces (differential setting.) In each case the frequency of collision is different and can be quantified by the aggregation kernel (β). In case of collision of particles due to Brownian motion the aggregation kernel is [16]:

$$\beta(L,\lambda) = \frac{2k_B T}{3\mu}\frac{(L+\lambda)^2}{L\lambda}, \tag{1.26}$$

where μ is the fluid viscosity and L and λ are the particle dimensions. If the colliding particles are of about the same size ($L \approx \lambda$) the kernel can be considered constant, and thus for water at room temperature:

$$\beta_0 = \frac{8k_B T}{3\mu} = 10^{-17} m^3/s. \tag{1.27}$$

If particle collisions are due to fluid motion, an expression for the aggregation kernel is as follows [16, 17]:

$$\beta(L,\lambda) = \frac{4}{3}\dot{\gamma}(L+\lambda)^3 \tag{1.28}$$

where $\dot{\gamma}$ is the shear stress. Depending on the type of flow (laminar or turbulent) and the size of the particles compared with the Kolmogorov microscale, this shear stress can be evaluated in different manners. For example, in the case of turbulent flows, and particles smaller than the Kolmogorov microscale, the shear rate can be replaced by the effective velocity gradient resulting in [18]:

$$\dot{\gamma} \propto \sqrt{\frac{\varepsilon}{\nu}}, \tag{1.29}$$

where ε is the turbulent dissipation rate and ν is the kinematic viscosity.

In general when dealing with turbulent flows the kernel has to be calculated as the sum of two contributions [19]:

$$\beta(L,\lambda) = \beta(L,\lambda)_b + \beta(L,\lambda)_t, \tag{1.30}$$

in which $\beta(L,\lambda)_b$ is the Brownian kernel given by Eq. 1.26, and $\beta(L,\lambda)_t$ is the turbulent kernel:

$$\beta(L,\lambda)_t = \frac{4}{3}\left(\frac{3\pi}{10}\right)^{1/2}\left(\frac{\varepsilon}{\nu}\right)^{1/2}(L+\lambda)^3. \tag{1.31}$$

From Eq. 1.31 it is clear that increasing the size of the particles the turbulent aggregation kernel increases, and depending on the value of ε it could degenerate in a system with few big particles. This situation is known as gelling, but occurs only in certain cases. Very important in these cases is the evaluation of the collision efficiency (α) that is a function of the velocity gradient ($\dot{\gamma}$, see Eq. 1.29) and the particle size (L)

$$\alpha = \left(\frac{A}{36\pi\mu\dot{\gamma}L^3}\right)^{0.18} \tag{1.32}$$

where A is the Hamaker constant [20]. This constant can be computed if the molecular properties of the materials under consideration are known [21]. Its order of magnitude for interactions in vacuum is 10^{-20}-10^{-19} J at room temperature, however for interactions across a medium is much lower (i.e., 10^{-22} J).

Useful pieces of information can be obtained by evaluating the Peclet number, defined as

$$Pe = \frac{3\pi\mu L^3\dot{\gamma}}{k_B T} \tag{1.33}$$

that is an estimate of the ratio between shear-induced and Brownian coagulation rate. When $Pe < 0.001$ only Brownian aggregation can be considered, whereas when $Pe > 10$ Brownian contribution is negligible.

1.4 Crystal morphology and shape factors

According to previous considerations, depending on the operating conditions adopted, different phenomena occur. At low concentration nucleation is heterogeneous, crystal growth rate is slow, and is controlled by surface processes. In this case well formed crystals are usually obtained and aggregation is not detected. Increasing concentration crystal growth goes under diffusion control. Solute is not able to be distributed along crystal faces, and then edges grow faster, dendrite crystals are thus obtained. A further increase causes the transition to homogeneous nucleation, and depending on colloid stability aggregation may take place. In this case morphology is the typical for agglomerated crystals.

The process of size enlargement is due to crystal growth from solution and aggregation of smaller crystals. Study of crystal morphology is very useful in determining the dominant process. Crystals can be conveniently described in terms of self similar fractal structures. The self-similarity can be quantitatively measured by using the fractal dimension. For its determination, the number of smaller objects or pieces is counted when an object is magnified by some factor M. The fractal dimension is then determined from [22]:

$$N = (M)^{d_f}, \tag{1.34}$$

where N is the number of new copies of an object observed after magnification, M is the factor by which the original object must be magnified to see the new copies and d_f the is the fractal dimension. In practice the fractal dimension can be determined by plotting the mass (or volume) of aggregates against the aggregate size. For regular three-dimensional objects such plot is linear and the slope is 3, whereas for a general aggregate may be still linear but with a non-integer slope.

As experiments demonstrate the fractal dimension is a characteristic of the growth process. During crystal growth from solution, for example $d_f = 3$, whereas aggregates formed by Brownian coagulation present a value of d_f in the range from about 1.8 to about 2.2 [23]. In the case of shear-induced coagulation, when particles of about the same size aggregate, $d_f = 1.8$, while when big particles growth because smaller particles stick on their surface d_f is close to 3 [24]. These two situations are represented in Fig. 1.4

Considering an aggregate of outer radius L made of monomers of radius a, it is possible to estimate the aggregate density as follows [25]:

$$\rho(L) = \rho_o \left(\frac{L}{a}\right)^{d_f - 3}, \tag{1.35}$$

where ρ_o is the density of the monomer. From this equation it is possible to see that the aggregate density is lower than the monomer density only if $d_f < 3$.

Concerning shape factors, experimental evidences showed that by using a laser particle sizer, when crystals are flat the crystal size detected by the instrument (d_{43}) is approximately the width of the crystal [26], whereas when crystals are round-shaped it is approximately the diameter of the sphere that includes the crystal. If these are chosen as characteristic dimensions, and $d_f = 3$, real shape factors (K_a, K_v) are defined as follows

$$V = K_v d_{43}^3, \tag{1.36}$$

$$A = K_a d_{43}^2. \tag{1.37}$$

Generally K_a/K_v is not equal to 6, that is the characteristic value for a system with equidimensional growth [27]. Equidimensioned regular objects require equal growth rates along every particle axis. However it can be shown that an intermediate diameter can always be chosen as the characteristic dimension L_{43} such that the shape factor ratio is equal to 6. As it will become clearer in the next chapters, this characteristic dimension is also the internal coordinate used to define the population balance. For this reason, average shape factors (k_a, k_v) must of course be in reference to this characteristic size, as follows:

$$V = k_v L_{43}^3, \tag{1.38}$$

$$A = k_a L_{43}^2. \tag{1.39}$$

In the case of equidimensional growth, equating the change of volume, for a growing particle, to the rate of advance of the particle's surface gives

$$\frac{\mathrm{d}V}{\mathrm{d}t} = \frac{1}{2} G A. \tag{1.40}$$

For particles having a different growth rate G_j for each crystal face A_j, the above relationship is only valid for the characteristic size L_{43} chosen as some suitable intermediate size. Repeating the previous calculation for this case

$$\frac{\mathrm{d}V}{\mathrm{d}t} = \sum_j \left(\frac{1}{2} G_j A_j\right), \tag{1.41}$$

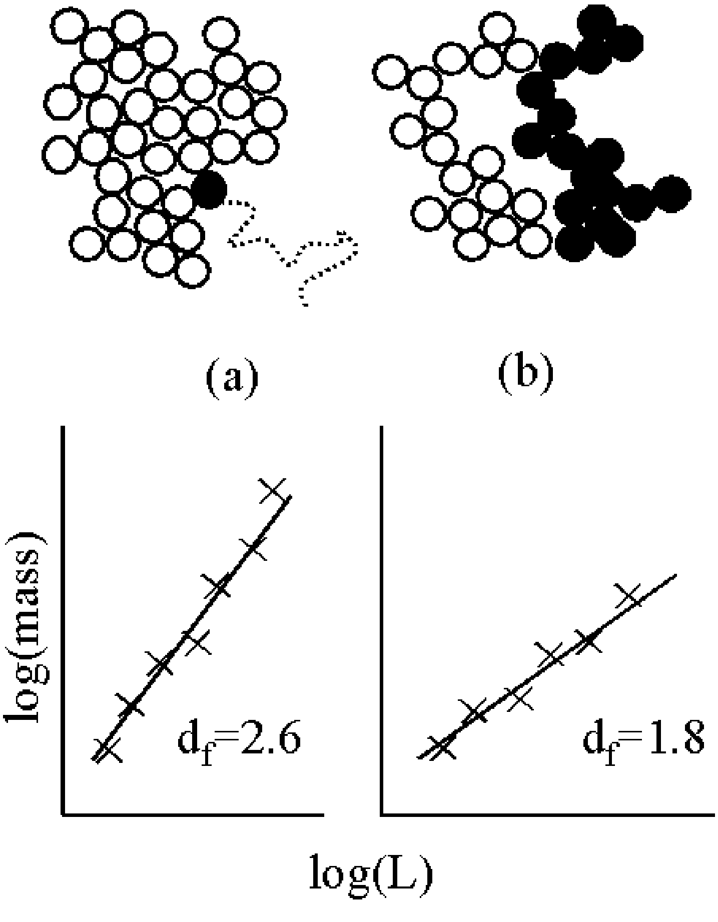

Figure 1.4: Fractal aggregates produced by (a) single-particle addition to an aggregate and (b) cluster-cluster aggregation. In the latter case, aggregates have a more open structure and have a lower fractal dimension.

and if the growth rate along each axis G_j is related to the growth rate along the characteristic axis L_{43}, by a constant factor $G_j = c_j G = (L_j/L_{43})G$, substituting Eq. 1.38 into Eq. 1.41 gives

$$\frac{\mathrm{d}}{\mathrm{d}t}(k_v L_{43}^3) = \frac{1}{2} G \sum_j c_j A_j, \tag{1.42}$$

and as a consequence

$$6 k_v L_{43}^2 = \sum_j c_j A_j = A. \tag{1.43}$$

Thus substituting Eq. 1.39 into Eq. 1.43 yields $k_a = 6k_v$. This last relationship can be preserved if L_{43} is chosen in such a way that $\sum_j c_j A_j = \sum_j (L_j/L_{43}) A_j = A$.

In practical applications, once real shape factors (K_v, K_a), are experimentally determined, average shape factors (k_v, k_a), have to be recalculated in terms of L_{43}

$$V = K_v d_{43}^3 = k_v L_{43}^3, \tag{1.44}$$

$$A = K_a d_{43}^2 = k_a L_{43}^2, \tag{1.45}$$

superimposing equidimensional growth,

$$k_a / k_v = 6. \tag{1.46}$$

With this approach new shape factors are obtained and the relationship between real and characteristic crystal size can be written as

$$d_{43} = \phi_c L_{43} \tag{1.47}$$

where ϕ_c is derived by solving Eqs. 1.44-1.45- 1.46.

Chapter 2

Governing equations

The governing equations for the transport of reactive scalars in fluid flows with constant density are as follows (repeated indices imply summation):

$$\frac{\partial u_i}{\partial x_i} = 0, \tag{2.1}$$

$$\frac{\partial u_i}{\partial t} + u_j \frac{\partial u_i}{\partial x_j} = -\frac{1}{\rho}\frac{\partial p}{\partial x_i} + \frac{1}{\rho}\frac{\partial \tau_{ij}}{\partial x_j}, \tag{2.2}$$

$$\frac{\partial \phi_\alpha}{\partial t} + u_j \frac{\partial \phi_\alpha}{\partial x_j} = \Gamma_\alpha \nabla^2 \phi_\alpha + S_\alpha(\boldsymbol{\phi}), \tag{2.3}$$

where the viscous stress tensor is defined as

$$\tau_{ij} = \mu \left(\frac{\partial u_i}{\partial x_j} + \frac{\partial u_j}{\partial x_i} \right). \tag{2.4}$$

In these equations u_i is the fluid velocity, p is the pressure, ρ is the fluid density, ϕ_α are the scalars under consideration (i.e., concentration, temperature, moments of the CSD), Γ_α is the molecular diffusivity of ϕ_α and $S_\alpha(\boldsymbol{\phi})$ is the chemical source term. In this chapter these equations will be presented and explained. Moreover, the transport equations of other useful variables will be derived, highlighting the presence of some unclosed terms. In the following chapters theories and results will be presented and used to discuss the closure problem.

2.1 Mean velocities and Reynolds stresses

As it will become clearer in the next chapter, when the flow is turbulent any instantaneous property of the flow can be seen as a random variation around a mean value:

$$u_i = \langle u_i \rangle + u_i', \tag{2.5}$$

where $\langle u_i \rangle$ is the mean velocity, and u_i' is the fluctuating term. Different mean values exist: according to the definition of Hinze [28], the time-average at a fixed position (for steady-state flows) is given by:

$$\langle u_i \rangle = \frac{1}{T}\int_0^T u_i dt, \tag{2.6}$$

where T is the time interval during which the determination of the mean takes place. In statistics one can also define an ensemble average. Let us consider a great number N of identical macroscopic flows. If the velocity is measured simultaneously at corresponding points in these flows, the ensemble average can be defined as:

$$\langle u_i \rangle = \frac{1}{N} \sum_{n=1}^{N} u_i^{(n)}. \tag{2.7}$$

Turbulent phenomena are assumed to be ergodic, hence time average and ensemble average are identical, supposed that N and T are big enough to catch the true mean value. Applying this approach (Reynolds decomposition) to the continuity equation results in [29]:

$$\frac{\partial \langle u_i \rangle}{\partial x_i} = 0, \tag{2.8}$$

whereas the Navier-Stokes equation becomes:

$$\frac{\partial \langle u_i \rangle}{\partial t} + \langle u_j \rangle \frac{\partial \langle u_i \rangle}{\partial x_j} = \nu \nabla^2 \langle u_i \rangle - \frac{1}{\rho} \frac{\partial \langle p \rangle}{\partial x_i} - \frac{\partial}{\partial x_j} \langle u_i' u_j' \rangle, \tag{2.9}$$

which is known as Reynolds-averaged Navier-Stokes (RANS) equation. The last term on the right-hand side is a symmetric second order tensor and is known as Reynolds stress tensor, and because of its presence Eq. 2.9 is unclosed. From the Navier-Stokes equation it is possible to derive the transport equation for the Reynolds stresses, yielding

$$\frac{\partial \langle u_i' u_j' \rangle}{\partial t} + \langle u_k \rangle \frac{\partial \langle u_i' u_j' \rangle}{\partial x_k} + \frac{\partial \langle u_i' u_j' u_k' \rangle}{\partial x_k} = P_{ij} + \Pi_{ij} + \nu \nabla^2 \langle u_i' u_j' \rangle - \varepsilon_{ij}, \tag{2.10}$$

where P_{ij} and Π_{ij} are the production term and the velocity-pressure-gradient term respectively:

$$P_{ij} = -\langle u_i' u_k' \rangle \frac{\partial \langle u_j \rangle}{\partial x_k} - \langle u_j' u_k' \rangle \frac{\partial \langle u_i \rangle}{\partial x_k}, \tag{2.11}$$

and

$$\Pi_{ij} = -\frac{1}{\rho} \left\langle u_i' \frac{\partial p}{\partial x_j} + u_j' \frac{\partial p}{\partial x_i} \right\rangle. \tag{2.12}$$

The production term represents the source for the Reynolds stresses due to mean velocity gradients and it is in closed form, whereas the velocity-pressure-gradient term accounts for the correlations between velocity fluctuations and the fluctuating pressure field and is unclosed. The unclosed dissipation rate tensor is defined as follows

$$\varepsilon_{ij} = 2\nu \left\langle \frac{\partial u_i'}{\partial x_k} \frac{\partial u_j'}{\partial x_k} \right\rangle, \tag{2.13}$$

and describes the dissipation of velocity fluctuations at the Kolmogorov microscale, as it will be explained in the next chapter. The molecular transport term $\nu \nabla^2 \langle u_i' u_j' \rangle$ is usually negligible at high-Reynolds-number flows, and in these conditions it is also possible to write the dissipation rate tensor ε_{ij} in terms of a scalar ε:

$$\varepsilon_{ij} = \frac{2}{3} \varepsilon \delta_{ij}. \tag{2.14}$$

2.2 Turbulent kinetic energy and turbulent dissipation rate

Summing over the diagonal of the Reynolds stress tensor results in the turbulent kinetic energy transport equation

$$\frac{\partial k}{\partial t}+\langle u_k\rangle\frac{\partial k}{\partial x_k}+\frac{1}{2}\frac{\partial\langle u'_j u'_j u'_i\rangle}{\partial x_i}+\frac{1}{\rho}\frac{\partial\langle u'_i p\rangle}{\partial x_i}=\mathcal{P}+\nu\nabla^2 k-\varepsilon^* \tag{2.15}$$

where k is the turbulent kinetic energy defined as

$$k=\frac{1}{2}\langle u'_i u'_i\rangle=\frac{1}{2}\left(\langle u'_1 u'_1\rangle+\langle u'_2 u'_2\rangle+\langle u'_3 u'_3\rangle\right), \tag{2.16}$$

the production term is

$$\mathcal{P}=-\langle u'_i u'_j\rangle\frac{\partial\langle u_i\rangle}{\partial x_j}, \tag{2.17}$$

and ε^* is the pseudo dissipation rate

$$\varepsilon^*=\varepsilon-\nu\frac{\partial^2\langle u'_i u'_j\rangle}{\partial x_i\partial x_j}, \tag{2.18}$$

that for high-Reynolds-number flows is approximately equal to ε. Starting from the transport equation of the fluctuating velocity gradient $\partial u'_i/\partial x_j$, it is possible to write the transport equation for the turbulent dissipation rate:

$$\frac{\partial\varepsilon}{\partial t}\langle u_i\rangle\frac{\partial\varepsilon}{\partial x_i}=\nu\nabla^2\varepsilon-\frac{\partial}{\partial x_i}\left[\langle u'_i\epsilon\rangle+T^{(p)}_{\varepsilon,i}\right]+\mathcal{S}_\varepsilon+\mathcal{C}_\varepsilon+\mathcal{V}_\varepsilon-\mathcal{D}_\varepsilon, \tag{2.19}$$

where $\varepsilon=\langle\epsilon\rangle$ and ϵ is the random dissipation rate, $\langle u'_i\epsilon\rangle$ is the unclosed term for the transport due to velocity fluctuations, $T^{(p)}_{\varepsilon,i}$ is the unclosed pressure transport term:

$$T^{(p)}_{\varepsilon,i}=\left\langle\frac{2\nu}{\rho}\frac{\partial u'_i}{\partial x_j}\frac{\partial p}{\partial x_j}\right\rangle, \tag{2.20}$$

$\mathcal{S}_\varepsilon$ is the mean-velocity-gradient production term, $\mathcal{C}_\varepsilon$ is the mean-velocity-gradient curvature term, $\mathcal{V}_\varepsilon$ is the vortex-straining term, and $\mathcal{D}_\varepsilon$ is the gradient-dissipation term. It can be shown that $\mathcal{S}_\varepsilon$ and $\mathcal{C}_\varepsilon$ at sufficiently high Reynolds number, can be neglected [29], whereas the remaining two terms $\mathcal{V}_\varepsilon$ and $\mathcal{D}_\varepsilon$ can be written in closed form under some simplifications in terms of the spectral energy transfer rate, that will be introduced in the next chapter.

2.3 Scalar mean and flux

Concerning the scalar transport equation (see Eq. 2.3), if Reynolds-average is applied results in:

$$\frac{\partial\langle\phi_\alpha\rangle}{\partial t}+\langle u_j\rangle\frac{\partial\langle\phi_\alpha\rangle}{\partial x_j}=\Gamma_\alpha\nabla^2\langle\phi_\alpha\rangle-\frac{\partial\langle u'_j\phi_\alpha\rangle}{\partial x_j}+\langle S_\alpha(\boldsymbol{\phi})\rangle, \tag{2.21}$$

the first term on the right-hand side is the molecular transport term, which is negligible in high-Reynolds-number flows, $\langle u'_j\phi_\alpha\rangle$ is the scalar flux, which takes into account the scalar transport due to velocity fluctuations, and $\langle S_\alpha(\boldsymbol{\phi})\rangle$ is the mean chemical source term. As for the Reynolds stresses also for the scalar flux it is possible to derive a transport equation

$$\begin{aligned}\frac{\partial\langle u_i'\phi_\alpha\rangle}{\partial t} + \langle u_j\rangle\frac{\partial\langle u_i'\phi_\alpha\rangle}{\partial x_j} = \frac{\partial}{\partial x_j}\left[\langle u_j'u_i'\phi_\alpha\rangle + \mathcal{T}_{ij}^k\right]+,\\ \mathcal{P}_i^\alpha + \Pi_i^\alpha - \varepsilon_i^\alpha + \langle u_i'S_\alpha(\boldsymbol{\phi})\rangle,\end{aligned} \tag{2.22}$$

where $\mathcal{T}_{ij}^\alpha$ contains the triple correlation term and molecular transport term that are responsible for spatial transport of scalar flux, $\mathcal{P}_i^\alpha$ is the production term, Π_i^α is the pressure- scrambling term, ε_i^α is the scalar flux dissipation, and the last term is the unclosed term for describing the correlation between fluctuating velocity and chemical-source term.

2.4 Scalar variance and scalar dissipation rate

The transport equation of the scalar variance can be easily derived if a not-reacting scalar (ϕ) is considered, and results in what follows [30]

$$\frac{\partial\langle\phi'^2\rangle}{\partial t} + \langle u_j\rangle\frac{\partial\langle\phi'^2\rangle}{\partial x_j} = \Gamma\nabla^2\langle\phi'^2\rangle - \frac{\partial\langle u_j'\phi'^2\rangle}{\partial x_j} + \mathcal{P}_\phi - \varepsilon_\phi, \tag{2.23}$$

where $\mathcal{P}_\phi$ is the production term of scalar variance, which is defined as:

$$\mathcal{P}_\phi = -2\langle u_j'\phi\rangle\frac{\partial\langle\phi\rangle}{\partial x_j}, \tag{2.24}$$

and ε_ϕ is the scalar dissipation rate defined by

$$\varepsilon_\phi = 2\Gamma\left\langle\frac{\partial\phi'}{\partial x_i}\frac{\partial\phi'}{\partial x_i}\right\rangle. \tag{2.25}$$

The production term is always positive and represents the generation of scalar variance by mean scalar gradients. The last term represents the molecular dissipation that occurs at the Batchelor microscale as it will be explained in the next chapter. Also for the scalar dissipation rate it is possible to derive a transport equation [30]

$$\begin{aligned}\frac{\partial\varepsilon_\phi}{\partial t} + \langle u_j\rangle\frac{\partial\varepsilon_\phi}{\partial x_j} = \Gamma\nabla^2\varepsilon_\phi - \frac{\partial\langle u_j'\varepsilon_\phi\rangle}{\partial x_j}+,\\ \mathcal{S}_\varepsilon{}^\phi + \mathcal{G}_\varepsilon{}^\phi + \mathcal{C}_\varepsilon{}^\phi + \mathcal{V}_\varepsilon{}^\phi - \mathcal{D}_\varepsilon{}^\phi,\end{aligned} \tag{2.26}$$

where $\mathcal{S}_\varepsilon{}^\phi$ is the mean-velocity-gradient term, $\mathcal{G}_\varepsilon{}^\phi$ is the mean-scalar-gradient term, $\mathcal{C}_\varepsilon{}^\phi$ is the mean-scalar-curvature term, $\mathcal{V}_\varepsilon{}^\phi$ is the vortex-stretching term, and $\mathcal{D}_\varepsilon{}^\phi$ is the gradient-dissipation term. In high-Reynolds-number flows the scalar dissipation flux $\langle u_j'\varepsilon_\phi\rangle$ is the dominant term, whereas $\mathcal{S}_\varepsilon{}^\phi$, $\mathcal{G}_\varepsilon{}^\phi$, and $\mathcal{C}_\varepsilon{}^\phi$ are negligible. As concerns $\mathcal{V}_\varepsilon{}^\phi$ and $\mathcal{D}_\varepsilon{}^\phi$, under some simplifications, they can be written as follows:

$$\mathcal{V}_\varepsilon{}^\phi \propto \frac{\varepsilon}{k}\varepsilon_\phi, \tag{2.27}$$

$$\mathcal{D}_\varepsilon{}^\phi \propto \frac{\varepsilon_\phi}{\langle\phi'^2\rangle}\varepsilon_\phi, \tag{2.28}$$

and thus in the case of homogeneous turbulent mixing the scalar dissipation rate transport equation becomes [30]

$$\frac{\mathrm{d}\varepsilon_\phi}{\mathrm{d}t} = \mathcal{V}_\varepsilon{}^\phi - \mathcal{D}_\varepsilon{}^\phi, \tag{2.29}$$

where is clear the role of production and dissipation of the two terms. For a fully-developed scalar spectrum, when the stationary solution is reached (i.e., $\mathrm{d}\varepsilon_\phi/\mathrm{d}t{=}0$) it results in

$$\mathcal{V}_{\varepsilon}{}^{\phi} \approx \mathcal{D}_{\varepsilon}{}^{\phi}, \tag{2.30}$$

and with the approximation of Eqs. 2.27 and 2.28 yields

$$\frac{\varepsilon_\phi}{\langle \phi'^2 \rangle} = C_\phi \frac{\varepsilon}{k}, \tag{2.31}$$

which is a widely used closure model for the scalar dissipation rate, as it will be explained later.

Chapter 3

Turbulence and turbulent mixing

As mentioned in the previous chapter, in turbulent flows any instantaneous property of the system is characterized by a random variation around a mean value. If the signal is subtracted by the mean value it appears as a highly disorganized fluctuation around zero and presents structures on all scales; another important property is that the system is extremely sensitive to initial conditions, and as a consequence the state of the system cannot be predicted, or in other words, the signal appears unpredictable in its detailed behavior. However, although the detailed properties of the signal appear not to be predictable, its statistical properties are reproducible. For this reason study of turbulence is based on a probabilistic description by means of the probability density function approach. However the description of the problem presented in the previous chapter is deterministic. How can this chaotic behavior arise from a purely deterministic context?

3.1 Turbulence as deterministic chaos

It is possible to answer to this question by considering the Navier-Stokes equation:

$$\frac{\partial u_i}{\partial t} = -u_j \frac{\partial u_i}{\partial x_j} + \nu \nabla^2 u_i - \frac{1}{\rho}\frac{\partial p}{\partial x_i}. \tag{3.1}$$

This equation describes the dynamic evolution of a nonlinear system, in which the velocity vector u_i ($i = 1, 2, 3$) defines a three-dimensional phase space, the so-called velocity space. The trajectory of such a system is a curve in a three-dimensional space. Instead of looking at the whole trajectory we consider its successive intersections with a two-dimensional surface S arbitrary chosen. The trajectory is thus replaced by an infinite set of discrete points, and as a consequence the properties of the trajectory itself are reflected into corresponding properties of the set of points. This set of points is generated by the repeated application of a mapping function, which is a difference equation. The poor man's Navier-Stokes equation [31]:

$$u_{t+1} = 1 - 2u_t^2. \tag{3.2}$$

is a mapping function where there is no spatial structure, and the comparison with the Navier-Stokes equation

$$\begin{aligned} u_{t+1} - u_t &= -2u_t^2 - u_t + 1, && (3.3)\\ \frac{\partial u_i}{\partial t} &= -u_j \frac{\partial u_i}{\partial x_j} + \nu \nabla^2 u_i - \frac{1}{\rho}\frac{\partial p}{\partial x_i}, && (3.4) \end{aligned}$$

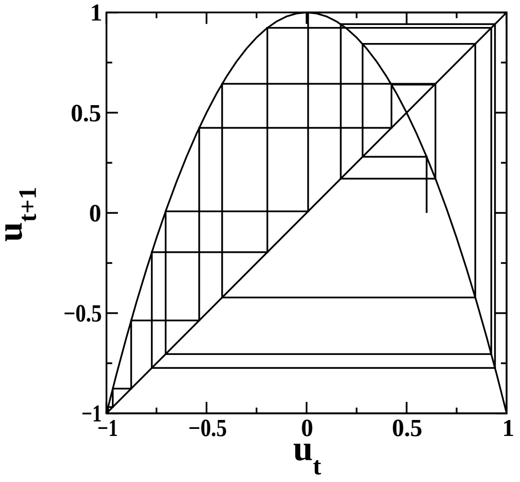

Figure 3.1: Orbit for the poor man's Navier Stokes map with $w = 0.60$.

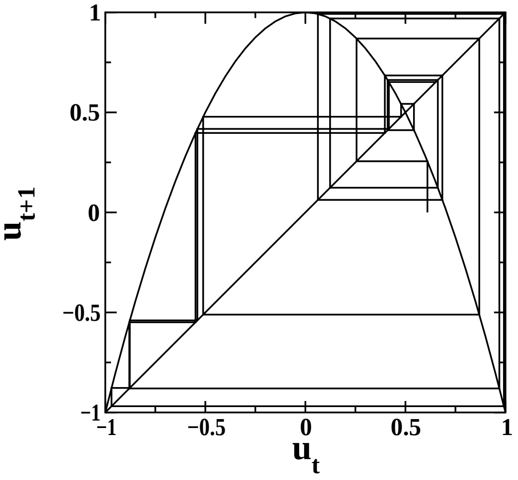

Figure 3.2: Orbit for the poor man's Navier Stokes map with $w = 0.61$.

shows that it has the equivalent of the nonlinear term, the viscous term and the force term, of the original equation. In this representation the velocity vector u_i is represented by u_t, which is a real number between -1 and +1. Given an initial value $u_0 = w$ a set of iterates $t = 0, 1, 2, ...$ is called an orbit in the phase space. As it is possible to see from Figs. 3.1 and 3.2 given two initial conditions which differ in a minute way, after iterations, will separate very quickly. This sensitivity to initial conditions is often loosely referred to as chaos.

Another important property is the existence of an invariant measure; in fact, by selecting the initial conditions in a uniform distributions within the interval [-1,+1], the maps gives back iterates in a uniform interval. It is now clear how the Navier-Stokes equations can be seen as a dynamic system, but nevertheless one should always remember that the poor man's model is only a simplified approach. In fact, when dealing with three dimensional Navier-Stokes equation the existence and uniqueness of the solution is not guaranteed. Moreover, it is typical for dissipative systems to have their invariant measure concentrated in an attractor with a fractal structure[1] and to have more than one attractor, and therefore more than one invariant measure. As a consequence the statistical properties of the solution will depend on which basin the initial condition belongs to.

3.2 Turbulence

3.2.1 The probability density function approach

As already mentioned any property of a turbulent flow can be seen as a random variation that can be described in terms of its probability density function (PDF). For example, for the velocity vector $u_i(\mathbf{x}, t)$:

$$f_u(\mathbf{v}; \mathbf{x}, t) = P[v_i < u_i(\mathbf{x}, t) < v_i + dv_i, i = 1, 2, 3], \tag{3.5}$$

where v_i represents the sample-space variable corresponding to the random variable $u_i(\mathbf{x}, t)$. This function is called the one-point, one-time, joint probability density function of velocity: it contains information about the velocity in one position and in one instant. In

---

[1] We shall come back to this aspect at pag. 68

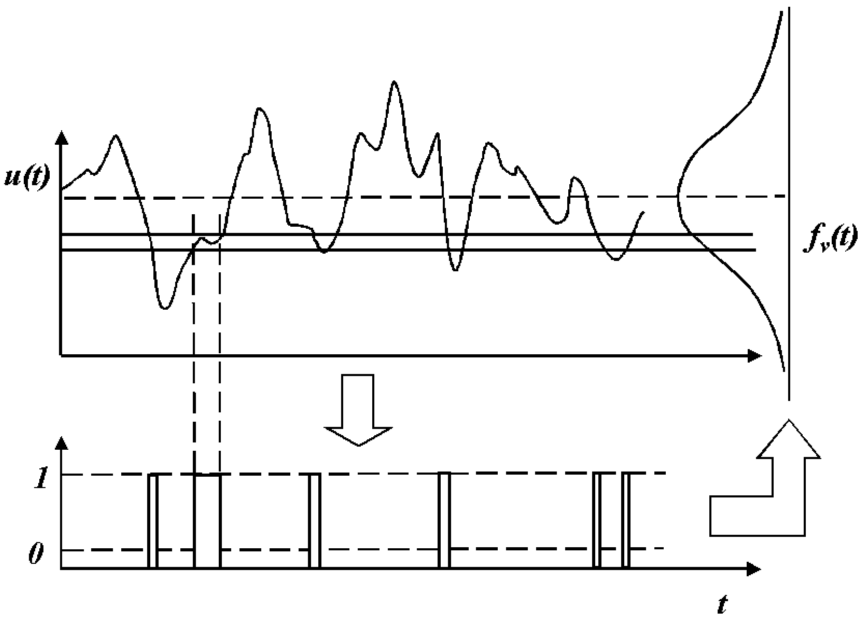

Figure 3.3: Measurement of the probability density function of a stationary function.

Fig. 3.3 the PDF of a statistically steady signal is reported. Starting from the fluctuating signal $u(t)$ it is possible to derive the PDF, as indicated in the figure. Using this approach the mean velocity field can be derived as follows:

$$\langle \mathbf{u}(\mathbf{x},t)\rangle = \int\!\!\int\!\!\int_{-\infty}^{+\infty} \mathbf{v} f_u(\mathbf{v};\mathbf{x},t)d\mathbf{v}. \tag{3.6}$$

The N-point, N-time joint PDF can be defined as an extension of the previous one. Let $(\mathbf{x}^{(n)}, t^{(n)})$ be a specified set of positions and times. Then it is possible to define $f_{u,N}(\mathbf{v^{(1)}}, \mathbf{x}^{(1)}, t^{(1)}; ...; \mathbf{v^{(N)}}, \mathbf{x}^{(N)}, t^{(N)})$ to be the joint PDF of the velocity at these N space-time points [29].

3.2.2 Structure functions and autocorrelation functions

Let us consider an homogeneous and isotropic turbulent field. The turbulence is homogeneous if $f_{u,N}$ is independent of the position, and is isotropic if it is invariant in respect to rotations and reflections of the coordinate axes. The second-order velocity structure function is the covariance of the difference in the velocity differences between two points $\mathbf{x}+\mathbf{r}$ and $\mathbf{x}$

$$D_{ij}(\mathbf{r},\mathbf{x},t) = \langle [u_i(\mathbf{r}+\mathbf{x},t) - u_i(\mathbf{x},t)][u_j(\mathbf{r}+\mathbf{x},t) - u_j(\mathbf{x},t)]\rangle\,. \tag{3.7}$$

Under the hypothesis of homogeneous and isotropic field it can be shown that D_{ij} is independent of the position, and can be written in terms of two scalar functions $D_{LL}(r,t)$ and $D_{NN}(r,t)$ which are called longitudinal and transverse structure functions:

$$D_{ij}(\mathbf{r},t) = D_{NN}(r,t)\delta_{ij} + [D_{LL}(r,t) - D_{NN}(r,t)]\frac{r_i r_j}{r^2}. \tag{3.8}$$

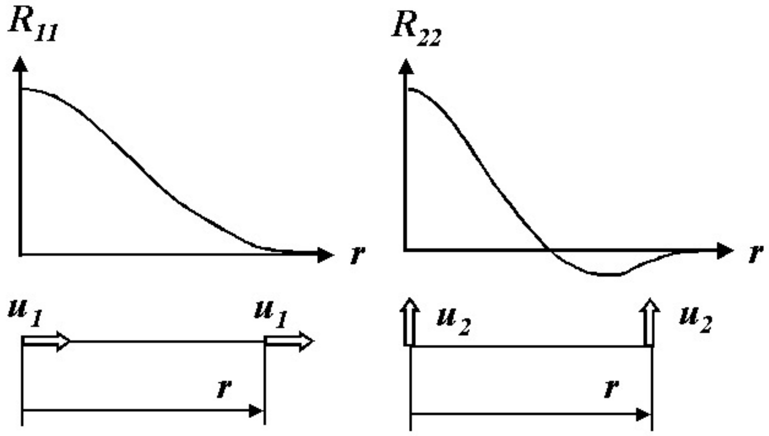

Figure 3.4: Longitudinal and transverse functions, defined in the figure as R_{11} and R_{22}.

From the continuity equation and Eq. 3.8, it is possible to show that D_{NN} is uniquely determined by D_{LL} as follows

$$D_{NN}(r,t) = D_{LL}(r,t) + \frac{r}{2}\frac{\partial}{\partial r}D_{LL}(r,t). \tag{3.9}$$

In parallel with what is done for D_{ij} it is possible to define the autocorrelation function according to

$$R_{ij}(\mathbf{r},t) = \langle u'_i(\mathbf{r}+\mathbf{x},t)u'_j(\mathbf{x},t)\rangle. \tag{3.10}$$

Notice that also in this case R_{ij} is independent of the position because of the hypothesis of homogeneous field. It is evident that at the origin

$$R_{ij}(0,t) = \langle u'_i u'_j\rangle, \tag{3.11}$$

the autocorrelation function is the Reynolds stress tensor, that has been defined in the previous chapter. Again a consequence of isotropy is that R_{ij} can be expressed in terms of two scalar functions

$$R_{ij}(\mathbf{r},t) = u'^2\left(g(r,t)\delta_{ij} + [f(r,t)-g(r,t)]\frac{r_i r_j}{r^2}\right), \tag{3.12}$$

where f and g are the longitudinal and transverse autocorrelation functions, and u'^2 is the root-mean-square of velocity. If the coordinate system is chosen so that r is the x_1 direction we obtain

$$\begin{aligned} f(r,t) &= R_{11}/u'^2 \\ g(r,t) &= R_{22}/u'^2 \\ R_{33} &= R_{22}, \\ R_{ij} &= 0 \quad i \neq j, \end{aligned}$$

that are reported in Fig. 3.4. In parallel with the properties of D_{ij} it can be shown that also g is completely determined by the longitudinal autocorrelation function f according to

$$g(r,t) = f(r,t) + \frac{r}{2}\frac{\partial}{\partial r} f(r,t). \tag{3.13}$$

From this two functions it is possible to derive some integral length scales. The longitudinal integral scale

$$L_{11}(t) = \int_0^\infty f(r,t)dr, \tag{3.14}$$

and the transverse integral scale

$$L_{22}(t) = \int_0^\infty g(r,t)dr, \tag{3.15}$$

that is just half of L_{11}. The integral scales L_{11} and L_{22} are proportional to a turbulent integral scale L_u defined as

$$L_u = \frac{k^{3/2}}{\varepsilon\nu}. \tag{3.16}$$

If the autocorrelation function is defined in terms of the time τ instead of the distance $\mathbf{r}$ an integrale time scale τ_u is found

$$\tau_u = \frac{k}{\varepsilon}. \tag{3.17}$$

Other important scales are the longitudinal Taylor microscale, defined as

$$\lambda_f(t) = [-\frac{1}{2} f''(0,t)]^{-1/2}, \tag{3.18}$$

that can be though of as the intersection on the abscissas axis of the osculating parabola of the longitudinal autocorrelation function, and the transverse Taylor microscale, which is defined as follows:

$$\lambda_g(t) = \frac{1}{\sqrt{2}}\lambda_f(t). \tag{3.19}$$

3.2.3 Velocity-spectrum tensor and energy-spectrum function

As it will become clearer in the next sections it is very useful to describe the homogeneous turbulence problem in terms of the Fourier-transform. The Fourier-transform of the two-point velocity correlation function (R_{ij}) is the velocity-spectrum tensor

$$\mathbf{\Phi}_{ij}(\boldsymbol{\kappa}) = \frac{1}{(2\pi)^3} \int\int_{-\infty}^{+\infty}\int R_{ij}(\mathbf{r}) e^{-i\boldsymbol{\kappa}\cdot\mathbf{r}} d\mathbf{r}, \tag{3.20}$$

where $\boldsymbol{\kappa}$ is the wave number vector. This tensor contains a great deal of information, and can be transformed in a function in which all directional information is removed. This can be done by integrating over all wave numbers of magnitude $|\boldsymbol{\kappa}| = \kappa$. Mathematically, this is an integration over a surface of radius κ. Thus the energy-spectrum is defined as

$$E(\kappa) = \oint \frac{1}{2}\mathbf{\Phi}_{ij}(\boldsymbol{\kappa}) dS(\kappa). \tag{3.21}$$

Interesting properties of this function are

$$k = \int_{0}^{+\infty} E(\kappa) d\kappa, \tag{3.22}$$

and

$$\varepsilon = \int_{0}^{+\infty} 2\nu k^2 E(\kappa) d\kappa. \tag{3.23}$$

It is evident that $E(\kappa)d\kappa$ is the contribution to the turbulent kinetic energy k from all the wave numbers κ in the infinitesimal shell of radius $\mid \kappa \mid$ in the wave number space.

3.2.4 The Kolmogorov 1941 theory

The celebrated Kolmogorov 1941 theory (K41) starts from the formulation of some hypothesis, compatible with the Navier-Stokes equations, and leads to additional predictions, that were compared with some basic experimental laws. One of the main experimental results concerning fully developed turbulent fields is the so-called **two-thirds law**:

> In a turbulent flow at very high Reynolds number, the longitudinal structure function behaves as the two-third power of the distance.

It can be shown that when the energy-spectrum is represented by a power law

$$E(\kappa) \propto \kappa^{-n} \tag{3.24}$$

the second-order velocity structure function is also a power law

$$D_{ij} \propto r^{n-1}. \tag{3.25}$$

A consequence of the two-third law is that there is a region where the energy-spectrum behaves as $k^{-5/3}$. For sufficiently high Reynolds number, this exponent is observed over a very substantial range of several decades of wavenumber. This range is called the inertial sub-range as it will be explained later. The K41 was able to predict this behavior as a result of the **four-fifth law**:

> In the limit of infinite Reynolds number, the third order longitudinal structure function $D_{LLL}(r,t)$ of homogeneous isotropic turbulence, evaluated for small spatial increments compared to the integral scale, is given in terms of the mean energy dissipation per unit mass ε by
>
> $$D_{LLL}(r,t) = -\frac{4}{5}\varepsilon r. \tag{3.26}$$

From this result it is possible to derive also an expression for the second order longitudinal structure function, leading to

$$D_{LL}(r,t) = C_2(\varepsilon r)^{2/3}, \tag{3.27}$$

where C_2 is a constant.

3.2.5 Energy cascade

A turbulent flow can be considered to be composed of eddies of different size and energy. For each bunch of eddies it is possible to define a characteristic size and velocity. The largest eddies have a size comparable to the flow scale, and their characteristic velocity is of the order of magnitude of the root mean square of the velocity fluctuation.

In this range the effect of the viscosity is negligible. This is the so-called energy-containing range ($\kappa < \kappa_{EI}$, see Fig. 3.5 at page 34) in which the energy is added by extracting from the mean flow field, as described by the kinetic energy production term (see Eq. 2.15). The large eddies are unstable and break up, transferring energy to smaller eddies. This is the Richarson's energy cascade: the energy is transferred to smaller and smaller eddies, and this range of the spectrum is known as the inertial sub-range ($\kappa_{EI} > \kappa > \kappa_{DI}$). When the Reynolds number of the eddy is sufficiently small that the eddy motion is stable, the molecular viscosity is effective in dissipating the kinetic energy. This range is called the dissipation range ($\kappa > \kappa_{DI}$).

For these two sub-ranges (inertial and dissipative) the time scales are small compared with the flow scale, and for this reason this region is called the universal range equilibrium. Under the hypothesis of local isotropy and of similarity, the statistics of the small-scale motions have an universal form that is uniquely determined by the kinematic viscosity ν and the turbulent dissipation rate ε. Given these two parameters there are unique length, velocity and time scales, that are the Kolmogorov microscales

$$\begin{aligned} \lambda_k &= (\nu^3/\varepsilon)^{1/4}, \\ u_k &= (\varepsilon\nu)^{1/4}, \\ \tau &= (\nu/\varepsilon)^{1/2}. \end{aligned} \tag{3.28}$$

It is interesting to notice that the Reynolds number at the Kolmogorov scale is equal to one. This is consistent with the idea of the cascade, that proceeds to smaller scales until the Reynolds number is small enough for dissipation to be effective. Thus the Kolmogorov microscale can be though of as the size of the smallest eddy of the flow. It is interesting to determine the relationship between the Taylor and the Kolmogorov microscales. For this purpose we define a Reynolds number to be

$$Re_L = \frac{k^{1/2} L_u}{\nu}, \tag{3.29}$$

and then the relationships are:

$$\begin{aligned} \frac{\lambda_g}{L_u} &= \sqrt{10} Re_L^{-1/2}, \\ \frac{\lambda_k}{L_u} &= Re_L^{-3/4}, \\ \frac{\lambda_k}{\lambda_g} &= \frac{Re_L^{-1/4}}{\sqrt{10}}. \end{aligned} \tag{3.30}$$

Thus at high Reynolds number, the Taylor scale is intermediate in size between the integral and the Kolmogorov scale. However it should be mentioned that λ_g does not have any physical meaning.

Another consequence of the universal theory is that in the equilibrium range the spectrum is uniquely determined by ν and ε. From a simple dimensional analysis it is possible to show that this universal relationship can be written as

$$E(\kappa) = \varepsilon^{2/3} \kappa^{-5/3} \Psi(\kappa \lambda_k), \tag{3.31}$$

and in the inertial sub-range, the function Ψ becomes independent of its argument, and tends to a constant C. This is the famous Kolmogorov spectrum, and C is the universal Kolmogorov constant. Experimental data support the value $C = 1.5$.

3.2.6 Spectral transport

This picture of the energy cascade can be quantified and summarized in the following transport equation [32]

$$\frac{\partial}{\partial t}E(\kappa, t) = \mathcal{P}_k(\kappa, t) - \frac{\partial}{\partial \kappa}\mathcal{T}_k(\kappa, t) - 2\nu\kappa^2 E(\kappa, t), \tag{3.32}$$

valid for homogeneous turbulence with imposed mean gradients. The production term $\mathcal{P}_k$ is mainly given by the mean velocity gradients, and represents the injection of energy at the large scales (energy-containing range). The spectral energy transfer rate $\mathcal{T}_k$ is the net rate at which the energy is transferred at the smaller scales. Since this term tends to zero at zero and infinite wave number, and since it contributes in the balance in terms of its derivative in respect with κ, its contribution to the balance of the turbulent kinetic energy is null. The last term is the dissipation due to viscosity. Integrating the energy-spectrum balance over the wave number κ in the energy-containing range, the dissipation contribution can be neglected, yielding

$$\frac{\partial k}{\partial t} = \mathcal{P} - \mathcal{T}_{EI}, \tag{3.33}$$

where $\mathcal{T}_{EI}$ is the value of the spectral transfer funtion at the border of the energy-containing range (κ_{EI}). In the inertial subrange both dissipation and production can be neglected, and only spectral transfer is significant

$$0 = \mathcal{T}_{EI} - \mathcal{T}_{DI}, \tag{3.34}$$

where $\mathcal{T}_{DI}$ is the value of the spectral transfer function at the border of the inertial sub-range κ_{DI}. In the dissipation range, production can be neglected yielding

$$0 = \mathcal{T}_{DI} - \varepsilon. \tag{3.35}$$

If these three equations are added together it results in the turbulent-kinetic-energy equation

$$\frac{\partial k}{\partial t} = \mathcal{P} - \varepsilon, \tag{3.36}$$

which highlights the essence of the energy cascade: energy is produced at large scales in a non-universal way, depending on the mean velocity gradients, then energy is transferred at smaller scales, and dissipated at the Kolmogorov scale by molecular dissipation.

3.3 Turbulent mixing

3.3.1 Spatial correlation for the scalar field

In parallel with what done for the velocity fluctuations, it is possible to define a spatial correlation in terms of the fluctuating scalar field:

$$R_\phi(\mathbf{r}, t) = \langle \phi'(\mathbf{x} + \mathbf{r}, t)\phi'(\mathbf{x}, t)\rangle. \tag{3.37}$$

As like for the velocity spatial correlation function, R_ϕ contains scale information about the scalar field. Let us consider an homogeneous and isotropic scalar field: this function can be normalized yielding

$$f_\phi(r,t) = R_\phi(r,t)/R_\phi(0,t). \tag{3.38}$$

From this function some length scales can be derived, such as the integral scale L_ϕ

$$L_\phi(t) = \int_{-\infty}^{+\infty} f_\phi(r,t)dr, \tag{3.39}$$

and the scalar Taylor microscale

$$\lambda_\phi(t) = \left(-\frac{1}{2}\frac{\partial^2 f_\phi}{\partial r^2}(0,t) \right)^{1/2}. \tag{3.40}$$

3.3.2 Scalar energy spectrum

The scalar spectrum $\Phi_\phi(\boldsymbol{\kappa},t)$ for an homogeneous scalar field, is defined through the following Fourier transform

$$\Phi_\phi(\boldsymbol{\kappa},t) = \frac{1}{(2\pi)^3}\int\int_{-\infty}^{+\infty}\int R_\phi(\mathbf{r},t)e^{-i\boldsymbol{\kappa}\cdot\mathbf{r}}d\mathbf{r}, \tag{3.41}$$

and from this definition it results also that, the scalar variance can be written as follows

$$R_\phi(0,t) = \langle \phi'^2 \rangle = \int\int_{-\infty}^{+\infty}\int \Phi_\phi(\boldsymbol{\kappa},t)d\boldsymbol{\kappa}. \tag{3.42}$$

As done for the energy spectrum, also for the scalar spectrum it is possible to integrate out all the directional information

$$E_\phi(\kappa,t) = \oint \frac{1}{2}\Phi_\phi(\boldsymbol{\kappa})dS(\kappa), \tag{3.43}$$

where $E_\phi(\kappa,t)$ is the so-called scalar energy spectrum. In Fig 3.5 a sketch of the spectrum is reported and compared with the turbulent energy spectrum. It must be mentioned here that the spectrum depends on the Scmidth number (Sc). The first part of the spectrum is known as inertial-convective subrange. In this range the exponent of the spectrum for the wave number κ is -5/3, as for the energy-spectrum. This region is limited by the Kolmogorov microscale λ_k (at the corresponding wave number κ_k.) For wavenumbers larger than κ_k the scalar energy spectrum will decay quickly into the viscous-convective subrange, where the exponent in the spectrum function for the wave number is -1. The limit of the viscous-diffusive subrange is the Batchelor-scale λ_B (or κ_B) defined as

$$\lambda_B = Sc^{-1/2}\lambda_k, \tag{3.44}$$

It is evident that the viscous-convective sub-range exists only if $Sc > 1$.

The cascade picture can be invoked, also to describe turbulent mixing. Scalar variance is introduced at large scales, and then by a cascade process is transferred to the smaller scales. This process can be seen as a kind of size-reduction of the blobs of unpremixed

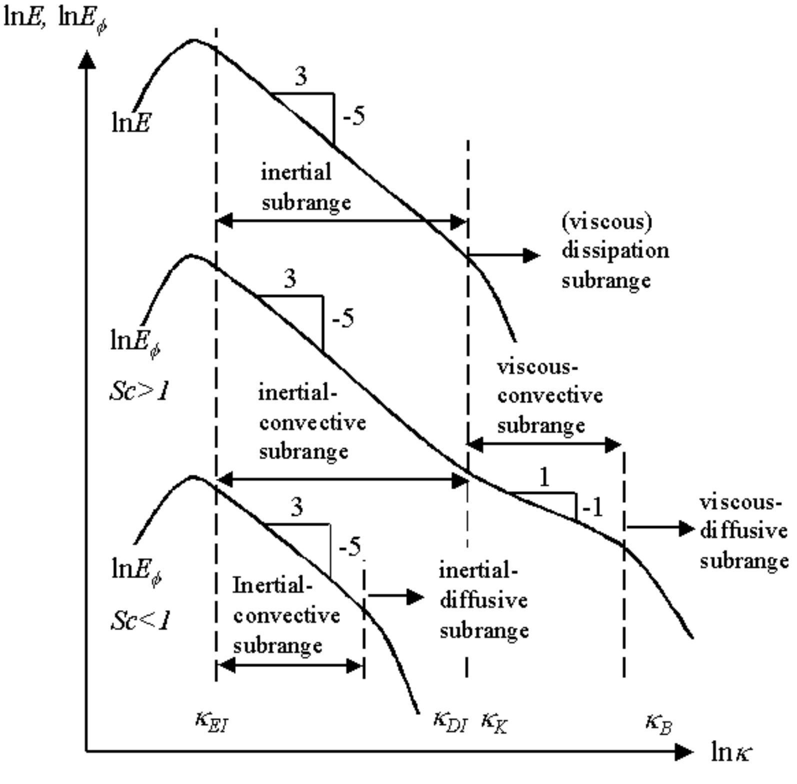

Figure 3.5: Turbulent energy spectrum and scalar energy spectrum.

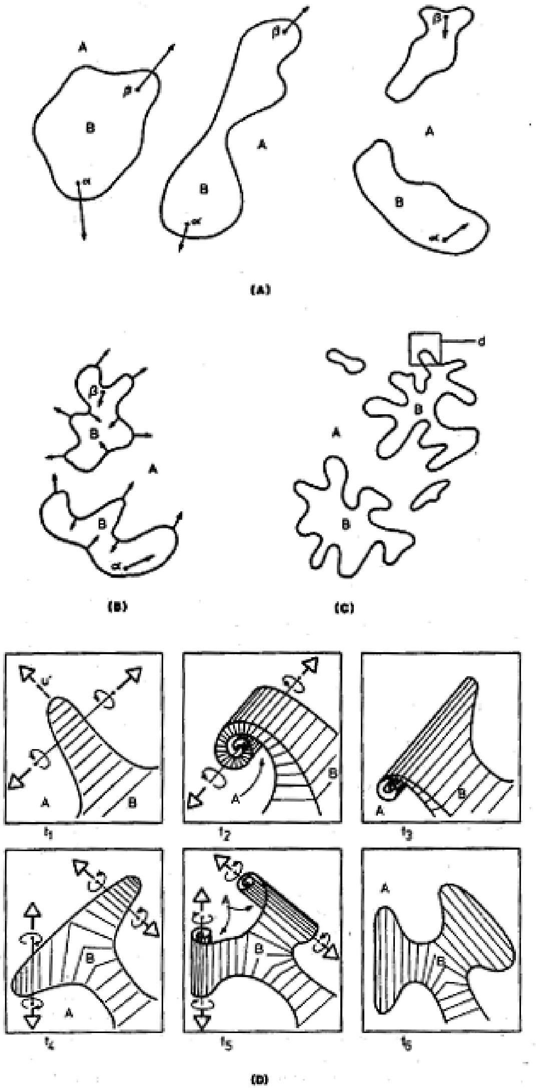

Figure 3.6: Fluid deformation and vorticity: A,B deformation in the inertial subrange; C deformation in the viscous subrange; D action of vorticity on fluid elements.

fluids down to the Kolmogorov scale, without molecular mixing [see Fig. 3.6 (A,B,C).] At this scale a further reduction of length scale occurs [see Fig. 3.6 (D)] until microscale gradients are so large that molecular diffusion takes place. This is the so-called Batchelor scale. A number of Lagrangian and Eulerian models have been formulated in terms on the previous considerations. For example the EDD (engulfment-deformation-diffusion) is one of the most popular and Fig. 3.6 refers to this model [33, 34].

It is interesting to remind that by definition the scalar variance can be found from the scalar spectrum by integrating over the wave number space

$$\langle \phi'^2 \rangle = \int\limits_{-\infty}^{+\infty} E_\phi(\kappa) d\kappa. \tag{3.45}$$

Therefore, it is evident that $E_\phi(\kappa)d\kappa$ represent the fraction of scalar variance located at the wave number κ. It is also interesting to highlight that the scalar energy spectrum is related to the scalar dissipation rate (defined in the previous chapter) by

$$\varepsilon_\phi = \int\limits_{-\infty}^{+\infty} 2\Gamma\kappa^2 E_\phi(\kappa) d\kappa, \tag{3.46}$$

and thus the scalar energy spectrum determines the mixing time

$$\tau_\phi = \frac{2\langle \phi'^2 \rangle}{\varepsilon_\phi}. \tag{3.47}$$

Invoking the cascade process, the mixing time can be seen as the time required for scalar variance (created at the integral scale) to be transported to the Batchelor scale, where it is dissipated by molecular diffusion.

Part II

Simulations and experiments

Chapter 4

Modeling and simulation

In this chapter the most important models for the simulation of turbulent reacting flows are derived. Particular attention is given to the finite-mode PDF model for micromixing and the quadrature method of moments for the population balance, that represent the main novelties of this work.

4.1 Turbulent flows

4.1.1 Turbulence models

All the equations presented in Chapter 2 contain unclosed terms. Different models have been proposed for the solution of the closure problem, and concerning turbulent flow, they are usually classified by the number of equations added to the Navier-Stokes equation to close the problem. A wide literature has been published in this field (see for example [35]) and nowadays commercial Computational Fluid Dynamics (CFD) codes offer a large library of many of these models. The discussion here is limited to the most important models and focuses on those used in this work. One of the simplest turbulence models available in commercial CFD codes is the standard $k-\varepsilon$ model, that employs the Boussinesq hypothesis to relate the Reynolds stresses to the mean velocity gradients

$$-\langle u_i' u_j' \rangle = \frac{\mu_t}{\rho}\left(\frac{\partial\langle u_i\rangle}{\partial x_j}+\frac{\partial\langle u_j\rangle}{\partial x_i}\right)-\frac{2}{3}\left(k+\frac{\mu_t}{\rho}\frac{\partial\langle u_i\rangle}{\partial x_i}\right)\delta_{ij}, \tag{4.1}$$

where μ_t is the turbulent viscosity, δ_{ij} is the Kroneker delta, and k is the turbulent kinetic energy defined in Eq. 2.16. With this approach eddies are seen as lumps of fluid, which exchange momentum according to their turbulent viscosity. This *eddy* or turbulent viscosity is computed as follows

$$\mu_t = \rho C_\mu \frac{k^2}{\varepsilon}, \tag{4.2}$$

where ε is the turbulent dissipation rate defined in Eq. 2.14. The transport equations for these two variables appear in the model in closed form, as follows

$$\begin{aligned}\frac{\partial k}{\partial t}+\langle u_k\rangle\frac{\partial k}{\partial x_k} = \frac{\partial}{\partial x_i}\left[\left(\nu+\frac{\mu_t}{\rho\sigma_k}\right)\frac{\partial k}{\partial x_i}\right]+ \\ \frac{\mu_t}{\rho}\left(\frac{\partial\langle u_j\rangle}{\partial x_i}+\frac{\partial\langle u_i\rangle}{\partial x_j}\right)\frac{\partial\langle u_j\rangle}{\partial x_i}-\varepsilon,\end{aligned} \tag{4.3}$$

where the production term $\mathcal{P}$ of Eq. 2.15 has been closed by using the Boussinesq hypothesis, and

$$\frac{\partial \varepsilon}{\partial t} + \langle u_i \rangle \frac{\partial \varepsilon}{\partial x_i} = \frac{\partial}{\partial x_i} \left[\left(\nu + \frac{\mu_t}{\rho \sigma_\varepsilon} \right) \frac{\partial \varepsilon}{\partial x_i} \right] + C_{1\varepsilon} \mathcal{P} \frac{\varepsilon}{k} - C_{2\varepsilon} \frac{\varepsilon^2}{k}. \tag{4.4}$$

The last two terms of Eq. 4.4 correspond to $\mathcal{V}_\varepsilon$ and $\mathcal{D}_\varepsilon$ of Eq. 2.19. These two terms were closed by assuming that the production-dissipation balance is controlled by large-scale velocity fluctuations, with a characteristic relaxation rate equal to ε/k (see Eq. 3.17.) In fact, if one considers that $\mathcal{V}_\varepsilon$ represents the rate at which dissipation is created by spectral energy passing from the inertial range to the dissipative range of the energy spectrum, and writes it in terms of the spectral energy transfer rate $\mathcal{T}_k(\kappa, t)$ (see Eq. 3.32) under the assumption of spectral equilibrium it is possible to demonstrate that [30]:

$$\mathcal{D}_\varepsilon \sim Re_L^{1/2} \frac{\varepsilon}{k} \varepsilon, \tag{4.5}$$

where Re_L has been defined in Eq. 3.29. Several constants appear in the model, such as $C_{1\varepsilon}$, $C_{2\varepsilon}$ and σ_k and σ_ε that are the turbulent Prandt numbers for k and ε respectively. A detailed description of the model can be found in the original work of Launder and Spalding [36]. Since two equations are added to close the problem the model and its successive modifications are known as two-equation models.

The RNG $k-\varepsilon$ is a modification of the standard $k-\varepsilon$ model, derived using a statistical technique called the Renormalization group theory. RNG method for turbulence takes advantage of the scale invariant properties of the system, meaning that the method can describe small scales, which are independent from any externally imposed time or length scale. The main idea of the method is the elimination of small scale eddies, through representation in terms of larger scales, in the range of energy containing eddies. This scale elimination procedure results in a differential equation for turbulent viscosity, and in an additional term for the ε transport equation. Concerning the first point it is interesting to notice that at high Reynolds number integration of this differential equation gives the usual expression for turbulent viscosity and the value of C_μ evaluated by the RNG theory (C_μ=0.0837) is in good agreement with the experimental value used in the standard $k-\varepsilon$ model (C_μ=0.09, see Eq. 4.2). Concerning the additional term in the ε transport equation, its role is to reduce the constant $C_{2\varepsilon}$ in regions where the strain rate is large, resulting in lower turbulent viscosity in comparison with the standard $k-\varepsilon$. As a consequence of this more accurate description the RNG $k-\varepsilon$ model gives better performances in the case of flows in curved geometry and flows that are strained by effects such as impingement or stagnation, low-Reynolds number and transitional flows, and flows with high swirl.

In the realizable $k-\varepsilon$ model equations are modified in order to satisfy certain mathematical constrains on the normal stresses. As a consequence, the ε transport equation is modified on the basis of the mean vorticity-square fluctuations, and the term C_μ is no longer constant, but is computed from:

$$C_\mu = \frac{1}{A_0 + A_S \frac{U^* k}{\varepsilon}}. \tag{4.6}$$

Without going into details it is possible to say that the terms contained in the above equation are function of the mean strain, of the rotation rate and of the angular velocity of the system rotation, since U^* is directly correlated to mean rate-of-rotation tensor, and of course C_μ is also a function of the turbulent field (k and ε.) This model has been validated in a wide range of practical applications and showed better performances than the standard $k - \varepsilon$ model.

Completely different is the approach used in the RSM[1], where the isotropic eddy-viscosity hyprothesis is abandoned by directly solving the transport equations for the Reynolds stresses (see Eq. 2.10.) In general, it is possible to say that use of the RSM is needed when the flow features of interest are the direct results of anisotropy in the Reynolds stress, but one should always remember that since the unknown terms are modeled by means of a second-order closure or introducing a transport equation, the fidelity of the RSM description is limited by the validity of the closure assumptions employed in the Reynolds stress transport equations. These assumptions are:

(i) isotropic dissipation for the three normal-stress components and zero dissipation in the shear stress components

(ii) proportionality between Reynolds stress diffusion and spatial gradient of the stress component itself

(iii) representation of the pressure fluctuations redistribution action by two groups of terms: the first one involving Reynolds stresses and ε/k and the second one product of stresses and mean velocity gradients.

4.1.2 Near wall treatment

Mainly there are two approaches that can be used:

(i) the near wall region is not modeled but only bridged by the wall functions themselves

(ii) the near-wall region is modeled all the way down to the wall

In most high-Reynolds-number flows, the wall function approach is recommended, whereas for low-Reynolds-number flows, the hypothesis underlying the wall functions cease to be valid, and therefore the second approach is recommended [37]. Concerning wall functions there are two possibilities: standard wall function and non-equilibrium wall function. In the first one, the log-law coupled with the linear laminar stress-strain relationship for the viscous sub-layer is used, whereas in the second one a non-equilibrium wall function is used. In the latter case the budget of turbulent kinetic energy in the wall-neighboring cells is computed and the log-law for mean velocity is sensitive to pressure gradients. On the contrary, using the near wall model, the domain is dived into a viscous-affected region and a fully-turbulent region (two-layer zonal model). The demarcation of the two regions is determined by a wall-distance-based turbulent Reynolds number, defined as

$$Re_y = \frac{\rho\sqrt{k}y}{\mu}, \tag{4.7}$$

where y is the normal distance from the wall. If Re_y >200 the cell is in the fully turbulent region and the normal turbulence models can be used. When Re_y <200 a one-equation model (Wolfstein model) is used. In this model the turbulent viscosity is computed from:

$$\mu_t = \rho C_\mu \sqrt{k} l_\mu, \tag{4.8}$$

---

[1] The RSM is a multi-equation model. In two-dimensional simulations the added equations are 4 (for the turbulent dissipation rate and three Reynolds stresses since the tensor is symmetric). In three-dimensional simulation the added equations are 7 (for the turbulent dissipation rate and the Reynolds stresses since the tensor is symmetric.)

and ε is computed from

$$\varepsilon = \frac{k^{3/2}}{l_\varepsilon}, \tag{4.9}$$

where l_μ and l_ε are two characteristic length scales (for details see [37] Cap. 9).

4.1.3 Scalar transport

Concerning the description of turbulent mixing, the Reynolds-averaged transport equation of a scalar has been presented in the previous chapter (see Eq. 2.21). In this equation some unclosed terms appear: the chemical source term and the scalar flux term. Closure of the first one is one of the major challenge is turbulent reacting flows and is non trivial for fast reactions with nonlinear source term, as it will be discussed in the followings. The other unclosed term is the scalar flux due to turbulent fluctuations $\langle u_i'\phi_\alpha\rangle$. This term obeys to a transport equation (see Eq. 2.22) but at high Reynolds number the scalar flux can be expressed by a linear equation

$$M_{ij}\langle u_i'\phi_\alpha\rangle = \langle u_i'u_j'\rangle \frac{\partial\langle\phi_\alpha\rangle}{\partial x_j}, \tag{4.10}$$

where M_{ij} is a second order tensor that can be derived from the scalar flux transport equation. In general this tensor is non-symmetric but a widely-employed simplification is to assume M_{ij} isotropic:

$$M_{ij} = \frac{1}{C_T}\frac{\varepsilon}{k}\delta_{ij}, \tag{4.11}$$

where C_T is a numerical constant, so that the scalar flux can be expressed as:

$$\langle u_i'\phi_\alpha\rangle = -C_T\frac{k}{\varepsilon}\langle u_i'u_j'\rangle\frac{\partial\langle\phi_\alpha\rangle}{\partial x_j}. \tag{4.12}$$

However, when a two equation model is used, and the Reynolds stresses are not known, the scalar flux can be closed as follows

$$\langle u_i'\phi_\alpha\rangle = -\Gamma_t\frac{\partial\langle\phi_\alpha\rangle}{\partial x_j}, \tag{4.13}$$

where

$$\Gamma_t = \frac{C_\mu}{Sc_t}\frac{k^2}{\varepsilon}, \tag{4.14}$$

and where Sc_t is the turbulent Schimdt number.

4.1.4 Scalar variance and scalar dissipation rate

The transport equation of the scalar variance has been presented in a previous chapter (see Eq. 2.23). This equation presents two unclosed terms, the production term and the flux term which can be closed by using the gradient assumption model. This results respectively in:

$$\mathcal{P}_\phi = -2\langle u_j'\phi\rangle\frac{\partial\langle\phi\rangle}{\partial x_j} = 2\Gamma_t\frac{\partial\langle\phi\rangle}{\partial x_j}\frac{\partial\langle\phi\rangle}{\partial x_j}, \tag{4.15}$$

and

$$\langle u_j' \phi'^2 \rangle = -\Gamma_t \frac{\partial \langle \phi'^2 \rangle}{\partial x_j}. \tag{4.16}$$

Thus the final equation is:

$$\frac{\partial \langle \phi'^2 \rangle}{\partial t} + \langle u_j \rangle \frac{\partial \langle \phi'^2 \rangle}{\partial x_j} = \frac{\partial}{\partial x_j} \left[(\Gamma + \Gamma_t) \frac{\partial \langle \phi'^2 \rangle}{\partial x_j} \right] + 2\Gamma_t \frac{\partial \langle \phi \rangle}{\partial x_j} \frac{\partial \langle \phi \rangle}{\partial x_j} - \varepsilon_\phi. \tag{4.17}$$

From Eq. 4.17 it is clear that scalar variance is produced by the large-scale gradients, transported by convection and turbulent diffusion and dissipated by ε_ϕ. It has been also highlighted that the mixing process can be seen, in a Lagrangian framework, as the time needed to reduce scalar variance from the large scales to the small scales where molecular diffusion is effective. In this sense the mixing time can be evaluated as[2]:

$$\tau_\phi = \frac{2 \langle {\phi'}^2 \rangle}{\varepsilon_\phi}, \tag{4.18}$$

and under fully-developed scalar spectrum, in the case of dynamic equilibrium results in[3]:

$$\tau_\phi = \frac{2}{C_\phi} \frac{k}{\varepsilon}. \tag{4.19}$$

This approach is based on the idea that the characteristic mixing time is related to the decay of velocity fluctuation and the constant C_ϕ was found to be of order of magnitude of unity. Another approach is based on the evaluation of the lifetime of a single eddy which is proportional to the Kolmogorov time-scale (see Eq. 3.28):

$$\tau_\phi = 17.31 \left(\frac{\nu}{\varepsilon} \right)^{1/2}. \tag{4.20}$$

This time constant was derived from a stationary energy spectrum at high-Reynolds number flows, and for this reason the numerical constant is independent of the Reynolds number. Corrsin [38] proposed a third model valid for isotropic and homogeneous turbulence, based on the spectral analysis, which is a sort of combination of the previous ones:

$$\tau_\phi = \frac{3}{2} \frac{k}{\varepsilon} + \frac{1}{2} \ln(Sc) \left(\frac{\nu}{\varepsilon} \right)^{1/2}. \tag{4.21}$$

Very important is also the ratio between the scalar and turbulent length scales, indicated by L_ϕ and L_u[4]. In general L_u is of order of magnitude of the impeller dimension in a stirred system, whereas L_ϕ depends on feed conditions (i.e., feed tube diameter and feed flow rate). When L_u is very different from L_ϕ, for example $L_u \gg L_\phi$, the scalar length scale distribution is not in equilibrium with the velocity spectrum, and a relaxation period is needed to reach equilibrium. During this relaxation period there has to be a progress of mixing on the molecular scale and possibly of chemical reaction.

A turbulent mixer model, based on three characteristic time constants, was proposed by Baldyga [39]. The scalar variance is divided in different subranges, depending on the

---

[2] This quantity has been already defined at pag. 36

[3] Notice that this definition for the mixing time is identical to what obtained in Eq. 2.31 at pag. 23

[4] These quantities have been defined in Eq. 3.16 at pag. 29 and Eq. 3.39 at pag 33.

related mechanism of mixing, that according to Fig. 3.5 are the intertial-convective σ_1^2, the viscous-convective σ_2^2, and the viscous-diffusive σ_3^2:

$$\langle \phi'^2 \rangle = \sigma_1^2 + \sigma_2^2 + \sigma_3^2. \tag{4.22}$$

The transport equation is as follows:

$$\frac{\partial \sigma_i^2}{\partial t} + \langle u_j \rangle \frac{\partial \sigma_i^2}{\partial x_j} = \frac{\partial}{\partial x_j} \left[(\Gamma + \Gamma_t) \frac{\partial \sigma_i^2}{\partial x_j} \right] + R_{Pi} - R_{Di}, \tag{4.23}$$

where R_{Pi} and R_{Di} stand for production and dissipation term. The rate of production of variance in the inertial-convective subrange is due to large-scale scalar gradients and thus is given by Eq 4.15. The rate of decay in the same subrange is:

$$R_{D1} = R_{P2} = C_\phi \frac{\varepsilon}{k} \sigma_1^2. \tag{4.24}$$

The viscous-convective mixing can be described by:

$$R_{D2} = R_{P3} = E \sigma_2^2, \tag{4.25}$$

where E is the Engulfment parameter, defined as follows:

$$E = 0.058 \left(\frac{\varepsilon}{\nu} \right)^{1/2}. \tag{4.26}$$

Decreasing the scale of segregation, the scalar variance goes into the viscous-diffusive subrange of the scalar energy spectrum, where molecular diffusion in the deforming slabs occurs, according to the following rate:

$$R_{D3} = G \sigma_3^2, \tag{4.27}$$

where

$$G = (0.303 + 17050/Sc)E. \tag{4.28}$$

Another important model is the spectral relaxation model, proposed by Fox [40, 41, 42]. This model is based on the description of scalar dissipation, and it introduces additional variables that can be seen as potential scalar dissipation rates at wave numbers smaller than the Batchelor scale. Also in this case there are three main subranges, describing a one-directional cascade from the lowest wave number to the Batchelor wave number. For a detailed description of the model see [40, 41, 42], here it is interesting to highlight that this model has been extended by employing the Lagrangian Probability Density Function approach, which will be described in the next sections.

All the presented methods can be used to evaluate the mixing time. It is in general difficult to say *a priori* which model can give best results. Valerio et al [43] compared the ability of predictions of models based on different mixing times, for the yield of an instantaneous chemical reaction in a tubular reactor with coaxial feeds. The best agreement was obtained by using Eq. 4.20, but if a very accurate description is needed, especially for jet-flow configuration, more complex closures must be used, for taking into account the contribution from all the turbulence scales. Kruis and Falk [44] compared the turbulent mixer model with the spectral relaxation model, and found that the latter leads to better results, probably due to a more rigorous physical explanation.

In the next sections the link between mixing of non-reacting materials, and turbulent reacting flows will be illustrated and cleared.

4.2 Evaluation of the source term

As already mentioned one of the major issues in turbulent reacting flow computations is the chemical source term; in fact, being nonlinear in most of the cases, its mean value is not known. As an example let us consider a second order reaction, where c_A and c_B are the reactant concentrations

$$S(c_A, c_B) = kc_A c_B, \tag{4.29}$$

in this case the chemical source term that appears in the Reynolds-averaged scalar transport equation, is

$$\langle S(c_A, c_B)\rangle = k\langle c_A\rangle\langle c_B\rangle + k\langle c'_A c'_B\rangle, \tag{4.30}$$

where $\langle c'_A c'_B\rangle$ is the covariance that, needless to say, is not known! It is evident that if the reaction follows a first-order kinetic, the problem is completely closed; also when the chemical reaction is slow in comparison with the mixing time the closure problem does not exist. In fact, if the time for the variance to reach the Batchelor scale from the integral scale is smaller than the reaction time, it means that reaction takes place when the variance is almost completely reduced, and thus the covariance can be neglected.

In the past, several models have been used: for example Toor [45] proposed a model to compute the covariance $\langle c'_A c'_B\rangle$ from the variance of a non-reacting scalar:

$$\langle c'_A c'_B\rangle = -\frac{\langle \xi'^2\rangle}{\langle\xi\rangle\left(\langle\xi\rangle - 1\right)}\langle c_A\rangle\langle c_B\rangle, \tag{4.31}$$

where ξ is the mixture fraction[5] that by definition lies between 0 and 1. The model is valid only for very fast reactions involving reactants with equal diffusivities, and if the volume ratio of the reactant solution is equal to one. Another important model developed in the past is the Eddy-breal-up model [46]. In this model the decay of turbulent energy is correlated to the rate at which fresh lumps of fluid are broken into smaller ones, and therefore it relates the rate of reaction to the rate of dissipation of the reactant and product containing eddies. The corrected rate of reaction is given by the smaller of the two following expressions:

$$\begin{aligned}\langle S(c_A, c_B)\rangle &= k\langle c_A\rangle\langle c_B\rangle,\\ \langle S(c_A, c_B)\rangle &= C_1\frac{\varepsilon}{k},\end{aligned} \tag{4.32}$$

where C_1 is an empirical constant. No general rule exists for the choice of this variable, in fact, it has been shown that the parameter depends on the reacting conditions [47] and in addition is not able to predict the yield and selectivity of a series of complex competitive reactions.

Another important approach makes use of probability density functions. Let us consider the joint-composition PDF of the scalars involved in a reacting system: by definition f_ϕ is

$$f_\phi(\boldsymbol{\psi}; \mathbf{x}, t) = P[\psi_\alpha < \phi_\alpha(\mathbf{x}, t) < \psi_\alpha + d\psi_\alpha, \alpha = A, B, ...], \tag{4.33}$$

---

[5] This variable will be defined in greater detail at pag. 49

defined similarly to the velocity PDF (see Eq. 3.5). The main advantage of using PDF methods lies in the fact that the chemical reaction term can be treated exactly

$$\langle S(\boldsymbol{\phi})\rangle = \int_0^{+\infty} \dots \int_0^{+\infty} S(\boldsymbol{\psi}) f_{\phi}(\boldsymbol{\psi};\mathbf{x},t)d\boldsymbol{\psi}. \tag{4.34}$$

PDF methods can be classified as full and presumed; both approaches need an accurate estimation of velocity and turbulent field of the reactor under study. This can be done by using CFD. With this approach the real reactor is represented by a computational grid, and usually transport equations are solved based on a finite-difference scheme.[6]

Several differences between full and presumed PDF approach exist, in terms of the discretization in the composition space, the spatial transport and the numerical approach adopted. For full PDF methods, for example, spatial transport is treated as a random diffusion process, while presumed PDF methods are based on an assumption concerning the scalar conditional mean concentrations. In the case of an inert scalar with uniform mean gradients, the full PDF method would predict that the joint scalar PDF is Gaussian (as seen in Direct Numerical Simulation), while the presumed PDF method cannot predict the correct limiting PDF. Moreover, unlike presumed PDF, full PDF methods do not need *a priori* knowledge of the shape of the joint composition PDF but are much more CPU intensive.

4.2.1 Full PDF methods

The full PDF description is performed with a set of notional particles that obey stochastic differential equations, and move in the computational domain mimicking the PDF transport in physical and composition space. A detailed description of PDF formulation and solution using Monte-Carlo methods can be found in [48], and here we limit the discussion to the transport equation of the composition probability density function $f_{\phi}(\boldsymbol{\psi};\mathbf{x},t)$.

This transport equation can be derived starting from the transport equation of a reacting scalar α as suggested by Pope [48]:

$$\frac{D\phi_\alpha}{Dt} = \frac{\partial \phi_\alpha}{\partial t} + \frac{\partial u_i \phi_\alpha}{\partial x_i} = \Theta_\alpha, \tag{4.35}$$

where

$$\Theta_\alpha = \Gamma_\alpha \nabla^2 \phi_\alpha + S_\alpha(\boldsymbol{\phi}). \tag{4.36}$$

As already mentioned, the main characteristic of the composition PDF is that for any arbitrary function of $\boldsymbol{\phi}$ the expected (or mean) value can be easily derived as follows

$$\langle Q\rangle = \int_{-\infty}^{+\infty} Q(\boldsymbol{\psi}) f_{\phi}(\boldsymbol{\psi};\mathbf{x},t)d\boldsymbol{\psi}, \tag{4.37}$$

and being the integral a linear operator the convected derivative is

$$\left\langle \frac{DQ}{Dt} \right\rangle = \frac{\partial \langle Q\rangle}{\partial t} + \frac{\partial \langle u_i Q\rangle}{\partial x_i}, \tag{4.38}$$

---

[6] We will come back later on this concept of coupling between CFD and scalar field (see Fig. 6.1 on pag. 76).

but the mean convected derivative of Q can be also written as follows

$$\left\langle \frac{DQ}{Dt} \right\rangle = \left\langle \frac{\partial Q}{\partial \phi_\alpha} \frac{D\phi_\alpha}{Dt} \right\rangle = \left\langle \frac{\partial Q}{\partial \phi_\alpha} \Theta_\alpha \right\rangle . \tag{4.39}$$

The first term on the right-hand side of Eq. 4.38 can be easily written as follows:

$$\frac{\partial \langle Q \rangle}{\partial t} = \int\limits_{-\infty}^{+\infty} Q(\boldsymbol{\psi}) \frac{\partial f_\phi}{\partial t} d\boldsymbol{\psi}. \tag{4.40}$$

Since the expected value of the function Q can be expressed in terms of the conditional expected value:

$$\langle Q \rangle = \int\limits_{-\infty}^{+\infty} f_\phi(\boldsymbol{\psi}) \langle Q \mid \boldsymbol{\psi} \rangle d\boldsymbol{\psi}, \tag{4.41}$$

the second term of the right-hand side of Eq. 4.38 can be written as

$$\begin{aligned} \frac{\partial \langle u_i Q \rangle}{\partial x_i} &= \frac{\partial}{\partial x_i} \int\limits_{-\infty}^{+\infty} f_\phi \langle u_i Q \mid \boldsymbol{\psi} \rangle d\boldsymbol{\psi} \\ &= \frac{\partial}{\partial x_i} \int\limits_{-\infty}^{+\infty} f_\phi Q(\boldsymbol{\psi}) \langle u_i \mid \boldsymbol{\psi} \rangle d\boldsymbol{\psi} \\ &= \int\limits_{-\infty}^{+\infty} Q(\boldsymbol{\psi}) \frac{\partial}{\partial x_i} \left[\langle u_i \mid \boldsymbol{\psi} \rangle f_\phi \right] d\boldsymbol{\psi}. \end{aligned} \tag{4.42}$$

As concerns Eq. 4.39 the integral can be solved by integrating by parts

$$\begin{aligned} \left\langle \frac{\partial Q}{\partial \phi_\alpha} \Theta_\alpha \right\rangle &= \int\limits_{-\infty}^{+\infty} Q(\boldsymbol{\psi}) \langle \Theta_\alpha \mid \boldsymbol{\psi} \rangle f_\phi d\boldsymbol{\psi} \Big|_{\psi_\alpha=-\infty}^{\psi_\alpha=+\infty} \\ &- \int\limits_{-\infty}^{+\infty} Q(\boldsymbol{\psi}) \frac{\partial}{\partial \psi_\alpha} [\langle \Theta_\alpha \mid \boldsymbol{\psi} \rangle f_\phi] d\boldsymbol{\psi}. \end{aligned} \tag{4.43}$$

The first term on the right-hand side is null, since for well-behaved PDF and almost all functions Q the probability flux at infinity is null, and thus:

$$\left\langle \frac{\partial Q}{\partial \phi_\alpha} \Theta_\alpha \right\rangle = - \int\limits_{-\infty}^{+\infty} Q(\boldsymbol{\psi}) \Big[\frac{\partial}{\partial \psi_\alpha} \langle \Gamma_\alpha \nabla^2 \phi_\alpha \mid \boldsymbol{\psi} \rangle f_\phi + \frac{\partial}{\partial \psi_\alpha} S_\alpha(\boldsymbol{\psi}) f_\phi \Big] d\boldsymbol{\psi}. \tag{4.44}$$

Equating Eqs. 4.38 and 4.39 and using the fact that the equality must hold for arbitrary choices of Q leads to

$$\frac{\partial f_\phi}{\partial t} + \frac{\partial}{\partial x_i} [\langle u_i \mid \boldsymbol{\psi} \rangle f_\phi] = - \frac{\partial}{\partial \psi_\alpha} \Big[\langle \Gamma_\alpha \nabla^2 \phi_\alpha \mid \boldsymbol{\psi} \rangle f_\phi \Big] - \frac{\partial}{\partial \psi_\alpha} \left[S_\alpha(\boldsymbol{\psi}) f_\phi \right], \tag{4.45}$$

and use of the Reynolds decomposition for the velocity yields the transport equation of the joint composition PDF:

$$\frac{\partial f_\phi}{\partial t} + \langle u_i \rangle \frac{\partial f_\phi}{\partial x_i} + \frac{\partial}{\partial \psi_\alpha} \left[S_\alpha(\boldsymbol{\psi}) f_\phi \right] = - \frac{\partial}{\partial x_i} \left[\langle u_i' \mid \boldsymbol{\psi} \rangle f_\phi \right] - \frac{\partial}{\partial \psi_\alpha} \Big[\langle \Gamma_\alpha \nabla^2 . \phi_\alpha \mid \boldsymbol{\psi} \rangle f_\phi \Big] \tag{4.46}$$

The first term on the right-hand side of Eq. 4.46 represents the convective transport due to the scalar conditioned velocity fluctuations. It can be closed by using a gradient-diffusion model that introduces a turbulent diffusion term:

$$\langle u_i' \mid \psi \rangle f_\phi = -\Gamma_t \frac{\partial f_\phi}{\partial x_i}. \tag{4.47}$$

The second term on the right-hand side of Eq. 4.46 represents the micromixing term that can be closed by using different approaches. In the case of non-reacting scalars it has been shown [48] that the micromixing model has to fulfill some constraints concerning the shape of the PDF: the mean values must be constant, the variance decay has to be exponential, and the asymptotic shape of the PDF has to be Gaussian. One of the most employed models is the interaction-with-the-mean (IEM) model [49, 50]. This model is also known as the Linear Mean Square Estimation (LMSE) model and is based on a linear relaxation of the scalars towards their mean values [51]:

$$\langle \Gamma_\alpha \nabla^2 \phi_\alpha \mid \psi \rangle = \frac{1}{2\tau_\phi}(\langle \phi_\alpha \rangle - \psi_\alpha) \tag{4.48}$$

where $\langle \phi_\alpha \rangle$ is the local scalar mean, and τ_ϕ is the local micromixing time. The IEM approach gives poor performances in the so-called partially segregated CSTR, where the combined effects of macro, meso, and micromixing are described by the micromixing model alone [52]. However, when properly used as a model for only micromixing and macro and mesomixing due to spatial transport are handled separately, the IEM model yields acceptable predictions, once the micromixing time is chosen correctly (see Section 4.1.4).

The solution of the PDF transport equation using standard finite-difference methods is computationally intractable due to the elevate number of independent variables, and the difficulty of ensuring that the PDF is non-negative and integrates to unity. Monte-Carlo simulations offer a tractable alternative that does not solve for the PDF directly, but by tracking a finite-number of notional particles through the computational domain, allows us to estimate the quantities of interest.

This representation corresponds to an approximation of the PDF by a set of N delta functions:

$$f_\phi \approx \frac{1}{N} \sum_{n=1}^{N} \delta(\boldsymbol{\phi}^{(n)} - \boldsymbol{\psi}), \tag{4.49}$$

where $\boldsymbol{\phi}^{(n)}$ is the value of $\boldsymbol{\phi}$ related to the nth delta function (generally N=80-100.) Each delta function correspond to a single notional particle, which is a sort of fluid element, but however one should always remember that this is a mathematical representation without physical meaning.

In Eq. 4.46 three operators are present

$$\frac{\partial f_\phi}{\partial t} = (P_1 + P_2 + P_3) f_\phi, \tag{4.50}$$

one responsible for convection and turbulent diffusion

$$P_1 = -\langle u_i \rangle \frac{\partial}{\partial x_i} + \Gamma_t \frac{\partial^2}{\partial x_i^2}, \tag{4.51}$$

one responsible for micromixing

$$P_2 = \left(\frac{1}{2\tau_\phi}\right)(\langle \phi_\alpha \rangle - \psi_\alpha) \frac{\partial}{\partial \psi_\alpha}, \tag{4.52}$$

and the last one responsible for the chemical reaction

$$P_3 = S_\alpha(\boldsymbol{\psi})\frac{\partial}{\partial \psi_\alpha}. \tag{4.53}$$

The transport equation is solved by means of the time splitting approach. This method is based on the idea that the three operators act in sequence if a sufficiently small time step is chosen.

The first step is the transport in physical space. This can be handled both in Eulerian and Lagrangian frameworks. If the code is written in Eulerian form, based on the mean velocity and turbulent diffusivity (evaluated by the CFD code), the effective flow rates into each cell of the computational domain are computed. Then once the time step is fixed the number of notional particles that flow into each cell from neighboring cells is computed. This approach offers the advantage that is easily adaptable to any computational grid for which the flow rates can be computed, but the major difficulty is associated with fixing the time step in order to ensure that the particle flux is everywhere non-negative and not rounded to zero. These difficulties can be overcome by using the Lagrangian approach, where the PDF transport equation is written in terms of a set of Stochastic Differential Equations for particle position. Since the velocity does not appear as a random variable, an isotropic Wiener [30] process is introduced, and generates a random walk in real space.

The second step is the transport in composition space due to molecular mixing in which notional particles are mixed together according to Eq. 4.48, and the last step is the chemical reaction that occurs in each notional particle according to the reaction rate.

4.2.2 Presumed PDF methods

In the presumed PDF approach the functional form of the PDF is assumed *a priori.* Two approaches are presented: the first one is the beta PDF proposed by Baldyga for liquid reactions [53], whereas the second one is the finite-mode PDF proposed by Fox [54] and first applied to precipitation in this work [55] and in [56]. Formulation of both models requires the definition of mixture fraction.

The mixture fraction PDF The mixing between two feed streams in a reactor can be described using the mixture fraction approach [57]. For a simple reaction (i.e., $A+B \rightarrow C$) in the case of two non- premixed feeds, the mixture fraction is a conserved scalar defined as follows:

$$\xi = \frac{c_A - c_B + c_{Bo}}{c_{Ao} + c_{Bo}} \tag{4.54}$$

where c_{Ao} and c_{Bo} are the inlet concentrations of the two reactants in their separate feed streams. From Eq. 4.54 it is clear that the mixture fraction is equal to 1 in one feed stream ($c_A = c_{Ao}$; $c_B = 0$) and 0 in the other ($c_A = 0$; $c_B = c_{Bo}$). The relationships between the mixture fraction and the reactant concentrations are:

$$\frac{c_A}{c_{Ao}} = \xi - \xi_s Y, \quad \frac{c_B}{c_{Bo}} = 1 - \xi - (1 - \xi_s)Y, \tag{4.55}$$

where

$$\xi_s = \frac{c_{Bo}}{c_{Ao} + c_{Bo}}. \tag{4.56}$$

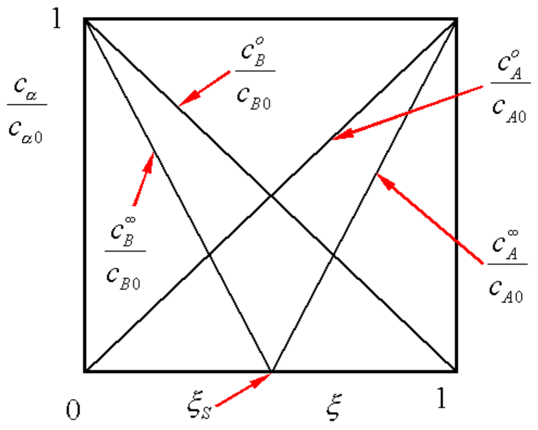

Figure 4.1: Relationships between mixture fraction and reactant concentration in the case of infinitely fast reaction and of no reaction.

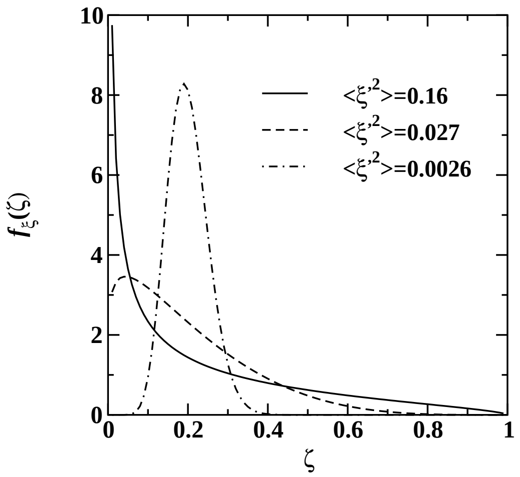

Figure 4.2: PDF at different values of mixture fraction variance and for $\langle\xi\rangle$=0.2

and where Y is the reaction progress variable. In the case of a non-reacting system $Y = 0$ whereas in the case of an instantaneous reaction, the two reactants cannot coexist at the same point, and the reaction progress variable can be evaluated as follows

$$Y_\infty(\xi) = \min\left(\frac{\xi}{\xi_s}, \frac{1-\xi}{1-\xi_s}\right). \tag{4.57}$$

Thus the original system identified by the composition vector of three components (c_A, c_B, c_C) is now identified by a vector of two components (ξ, Y), where ξ is a non-reacting scalar and Y is a reacting scalar. In Fig. 4.1 the relationships between concentrations and mixture fraction are reported.

What happens when there is a chemical reaction but with a finite rate? In this case the PDF no longer has a one dimensional support and another random variable must be added (e.g., reaction progress variable). This can be normally handled in full PDF codes by adding a new particle variable and by solving the corresponding transport equation in each notional particle. But when dealing with presumed mixture fraction PDF a conditional mean must be introduced. In fact the composition PDF is a joint function of the mixture fraction ξ and of the reaction progress variable Y. However can write the PDF

$$f_{\xi,Y} = f_{Y|\xi} f_\xi, \tag{4.58}$$

as the product of a conditional PDF and the mixture fraction PDF (which is known). The problem is now how to model this conditional PDF. Let as consider a specific problem. The source term for the reaction progress variable can be written as

$$S_Y = \frac{R}{\gamma_1}, \tag{4.59}$$

where R is the reaction rate of the chemical reaction $(A+B \leftarrow C)$ and $\gamma_1 = c_{A0}c_{B0}/(c_{A0} + c_{B0})$ is a scaling constant. Supposing the following kinetic scheme

$$R = kc_Ac_B, \tag{4.60}$$

and substituting, it results in

$$S_Y(\xi, Y) = k\gamma_1 \left(\frac{\xi}{\xi_s} - Y \right) \left(\frac{1-\xi}{1-\xi_s} - Y \right), \tag{4.61}$$

whose mean value due to scalar fluctuation is not known. The mean reaction progress variable is defined as follows

$$\langle Y \rangle = \int_0^1 \int_0^1 \Upsilon f_{\xi,Y} \mathrm{d}\Upsilon \mathrm{d}\zeta \tag{4.62}$$

and using the conditional PDF it becomes

$$\langle Y \rangle = \int_0^1 \left(\int_0^1 \Upsilon f_{Y|\xi} \mathrm{d}\Upsilon \right) f_\xi \mathrm{d}\zeta = \int_0^1 \langle Y \mid \zeta \rangle f_\xi \mathrm{d}\zeta \tag{4.63}$$

where $\langle Y \mid \zeta \rangle$ is the conditional reaction progress variable. In the case of mixing without reaction $Y = 0$ for each value of ξ and thus $\langle Y \mid \zeta \rangle = 0$. In the case of instateneous reaction $Y = Y_\infty(\xi)$ and thus $\langle Y \mid \zeta \rangle = Y_\infty(\zeta)$. The case of finite-rate reaction is somewhere between the two limit cases. This case be expressed in terms of the linear interpolation [53, 30]

$$\langle Y \mid \zeta \rangle = \alpha Y_\infty(\zeta), \tag{4.64}$$

where α is the interpolation parameter, that can be determined if the reaction progress variable is forced to yield the correct unconditional mean

$$\langle Y \rangle = \int_0^1 \langle Y \mid \zeta \rangle f_\xi \mathrm{d}\zeta = \alpha \langle Y_\infty \rangle \tag{4.65}$$

and thus

$$\alpha = \frac{\langle Y \rangle}{\langle Y_\infty \rangle}. \tag{4.66}$$

As a consequence the mean source term for the reaction progress variable is

$$\langle S_Y \rangle = k\gamma_1 \int_0^1 \left(\frac{\zeta}{\xi_s} - \frac{\langle Y \rangle}{\langle Y_\infty \rangle} Y_\infty(\zeta) \right) \left(\frac{1-\zeta}{1-\xi_s} - \frac{\langle Y \rangle}{\langle Y_\infty \rangle} Y_\infty(\zeta) \right) \mathrm{d}\zeta. \tag{4.67}$$

Beta PDF The Beta PDF can be conveniently used to describe the mixture fraction PDF in a number of cases [53, 58, 59]. The Beta PDF is uniquely determined by the mean mixture fraction $\langle \xi \rangle$ and the mixture fraction variance[7] $\langle \xi'^2 \rangle$:

$$\begin{aligned} f_\xi(\zeta) &= \frac{\zeta^{v-1}(1-\zeta)^{w-1}}{B(v,w)}, \\ v &= \langle \xi \rangle \left(\frac{\langle \xi \rangle (1 - \langle \xi \rangle)}{\langle \xi'^2 \rangle} - 1 \right), \\ w &= (1 - \langle \xi \rangle) \left(\frac{\langle \xi \rangle (1 - \langle \xi \rangle)}{\langle \xi'^2 \rangle} - 1 \right), \\ B(v,w) &= \int_0^1 x^{v-1}(1-x)^{w-1} dx. \end{aligned} \tag{4.68}$$

---

[7] Notice that ζ represents the sample-space variable corresponding to the random variable ξ.

Once the distribution of $\langle \xi \rangle$ and of $\langle {\xi'}^2 \rangle$ are known one can apply the Beta PDF to calculate the chemical source term. The distribution of $\langle \xi \rangle$ and of $\langle {\xi'}^2 \rangle$ can be calculated by solving Eqs. 2.21 and 2.23 with an appropriate model for the scalar dissipation rate. The shape of the beta PDF for $\langle \xi \rangle$=0.2 and for different values of $\langle {\xi'}^2 \rangle$ is reported in Fig. 4.2.

The Beta PDF approach is of immediate use for instantaneous chemical reactions, since in this case the relationship between concentrations and mixture fraction is given by Eq. 4.55 and Eq. 4.57. As already mentioned, when dealing with finite-rate chemical reactions the relationship between concentration and mixture fraction can be estimated by linear interpolation between the value for instantaneous reaction and for mixing without reaction. Thus the mean reaction rate can be computed as follows

$$\langle S_\alpha(\boldsymbol{\phi}) \rangle = \int_0^1 S_\alpha(\boldsymbol{\phi}(\zeta)) f_\xi(\zeta) d\zeta, \tag{4.69}$$

where the relationship between concentrations and mixture fraction is contained in $\boldsymbol{\phi}(\zeta)$.

As highlighted by Fox [57] the use of Beta PDF has some important limitations, and moreover solution of integrals involving the Beta PDF can be computationally expensive.

Finite-Mode PDF Using this approach every cell of the computational domain contains N_e different modes or environments, which correspond to a discretization of the composition PDF in a finite set of delta functions[8] [54]:

$$f_\phi(\psi; \mathbf{x}, t) \equiv \sum_{n=1}^{N_e} p_n(\mathbf{x}, t) \prod_{\alpha=1}^{m} \delta\left(\psi_\alpha - \langle \phi_\alpha \rangle_n(\mathbf{x}, t)\right) \tag{4.70}$$

where $p_n(\mathbf{x}, t)$ is the probability of mode n, $\langle \phi_\alpha \rangle_n(\mathbf{x}, t)$ is the value of scalar α corresponding to mode n, N_e is the total number of modes, and m is the total number of scalars. By definition, the probabilities p_n sum to unity and the average value of any scalar is defined by integration with respect to ψ. As already mentioned the PDF can be expressed in terms of the mixture fraction. Thus we will take the first scalar to be the mixture fraction: $\phi_1(\mathbf{x}, t) \equiv \xi(\mathbf{x}, t)$.

From Eq. 4.70, the average value of the mixture fraction is given by

$$\langle \xi \rangle \equiv \sum_{n=1}^{N_e} p_n \langle \xi \rangle_n, \tag{4.71}$$

whereas the mixture fraction variance is

$$\langle \xi'^2 \rangle = \langle \xi^2 \rangle - \langle \xi \rangle^2, \tag{4.72}$$

where $\langle \xi^2 \rangle$ is the second moment of the mixture fraction:

$$\langle \xi^2 \rangle \equiv \sum_{n=1}^{N} p_n \langle \xi \rangle_n^2. \tag{4.73}$$

---

[8] If Eqs. 4.70 and 4.49 are compared it is evident that in the full PDF representation each mode (or notional particle) has the same weight, whereas in the finite-mode PDF representation each mode is identified by a probability. Moreover generally the number of modes N_e is much lower than the number of notional particles N, allowing the use of a purely deterministic formulation of the problem.

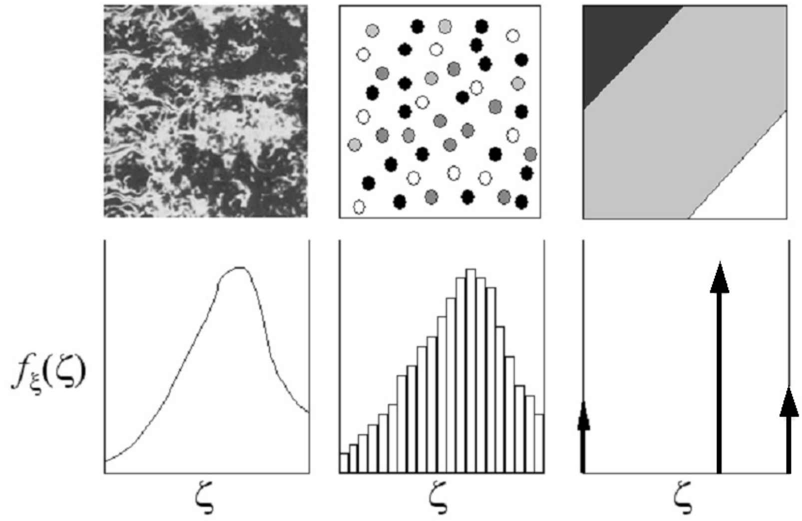

Figure 4.3: Different representations of the micromixing process and resulting probability density functions. From left to right: (a) real fluid (b) full PDF (c) finite-mode PDF.

Let us consider a number of modes N_e equal to three[9]; in this case the model is a finite-mode PDF model with three modes, and it can be thought of as the discretization of the reacting system in three environments, where Environments 1 and 2 contain unmixed reactants A and B, respectively, and reaction/particle formation occurs in Environment 3. It is interesting to highlight the different representations of the real fluid in the methods presented. In Fig. 4.3 the real fluid and the representation of the fluid in terms of notional particles (full PDF) and environments (finite-mode PDF) are shown. In the bottom the resulting representations of the PDF are also reported.

The scalar transport equations for the probabilities of modes 1 and 2, and for the weighted mixture fraction in Environment 3 ($\langle s_\xi \rangle_3 \equiv p_3 \langle \xi \rangle_3$) are

$$\frac{\partial p_1}{\partial t} + \frac{\partial}{\partial x_i}(\langle u_i \rangle p_1) = \frac{\partial}{\partial x_i}\left(\Gamma_t \frac{\partial p_1}{\partial x_i}\right) + \gamma_s p_3 - \gamma p_1 (1 - p_1), \tag{4.74}$$

$$\frac{\partial p_2}{\partial t} + \frac{\partial}{\partial x_i}(\langle u_i \rangle p_2) = \frac{\partial}{\partial x_i}\left(\Gamma_t \frac{\partial p_2}{\partial x_i}\right) + \gamma_s p_3 - \gamma p_2 (1 - p_2), \tag{4.75}$$

$$\begin{aligned} \frac{\partial \langle s_\xi \rangle_3}{\partial t} + \frac{\partial}{\partial x_i}(\langle u_i \rangle \langle s_\xi \rangle_3) = \frac{\partial}{\partial x_i}\left(\Gamma_t \frac{\partial \langle s_\xi \rangle_3}{\partial x_i}\right) - \gamma_s p_3 (\langle \xi \rangle_1 + \langle \xi \rangle_2) \\ + \gamma p_1 (1 - p_1) \langle \xi \rangle_1 + \gamma p_2 (1 - p_2) \langle \xi \rangle_2 . \end{aligned} \tag{4.76}$$

where $p_3 = 1 - p_1 - p_2$, and γ and γ_s are respectively the micromixing rate, and the spurious dissipation rate. Note that γ_s is required to eliminate spurious scalar dissipation resulting

---

[9] Here the choice of N_e=3 could seem arbitrary, however we shall look at questions concerning the number of modes in great details in Chapter 6, where a more general formulation of the model is presented.

from the finite-mode representation. The formulation of these transport equations was done in order to ensure mass balance for a non-reacting scalar (i.e., mixture fraction,) whereas the functional form of the terms γ and γ_s can be explicitated by forcing the resulting mixture fraction variance to obey the correct transport equation. Let us derive γ and γ_s: the mixture fraction in Environments 1 and 2 are, respectively, $\langle\xi\rangle_1 = 1$ and $\langle\xi\rangle_2 = 0$, and thus the mean mixture fraction is equal to

$$\langle\xi\rangle = p_1 + \langle s_\xi\rangle_3, \tag{4.77}$$

whereas the variance is given by

$$\langle\xi'^2\rangle = p_1 + \frac{\langle s_\xi\rangle_3^2}{p_3} - \langle\xi\rangle^2. \tag{4.78}$$

Manipulation of Eq. 4.77 leads to the transport equation of a conserved passive scalar:

$$\frac{\partial\langle\xi\rangle}{\partial t} + \frac{\partial}{\partial x_i}(\langle u_i\rangle\langle\xi'^2\rangle) = \frac{\partial}{\partial x_i}\left(\Gamma_t\frac{\partial\langle\xi\rangle}{\partial x_i}\right), \tag{4.79}$$

and manipulation of Eq. 4.78 leads to:

$$\frac{\partial\langle\xi'^2\rangle}{\partial t} + \frac{\partial}{\partial x_i}(\langle u_i\rangle\langle\xi'^2\rangle) = \frac{\partial}{\partial x_i}\left(\Gamma_t\frac{\partial\langle\xi'^2\rangle}{\partial x_i}\right) + 2\Gamma_t\frac{\partial\langle\xi\rangle}{\partial x_i}\frac{\partial\langle\xi\rangle}{\partial x_i} - 2\langle\varepsilon_\xi\rangle_s - 2\langle\varepsilon_\xi\rangle \tag{4.80}$$

where $\langle\varepsilon_\xi\rangle_s$ and $\langle\varepsilon_\xi\rangle$ are

$$\langle\varepsilon_\xi\rangle_s = \Gamma_t p_3\frac{\partial\langle\xi\rangle_3}{\partial x_i}\frac{\partial\langle\xi\rangle_3}{\partial x_i} - \frac{\gamma_s}{2}p_3\left[1 + 2\langle\xi\rangle_3^2 - 2\langle\xi\rangle_3\right], \tag{4.81}$$

$$\langle\varepsilon_\xi\rangle = \frac{\gamma}{2}\left[p_1(1-p_1)\left(1-\langle\xi\rangle_3\right)^2 + p_2(1-p_2)\langle\xi\rangle_3^2\right], \tag{4.82}$$

and $\langle\xi\rangle_3 = \langle s_\xi\rangle_3/p_3$ is the local mixture fraction in Environment 3.

Except for the spurious scalar dissipation rate $\langle\varepsilon_\xi\rangle_s$, Eq. 4.80 is identical to the scalar variance transport equation for a conserved passive scalar (see Eq. 4.17). However, from Eq. 4.81 it can be seen that $\langle\varepsilon_\xi\rangle_s$ can be eliminated by setting γ_s as follows:

$$\gamma_s = \frac{2\Gamma_t}{1 - 2\langle\xi\rangle_3(1-\langle\xi\rangle_3)}\frac{\partial\langle\xi\rangle_3}{\partial x_i}\frac{\partial\langle\xi\rangle_3}{\partial x_i}. \tag{4.83}$$

The term $\langle\varepsilon_\xi\rangle$ is the scalar dissipation rate due to micromixing. Reversing Eq. 4.82 an expression for γ is found:

$$\gamma = \frac{\langle\varepsilon_\xi\rangle}{[p_1(1-p_1)(1-\langle\xi\rangle_3)^2 + p_2(1-p_2)\langle\xi\rangle_3^2]}. \tag{4.84}$$

Thus given a generic chemical system that is identified by the composition vector $\boldsymbol{\phi}$, the mean value is:

$$\langle\boldsymbol{\phi}\rangle = \sum_{n=1}^{3} p_n\langle\boldsymbol{\phi}\rangle_n = \sum_{n=1}^{3}\langle\mathbf{s}\rangle_n, \tag{4.85}$$

where $\langle\boldsymbol{\phi}\rangle_n$ is the local composition vector in Environment/mode n and $\langle\mathbf{s}\rangle_n$ is the weighted composition vector in Environment/mode n, according to the following definition:

$$\langle\boldsymbol{\phi}\rangle_n = \langle\mathbf{s}\rangle_n/p_n. \tag{4.86}$$

The transport equation for the weighted composition vector in Environment/mode 3 is (compare Eq. 4.76 and 2.21)

$$\frac{\partial \langle \mathbf{s} \rangle_3}{\partial t} + \frac{\partial}{\partial x_i}(\langle u_i \rangle \langle \mathbf{s} \rangle_3) = \frac{\partial}{\partial x_i}\left(\Gamma_t \frac{\partial \langle \mathbf{s} \rangle_3}{\partial x_i}\right) - \gamma_s p_3(\langle \boldsymbol{\phi} \rangle_1 + \langle \boldsymbol{\phi} \rangle_2)$$
$$+\gamma p_1(1-p_1)\langle \boldsymbol{\phi} \rangle_1 + \gamma p_2(1-p_2)\langle \boldsymbol{\phi} \rangle_2 + p_3 S(\langle \boldsymbol{\phi} \rangle_3). \quad (4.87)$$

This transport equation shows how reactants (introduced through Environment/mode 1 and 2) reached Environment/mode 3 because of the probability flux, and in Environment/mode 3 react. It is also clear how the closure problem is handled with this model: the mean chemical source term is calculated by using local concentrations $\langle \boldsymbol{\phi} \rangle_3$ and p_3 is used to get the mean value.

As a conclusion it is possible to say that micromixing influences the predictions of the model in regions where $p_3 < 1$, whereas in perfectly micromixed regions p_3=1. The local composition vector $\langle \boldsymbol{\phi} \rangle_3$ will thus be greater than the mean composition vector $\langle \mathbf{s} \rangle_3$ whenever $p_3 < 1$, resulting in increased chemical source term.

4.3 Solid evolution and population balance

The population balance is a continuity statement based on the number density function. This function is defined in several ways depending on the properties of the system under observation. Given the coordinates of the property vector $\boldsymbol{\eta} \equiv (\eta_1, \ldots, \eta_K)$ that specify the state of the particle, the number density function $n(\boldsymbol{\eta}; \mathbf{x}, t)$ is defined as follows

$$n(\boldsymbol{\eta}; \mathbf{x}, t) d\eta_1 \ldots d\eta_K = n(\boldsymbol{\eta}; \mathbf{x}, t) d\boldsymbol{\eta}, \quad (4.88)$$

and represents the number of particles with a value of the property vector between $\boldsymbol{\eta}$ and $\boldsymbol{\eta} + d\boldsymbol{\eta}$. For a *homogeneous* particulate system the governing equation is (repeated indices imply summation)

$$\frac{\partial n(\boldsymbol{\eta}; t)}{\partial t} + \frac{\partial}{\partial \eta_i}[n(\boldsymbol{\eta}; t)\zeta_i] = h(\boldsymbol{\eta}; t) \quad (4.89)$$

where the "flux in $\boldsymbol{\eta}$-space" is denoted by

$$\zeta_i \equiv \frac{d\eta_i}{dt} \quad i \in 1, \ldots, K \quad (4.90)$$

and $h(\boldsymbol{\eta}; t)$ represents the net rate of introduction of new particles into the system [60].

Depending on the system of interest, the number density function may have only one internal coordinate (e.g., particle length or volume), or multiple coordinates (e.g., particle volume and surface area). Usually when dealing with nucleation and growth problems, the internal coordinate is a characteristic length, whereas when dealing with aggregation and breakage, the internal coordinate is the particle volume. We will consider a number density function defined in terms of the particle length ($\eta_1 \equiv L$), and then the homogeneous population balance is

$$\frac{\partial n(L; t)}{\partial t} + \frac{\partial}{\partial L}[G(L) n(L; t)] = B(L; t) - D(L; t) \quad (4.91)$$

where $G(L)$ is the growth rate, and $B(L; t)$ and $D(L; t)$ are, respectively, the birth and the death rates due to aggregation.

The study of aggregation started from the work of Smoluchowsky [16] who first defined the birth and the death rate for a discrete system composed of interacting monomers. The equations can be rewritten for a continuous system in terms of the particle volume (v) as follows:

$$B'(v;t) = \frac{1}{2}\int_0^v \beta'(v-\epsilon,\epsilon)n'(v-\epsilon;t)n'(\epsilon;t)d\epsilon, \tag{4.92}$$

$$D'(v;t) = n'(v;t)\int_0^{+\infty} \beta'(v,\epsilon)n'(\epsilon;t)d\epsilon, \tag{4.93}$$

where $n'(v;t)$ is the particle number density with particle volume as internal coordinate, and $\beta'(v,\epsilon)$ is the aggregation kernel. The latter is a measure of the frequency of collision of particles of volume v and ϵ.

In order to introduce these terms in Eq. 4.91, a one further operation is needed. Assuming that length and volume are related by $v \propto L^3$, it is easily shown that Eqs. 4.92 and 4.93 expressed in a length-based form are as follows:

$$B(L;t) = \frac{L^2}{2}\int_0^L \frac{\beta\left((L^3-\lambda^3)^{1/3},\lambda\right)}{(L^3-\lambda^3)^{2/3}} n\left((L^3-\lambda^3)^{1/3};t\right)n(\lambda;t)d\lambda, \tag{4.94}$$

$$D(L;t) = n(L;t)\int_0^{+\infty} \beta(L,\lambda)n(\lambda;t)d\lambda, \tag{4.95}$$

where L and λ are the dimensions of the particles with volumes v and ϵ, respectively.

Several numerical methods to solve this equation have been proposed. The most common methods are based on the discretization of the particle internal coordinate(s), leading to a discretized population balance (DPB). Depending on the philosophy of this discretization, different methods have been developed for aggregation and breakage [61, 62, 63] and aggregation and crystal growth [64, 65, 66, 67]. The available methods for aggregation-breakage problems basically differ on the discretization used, but in general nonlinear discretization is used. The situation is completely different for cases with crystal growth, not only because the problem is formulated using particle length as the internal coordinate, but also because in this case a linear discretization is the best approach. Another completely different approach is based on Monte-Carlo methods, in which a population of particles is considered and undergoes a birth-death process [68].

A review of the state of the art of population balances limited to the aggregation-breakage problem can be found in [69], whereas in [70] a detailed comparison of different methods is studied and discussed. Likewise, Ramkrishna [71] presents a lucid explanation of the mathematical issues involved.

In general, the DPB approach describes the population balance accurately, but can involve an extremely high number of scalars. If the final application is the implementation of the population balance in a CFD code, then the solution of the scalars has to be done in every cell of the computational domain, resulting in a very high calculation time. Thus, in order to study the effects of mixing using CFD, it will be necessary to develop alternative approaches that have nearly the same accuracy as the DPB approach, but use less scalars.

4.3.1 Moment methods

A computationally-attractive alternative approach is the standard moment method (SMM) in which the key is the formulation of the problem in terms of the lower-order moments in closed form (i.e., involving only function of the moments themselves). For a homogeneous system, the k^{th} moment is defined by

$$m_k(t) = \int_0^\infty L^k n(L;t)dL \tag{4.96}$$

The first five moments ($k \in 0, \ldots, 4$) are of particular interest, since they are related to the total number particle density ($N_t = m_0$), the total particle area ($A_t = k_a m_2$) and the total solids volume ($V_t = k_v m_3$) by shape factors (k_a, k_v) that depend on particle morphology. Moreover, using this approach a mean crystal size can be defined as follows:

$$L_{43} = \frac{m_4}{m_3}, \tag{4.97}$$

and the solids concentration is given by

$$c_s = \frac{\rho k_v m_3}{M}, \tag{4.98}$$

where ρ is the crystal density, k_v is the volume shape factor, and M is the molecular weight of the crystal.

In a homogeneous system, the resulting transport equation for the k^{th} moment is as follows

$$\frac{dm_k(t)}{dt} = (0)^k J(t) + \int_0^\infty kL^{k-1}G(L)n(L;t)dL + \overline{B}_k(t) - \overline{D}_k(t), \tag{4.99}$$

where $J(t)$ is the nucleation rate and the last two terms represent the effects of birth and death, respectively, due to aggregation. The first of these can be rewritten by setting $u^3 = L^3 - \lambda^3$ and reversing the order of integration [66]:

$$\overline{B}_k(t) = \frac{1}{2}\int_0^\infty n(\lambda;t)\int_0^\infty \beta(u,\lambda)\left(u^3 + \lambda^3\right)^{k/3} n(u;t)dud\lambda, \tag{4.100}$$

whereas the second one is

$$\overline{D}_k(t) = \int_0^\infty L^k n(L;t)\int_0^\infty \beta(L,\lambda)n(\lambda;t)d\lambda dL. \tag{4.101}$$

In the case of size-independent growth rate (G constant) and without aggregation and breakage ($\overline{B}_k$ and $\overline{D}_k$ null), the moments can be computed directly without requiring additional knowledge of the number density function. In all the other cases, unless one makes use of simplifications, the SMM is not applicable[10].

---

[10] In Chapter 6 a possible solution of the nucleation, growth, and aggregation problem, by using the SMM, will be presented and discussed (see pag. 122.)

4.3.2 Discretized population balances

A number of discretized population balances (DPB) or classes method (CM) have been proposed for simultaneous modeling of nucleation, growth and aggregation. Here we discuss the method proposed by Hounslow and co-workers [67]. The Hounslow's approach is based on the idea that aggregates are formed of particles of 2^{i-1} monomers (as if only particles made by 1,2,4,8, ... monomers exist). In terms of length-based expressions, it becomes $L_{i+1} = L_i 2^{1/3}$. More recently, a revised version of the model has been proposed [66], using an adjustable discretized population balance, by means of a parameter q, and thus the discretization scheme becomes $L_{i+1} = L_i \left(2^{1/q}\right)^{1/3}$. However, it should be noticed that this modification improves results for very extensive aggregation, that usually is not the case of crystallizer/precipitator. Defining N_i as a function such that

$$m_k = \sum_{i}^{N_c} \overline{L_i^k} N_i \tag{4.102}$$

where $\overline{L_i^k}$ is the appropriate mean size, results in the following set of equations[11]:

$$\left(\frac{dN_i}{dt}\right)_{agg} = N_{i-1} \sum_{j=1}^{i-1} 2^{j-i+1} \beta_{i-1,j} N_j + \frac{1}{2} \beta_{i-1,j-1} N_{i-1}^2 \tag{4.103}$$

$$-N_i \sum_{j=1}^{i-1} 2^{j-i} \beta_{i,j} N_j - N_i \sum_{j=i}^{\infty} \beta_{i,j} N_j \quad i \in 1, \ldots, N_c, \tag{4.104}$$

whereas for crystal growth

$$\left(\frac{dN_i}{dt}\right)_{growth} = \frac{2G}{(1+r)L_i} \left(\frac{r}{r^2-1} N_{i-1} + N_i - \frac{r}{r^2-1} N_{i+1},\right) \tag{4.105}$$

where $r = L_{i+1}/L_i$. This approach gives quite good performances in the case of aggregation with simultaneous nucleation and growth. Other methods exist, but give good performances only in the case of purely aggregation, or purely nucleation and growth. These methods however present the inconvenient that in order to work with good accuracy an elevate number of classes are needed (e.g., 20-30 for simple problems, and 100-200 for complex problems.) As already mentioned for CFD applications this could results in an enormous amount of calculations, since this elevate number of transport equations have to be solved in every cell of the computational domain.

4.3.3 Quadrature method of moments

The quadrature method of moments (QMOM) was first proposed by McGraw [72] for studying aerosol evolution under size-dependent growth rate. This method is based on the idea of constructing a quadrature approximation as follows:

$$n(L;t) \approx \sum_{i=1}^{N_q} w_i(t) \delta \left(L - L_i(t)\right), \tag{4.106}$$

---

[11] The model is derived by defining 4 binary interaction mechanisms that produce a birth or a death in the i^{th} interval. Aggregation between a particle in the $(i-1)^{th}$ and of a particle in the first to $(i-2)^{th}$ interval produces a new particle in the i^{th} interval. Aggregation between two particles both in the $(i-1)^{th}$ interval results in the formation of a particle in the i^{th} interval. Death occurs to a particle in the i^{th} interval should it aggregate with a particle of sufficient size for the resultant aggregate to be larger than the upper size limit of the i^{th} interval. If a particle in the i^{th} interval aggregates with a particle from that or a higher interval, a death occurs in the i^{th} interval.

so that, for example,

$$m_k(t) \approx \sum_{i=1}^{N_q} w_i(t) L_i^k(t). \tag{4.107}$$

The essence of this method is the fact that the abscissas $L_i(t)$ and the weights $w_i(t)$ can be specified from the lower-order moments. In fact, in order to build a quadrature approximation of order N_q, it suffices to know the first $2N_q$ moments. Thus, for example, the first six moments $(m_0, \ldots, m_5)$ suffice to build a QMOM approximation of order $N_q = 3$.

Once abscissas and weights have been computed, any integral involving the number distribution function $n(L;t)$ can be approximated using Eq. 4.106. The procedure used to find w_i and L_i from the moments is based on the product-difference (PD) algorithm proposed by Gordon [73]. The first step is the construction of a matrix $\mathbf{P}$ with components $P_{i,j}$ starting from the moments [72]. The components in the first column of $\mathbf{P}$ are

$$P_{i,1} = \delta_{i1} \quad i \in 1, \ldots, 2N_q + 1, \tag{4.108}$$

where δ_{i1} is the Kronecker delta. The components in the second column of $\mathbf{P}$ are

$$P_{i,2} = (-1)^{i-1} m_{i-1} \quad i \in 1, \ldots, 2N_q + 1. \tag{4.109}$$

Since the final weights can be corrected by multiplying by the true m_0, the calculations can be done assuming a normalized distribution (i.e., $m_0 = 1$). Then the remaining components are found from the PD algorithm:

$$P_{i,j} = P_{1,j-1} P_{i+1,j-2} - P_{i,j-2} P_{i+1,j-1} \tag{4.110}$$

where $j \in 3, \ldots, 2N_q + 1$ and $i \in 1, \ldots, 2N_q + 2 - j$. If, for example, $N_q = 2$ then $\mathbf{P}$ becomes

$$\mathbf{P} = \begin{pmatrix} 1 & 1 & m_1 & m_2 - m_1^2 & m_3 m_1 - m_2^2 \\ 0 & -m_1 & -m_2 & -m_3 + m_2 m_1 & 0 \\ 0 & m_2 & m_3 & 0 & 0 \\ 0 & -m_3 & 0 & 0 & 0 \\ 0 & 0 & 0 & 0 & 0 \end{pmatrix}. \tag{4.111}$$

The coefficients of the continued fraction (α_i) are generated by setting the first element to zero $(\alpha_1 = 0)$, and computing the others according to the following recursive relationship:

$$\alpha_i = \frac{P_{1,i+1}}{P_{1,i} P_{1,i-1}} \quad i \in 2, \ldots, 2N_q. \tag{4.112}$$

A symmetric tridiagonal matrix is obtained from sums and products of α_i:

$$a_i = \alpha_{2i} + \alpha_{2i-1} \quad i \in 1, \ldots, 2N_q - 1 \tag{4.113}$$

and

$$b_i = -\sqrt{\alpha_{2i+1} \alpha_{2i-1}} \quad i \in 1, \ldots, 2N_q - 2, \tag{4.114}$$

where a_i and b_i are, respectively, the diagonal and the co-diagonal of the Jacobi matrix. Once the matrix is determined, generation of the weights and abscissas is done by finding the eigenvalues and the eigenvectors of the matrix. In fact, the eigenvalues are the abscissas and the weights can be found as follows:

$$w_j = m_0 v_{j1}^2 \tag{4.115}$$

where v_{j1} is the first component of the j^{th} eigenvector $\mathbf{v}_j$.

When working with the first six moments $(m_0, \ldots, m_5)$, the method is based on the approximation of the number density function with a sum of $N_q = 3$ delta functions

$$\begin{aligned} n(L;t) = w_1(t)\delta\left(L - L_1(t)\right) + w_2(t)\delta\left(L - L_2(t)\right) \\ + w_3(t)\delta\left(L - L_3(t)\right) \end{aligned} \tag{4.116}$$

and represents a population made up of three classes of particles with dimension $L_1(t)$, $L_2(t)$, and $L_3(t)$ and number densities $w_1(t)$, $w_2(t)$, $w_3(t)$. As an example, consider a population with $L_1(0) = 1$, $L_2(0) = 2$, $L_3(0) = 3$ arbitrary unit (a.u.), $w_1(0) = 0.2$, $w_2(0) = 0.1$, and $w_3(0) = 0.7$, and with a constant growth rate $G = 1$ a.u./s. The moment equations for this system are

$$\frac{dm_k}{dt} = kGm_{k-1} \quad k \in 0, \ldots, 5, \tag{4.117}$$

with initial conditions

$$m_k(0) = \sum_{i=1}^{3} w_i(0) L_i(0)^k \quad k \in 0, \ldots, 5. \tag{4.118}$$

From the first six moments $(m_0, \ldots, m_5)$, the PD algorithm can be used to compute the three weights and abscissas. Results are reported in Fig. 4.4, where it is shown that $w_i(t)$ remains constant whereas $L_i(t)$ increases following the real increase of length of the three classes.

For the case where $L_1(0) = 2$, $L_2(0) = 3$ and $L_3(0) = \left(L_1(0)^3 + L_2(0)^3\right)^{1/3}$ and $w_1(0) = 0.5$, $w_2(0) = 0.5$, $w_3(0) = 0.0$ and particles L_1 aggregates with particles L_2 to give particles L_3 preserving the volume (without nucleation and growth), the source terms for aggregation are very simple and the population balance can be written in terms of the moments as follows:

$$\begin{aligned} \frac{dm_k(t)}{dt} = \left(-L_1(t)^k - L_2(t)^k + L_3(t)^k\right)\left[m_0(t) - \frac{m_0(0)}{2}\right] \\ k \in 0, \ldots, 5. \end{aligned} \tag{4.119}$$

Supposing an aggregation rate of $[m_0(t) - m_0(0)/2]$ and tracking again abscissas and weights by using the PD algorithm, three different eigenvalues equal to $L_1(t) = 2$, $L_2(t) = 3$, $L_3(t) = \left(L_1(t)^3 + L_2(t)^3\right)^{1/3}$ and the three weights reported in Fig. 4.5 are found. As it is possible to see, $w_1(t)$ and $w_2(t)$ go to zero and $w_3(t)$ goes to 0.5. In fact, the total number of particles is one half after all particles of dimension $L_1(t)$ and $L_2(t)$ have aggregated. Obviously anytime the moments refer to a number density function that cannot be exactly represented by three classes of particles, Eq. 4.116 is no longer exact. For these cases, validation of the method is required[12].

---

[12] Part of the validation has been already carried out and preliminary results are reported in Section 6.1.2.

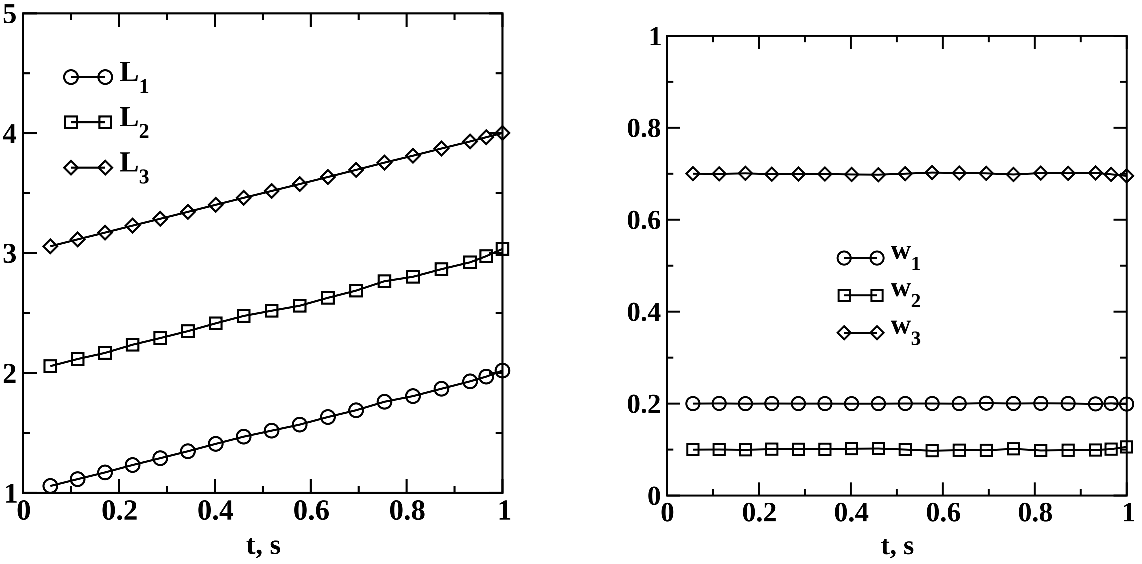

Figure 4.4: Evolution with time of the abscissas (L_i) and weights (w_i) for three classes of particles in case of size-independent growth.

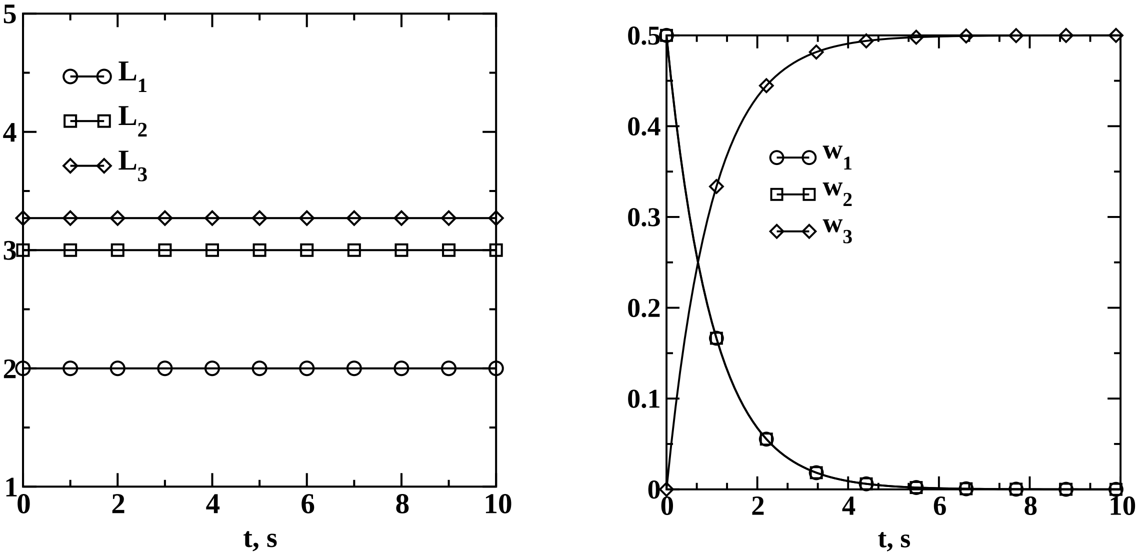

Figure 4.5: Evolution with time of the abscissas (L_i) and weights (w_i) for three classes of particles with aggregation.

Chapter 5

Experimental set-up and operating conditions

In this chapter the experimental set-up is presented. Two different reactors have been investigated: a Taylor-Couette reactor and a tubular reactor. Since the flow field in the first system is quite particular a preliminary validation of flow field and tracer dispersion predictions have been carried out, by using Laser techniques. As concerns the tubular reactor the validation was carried out in a previous work [74]. Two types of fast reactions have been used for studying the effect of mixing: parallel-competitive reactions and precipitation reaction.

5.1 Parallel reactions

Parallel reactions have been often used in past years to characterized mixing efficiency in chemical reactors. Different systems have been proposed in literature, but they can be always reduced in the following scheme:

$$\begin{aligned} B + A &\rightarrow R, \\ C + A &\rightarrow S, \end{aligned} \tag{5.1}$$

where the first reaction is quasi-instantaneous, whereas the second one is fast. In this work we used the iodide-iodate reaction [75], where

$$\begin{aligned} A &= \mathrm{H}^+, \\ B &= \mathrm{H_2BO_3^-}, \\ C &= 5/6\ \mathrm{I}^- + 1/6\ \mathrm{IO_3^-}, \\ R &= \mathrm{H_3BO_3}, \\ S &= 1/2\ \mathrm{I_2}. \end{aligned}$$

The procedure consists in adding a small quantity of concentrated solution of A, as limiting reactant, to a mixture of B and C. In perfectly mixed systems, A is immediately mixed through the solution and only the first reaction occurs; but if mixing is not perfect a local excess of A remains and reacts according to the second reaction scheme. It is clear that the quantity of S formed is a measure of the intensity of segregation of the chemical reactor. The selectivity of the second reaction is defined as the ratio of the acid mole number consumed by the second reaction dived by the acid mole number injected

$$\sigma = \frac{2n_{\mathrm{I}_2}}{n^o_{\mathrm{H}^+}} = \frac{2V_R c_S}{v_i c_{Ao}}, \tag{5.2}$$

where V_R is the chemical reactor volume, v_i is the injected volume, and c_{Ao} is the concentration of the injected solution. In the case of total segregation it results in

$$\sigma_{ST} = \frac{c_{Co}/c_{Bo}}{c_{Co}/c_{Bo}+1}. \tag{5.3}$$

The degree of segregation of the reactor can be quantified by the segregation index defined by:

$$X_s = \frac{\sigma}{\sigma_{ST}}. \tag{5.4}$$

This quantity is null in prefect mixing conditions and equal to unity in total segregation conditions.

5.2 Precipitation reaction

Precipitation can be seen as a consecutive-competitive reaction, where barium sulfate molecules are unstable and form solid nuclei (first reaction), which can grow to form macroscopic crystals (second reaction.) The first reaction is nucleation and is quasi-instantaneous, whereas the second one is crystal growth and is fast. A measure of the degree of segregation of the system is the crystal size distribution (CSD) of the solid formed; in fact if nucleation is favored crystals are smaller. The mean crystal size[1] d_{43} can be used to quantify these effects. However one should never forget that crystals can growth according to other mechanisms (e.g., aggregation) and can also undergo break-up processes. These processes modify the CSD but can not be directly linked to molecular mixing. In this work barium sulfate precipitation was investigated. Barium sulfate was precipitated from aqueous solutions of barium chloride and sodium sulfate.

5.3 The Taylor-Couette reactor

The Taylor-Couette reactor is made of two coaxial cylinders with the inner one rotating. The fluid is contained in the annular gap and depending on the rotational velocity of the inner cylinder several fluid dynamic regimes are achieved. This system has attracted much attention in the study of flow instabilities of fluids past solid boundaries. Taylor [76] carried out the first systematic study on this device and found that depending on the viscosity of the fluid, on the configuration and the motion of the boundaries, when the velocity of the fluid exceeds a certain limit, the steady state motion breaks down and eddying flow sets in (see Fig 5.1).

A detailed review of the theoretical and mathematical aspects of the instabilities in circular Taylor-Couette flows can be found in [77], here we limit our discussion to a brief

---

[1] This quantity is calculated as the ratio of the 4^{th} and 3^{th} moments of the normalized CSD, and has been defined at pag. 16.

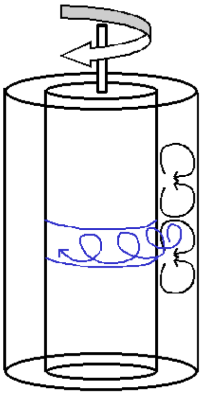

Figure 5.1: Skecth of the Taylor-Couette reactor. In the figure the toroidal structure of the flow is also reported.

presentation of the several fluid dynamic regimes in this device. It is useful to define some dimensionless quantities, such as the Reynolds number

$$Re_r = \frac{\Omega_1 r_1 d}{\nu} \tag{5.5}$$

and the Taylor number

$$Ta = \frac{\Omega_1^2 r_1 d^3}{\nu^2} \tag{5.6}$$

where r_1 is the radius of the inner cylinder, Ω_1 is the rotational velocity of the inner cylinder, d is the annular gap, r_2 is the radius of the outer cylinder, and ν is the kinematic viscosity of the fluid. When the Reynolds (or Taylor) number is lower than a critical value the flow is stable and is known as Laminar Couette Flow (LCF), whereas when the Reynolds number is greater than this critical value the flow becomes unstable and infinitesimal disturbances are amplified, causing the formation of toroidal equispaced vortices. This latest is called Laminar Taylor Vortex Flow (LTVF). In his pioneering work Taylor by using the linear instability theory achieved the first success in the calculation of fluid instability, and was able to predict the critical Taylor number for the first transition:

$$Ta_c = \frac{\pi\left(1+\frac{d}{2r_1}\right)}{0.0571\left(1-0.652\frac{d}{r_1}\right)+\frac{0.00056}{\left(1-0.652\frac{d}{r_1}\right)}}, \tag{5.7}$$

or in terms of the Reynolds number:

$$Re_c = \left(Ta_c\frac{r_1}{d}\right)^{1/2}, \tag{5.8}$$

but his theory could not correctly describe the characteristics of this flow. Using a nonlinear theory [78, 79, 80] it is possible to rigorously calculate for the LTVF the equilibrium values of velocity disturbances .

As the Reynolds number is increased further, the axialsymmetric LTVF becomes unstable leading to a time-dependent vortex flow called Singly Periodic Wavy Vortex Flow (SPWVF), and Re_s is the critical Reynolds number at which this transition occurs. Systematic investigations of this flow [81] show that it is possible to achieve several stable states at a given Reynolds number. Power spectra of radial component of velocity fluctuations were analyzed for this flow regime [82] and for Reynolds number slightly greater than Re_s only a single frequency component was detected, that is the frequency of traveling azimuthal waves passing a fixed point.

As the Reynolds number is raised further the SPWVF becomes more complex; in fact, the amplitude of the azimuthal waves varies periodically with time. As a matter of fact, in this regime a second fundamental frequency appears in the power spectrum, that can be identified with the frequency of amplitude modulation of the first fundamental mode. This transition occurs when the Reynolds number is equal to Re_q and the established regime is known as Quasi Periodic Wavy Vortex flow (QPWVF).

As the Reynolds number goes beyond a critical value (Re_t) the azimuthal waves cease preserving the vortex structure. Power spectra in this range no longer contain the two fundamental frequencies, and this is the sign of the generation of chaotic turbulence.

A further increase in Re_r beyond another critical value (Re_f) causes the destruction of the vortex structure leading to a fully turbulent flow (FTF) without vortices [83]. Although, it is not possible to correctly predict the exact value at which this sequence of transitions occurs and often not even the type of fluid dynamic regime achieved, it is possible to outline a likely sequence of transitions as follows

$$LCF \rightarrow LTVF \rightarrow SPWVF \rightarrow QPWVF \rightarrow TVF \rightarrow FTF. \tag{5.9}$$

However it should be highlighted that if the ratio of the radii of the inner and outer cylinder is lower than 0.714 the SPWVF and the QPWVF are generally unstable and then there is a direct transition from LTVF to TVF. It is also possible to define for each transition an approximate value of Re_r at which the transition occurs, in terms of Re_c that identifies the first transition. The Taylor-Couette reactor used in this work has the inner radius r_1= 4.1 mm, the outer radius r_2=5.5 mm and the height H=205 mm. In Tab. 5.1 the different transitions are reported. The sequence of transitions reported in Tab. 5.1 can be explained also in terms of the period-doubling cascade [84] . If the axial component of the velocity in one point of the reactor is reported against the Re_r number the solution diagram is obtained (see Fig. 5.2.)

In this diagram the stable and unstable solutions of the system are reported with a particular notation that is explained below. When $Re_r < Re_c$ the axial velocity is null, since no eddy flow occurs, but as Re_r turns the first critical value the LTVF is established. In this operating condition the axial velocity is not null, and increases increasing Re_r. However the flow is time-independent and this is represented by a continuous line in the diagram. When Re_s is reached the SPWVF is established, the axial velocity varies periodically, and forms a limit cycle in the velocity space. This transition is a Hopf bifurcation. This is represented by filled circles in the diagram, and the two branches represent the upper and lower bound of the axial velocity. At Re_q the transition to the QPWVF occurs, and as already mentioned a new frequency appears, and the limit cycle lies on a toroidal surface and not anymore on a circle. Then a period-doubling cascade is generated and when Re_r=Re_t the flow is completely chaotic.

Table 5.1: Summary of the estimated numerical values of the critical Re_r numbers and critical rotational speeds of the inner cylinder N .

	Re_r	Re_r	N, rpm
Re_c		86	1.4
Re_s	1.2 Re_c	103	1.7
Re_q	10 Re_c	860	14
Re_t	22 Re_c	1892	31
Re_f	700 Re_c	60200	1000

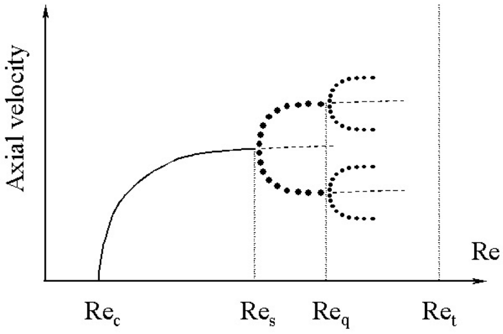

Figure 5.2: Solution diagram showing the period-doubling cascade.

In order to picture the level of chaos, or with more appropriate words, in order to analyze the properties of this dissipative nonlinear dynamic system, one makes use of power spectra, phase space reconstructions, Poincaré sections, returns map and fractal dimensions. A section of the evolution in the phase space of the dynamic system is a Poincaré section, whereas a projection of the time evolution of the phase space on a plane orthogonal to the time axis, shows the presence of an attractor.

In the study of chaos very useful is also the determination of the Liapunov exponents, that can be seen as a measure of the sensitivity on initial conditions[2]. In the case of turbulent flows we deal with *strange attractors*, which exhibit fractal features. In fact due to dissipation, volume in phase space shrink and therefore lengths cannot expand in all directions, and because of the finite boundary of the attractive basin, volume elements are folded at the same time. This stretching, shrinking and folding process leads to the self-similar structure of the attractor [86]. The determination of the fractal dimension of the attractor gives very interesting information on the order to disorder transition that occurs increasing the Re number. It has been shown for example that in the transition to chaos the fractal dimension behaves as the one-fourth power of the control parameter (Re) a value very similar to a continuous phase transition [87]. It is now clear that the fractal dimension can be used as an order parameter to characterize these transitions.

5.3.1 Experimental investigation of flow and non-reacting scalar field

Experimental information concerning the flow field and the scalar field are provided by using three measurement techniques: Laser sheet visualization, Laser Doppler Anenometry (LDA), Laser Induced Fluorescence (LIF).

The **laser sheet** is created by a 10 mW Ionized Argon Laser whose beam is vertically diverted by a mirror in order to cross two collimating lenses. This sheet visualizes a meridian plane (as show in Fig. 5.3) of the flow field seeded by solid refractive particles. This technique can be used to gather qualitative information on the flow field and to determine some important characteristics, such as, time dependencies, number of vortices, and stability.

The **laser doppler anenometry (LDA)** technique is particularly devoted to steady state flow field and provides mean velocities, and velocities cross correlations. The apparatus used in this work can simultaneously measure 2 velocity components, axial velocity (u_z) and azimuthal velocity (u_θ) as shown in Fig. 5.4. The technique consists in measuring velocity of very small refractive particles (10 μm.) Two pairs of laser beams generated by an Ionized Argon Laser at 2 different wave lengths (541 nm and 488 nm) are focused in such a way that the four beams cross in a common confined volume. Particles that cross this probe volume emit in all directions with a new frequency: the emitted light is concentrated and led to a photomultiplier. The frequency shift between incident light and emitted light is called Doppler frequency and it is proportional to velocity. After acquisition, data are statistically treated giving: mean axial velocity $\langle u_z \rangle$, mean azimuthal velocity $\langle u_\theta \rangle$, and three components of the Reynolds stress tensor: $\langle u'_z u'_z \rangle$, $\langle u'_\theta u'_\theta \rangle$ and $\langle u'_z u'_\theta \rangle$.

The **Laser Induced Fluorescence (LIF)** technique provides evolution of mean concentration of a non-reacting scalar in steady and unsteady conditions. The fluorescent dye used in this work is Rhodamin B whose absorption spectrum is centered around 580 nm. The green light of the Ionized Argon Laser (514 nm) excites Rhodamin B molecules,

---

[2] For more details on Liapounov exponents and nonlinear dynamics see also [85].

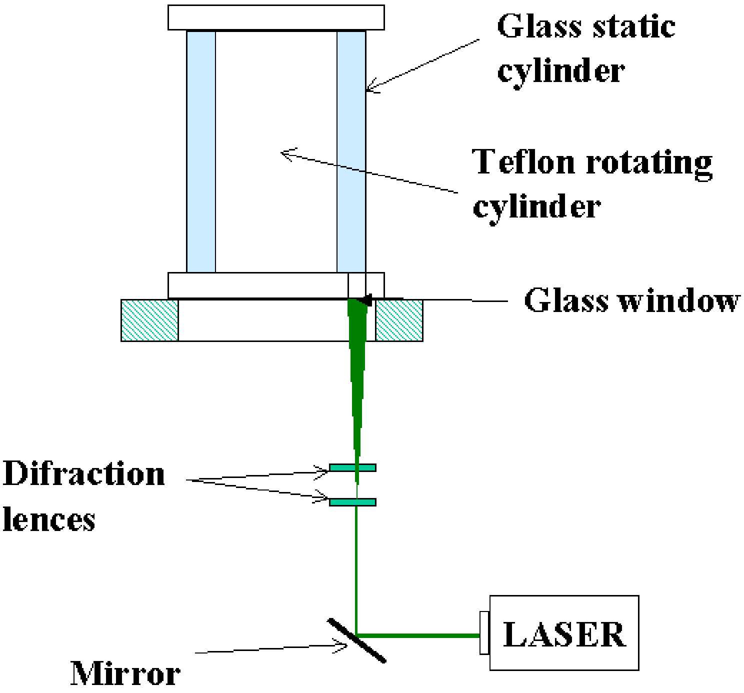

Figure 5.3: Experimental setup used is the lasersheet visualization tests.

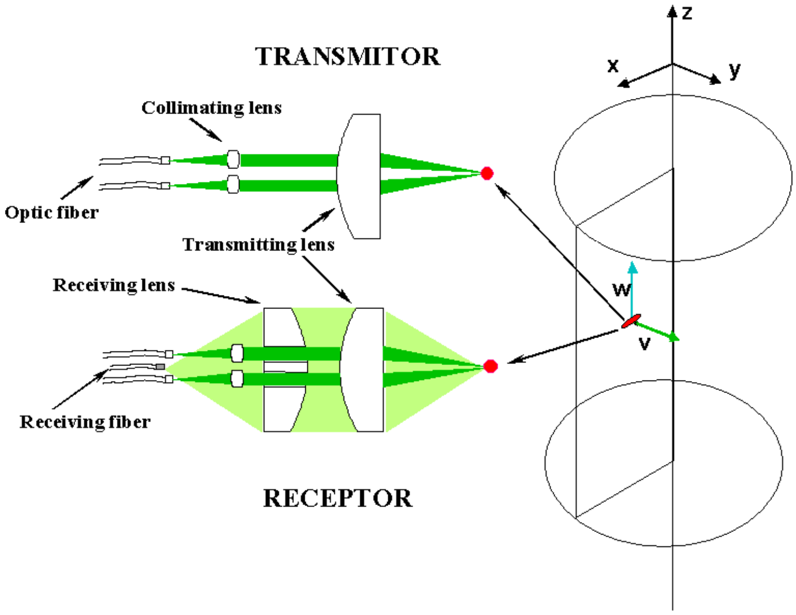

Figure 5.4: Sketch of the Laser Doppler Anenometry device used in the experiments. Laser beams are collected by the transmitting lens and focus on the probe volume. Emitted beams are collected by two lens and are focused on the receiving fiber.

that decay to the fundamental energy state by emitting a light whose spectrum is centered around 590nm. The emitted light is collected, led to a photomultiplier, and analyzed.

As mentioned before (see Tab. 5.1), the transition to TVF is estimated to occurs at Re=1,892 whereas the transition to FTF at Re=60,200 that correspond respectively to 31 rpm and 1,000 rpm. However, it is useful to highlight that these values must be used as approximate indications. In this work the behavior of the reactor was investigated in the turbulent region. Three different types of analysis have been carried out. In the first type the number of vortices has been counted by using the Laser sheet visualization technique and LDA measurements only for few radial positions scanning the axial direction. In this part of the work the rotational speed of the inner cylinder was varied between 35 rpm and 500 rpm. Then a deeper study at 300 rpm was carried out. For this rotational speed the mean axial velocity, the swirl velocity, and three Reynolds-stresses, were measured by scanning through a fine two- dimensional grid (scanning the axial and radial direction) in one meridian plane. Then the effect of injector and of injection were studied. Four different injection positions were investigated indicated with FP1, FP2, FP3, and FP4. The injector was made of a small tube (OD: 2 mm, ID: 1mm) positioned in the middle of the annular gap at 0 mm (FP1), 70 mm (FP2), 95 mm (FP3) and 105 mm (FP4) from the top. The extremity of the injector was curved in order to lead the injected fluid in the direction of the mean flow. Eventually the dispersion of an inert tracer was studied. The tracer was injected in the four different positions with an injection velocity equal to 30 ml/min and LIF was used to determine local values of tracer concentration. Tracer concentration was determined in a meridian plane that forms an angle of 270 degrees with the injection plane. Measurements were taken on this plane at five different points, namely

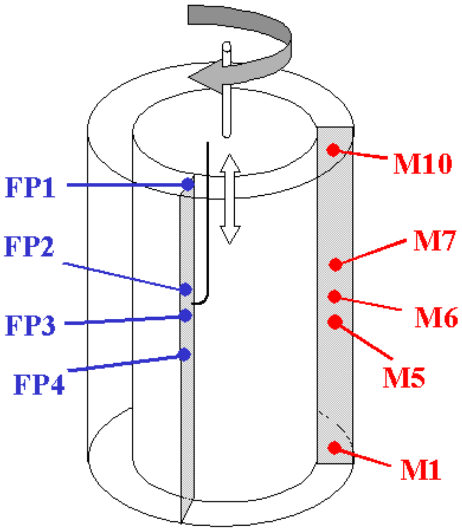

Figure 5.5: Sketch of the reactor. With FP1-FP2-FP3-FP4 are indicated the four injection positions, and with M1-M5-M6-M7-M10 are indicated the five measurement points.

M1, M5, M6, M7, M10 that correspond to an axial position of 7, 92, 112, 129, 197 mm from the bottom of the reactor, as shown in Fig. 5.5.

5.3.2 Experimental investigation of fast reactions

Parallel reaction The experimental procedure [88] prescribes injection of a volume equal to v_i=4 ml of sulphuric acid [H_2SO_4]=1 M, in a reactor of volume V_R containing iodate [IO_3^-]=0.0023 M, iodide [I^-]=0.0117 M and borate [$H_2BO_3^-$]=0.0909 M, or in terms of the symbolic notation c_{Ao}=2 M, c_{Bo}=0.0909 M, c_{Co}=0.014 M. Notice that iodide and iodate ions form a stoichiometric mixture, according to the reaction coefficient ratio (5 : 1) and that borate ions are added in the mixture with sodium idroxide, producing a buffer solution in order to keep the pH at a constant value. The iodine further reacts with iodide ions I^- yielding I_3^- according to the following equilibrium:

$$I_2 + I^- \leftrightarrow I_3^-, \tag{5.10}$$

[I_3^-] can be easily measured by spectrophotometer at 353 nm. Knowledge of $[I_3^-]$ and of the equilibrium constant K_B=702 l/mol suffices to determine the iodine formed by the second reaction. These tests were carried out at 100 rpm and 300 rpm, and injecting 4 ml of acid in positions FP1 and FP2. The effect of the injection time was studied in the range between 5 and 300 seconds.

Precipitation reaction Experiments for barium sulfate precipitation were carried out in the Taylor-Couette reactor from aqueous solutions of sodium sulfate and barium chloride. Micro-filtered water and analytical chemicals were used to prepare the solutions. The reactor was first filled with a sodium sulfate solution, and barium chloride was then added with a constant injection velocity. Hereinafter with A it is meant the reactant injected in the reactor (in this case barium chloride) and with B the reactant already present in the reactor (sodium sulfate.) After 200 seconds, samples taken from the bottom of the reactor were analyzed. The CSD was determined using a laser granulometer (Coulter LS230, by using the "small volume cell") whereas the solid concentration was calculated by measuring the residual reactant concentrations with a conductimetric technique.

The rotational speed of the inner cylinder was varied between 100 and 1000 rpm, whereas the initial concentration of sodium sulfate (c_{Bo}) was varied between 1 mol/m^3 and 10 mol/m^3. The effect of the injection velocity was studied in the range between 30 and 100 ml/min and the ratio between reactant concentrations $\alpha = c_{Bo}/c_{Ao}$, which represents the ratio between the concentration of the sodium sulfate present in the reactor divided by the concentration of the barium chloride injected, was varied between 0.1 and 0.001. The volume injected in the reactor and injection time were chosen such that the overall stoichiometric ratio was always 1:1, meaning that reactants were fed in order to have a final ratio of reactant concentrations in the case of complete mixing without reaction equal to one.

In these operating conditions it is useful to define the initial nominal supersaturation ratio as the ratio of the product of the reactant concentrations in the case of complete mixing without reaction (i.e., $\langle c_A^0 \rangle$ and $\langle c_B^0 \rangle$) and the solubility product of barium sulfate (k_s):

$$S_o = \frac{\langle c_A^0 \rangle \langle c_B^0 \rangle}{k_s}. \tag{5.11}$$

When the concentration of reactant B (in this case sodium sulfate) varies between 1 and 10 mol/m^3 the initial nominal supersaturation ratio (S_o) varies between 10^4 and 10^6.

5.4 Tubular reactor

Barium sulfate precipitation was also carried out in a tubular reactor with a single jet configuration. The tubular reactor is 2.1 m long and has an internal diameter of 1 cm. The jet is positioned on the reactor axis, and is made of a small pipe (ID = 1 mm and OD = 1.5 mm). The two reactants were separately fed in the small tube and in the annular region. Distilled water and analytical grade reagents were used to prepare barium chloride and sodium sulfate solution.

Two different series of measurements were performed: on- and off-line. In the first ones the reactor outlet was connected with the laser particle sizer (Coulter LS 230), as reported in Fig. 5.6, and the CSD was directly measured on the particles flowing in the outlet fluid.

In this case the laser particle sizer was used with the "fluid cell" device. These experiments were carried out because in certain cases the reaction was not complete and would have progressed during sampling and analysis. On-line measurements were complicated by particle deposition over the cell lens. In order to minimize particle deposition the measurement time was reduced from 60 to 15 seconds and after each run all the line, including piping, tubular reactor and particle sizer were cleaned with washing water and the particle sizer cell was mechanically cleaned.

Although all the precautions to avoid particle deposition, after each run, deposited particles were found over optical lens. The main point was to verify if the amount of deposited particles was adding further appreciable scattering and thus altering measurements. After cleaning the line with distilled water another measurement was carried out.

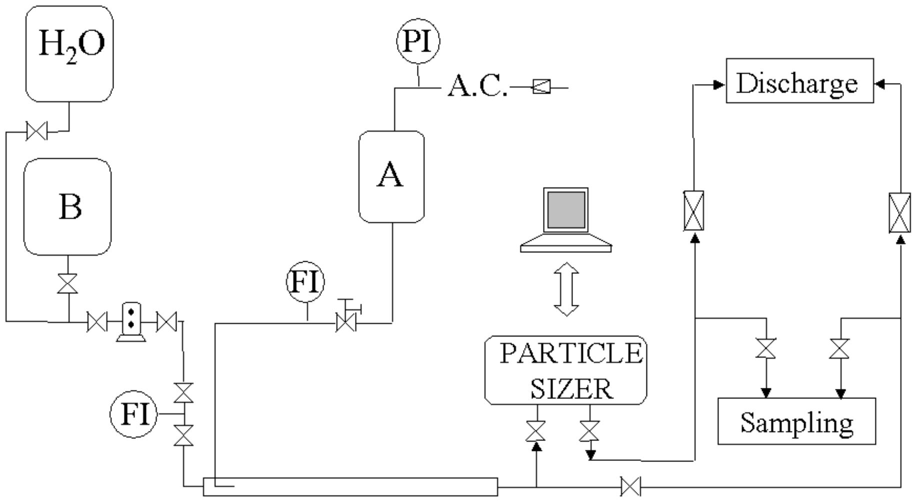

Figure 5.6: Experimental set-up for the tubular reactor.

In complete absence of particle deposition, this would result in the blank test, with particle deposition would result in the CSD of deposited particles. In several runs the amount of deposition was so small not to allow the instrument to detected it, and when it was detected results showed that there was small overlapping between the CSDs of flowing and deposited particles. Each experiments was repeated 5-6 times in order to deal with the poor reproducibility typical of precipitation.

In the off-line measurements samples from the reactor outlet were taken and gently stirred. The CSD was measured by using the particle sizer with the "small volume cell", at different time steps, and moreover a part of these samples was simultaneously filtered. Filtered particles were dried in a stove at 120°C, and after redispersion in acetone prepared for SEM observation.

The inlet velocity in the annular region was kept equal to 1 m/s, because of on-line measurement constrains, so that the macroscopic Reynolds number[3] was equal to 10,000. This Reynolds number is well above turbulence transition but is lower than in other works in literature [89]. Generally the Reynolds number is kept at higher values to ensure a fully developed turbulent flow, since only in this condition turbulence models and turbulent mixing models are applicable. This requirement was irreconcilable with on-line measurements. In fact increasing Re the residence time of particles in the particle sizer cell decreases, and under a certain value the measurement was not possible. All the experiments were carried out with the ratio between the velocity in the feed stream in the nozzle and the feed stream in the annular region (VR) equal to one.

With A is indicated the reactant fed in the nozzle and B the reactant fed in the annular region. However in this case barium chloride was fed either in the nozzle or in the annular region while sodium sulfate was fed in the other region. Initial reactant concentrations (c_{Ao}, c_{Bo}) used in the experiments are reported in Tab. 5.2 with the relative measurements carried out.

The first column (case 1) refers to experiments carried out at low concentration level with barium chloride in the nozzle and sodium sulfate in the annular flow. Concentration

---

[3] The macroscopic Reynolds number is defined as $Re = uD/\nu$ where u is the mean velocity in the axial direction, D is the pipe diameter, and ν is the kinematic viscosity.

Table 5.2: Summary of the operating conditions of experiments.

Reactant fed in the inner tube			
$\alpha = \frac{c_{Bo}}{c_{Ao}}$	$BaCl_2$	Na_2SO_4	$BaCl_2$
-	c_{Ao}=34 mol/m^3	c_{Ao}=34 mol/m^3	c_{Ao}=341 mol/m^3
0.01	**OT**	**OT**	**OT**
0.10	**OTM**	**OT**	**OTM**
1.00	**OTM**	**OT**	**OTM**
1.50	**OTM**	**OT**	**T**
3.00	**OTM**	**OTM**	**T**
O on-line meas.; **T** off-line meas.; **M** SEM obs.			

of the reactant fed in the nozzle (barium chloride in this case) was the same in all the runs of this series, whereas the concentration of the reactant fed in the annular region was varied in order to have a ratio between the two concentrations ($\alpha = c_{Bo}/c_{Ao}$) between 0.01 and 3. Notice that, being the ratio of the two feed stream rates (Q_{Bo}/Q_{Ao}) equal to 100, the condition for α=0.01 yields equal concentrations after complete mixing without reaction ($c_{Ao}Q_{Ao} = c_{Bo}Q_{Bo}$), respecting stoichiometric ratio.

The feed positions were inverted in the second series: sodium sulfate was fed in the nozzle and barium chloride in the annular region, keeping the over-all concentration level at same values (second column, case 2). Moreover, as at these initial reactant concentrations the final solid concentration was too low to have extended aggregation, keeping as basic configuration experiments in the first column, concentrations were increased by a factor of ten. Then experiments at high concentration (third column, case 3) were carried out with barium chloride in the nozzle and sodium sulfate in the annular flow.

Chapter 6

Results and discussion

In this Chapter experimental and modeling results are presented. The Chapter is divided in four sections. In section 6.1 the validation of the finite-mode PDF model by comparison with a more sophisticated model is presented and discussed.

As already mentioned in the Introduction CFD calculations were carried out by using the Standard Moments Method (SMM) for the population balance, however the results that will be presented in the following sections show that this approach is not adequate in certain operating conditions. For this reason in section 6.1 the validation of the Quadrature Method of Moments (QMOM) for the population balance is also presented. However since the use of this method for CFD calculations requires a complete redesign of the numerical approach used, its introduction in CFD codes represents a possible improvement of the presented model, and will be the object of our future work, as highlighted in the Conclusions section.

In section 6.2 CFD predictions (FLUENT) concerning flow field and tracer dispersion are validated by comparison with experimental data. In section 6.3 experimental results concerning the reactive runs are presented and compared with model predictions.

Eventually in section 6.4 CFD predictions obtained with the finite-mode PDF model are compared with full PDF predictions for a real case: turbulent precipitation in the tubular reactor.

6.1 Simplified models validation

In this section the finite-mode PDF model and the Quadrature method of moments are validated by comparison with more sophisticated models. For the finite-mode PDF model the comparison was carried out with the full PDF model, whereas for the Quadrature method of moments a Discretized Population Balance (DPB) was used. As already mentioned simulations by using the full PDF approach for modeling micromixing or the Discretized Population Balance for modeling the solid evolution are computationally expensive. The models proposed here present the main advantage of requiring much less computational resources, but of course give less accurate performances.

However, both the approaches (detailed versus simplified) need an accurate description of the flow field and of the turbulent field, and for this reason must be coupled with CFD codes (see Fig. 6.1). By using CFD every cell of the computational domain can be seen as a perfectly mixed reactor which exchanges mass and energy with the surrounding cells because of mean velocities and turbulent dispersion. Since both the detailed and the

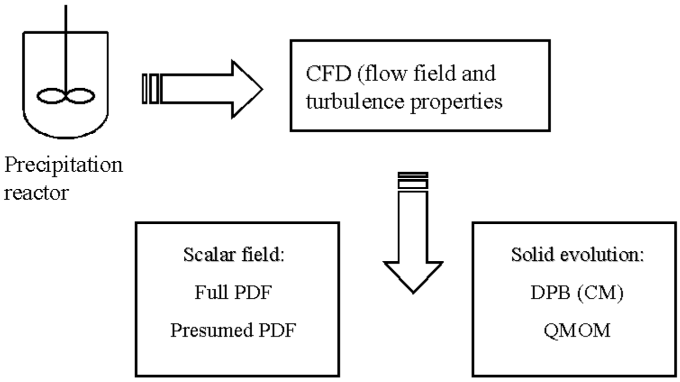

Figure 6.1: Coupling between CFD code and models for scalar field and solid evolution

simplified description are linked with the CFD code, use of one of the two affects model predictions locally. Aim of the comparison is the investigation of this local loss of accuracy. Both validations are carried out in a simple fluid dynamic system: the perfectly mixed reactor (i.e., a single cell of the computational domain.) In this ideal reactor no spatial macro-gradients exist, and therefore properties of the system are constant throughout the domain.

6.1.1 Finite-mode PDF

The finite-mode PDF model has been presented in section 4.2.2 (see pag. 52) for the particular case $N_e = 3$. However this model has a more general formulation, in which N_e is a parameter [30]. Let us consider the general formulation of the finite-mode composition PDF:

$$f_\phi(\boldsymbol{\phi};\mathbf{x},t) = \sum_{n=1}^{N_e} p_n(\mathbf{x},t) \prod_{\alpha=1}^{M} \delta[\psi_\alpha - \langle\phi_\alpha\rangle_n(\mathbf{x},t)], \tag{6.1}$$

where N_e is the total number of modes, p_n is the probability of mode n, $\langle\boldsymbol{\phi}\rangle_n$ is the local composition vector in mode n. The transport equation of the probability vector $\mathbf{p} = (p_1, p_2, \ldots, p_{N_e})$ in homogeneous flows is

$$\frac{\mathrm{d}\mathbf{p}}{\mathrm{d}t} = \gamma\mathbf{G}(\mathbf{p}), \tag{6.2}$$

and that of the weighted concentrations

$$\frac{\mathrm{d}\langle\mathbf{s}\rangle_n}{\mathrm{d}t} = \gamma\mathbf{M}^{(n)}(\mathbf{p}, \langle\mathbf{s}\rangle_1, \ldots, \langle\mathbf{s}\rangle_{N_e}) + p_n\mathbf{S}(\langle\boldsymbol{\phi}\rangle_n), \tag{6.3}$$

where the functions $\mathbf{G}$ and $\mathbf{M}^{(n)}$ represent the rate of change of $\mathbf{p}$ and $\langle\mathbf{s}\rangle_n$ due to micromixing, $\langle\mathbf{s}\rangle_n = p_n\langle\boldsymbol{\phi}\rangle_n$ is the weighted composition vector in mode n, and $\langle\boldsymbol{\phi}\rangle_n$ is the local composition vector in mode n. The functional form of $\mathbf{G}$ and $\mathbf{M}^{(n)}$ depends on the micromixing model, however some properties have to be respected; for example, probabilities sum to unity and thus:

$$\sum_{n=1}^{N_e} G_n(\mathbf{p}) = 0. \tag{6.4}$$

The mean composition vector is obtained by

$$\langle \boldsymbol{\phi} \rangle = \sum_{n=1}^{N_e} p_n \langle \boldsymbol{\phi} \rangle_n = \sum_{n=1}^{N_e} \langle \mathbf{s} \rangle_n, \tag{6.5}$$

and since summation of Eq. 6.3 over all modes must yield the correct transport equation for the mean composition:

$$\frac{\mathrm{d}\langle \boldsymbol{\phi} \rangle}{\mathrm{d}t} = \sum_{n=1}^{N_e} \gamma \mathbf{M}^{(n)}(\mathbf{p}, \langle \mathbf{s} \rangle_1, \ldots, \langle \mathbf{s} \rangle_{N_e}) + \langle \mathbf{S}(\boldsymbol{\phi}) \rangle, \tag{6.6}$$

micromixing functions must obey the following constrain

$$\sum_{n=1}^{N_e} \mathbf{M}^{(n)}(\mathbf{p}, \langle \mathbf{s} \rangle_1, \ldots, \langle \mathbf{s} \rangle_{N_e}) = 0. \tag{6.7}$$

From model equations it is also possible to derive an expression for the scalar variance of a non-reacting scalar. The scalar variance in defined as:

$$\begin{aligned} \langle \phi'^2 \rangle &= \langle \phi^2 \rangle - \langle \phi \rangle^2 \\ &= \sum_{n=1}^{N_e} p_n \langle \phi \rangle_n^2 - \left(\sum_{n=1}^{N_e} p_n \langle \phi \rangle_n \right)^2, \end{aligned} \tag{6.8}$$

and thus the equation for the scalar variance is:

$$\frac{\mathrm{d}\langle \phi'^2 \rangle}{\mathrm{d}t} = -\gamma h(\mathbf{p}, \langle \phi \rangle_1, \ldots, \langle \phi \rangle_{N_e}), \tag{6.9}$$

but for homogeneous flows (see Eq. 4.17)

$$\frac{\mathrm{d}\langle \phi'^2 \rangle}{\mathrm{d}t} = \varepsilon_\phi, \tag{6.10}$$

and then it is possible to derive the value of γ in order to force the scalar variance of a non-reacting scalar to follow the correct equation[1]

$$\gamma = \frac{\varepsilon_\phi}{h(\mathbf{p}, \langle \phi \rangle_1, \ldots, \langle \phi \rangle_{N_e})}. \tag{6.11}$$

The micromixing functions can be defined in terms of linear combination of the probability exchange rate $\mathbf{r} = (r_1, \ldots, r_{N_e})$:

$$G_n = a_1 r_1 + \ldots + a_{N_e} r_{N_e} \tag{6.12}$$

and

$$M^{(n)} = a_1 \langle \boldsymbol{\phi} \rangle_1 r_1 + \ldots + a_{N_e} \langle \boldsymbol{\phi} \rangle_{N_e} r_{N_e}, \tag{6.13}$$

coefficients a_n are chosen depending on N_e and the formulation of the problem, whereas for the choice of the exchange rate $\mathbf{r}$ see [90].

Let us consider the formulation of this finite-mode PDF model with the mixture fraction as the first scalar and for different value of N_e. When N_e=1 the reacting system is

---

[1] In this case the evaluation of the functional form of γ_s is not required, since in homogeneous scalar field the spurious dissipation term is always null.

represented by one environment, and the PDF is a delta function centered on the mean value. In this case weighted concentrations and local concentrations coincide and only the mean mixture fraction is predicted correctly. In fact in this case the mixture fraction variance is always null since $\langle \xi^2 \rangle = \langle \xi \rangle^2$, (only the first moment of the mixture fraction can be correctly predicted.) This is the default solution available in CFD code, and by using this option micro-mixing is evidently neglected[2].

When N_e=2 the reacting system is represented by two modes. Generally one of the co-reactants is introduced in mode 1 where $\langle \xi \rangle_1$=1, whereas the other one is introduced in mode 2 where $\langle \xi \rangle_2$=0. The effect of micromixing is to decrease probability of mode 2 whereas mode 1 always grows in probability. This is the so-called Engulfment model. In this model the micromixing process is thought of as a sort of engulfment of the portion of fluid contained in mode 2 by the fluid in mode 1. In this case the first and the second moment of the mixture fraction can be correctly predicted (mean mixture fraction and mixture fraction variance.) In Tab. 6.1 the governing equations for this case are reported.

As already mentioned when N_e=2 the model is not symmetric, since mixing goes from mode 1 to mode 2 and not viceversa. In general this is not a desirable feature for a CFD-based micromixing model, and can be improved by setting N_e=3, and letting mode 3 represent the reacting environment. Thus, when N_e=3, modes 1 and 2 contain unmixed reactants where $\langle \xi \rangle_1$=1 and $\langle \xi \rangle_2$=0, and due to micromixing probabilities of mode 1 and 2 decrease whereas mode 3 always grows in probability. Notice that in this case reaction occurs in mode 3 and that also the mixture fraction skweness can be correctly predicted. Governing equation for this case have already been presented (see pag. 53) but for completeness are reported in Tab. 6.2.

The last case discussed here is when N_e=4. In this case unmixed reactants are introduced through modes 1 and 4 ($\langle \xi \rangle_1$=1 and $\langle \xi \rangle_4$=0). Probability of modes 1 and 4 decrease and modes 2 and 3 are formed. The probability flux goes from mode 1 to 2 and from mode 4 to 3. Modes 3 and 4 are connected by symmetric probability fluxes. Reaction takes place in modes 3 and 4, and thus this model requires more computational effort than the others presented in this section. Governing equations for this case are reported in Tab. 6.3.

---

[2] The Chemical Reaction Engineering (CRE) approach based on Lagrangian formulation suggests the existence of *regions*: macromixing is the region controlled by large-scale eddies and micromixing is the region controlled by small scales eddies. In this definition macromixing is due to turbulent diffusion and convection, whereas micromixing is due to molecular diffusion. An intermediate region named mesomixing has been also defined. Mesomixing is responsible for breaking up the large blobs of fluid and creates the environment in which micromixing occurs. Thus by using CFD alone for modeling turbulent reacting flows only the effects of macromixing are taken into account, whereas micromixing effects are completely neglected.

Table 6.1: Governing equation for N_e=2. Notice that since probabilities sum to unity $p_2 = 1 - p_1$ thus only an equation for p_1 is needed. Reaction occurs only in mode 1 thus in mode 2 local concentrations are constant and the transport equation for $\langle \mathbf{s} \rangle_2$ is not needed. In this case $\gamma = \varepsilon_\xi / [p_1 p_2 \langle \xi \rangle_1^2]$.

Models Variables	$\gamma\mathbf{G}$ or $\gamma\mathbf{M}^{(n)}$
p_1	$\gamma p_1(1-p_1)$
$\langle \mathbf{s} \rangle_1$	$\gamma p_1 \langle \mathbf{s} \rangle_2$

Table 6.2: Governing equation for N_e=3. Notice that since probabilities sum to unity $p_3 = 1 - p_1 - p_2$ thus the transport equation for p_3 is not needed. Reaction occurs only in mode 3 thus in modes 1 and 2 local concentrations are constant and the transport equations for $\langle \mathbf{s} \rangle_1$ and $\langle \mathbf{s} \rangle_2$ are not needed. In this case $\gamma = \varepsilon_\xi / [p_1(1-p_1)(1-\langle \xi \rangle_3)^2 + p_2(1-p_2)\langle \xi \rangle_3^2]$.

Models Variables	$\gamma\mathbf{G}$ or $\gamma\mathbf{M}^{(n)}$
p_1	$-\gamma p_1(1-p_1)$
p_2	$-\gamma p_2(1-p_2)$
$\langle \mathbf{s} \rangle_3$	$\gamma[(1-p_1)\langle \mathbf{s} \rangle_1 + (1-p_2)\langle \mathbf{s} \rangle_2]$

Table 6.3: Governing equation for N_e=4. Notice that since probabilities sum to unity $p_4 = 1 - p_1 - p_2 - p_3$ thus the transport equation for p_4 is not needed. Reaction occurs only in modes 2 and 3 thus in modes 1 and 4 local concentrations are constant and the transport equations for $\langle \mathbf{s} \rangle_1$ and $\langle \mathbf{s} \rangle_4$ are not needed. In this case $\gamma = \varepsilon_\xi / [p_1(1-p_1)(1-\langle \xi \rangle_2)^2 + (p_2+p_3)(\langle \xi \rangle_2 - \langle \xi \rangle_3)^2 + p_4(1-p_4)\langle \xi \rangle_3^2]$.

Models Variables	$\gamma\mathbf{G}$ or $\gamma\mathbf{M}^{(n)}$
p_1	$-\gamma p_1(1-p_1)$
p_2	$-\gamma[p_1(1-p_1) - p_2 + p_3]$
p_3	$-\gamma[p_2 - p_3 + p_4(1-p_4)]$
$\langle \mathbf{s} \rangle_2$	$\gamma[(1-p_1)\langle \mathbf{s} \rangle_1 - \langle \mathbf{s} \rangle_2 + \langle \mathbf{s} \rangle_3]$
$\langle \mathbf{s} \rangle_3$	$\gamma[\langle \mathbf{s} \rangle_2 - \langle \mathbf{s} \rangle_3 + (1-p_4)\langle \mathbf{s} \rangle_4]$

The finite-mode PDF predictions with $N_e = 2, 3, 4$ have been compared with N_e=1 (without any closure) and with full PDF predictions for barium sulfate precipitation. The full PDF transport equation (Eq. 4.46) was presented at pag. 47, and here is applied in the case of homogeneous flow:

$$\frac{\partial f_\phi}{\partial t} + \frac{\partial}{\partial \psi_\alpha} [S_\alpha(\boldsymbol{\psi}) f_\phi] = -\frac{\partial}{\partial \psi_\alpha} \left[\langle \Gamma_\alpha \nabla^2 \phi_\alpha \mid \boldsymbol{\psi} \rangle f_\phi \right]. \tag{6.14}$$

In the full PDF simulations the reactor was modeled by using 100 notional particles. A fraction of the particles was initialized with ξ=1 whereas the rest of the particles were initialized with ξ=0. Simulations were carried out with two different values of $\langle\xi\rangle$: 0.1 and 0.01. Subsequently particles were mixed by using a random process (coalescence and dispersion model.) Couples of particles were randomly chosen and mixed. After each event, mixture fraction variance was determined and the simulation time was updated. This was done by using a very simple model for the scalar variance dissipation rate

$$\frac{\mathrm{d}\langle \xi'^2 \rangle}{\mathrm{d}t} = -\varepsilon_\xi = -\frac{\langle \xi'^2 \rangle}{\tau_\xi}, \tag{6.15}$$

where evidently τ_ξ is the micromixing time. The analytical solution of this expression, in terms of the intensity of segregation $I_s = \langle \xi'^2 \rangle / [\langle \xi \rangle (1 - \langle \xi \rangle)]$ can be written as follows:

$$I_s = \exp(-t/\tau_\xi). \tag{6.16}$$

Knowledge of the mixture fraction variance and thus of the intensity of segregation, suffices the evaluation of the real time during the simulation after each mixing event. Then scalars are updated in each notional particle according to the source term. In this case we have to consider a finite-rate chemical reaction (e.g.,$A + B \to C$.) The chemical source term can be described in terms of the reaction progress variable, and the relationships between concentrations, the mixture fraction, and the reaction progress variable (Y) are

$$\frac{c_A}{c_{Ao}} = \xi - \xi_s Y, \qquad \frac{c_B}{c_{Bo}} = (1 - \xi) - (1 - \xi_s) Y, \tag{6.17}$$

which appear to be in between the relationships for infinitely fast reaction and for mixing without reaction (see Fig. 4.1). The source term for Y is

$$\frac{\mathrm{d}Y}{\mathrm{d}t} = \frac{S(c_A, c_B)}{\xi_s c_{Ao}} \tag{6.18}$$

where $S(c_A, c_B)$ is the source term for the chemical reaction, and c_A and c_B are defined in terms of ξ and Y by Eq. 6.17. Initial reactant concentrations of sodium sulfate and barium chloride were fixed as follows

$$\begin{aligned} c_{Ao} &= \frac{1.067}{\langle \xi \rangle} \mathrm{mol/m^3}, \\ c_{Bo} &= \frac{1.067}{1 - \langle \xi \rangle} \mathrm{mol/m^3}. \end{aligned} \tag{6.19}$$

The population balance was solved by using the Standard Moment Method (see Eq. 4.99,) neglecting the effect of aggregation ($\overline{B}_k$=0 and $\overline{D}_k$=0.) Only the first five moments were tracked ($m_k \quad k \in 0, \ldots, 4$).

For the nucleation rate and the growth rate Eqs. 1.11 and 1.18 were used, whereas for shape factors an average value was used (k_v=5 and k_a=30.) It should be mentioned here that the parameters used in these simulations (i.e., τ_ξ,k_v,k_a) as well as kinetic expressions play a relative importance; in fact, since the aim of this part of the work is the comparison between two different models it is of first importance to use the same values, but however these values have to be reasonable. The finite-mode PDF simulations with N_e=2,3,4 were carried out with the following initial conditions:

$$\begin{aligned} p_1(t=0) &= \langle\xi\rangle, \\ p_n(t=0) &= 1-\langle\xi\rangle, \end{aligned}$$

with n equal to 2 for N_e=2, 2 for N_e=3 and 4 for N_e=4. Notice that for all the models no transport equation for ξ is needed since its value is constant and equal to its initial value. The validation process requires the solution of a system of ordinary differential equations (ODE) that was solved by using the ODE package ODEPACK (LSODE fortran double precision subroutine.)

All the models were tested by using the same variance decay (or intensity of segregation decay) for several characteristic micro-mixing times. In Fig. 6.2 the intensity of segregation decay of the different models are presented. Data are reported against the dimensionless time ($\theta = t/t_{batch}$) where t_{batch}=200 seconds. As already mentioned, given the value of τ_ξ, all the models show the same variance decay rate.

In order to verify the correct behavior of the different models the effect of the time constant τ_ξ was investigated. In Fig. 6.3 and 6.4 the mean crystal size (d_{43}) predicted by the finite-mode PDF model with N_e=2 and the full PDF model, for $\langle\xi\rangle$=0.1 and for $\langle\xi\rangle$=0.01, and at different values of the time constant are compared. The results reported in the two figures show that decreasing τ_ξ the final mean crystal size when reaction is complete (i.e., θ=1) decreases. This is due to the fact that a decrease in τ_ξ accelerate micro-mixing, thus reactants mix faster and nucleation is favored (being quasi-istantaneous) over crystal growth (which is much slower.) This trend was observed in all the models. Moreover it is interesting to notice that, for all the models when $\tau_\xi < 0.01$, the predicted evolution was equal to that of the 1 Environment model (i.e., N_e=1 model with only one mode neglecting micromixing.) This result confirms that when micromixing in faster than the chemical reaction the prediction of the micromixing model is equal to the prediction of the model without micromixing. Moreover this result gives an order of magnitude for the characteristic reaction time, that in this operating condition is around 0.01 second. Comparison of mean crystal size (d_{43}) and total particle number density (m_0) predicted by the different models for $\langle\xi\rangle$=0.1 and 0.01 and for τ_ξ=1 second is reported in Figs. 6.5 and 6.6. Data are presented for this value of τ_ξ since it seems to be reasonable; if τ_ξ=10 seconds the model would have been tested in more stressed conditions, but however this appears not to be a likely scenario.

The results show that if no micromixing model is used the mean crystal size is sensibly underestimated and the total particle number density is overestimated. The finite-mode PDF model in all its configurations shows quite good agreement with the full PDF model, although when N_e=4 the model seems to work better. However, since the finite-mode PDF model with 4 modes requires the solution of reaction and of particle evolution in modes 2 and 3, it is more computational expensive. Thus considering that the improvement in performances between the model with N_e=4 and N_e=3 is very small, hereinafter the 3E model will be used. Another result that supports the use of three modes is that when using four modes concentration profiles of mode 2 and 3 are very similar, showing that with this reaction scheme N_e=3 should represent with sufficient detail the reacting system.

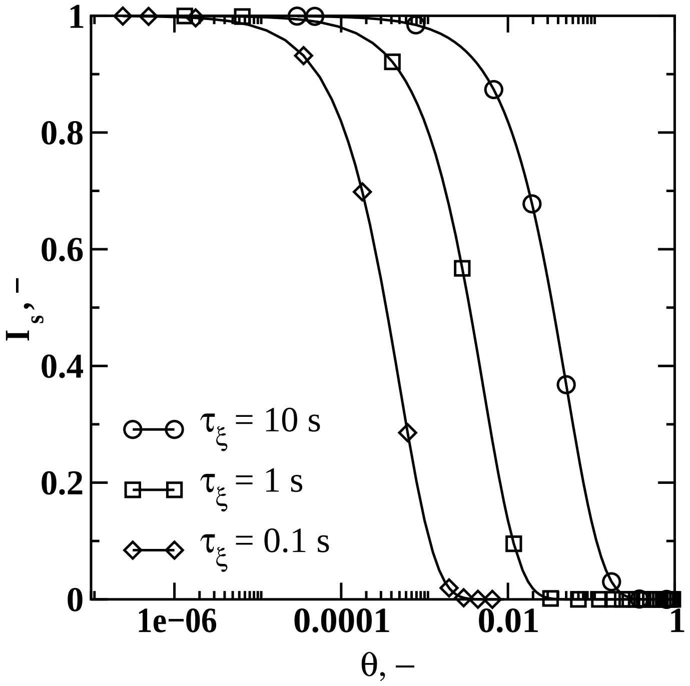

Figure 6.2: Intensity of segregation decay with time for the tested models at different values of τ_ξ.

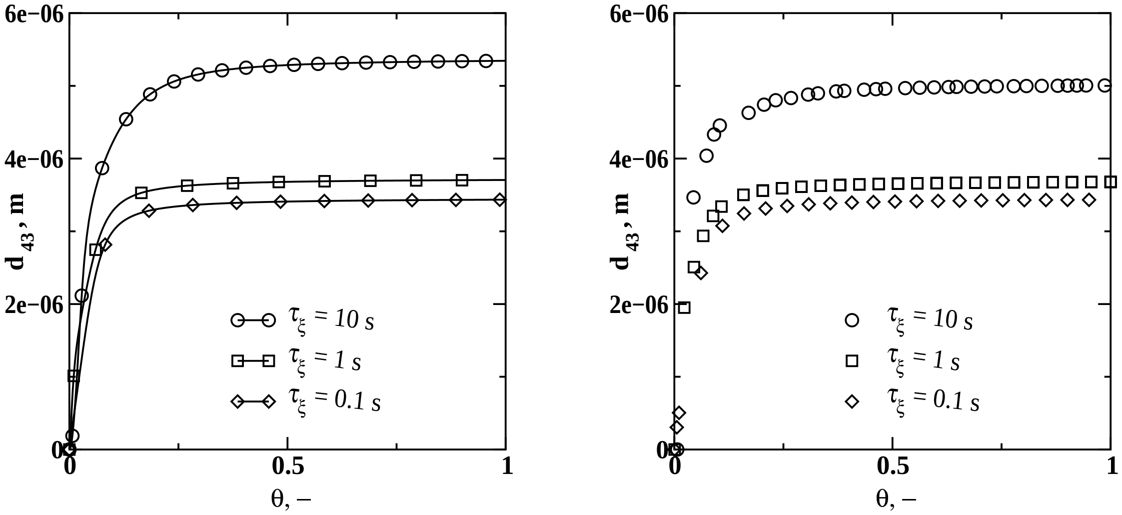

Figure 6.3: Mean crystal size evolution predicted by the finite-mode PDF model N_e=2 (left) and the full PDF model (right) for $\langle\xi\rangle$=0.1.

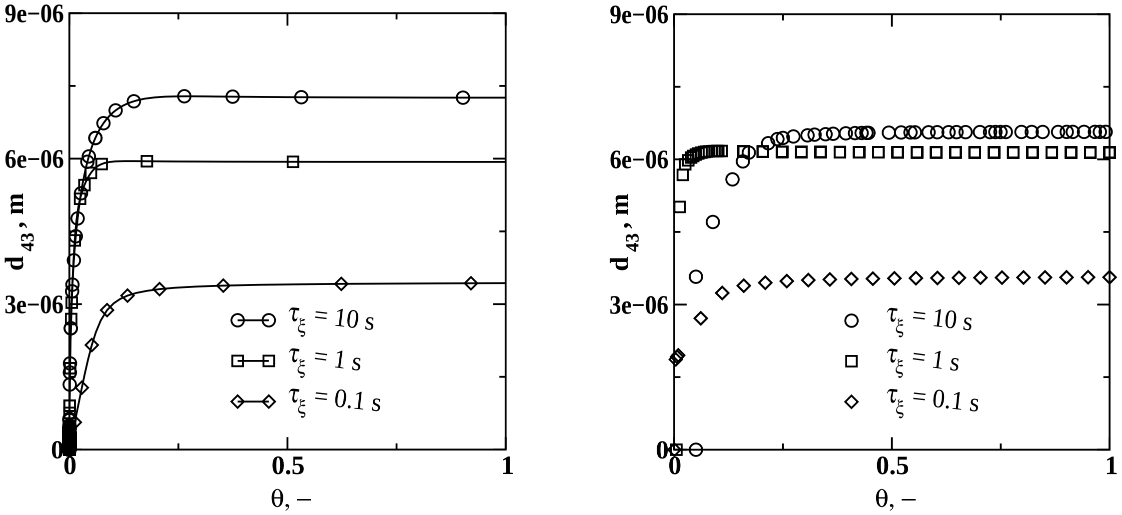

Figure 6.4: Mean crystal size evolution predicted by the finite-mode PDF model N_e=2 (left) and the full PDF model (right) for $\langle\xi\rangle$=0.01.

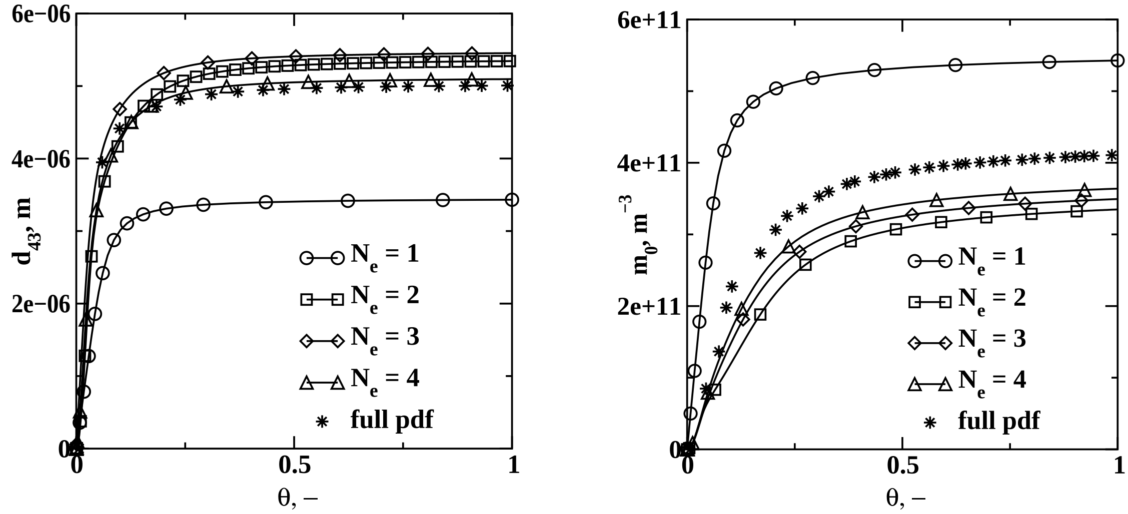

Figure 6.5: Mean crystal size evolution (left) and total particle number density (right) predicted by the tested models for $\langle\xi\rangle$=0.1 and τ_ξ=1.

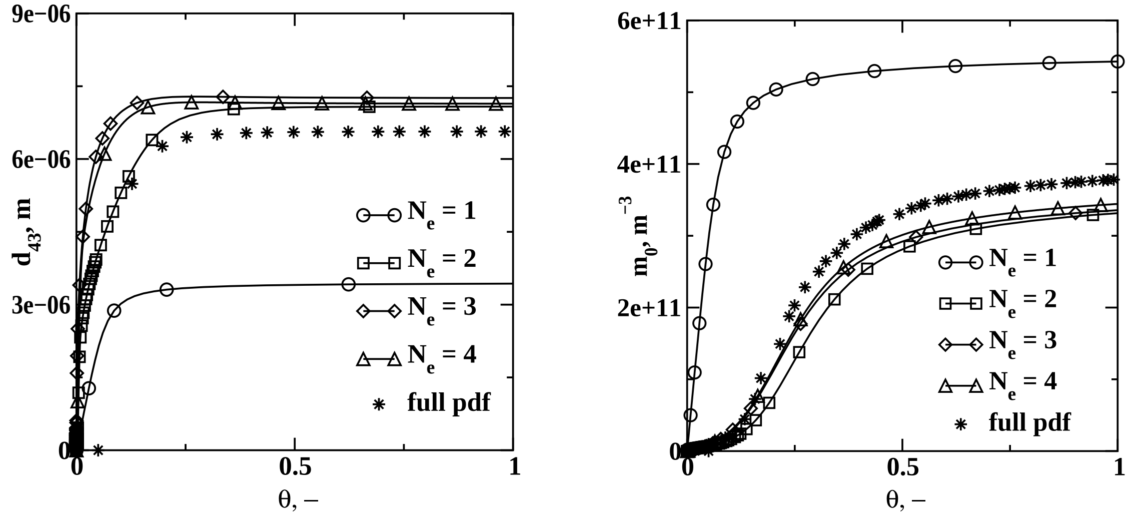

Figure 6.6: Mean crystal size evolution (left) and total particle number density (right) predicted by the tested models for $\langle\xi\rangle$=0.01 and τ_ξ=1.

6.1.2 Quadrature method of moments

The validation of the QMOM has been done in two steps. In the first step the ability of the QMOM to model crystal growth with size-dependent growth rates was verified. In the second step, a DPB with nonlinear discretization was used to validate the QMOM ability to predict aggregation. The validation process requires the solution of a system of ordinary differential equations (ODE) and the solution of the eigenvalues problem. The first one was solved by using the ODE package ODEPACK (LSODE fortran double precision subroutine), whereas for the second one the linear algebra package EISPACK (IMTQL2 fortran double precision subroutine) was used.

Size-independent growth rate: For this case, moment equations can be expressed in closed form:

$$\frac{\mathrm{d}m_k}{\mathrm{d}t} = kGm_{k-1} \quad k \in 0, \ldots, 5. \tag{6.20}$$

Solving the system either by using the moments themselves or by using the moments recalculated from the quadrature approximation, excellent agreement was found, proving that the abscissas and weights so obtained are able to give back the exact value of the moments. Different initial CSDs were used such as Dirac-delta and step functions. In Fig. 6.7 the first six normalized moments are reported for the following initial CSD:

$$n(L;0) = 1.0 \times 10^{20} \quad \text{for } L \leq 10^{-6} \tag{6.21}$$

$$= 0.0 \quad \text{for } L > 10^{-6} \tag{6.22}$$

and a constant growth rate $G = 1.0 \times 10^{-6}$ m/s. Results show that the total number density is constant, whereas m_1 varies linearly. For all the moments the agreement was excellent.

Size-dependent growth rate: For this case, since the equation for m_1 contains m_{-1}, the set of moment equations cannot be solved by using the Standard Moments Method (SMM.) Instead, by using the Quadrature Method of Moments (QMOM) with three nodes[3] the problem is formulated in closed form:

$$\frac{\mathrm{d}m_k}{\mathrm{d}t} = \int_0^\infty kG(L)n(L;t)L^{k-1}L \approx k\sum_{i=1}^{3} G\left(L_i(t)\right) L_i(t)^{k-1} w_i(t) \quad k \in 0, \ldots, 5. \tag{6.23}$$

Mcgraw [72] showed that QMOM is able to correctly predict the first six moments for a growth law of the form

$$G(L) = \frac{G_o}{L}. \tag{6.24}$$

From his calculations, the error was estimated to be lower than 0.1%. In this work comparison was made by using the same initial condition as in the previous case and $G_o = 1.0 \times 10^{-13}$ s^{-1}. Results from QMOM were compared with predictions of a discretized population balance:

$$\frac{\mathrm{d}n(L_i;t)}{\mathrm{d}t} = -\frac{G(L_{i+1})n(L_{i+1};t) - G(L_{i-1})n(L_{i-1};t)}{L_{i+1} - L_{1-i}} \quad i \in 1, \ldots, N_q, \tag{6.25}$$

---

[3] For details see the model formulation at pag. 58.

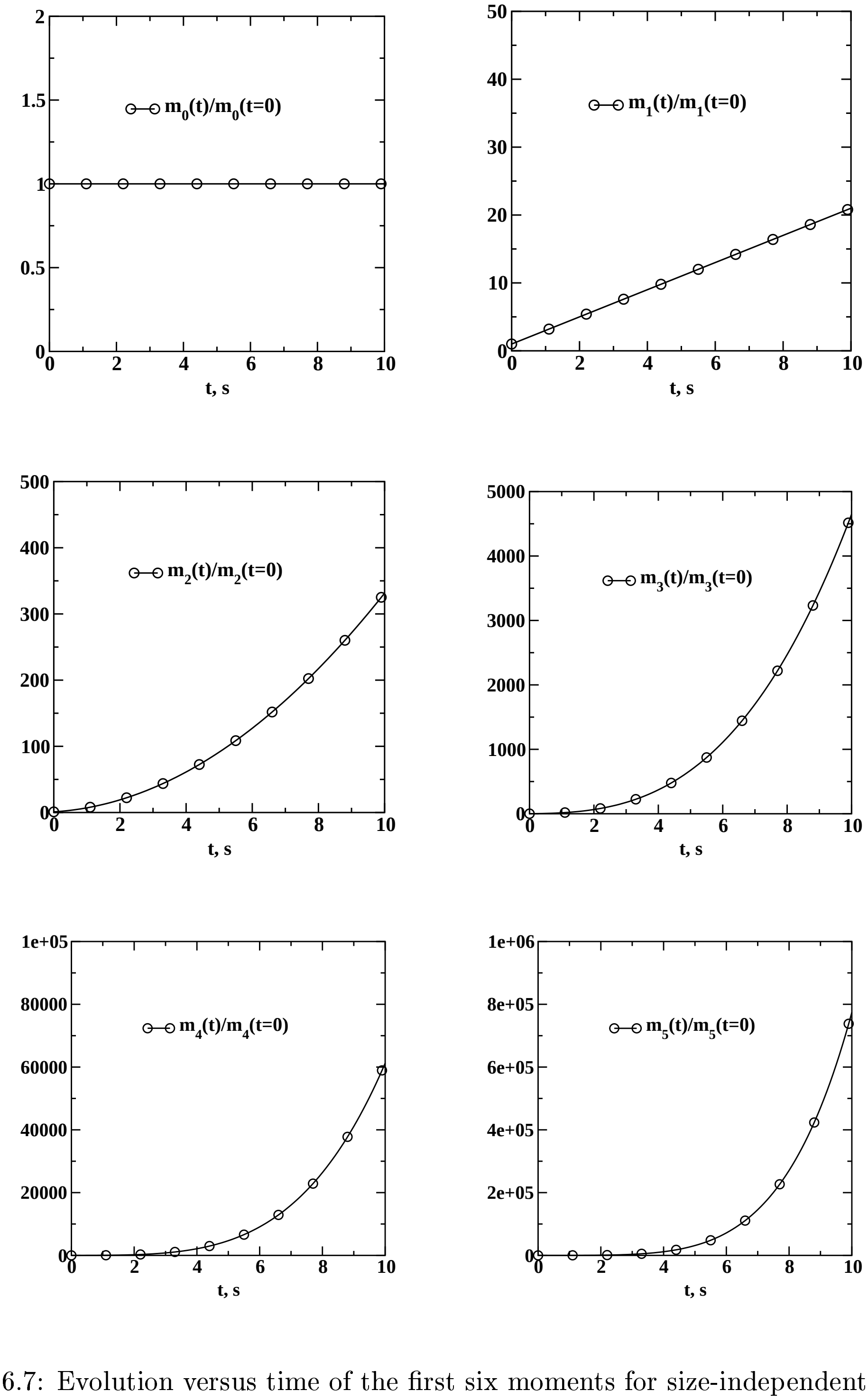

Figure 6.7: Evolution versus time of the first six moments for size-independent growth.

with $N_d = 200$, $L_{min} = 0$ and $L_{max} = 2.0 \times 10^{-5}$. In Fig. 6.8 the first six moments are reported against time. As it is possible to see, $m_0(t)$ is again constant whereas in this case $m_2(t)$ varies linearly with time. This is confirmed by the exact relationship (available only for even moments):

$$\frac{\mathrm{d}m_2}{\mathrm{d}t} = 2G_o m_0. \tag{6.26}$$

Also in this case excellent agreement was found with a maximum error of 0.3% after 10 seconds of evolution.

Aggregation: Concerning aggregation, validation was first carried out by comparison with analytical solutions. For example the exponential CSD reported below:

$$n(v) = \frac{N_o}{v_o} \exp(-v/v_o) \tag{6.27}$$

provides analytical solutions but in a limited number of cases [91]. First results showed quite good agreement, however in order to investigate model performances in a wider range of initial conditions and by using different aggregation kernels, the comparison was done also with a specific DPB method for simultaneous nucleation, growth and aggregation. For this purpose the DPB approach proposed by Hounslow and co-workers[4] was used [67].

Using QMOM for this system yields

$$\begin{aligned} \frac{\mathrm{d}m_k}{\mathrm{d}t} &= \frac{1}{2}\int_0^\infty n(\lambda;t)\int_0^\infty \beta(\lambda,u)(u^3+\lambda^3)^{k/3} n(u;t)u\lambda \\ &- \int_0^\infty L^k n(L;t)\int_0^\infty \beta(L,\lambda)n(\lambda;t)\lambda L, \\ &\approx \frac{1}{2}\sum_{i=1}^{3} w_i \sum_{j=1}^{3} w_j \beta(L_i,L_j)\left(L_i^3+L_j^3\right)^{k/3} \\ &- \sum_{i=1}^{3} w_i L_i^k \sum_{j=1}^{3} w_j \beta(L_i,L_j) \quad k \in 0,\ldots,5. \end{aligned} \tag{6.28}$$

The QMOM was validated in three different conditions:

1. Constant kernel:

$$\beta(L,\lambda) = \beta_0, \tag{6.29}$$

2. Brownian kernel:

$$\beta(L,\lambda) = \beta_0 \frac{(L+\lambda)^2}{L\lambda}, \tag{6.30}$$

3. Hydrodynamic kernel:

$$\beta(L,\lambda) = \beta_0 (L+\lambda)^3. \tag{6.31}$$

---

[4] This model has been already presented and commented, see Eqs. 4.104 and 4.105 at pag.58

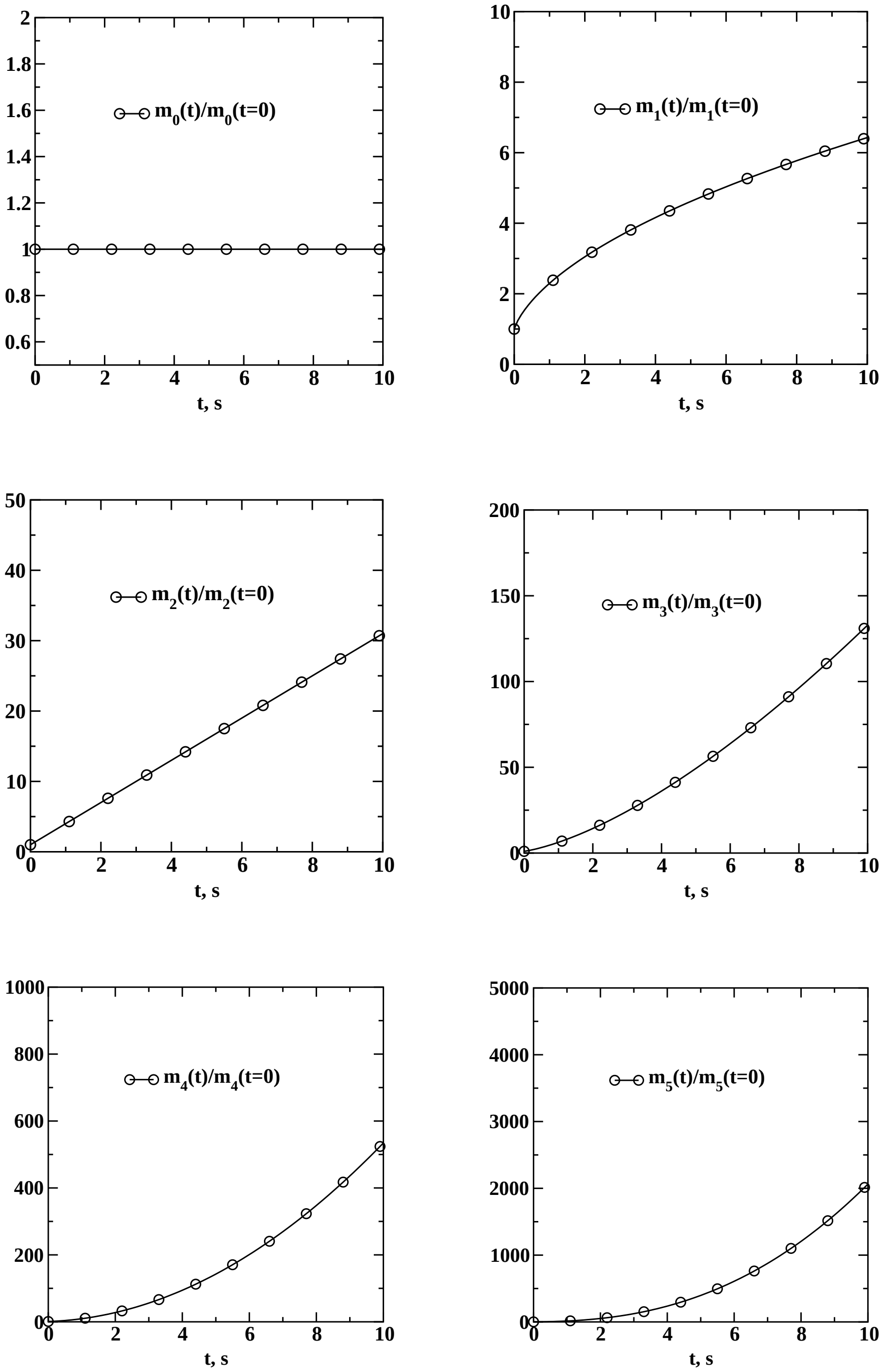

Figure 6.8: Evolution versus time of the first six moments for size-dependent growth.

The three cases were tested with different initial CSDs and here results for unimodal and a bimodal initial CSDs will be presented.

The unimodal CSD is shown in Fig. 6.9a, and in the same figure is also reported the CSD at different time steps after aggregation with constant kernel ($\beta_0 = 10^{-17}$ m^3/s) by using DPB with $N_c = 100$. As it is possible to see aggregation causes the disappearance of smaller particles to form bigger particles. The evolution of the moments is reported in Fig. 6.10a. Results clearly show that m_3 remains constant, since during aggregation total particle volume is conserved. The moments of order lower than three decrease whereas the others increase.

In order to quantify the ability of the model to predict system properties it is useful to define the intensity of aggregation [92]:

$$I_{agg} = 1 - \frac{m_0(t)}{m_0(0)}. \tag{6.32}$$

I_{agg} is 0 when the number of aggregation events is null and goes to 1 as this number increases. In the case under investigation an error of 4% was detected when $I_{agg} = 0.95$. In Fig. 6.9b the error committed by using QMOM (assuming the prediction of the DPB to be exact) is reported against I_{agg}. As it is possible to see the error on moments of order lower than three is less than 2%, whereas the third moment is perfectly predicted. For moments of order greater than three the error is still less than 10% for $I_{agg} \approx 1$. Note that in normal crystallization/precipitation reactors I_{agg} typically falls in the range between 0.5-0.6, where the errors are lower. Moreover in this case the error is greater for m_5, which is calculated only because it is needed in the PD algorithm; in fact, the highest-order moment that is used for comparison with experimental data is m_4 (that appears in Eq. 4.97) for which the error is lower.

The behavior of the bimodal CSD in case of aggregation with constant kernel is shown in Fig. 6.11a. In Fig. 6.11b the percentage errors for the first six moments are reported. As it is possible to see the situation is slightly different, in fact the error on m_0 is quite high and when $I_{agg} = 0.5$ becomes stable at about 10%. All the other moments behave in a similar way, but the errors are greater than for the unimodal case.

In the case of Brownian aggregation, the CSD at different time steps is reported in Fig. 6.12a using the same initial conditions, but with $\beta_0 = 2.5 \times 10^{-18}$ m^3/s. This different value of β_0 was used in order to have comparable value of I_{agg}. As it is possible the see, the evolution is slightly different, especially for smaller particles that seem to aggregate faster. Also in this case agreement with the two methods was excellent, as reported in Fig. 6.12b. Moreover results confirm that in this case (and generally for the unimodal distribution) the case of Brownian aggregation can be treated with constant kernel, in fact under the hypothesis of aggregating particles of the same size:

$$\beta(L, \lambda) = \beta_0 \frac{(L+\lambda)^2}{L\lambda} \approx 4\beta_0. \tag{6.33}$$

For the bimodal distribution, results are very similar. In Fig. 6.13a the CSD at different time steps is reported. Again in this case smaller particles aggregate faster, but their weight on the final mean crystal size is small. Also in this case the error in m_0 is quite high, but remains lower then 10% until $I_{agg} < 0.5$ (see Fig. 6.13b).

In the case of hydrodynamic kernel, the same initial conditions were used with $\beta_0 = 1.5 \times 10^6$ m^3/s. This value of β_0 was used in order to obtain comparable values of I_{agg}. The evolution of the CSD predicted by the DPB is reported in Fig. 6.14a. As it is possible to note, the tail of the CSD increases faster with time as a proof of the increased ability of bigger particles to collide and aggregate. In this case agreement between the two models is not as good as in the previous cases, in fact the integrant function contains the number density function multiplied by $(L+\lambda)^3$ that is responsible for the long "tail" of the function. However, it is useful to highlight that for moderate aggregation rates ($I_{agg} < 0.5$) error are around 10-15% (see Fig. 6.14b).

In Fig. 6.15a the CSD at different time steps, in the case of initial bimodal distribution for the hydrodynamic kernel, is reported. Note that in this case in order to obtain the same range of I_{agg} a different β_0 was used ($\beta_0 = 5.0 \times 10^4$). Up to $I_{agg} = 0.5$ all the errors are lower than 10%, but for I_{agg} close to one the m_4 error goes up to 800%. Since the percentage error increases with the order of the moments, there is not a big difference between the unimodal and the bimodal initial distributions.

It is very interesting, for this last case, to investigate the effect of the number of nodes in the quadrature approximation. In Fig. 6.16 the mean crystal size versus I_{agg} calculated with the DPB and the QMOM with 3,4,5 nodes is reported. As it is possible to see the order of magnitude of the errors are very similar, however increasing the number of nodes a small improvement in QMOM performances was detected. On the other hand, use of a greater number of nodes requires the calculation of higher-order moments, that are involved in $\mathbf{P}$ determination (see Eq. 4.111,) and it could result in numerical instabilities and underflow problems. Thus use of a three nodes based QMOM is strongly recommended.

The validation process leads us to the conclusion that in the case of constant or Brownian kernel, QMOM works quite well by tracking only the first six moments. Agreement between QMOM and a DPB using 100 classes was satisfactory. However, also in this simple case some limitations were detected. In fact the model performance in the case of initial bimodal CSD was worse than with a unimodal CSD. Moreover results showed that it is difficult to find a criterion for error estimation. For example, the rule that errors increase with moment order is not always valid. Nevertheless QMOM can be used also in case of hydrodynamic aggregation for moderate aggregation rates.

Despite the limitations discussed above, the QMOM method is indeed fascinating for several reasons. The method is very fast, in fact the reduction of the number of scalars to be tracked is drastic (from 50-100 to 6) and in general does not depend on the width of the CSD. This reduction of scalars has a strong impact on CPU time, in fact by using the QMOM method a reduction of 150-200 times was detected with respect to the DPB. In addition, as mentioned before, the method proposed does not present the problem of fixing the intervals to be considered in the simulations. Thus, unlike the DPB approach, it can be used without any modification for different CSDs.

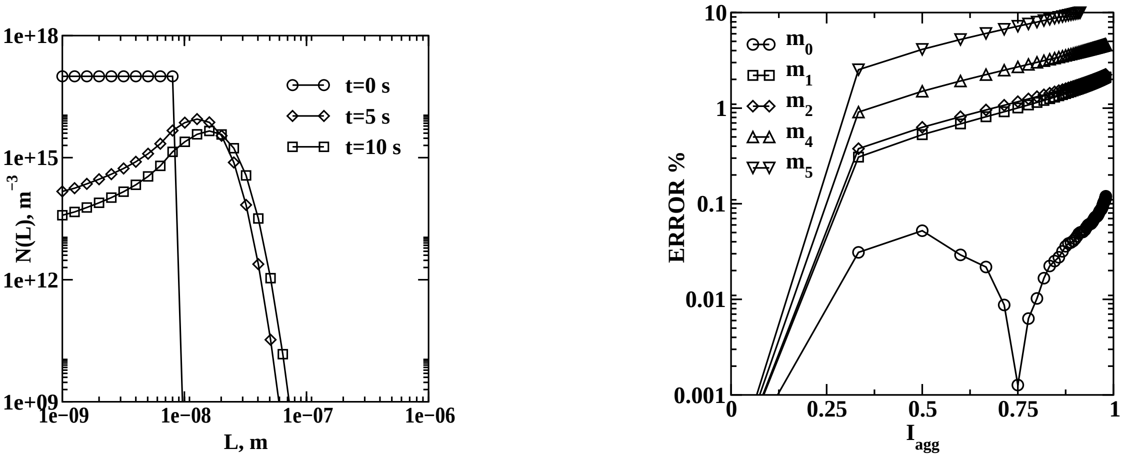

Figure 6.9: Aggregation with constant kernel ($\beta_0 = 10^{-17}$ m^3/s): (a) CSD at different time steps calculated with the DPB approach. (b) Percent error of the first six moments calculated by the QMOM. (m_3 is not reported since the error is lower than 10^{-5}%.)

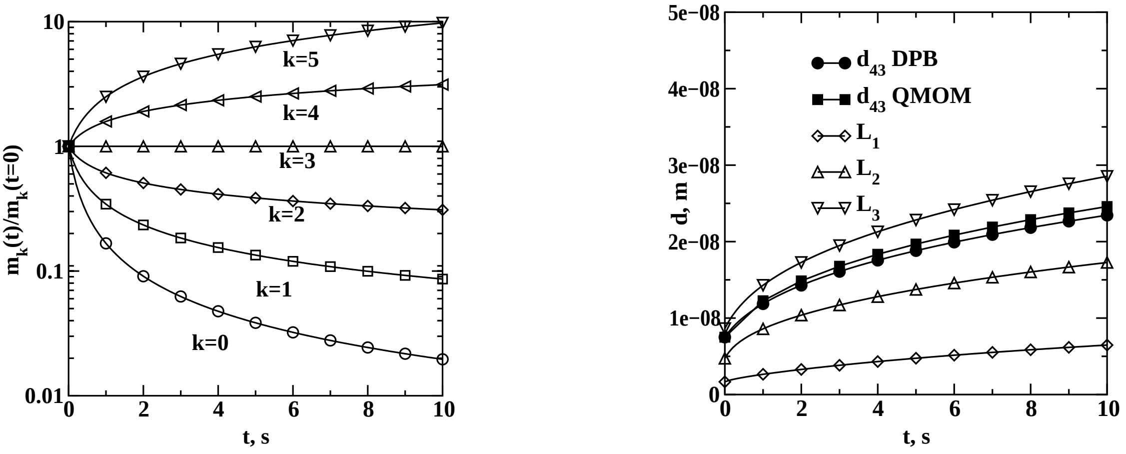

Figure 6.10: Aggregation with constant kernel ($\beta_0 = 10^{-17}$ m^3/s) : (a) Normalized moments of the CSD against time for constant kernel predicted by the DPB. (b) Mean crystal size (d_{43}) predicted by the two models (DPB and QMOM filled symbols) and abscissas (L_1,L_2,L_3) for the QMOM (open symbols.)

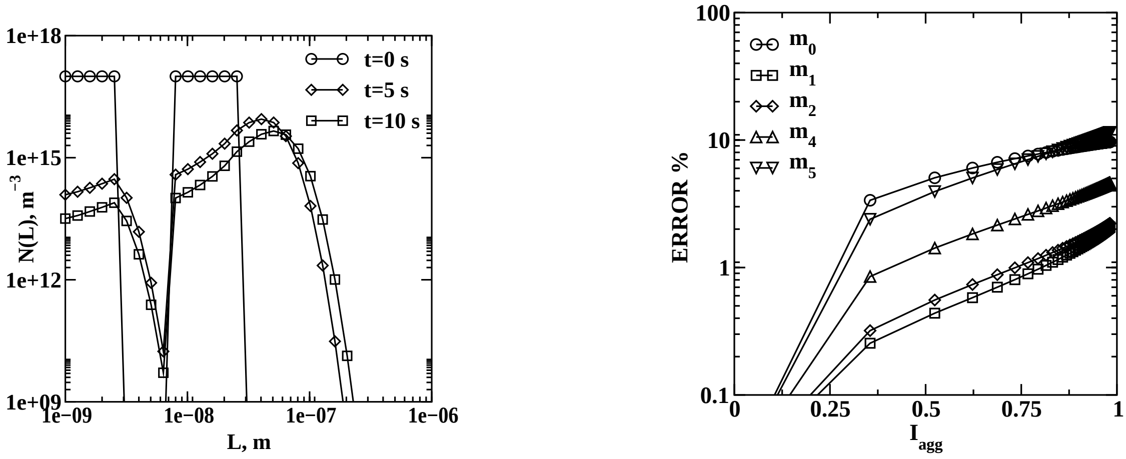

Figure 6.11: Aggregation with constant kernel ($\beta_0 = 10^{-17}$ m^3/s): (a) CSD at different time steps calculated with the DPB approach. (b) Percent error of the first six moments calculated by the QMOM. (m_3 is not reported since the error is lower than 10^{-5}%.)

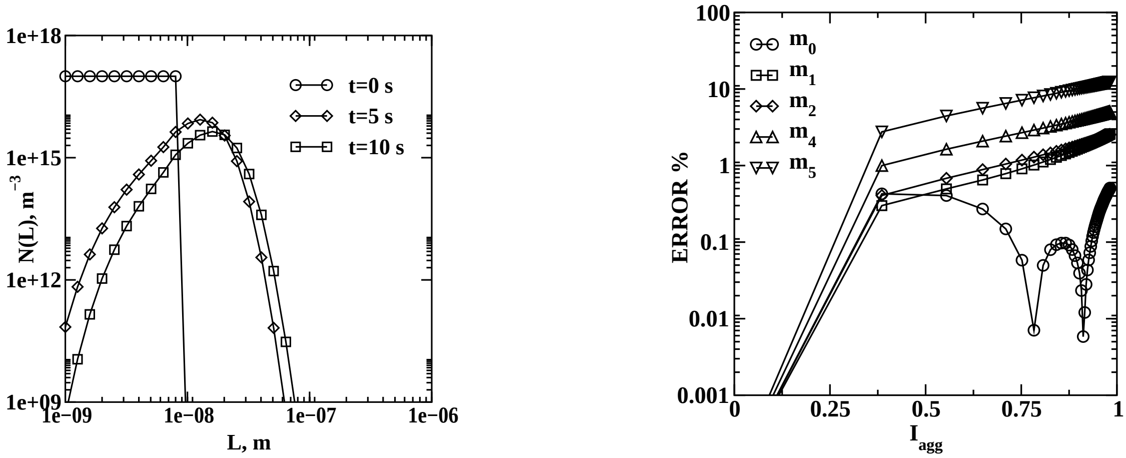

Figure 6.12: Aggregation with Brownian kernel ($\beta_0 = 2.5 \times 10^{-18}$ m^3/s): (a) CSD at different time steps calculated with the DPB approach. (b) Percent error of the first six moments calculated by the QMOM. (m_3 is not reported since the error is lower than 10^{-5}%.)

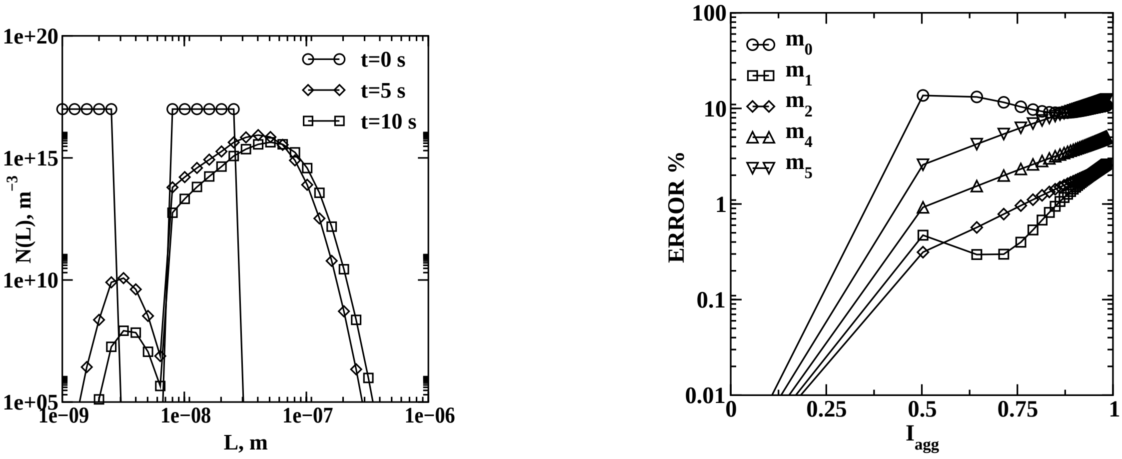

Figure 6.13: Aggregation with Brownian kernel ($\beta_0 = 2.5 \times 10^{-18}$ m^3/s): (a) CSD at different time steps calculated with the DPB approach. (b) Percent error of the first six moments calculated by the QMOM. (m_3 is not reported since the error is lower than 10^{-5}%.)

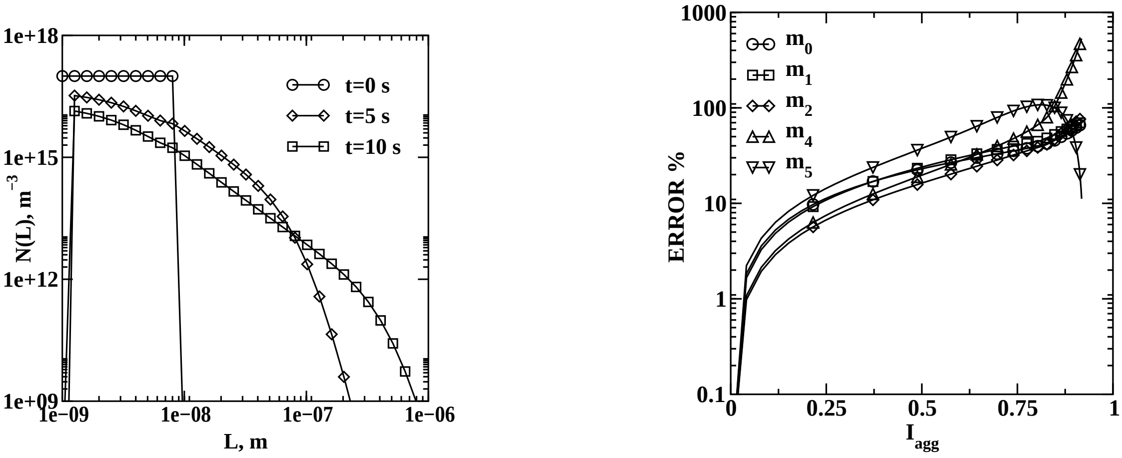

Figure 6.14: Aggregation with hydrodynamic kernel ($\beta_0 = 1.5 \times 10^6$ s^{-1}): (a) CSD at different time steps calculated with the DPB approach. (b) Percent error of the first six moments calculated by the QMOM. (m_3 is not reported since the error is lower than 10^{-5}%.)

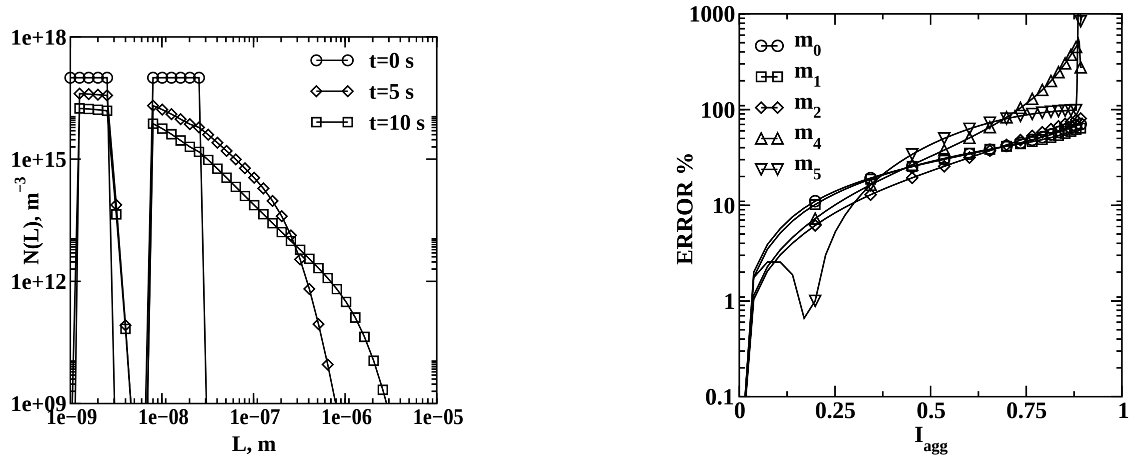

Figure 6.15: Aggregation with hydrodynamic kernel ($\beta_0 = 5.4 \times 10^4$ s^{-1}): (a) CSD at different time steps calculated with the DPB approach. (b) Percent error of the first six moments calculated by the QMOM. (m_3 is not reported since the error is lower than 10^{-5}%.)

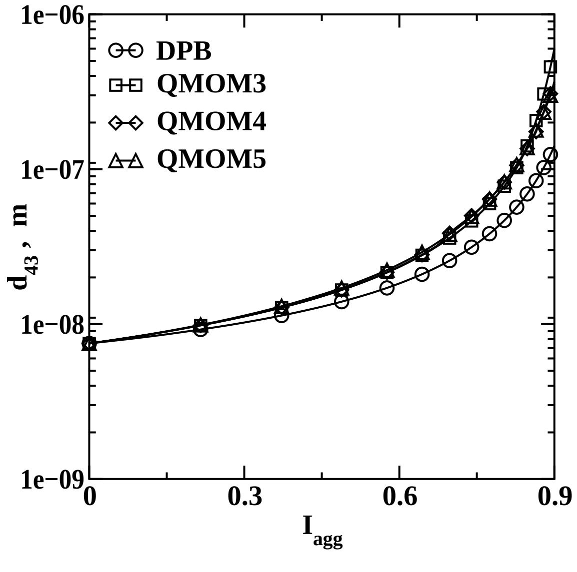

Figure 6.16: Effect of the number of nodes in the quadrature approximation on the prediction of mean crystal size for aggregation with hydrodynamic kernel with initial bimodal CSD.

6.2 Validation of the flow field and tracer dispersion predictions in the Taylor-Couette reactor

In section 5.3 the fluid dynamic regimes that can be achieved in the Taylor-Couette reactor have been illustrated. Since the flow field in this reactor is very particular an experimental validation is required. As already mentioned for the tubular reactor this validation was carried out in a previous work [74].

In Fig. 6.17 a typical result from a visualization experiment is reported. This particular picture refers to 35 rpm and in this case 7 vortices are visible. However, as in the figure only one half of the reactor is reported the total number of vortices detected in this case is 14. Notice that the aspect ratio $\Gamma = H/d$ is about 14; if the vortices have equal axial and radial dimensions it would lead to 14 vortices, that is exactly the situation observed experimentally, as shown in the figure. However this is not the unique solution found in this case. In fact, this is the flow field established if initially the fluid was at rest. If this configuration was achieved starting from higher rotational speeds the number of vortices detected was 12. This result is confirmed by other works, where the existence of multiple steady-state solutions and of hysteresis is widely documented. The explanation lies in the mathematical description of the problem: the Navier-Stokes equation represents a dynamic nonlinear system, and thus multiple steady-state solutions are a natural consequence of this non-linearity.

For all the cases investigated the vortices were always even in number and counter-rotating; moreover the vortices in the top and in the bottom of the reactor were always formed in such a way to force the fluid to go from the outer cylinder to the inner one. Increasing the rotational speed of the inner cylinder up to 300 rpm the number of vortices is reduced down to 10, and for 400 rpm and 500 rpm the flow was found not to be stable. The number of vortices in this case was not constant, due to strong instabilities in the top and in the bottom of the reactor. In these regions vortices split apart and then merge again periodically. A further increase in the rotational speed causes the transition to the fully turbulent flow without vortices.

The number of vortices was determined both with laser visualization and with LDA measurements. In Tab. 6.4 a summary is reported. Experimental data were compared with CFD predictions (in this work the commercial code FLUENT version 5.4 was used.) In this first part of the work 2D simulations in a meridian section of the reactor were carried out. Different grids were tested in order to find a grid independent solution. The final grid for this 2D simulations was with 15 nodes in the radial direction and 206 in the axial direction for a total of 3090 nodes. Different turbulence models and near-wall treatments were tested. The comparison, in terms of the number of vortices is reported in Tab. 6.4.

The comparison shows that depending on the rotational speed of the inner cylinder several combinations of turbulence models and near wall treatments give good agreement with the experimental data. However the RSM with standard wall function seems to be the best one. This is also confirmed by a more detailed comparison between CFD predictions and experimental data. In this case experimental data used for the comparison are axial profiles of axial $\langle u_z \rangle$ and azimuthal $\langle u_\theta \rangle$ velocity at several rotational speeds (see Fig. 6.18.) The comparison was done at a fixed radial position located at three third of the annular gap starting from the inner cylinder (r = 0.0515 m.) As a general comment it should be said that the experimental determination using LDA is affected by a certain error in

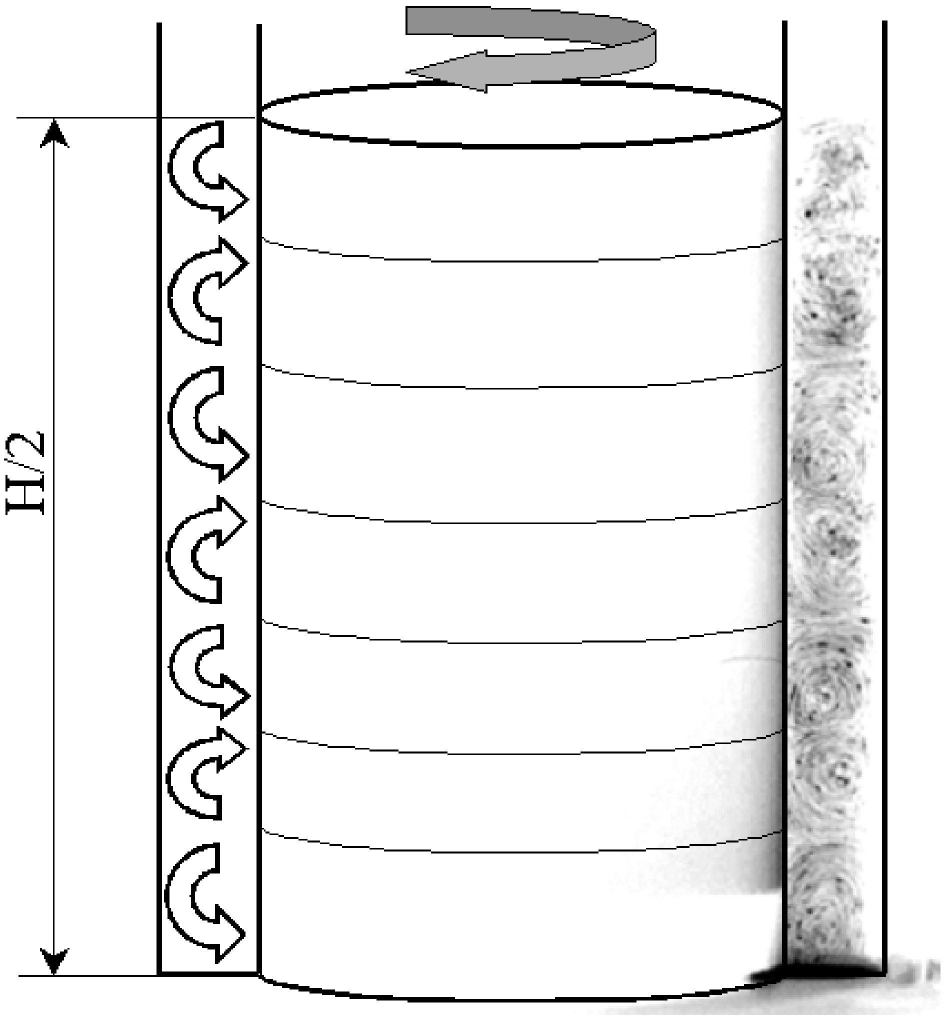

Figure 6.17: Experimental determination of the number of vortices for N=35 rpm (fluid initially at rest.)

Table 6.4: Summary of the number of vortices experimentally detected (Exp) and relative comparison with CFD predictions. Std: standard wall function; Non-eq: non-equilibrium wall function; Two-eq: two-equation model. RNG $k-\varepsilon$: RNG $k-\varepsilon$ model; Real. $k-\varepsilon$: Realizable $k-\varepsilon$ model; RSM: Reynolds Stress Model; *: after 100,000 iterations the convergence criteria were not satisfied.

N, rpm	wall fnc	RNG $k-\varepsilon$	Real. $k-\varepsilon$	RSM	Exp.
35	Std	14	14	12	14-12
	Non-Eq	2	2	2	
	Two-Eq	12	12	2*	
100	Std	14	14	12	12
	Non-Eq	8	2	8	
	Two-Eq	12	12	2*	
200	Std	14	14	10	10
	Non-Eq	12	8	10	
	Two-Eq	12	12	2*	
300	Std	12	12	10	10
	Non-Eq	10	10	10	
	Two-Eq	12	8	2*	
400	Std	8	8*	10	Not stable
	Non-Eq	8	8*	10	
	Two-Eq	12	12	2*	
500	Std	8	8*	10	Not stable
	Non-Eq	8	8*	10	
	Two-Eq	12	12	2*	

determining the actual position of the probe volume. This position was determined by using some reference points, such as the top and the bottom, the inner cylinder and the outer cylinder, but still this position is known with a small uncertainty. This could explain why in certain cases the overall agreement is good but would improve with a small shift on the axial position.

The comparison shows that in general the agreement is good. At low rotational speeds the azimuthal velocity is in good agreement with experimental data whereas increasing this parameter is underestimated by the CFD code. Concerning the axial velocity the over-all agreement is quite good and the fact that the data are quite spread at low rotational speed can be explained in terms of the difficulties in carrying out the experiments in these operating conditions.

In Figs. 6.19-6.22 the comparison between CFD predictions and experimental data for mean axial velocity, mean azimuthal velocity, and two components of the Reynolds Stress tensor $\langle u'_z u'_z \rangle$ and $\langle u'_\theta u'_\theta \rangle$ at 300 rpm are reported. The agreement in general is good although it should be again mentioned that the azimuthal velocity is underestimated, as well as the two components of the Reynolds stress tensor.

Hereinafter the RSM with standard wall function is used for modeling the flow field in the Taylor-Couette reactor.

The CFD calculations presented in this first part were carried out by using two-dimensional grids. However also three-dimensional simulations have been carried out. In Fig. 6.23 the three-dimensional grid used in these simulations is reported and compared with the two-dimensional one. It is composed by 120 cells in the axial direction, 60 cells in the azimuthal direction and 14 cells in the radial one, for a total of 100,800 cells. From the figure it is clear that when modeling the system in 2D no azimuthal gradient exist and the reactor is modeled under the hypothesis of axial symmetry, however we will come back to this aspect later. Concerning flow field predictions comparison between 2D and 3D simulations shows small differences, confirming that in these operating conditions the flow field can be modeled by using a 2D approach.

In a second part of the validation also tracer dispersion experiments have been considered for comparison. Although using the RSM the Reynolds stresses are known, and Eq. 4.10 could have been used, transport of a non-reacting scalar is modeled by using Eq. 4.14:

$$\frac{\partial\langle\xi\rangle}{\partial t} + \frac{\partial}{\partial x_i}(\langle u_i\rangle\langle\xi\rangle) - \frac{\partial}{\partial x_i}\left(\Gamma_t \frac{\partial\langle\xi\rangle}{\partial x_i}\right) = 0, \tag{6.34}$$

where:

$$\Gamma_t = \frac{C_\mu}{Sc_t}\frac{k^2}{\varepsilon}, \tag{6.35}$$

with $Sc_t = 0.7$ and $C_\mu = 0.09$. The transport equation for this non-reacting scalar is implemented in the CFD code by means of user-defined subroutines. With the CFD code FLUENT (as well as almost all the commercial CFD codes) it is possible to solve, besides the Navier-Stokes and continuity equation, other transport equations defined by the user. These transport equations are added to FLUENT as user-defined scalars. For every user-defined scalar a transport equation of the form

$$\rho\frac{\partial\phi_k}{\partial t} + \frac{\partial}{\partial x_i}\left(\rho\langle u_i\rangle\phi_k - \rho\Gamma_k\frac{\partial\phi_k}{\partial x_i}\right) = S_{\phi_k} \tag{6.36}$$

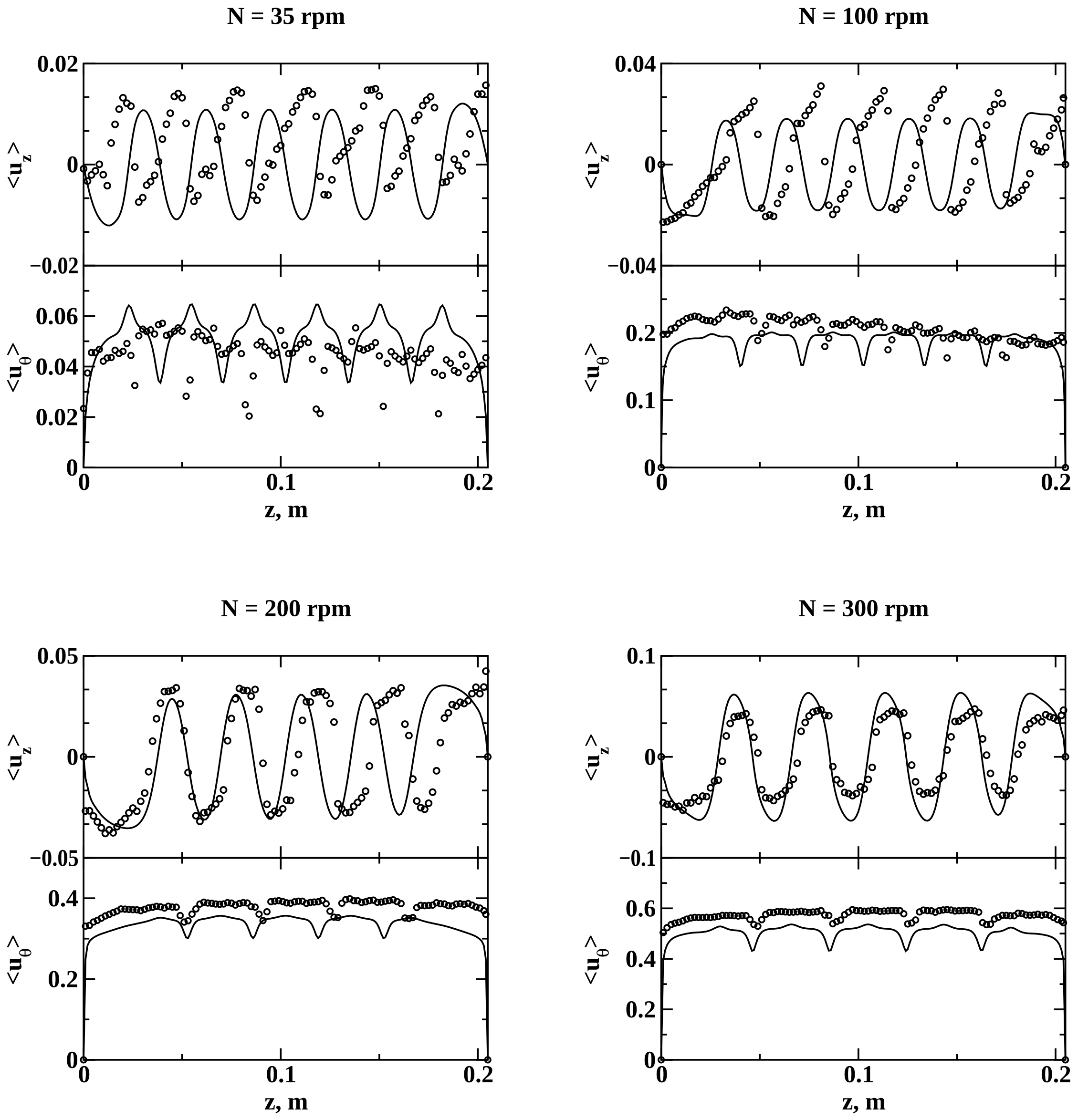

Figure 6.18: Comparison of experimental and predicted axial profiles of mean axial velocity $\langle u_z \rangle$ and mean azimuthal velocity $\langle u_\theta \rangle$ at $r = 0.0515$ m and at several rotational speeds. Continuous line: CFD predictions by using the RSM with standard wall function; circle: LDA measurement.

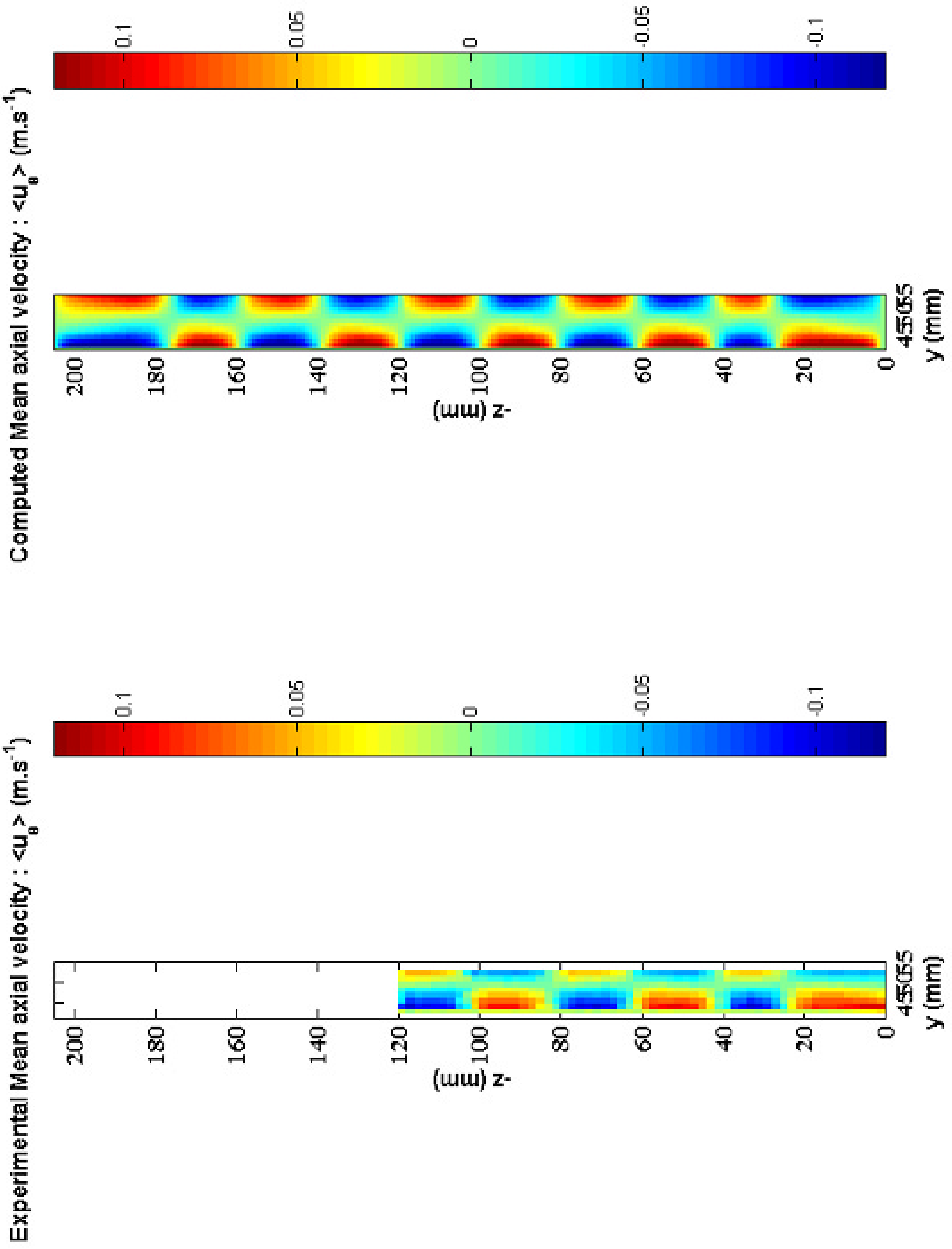

Figure 6.19: Comparison between experimental data and CFD predictions for the axial velocity $\langle u_z \rangle$ at 300 rpm.

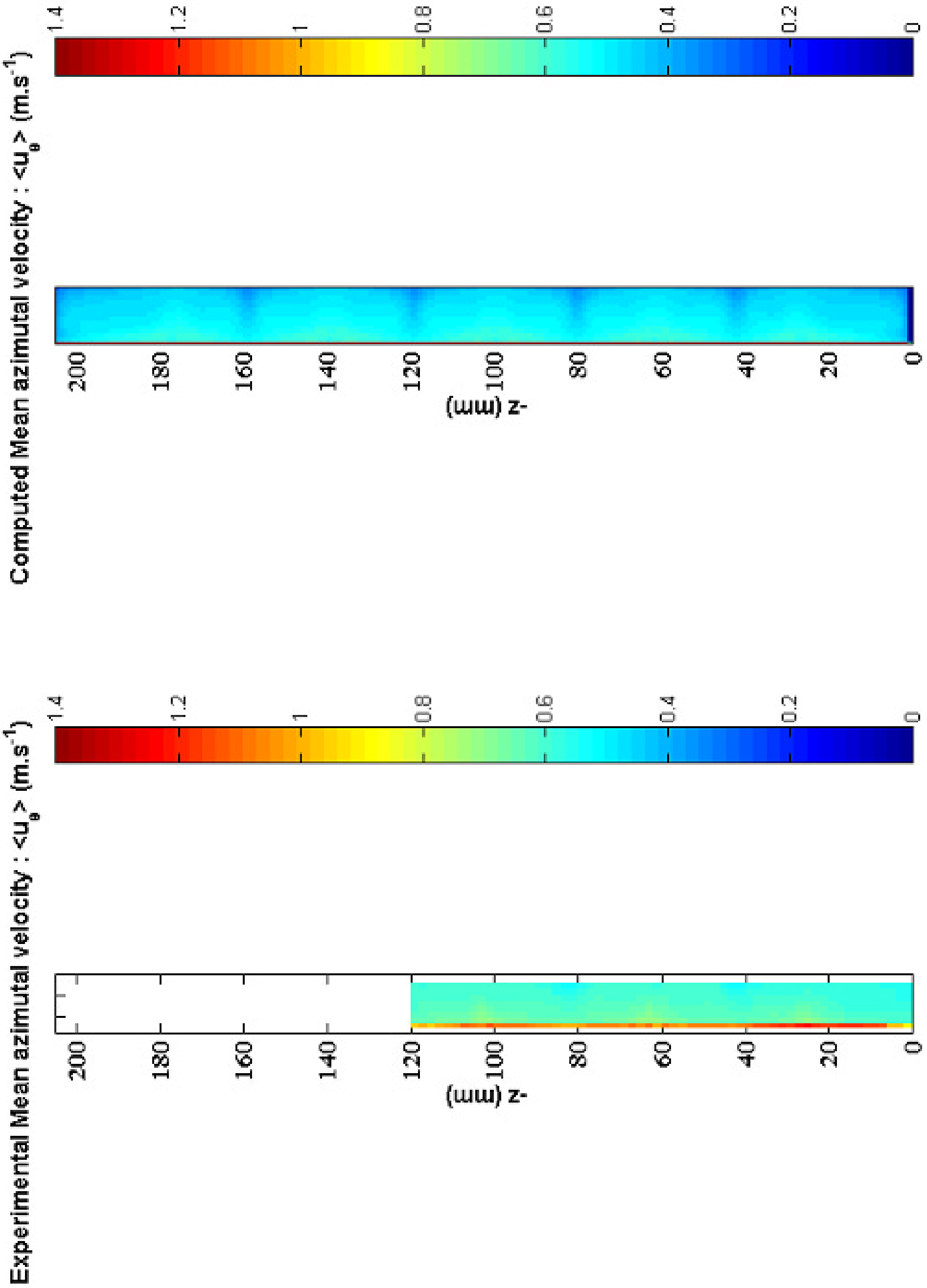

Figure 6.20: Comparison between experimental data and CFD predictions for the azimuthal velocity $\langle u_\theta \rangle$ at 300 rpm.

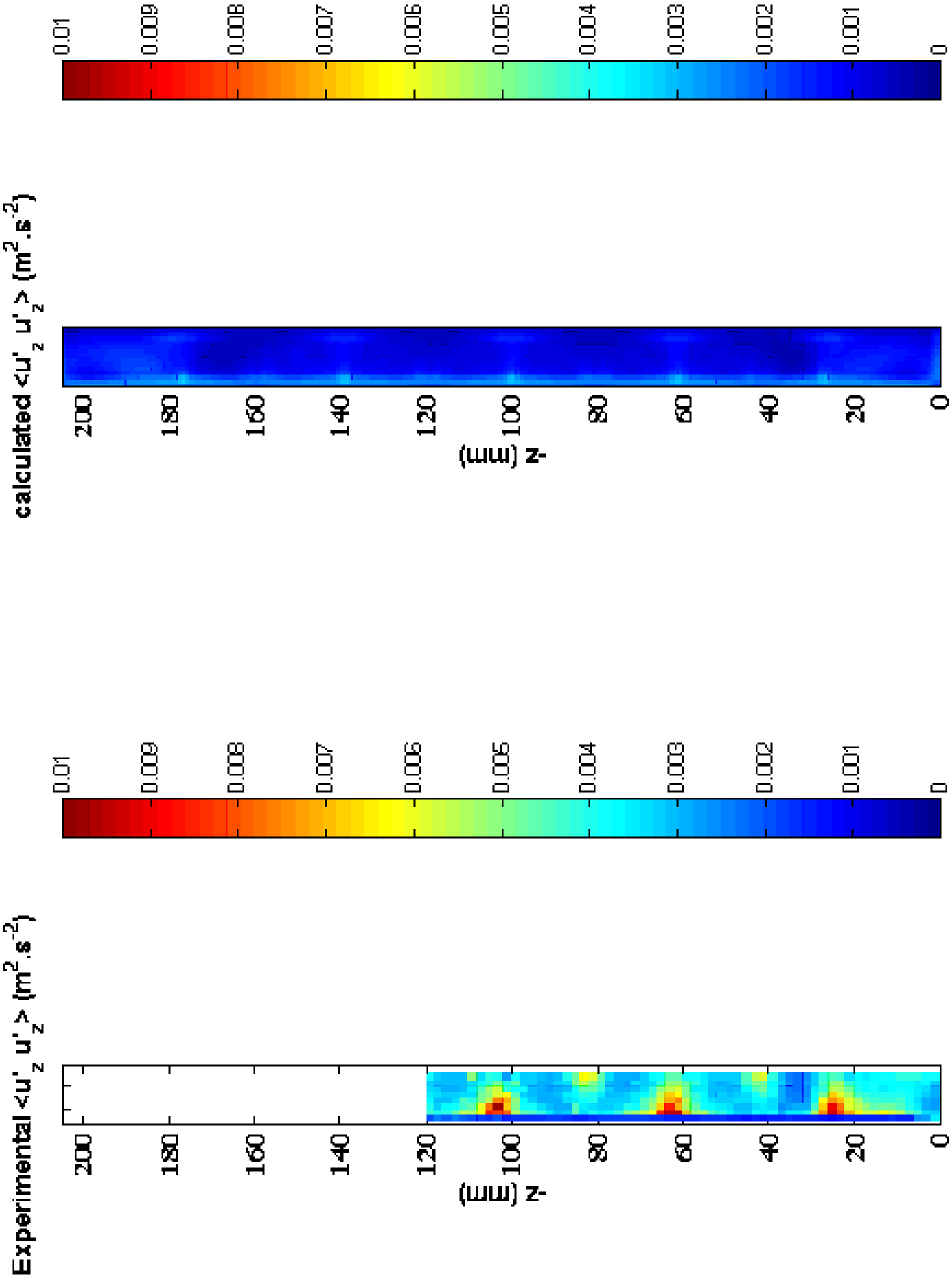

Figure 6.21: Comparison between experimental data and CFD predictions for $\langle u'_z u'_z \rangle$ at 300 rpm.

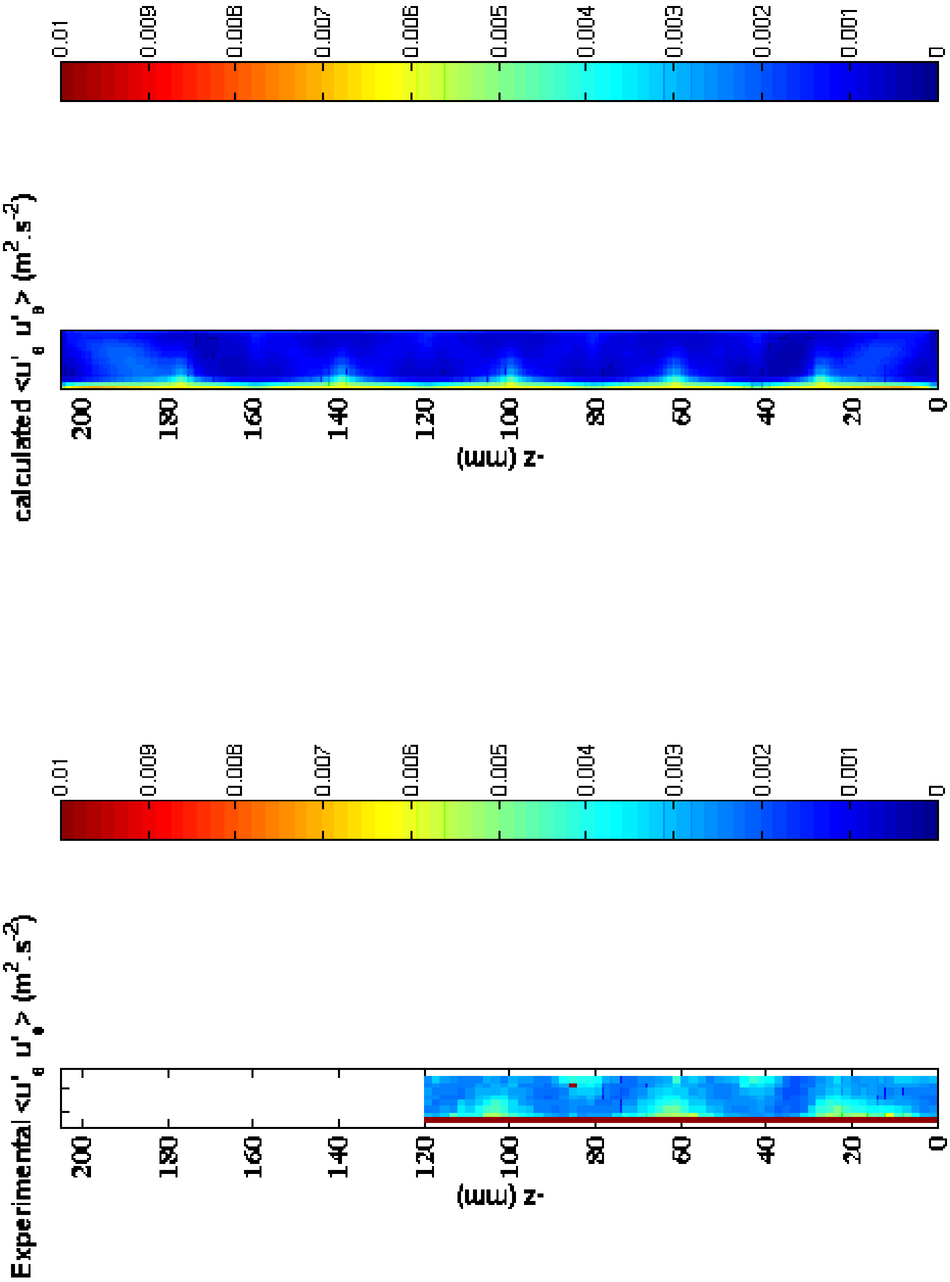

Figure 6.22: Comparison between experimental data and CFD predictions for $\langle u'_\theta u'_\theta \rangle$ at 300 rpm.

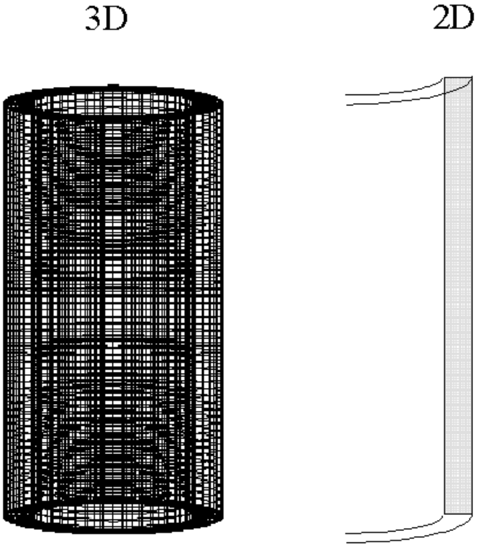

Figure 6.23: Computational grids used in the 3D and 2D simulations.

is solved, where ϕ_k is the k^{th} scalars, ρ is the fluid density and Γ_k, and S_{ϕ_k} are the diffusivity and the source term for the k^{th} scalar, respectively. In this work the diffusivity Γ_k has been set equal to the turbulent diffusivity (Γ_t) for all scalars. Note that the source term must be consistent with the dimensions of the other terms in Eq. 6.36. For this reason the source terms appearing in model equations must be multiplied by the fluid density. However for the user-defined scalar that represent the tracer concentration the source term is null (since it is a non-reacting scalar.)

Injection of tracer was investigate at 300 rpm and at 30 ml/min in four different positions: FP1, FP2, FP3, FP4 (see pag. 70 for details.) In Figs. 6.24 and 6.25 the tracer dispersion evolution computed with 3D simulations by using the RSM with standard wall functions is reported for two injection positions: FP1 and FP2. From the figure it is possible to notice that when the injection is done in FP1 the flow field is probably not disturbed by the injection, since the velocity of the injected fluid is much lower than the velocity of the surrounding fluid. However when injection is done in FP2-FP3-FP4 due to the presence of the injector some distortion of the flow field are expected. CFD simulations show that in general the flow field is locally modified but the structure seems to be very similar. This results is confirmed by some experimental data obtained with the specific purpose of investigating the effect of the injector.

During the simulations the tracer concentration at different meridian planes (every 45°) in points at equal axial and radial positions has been monitored. The comparison showed that tracer dispersion evolution is very similar in different planes, suggesting the use of the axial symmetric hypothesis also for tracer dispersion simulation. Further investigations showed that this hypothesis is held in the range of rotational speeds used in this work. When the system is modeled in 2D the injection point is represented by a small region in the computational domain. However, because of the hypothesis of axial symmetry, this region corresponds to a toroidal surface in the real system. Although this strong simplification in the representation of the reactor, 2D and 3D predictions for tracer dispersion are very

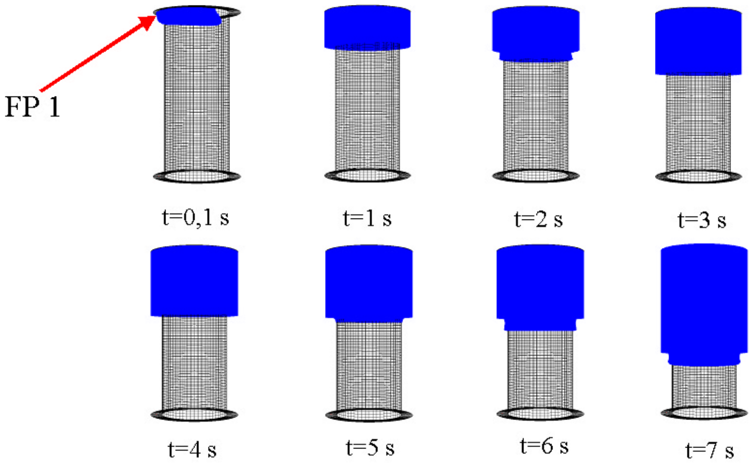

Figure 6.24: Tracer dispersion for FP1, N = 300 rpm, and an injection velocity v_i = 30 ml/min. Volume of the computational domain for which $0.0008 < c/c_o < 1.0$.

similar.

The effect of Sc_t was investigated in the range from 0.2 to 2 and tracer dispersion was shown to be relatively insensitive to this parameter, showing that in the reactor scalar transport is dominated by convection due to the presence of the vortices. In Fig. 6.26 the comparison between experimental data and two-dimensional CFD predictions for the tracer concentration is reported. Data are presented in terms of the normalized tracer concentration against time, where t=0 is the beginning of the injection. Experimental data are obtained via LIF measurements in five points (see Fig. 5.5.) As it is possible to see the agreement is quite good although for points far from the injection CFD predictions show a dispersion efficiency lower than the measured one.

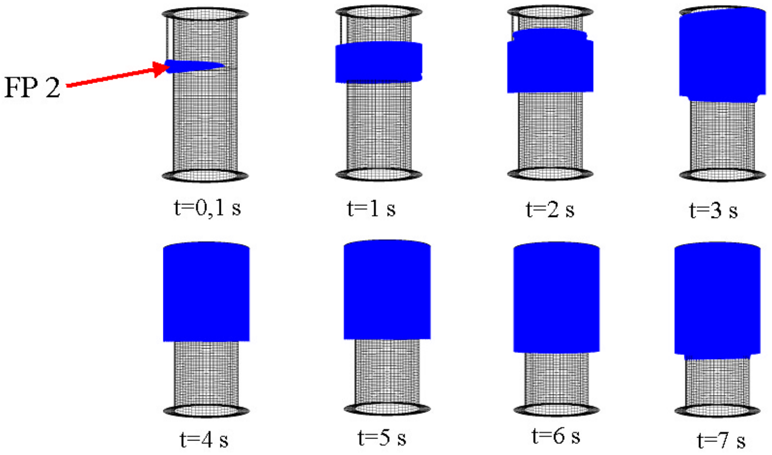

Figure 6.25: Tracer dispersion for FP2, N = 300 rpm, and an injection velocity v_i = 30 ml/min. Volume of the computational domain for which $0.0008 < c/c_o < 1.0$.

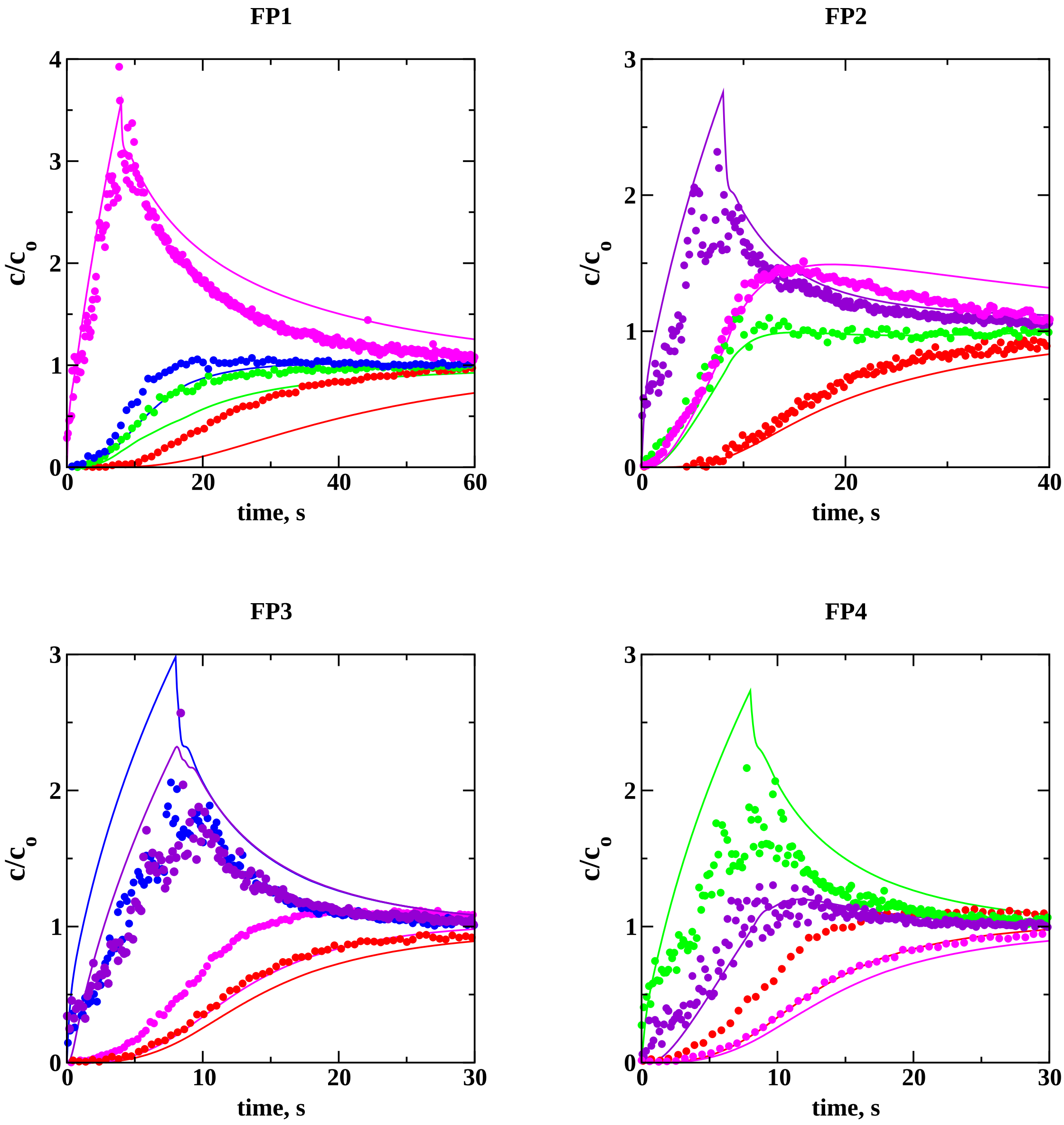

Figure 6.26: Comparison of experiments and CFD predictions for the normalized tracer concentration (N=300rpm; v=30 ml/min; injected volume: 4 ml.) Symbols: experimental data. Lines: CFD predictions; red: M1; green: M5; blue: M6; violet: M7; magenta: M10.

6.3 Reactive tests

In this section the experimental data from reactive tests are presented and compared with model predictions. As already mentioned, precipitation was investigated both in a Taylor-Couette reactor and in a tubular reactor. The first results from the Taylor-Couette reactor showed that the influence of mixing on precipitation is indeed quite strong but due to the number of complex phenomena involved it was sometimes very difficult to understand the role of every single parameter. For this reason, in order to investigate the mixing properties of this reactor in addition to precipitation experiments a series of tests using competitive parallel reactions were carried out (iodide/iodate reaction.) The section is divided into three subsections: in section 6.3.1 the results from the iodide/iodate reaction in the Taylor-Couette reactor are presented and some conclusions on the mixing properties of this device are drawn; in section 6.3.2 the results from the precipitation tests in the same reactor are discussed, and finally in section 6.3.3 the precipitation tests carried out in the tubular reactor are presented.

6.3.1 Iodide/iodate reaction in the Taylor-Couette reactor

Experimental data The effect of the rotational speed of the inner cylinder, the injection velocity and the feed position (only FP1 and FP2 locations) on the segregation index was investigated. The experimental results are showed in Fig. 6.27. As already explained (see pag. 71) a constant volume of 4 ml was injected at different injection velocities and thus with different injection times. During injection blobs of A is introduced in the reactor that contains a mixture of B and C. This blob is mixed at the macroscopic level by convection and turbulent diffusion and is mixed at the microscopic level by molecular mixing. If the injection is instantaneous, the blob containing A is introduced in an infinitesimal small interval of time and it has to undergo the overall mixing process: macroscale gradients are destroyed by convection and turbulent diffusion and microscale gradients are destroyed by molecular mixing. If the injection occurs during a sufficiently long interval of time, reaction takes place in a pseudo-homogeneous system, and the segregation can be attributed only to micromixing.

In other words for rapid injection conditions, the acid plume is not well dispersed in the reactor and macroscopic concentration gradients may influence the results, yielding higher values of the segregation index. In the opposite situation, when acid injection is infinitely low, macromixing effects are eliminated and the final segregation index is only micromixing relevant. The results reported in Fig. 6.27 are the experimental evidence of this: the segregation index decreases increasing the injection time and reaches a constant value for sufficiently long injection times.

In the figure is also clear which is the effect of the rotational speed of the inner cylinder: increasing this parameter the segregation index decreases since mixing is faster (at the macroscopic and microscopic level.) It is also interesting to highlight the effect of the injection position. Moving the injection from FP1 to FP2 the effect of the rotational speed of the inner cylinder is reduced. This can be explained by the fact that since the injection is in the middle of the reactor mixing is more efficient and less sensitive to the rotational speed. However small differences are detected in the limiting value of X_s for long injection time, showing that the change in the injection position produces a strong change in the quality of mixing at the macroscopic level, but imitate improvements in the mixing at the molecular level.

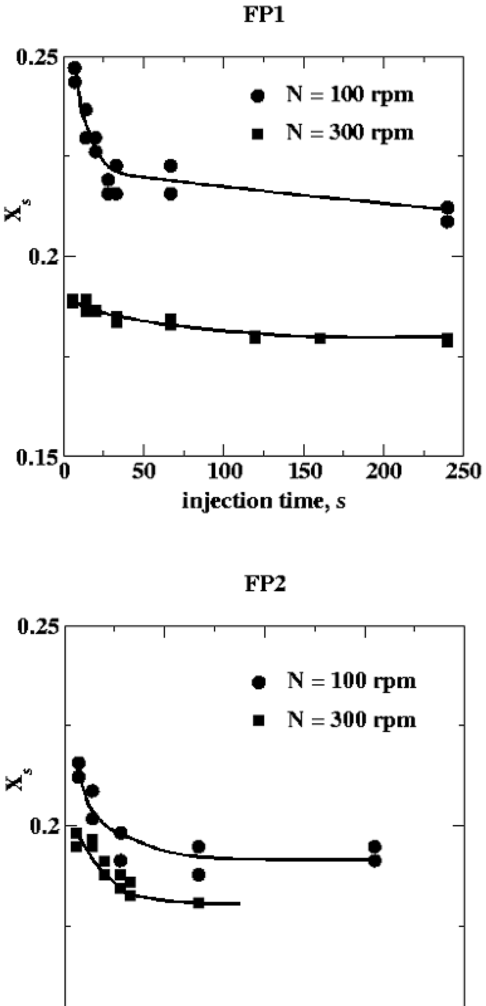

Figure 6.27: Experimental segregation index obtained injecting 4 ml of acid with different injection times at 100 and 300 rpm in the two feed locations FP1 and FP2.

This method has been also suggested for the experimental determination of turbulent dissipation rate in chemical reactors [93]. In fact, as already mentioned, for sufficiently long injection times the segregation index is only micromixing relevant, and in these conditions it is possible to apply the Engulfment model [52] to determine the relationship between segregation index and turbulent dissipation rate [5]. This is shown in Fig. 6.28. From this relationship and the asymptotic value of the segregation index at several rotational speeds it is possible to determine the corresponding value of ε. This value was compared with the volume-averaged ε obtained from CFD simulations, and with the values obtained from relationships available in literature. In particular ε can be evaluated as follows:

$$\varepsilon = \frac{G\Omega_1}{\rho V_R}, \tag{6.37}$$

where G is the torque required for one cylinder to rotate at a desired rotational speed (Ω_1), ρ is the fluid density, and V_R is the reactor volume. The torque can be evaluated by using different relations [77]. One of the dimensionless relations (A) is as follows:

$$\begin{aligned} f &= 0.46 \left(\frac{r_2 d}{r_1^2}\right)^{1/4} Re_r^{-0.5} \quad 4 \times 10^2 < Re < 10^4 \\ f &= 0.073 \left(\frac{r_2 d}{r_1^2}\right)^{1/4} Re_r^{-0.3} \quad Re > 10^4. \end{aligned} \tag{6.38}$$

where r_1 is the radius of the inner cylinder, r_2 is the radius of the outer cylinder, $d = r_2 - r_1$ is the annular gap, Re_r is the rotational Reynolds number defined in Eq. 5.5 and f is the friction factor:

$$f = \frac{G}{\pi H \rho (r_1 \Omega_1)^2 r_1^2}. \tag{6.39}$$

Another relation (B) is the following:

$$\frac{f}{f_{lam}} = 0.128 Re_m^{0.58} \quad 10^3 < Re_m < 10^6, \tag{6.40}$$

where Re_m is the modified Reynolds number defined as follows:

$$Re_m = Re_r \left(\frac{d}{r_1}\right)^{1/2}, \tag{6.41}$$

and the laminar friction factor defined by:

$$f_{lam} = \frac{4 r_2^2}{r_1 (r_1 + r_2) \frac{1}{Re_r}}. \tag{6.42}$$

Concerning CFD simulations the results showed that the volume-averaged turbulent dissipation rate is strongly affected by the near-wall treatment rather than the turbulence model adopted. For this reason CFD results have been presented for different near-wall treatments[6]. The comparison is shown in Fig. 6.29. In this logarithmic diagram the power law between turbulent dissipation rate and rotational speed is represented by a linear plot.

---

[5] Since in these operating conditions macro-scale gradients are very small the reactor can be modeled as an homogeneous system. The micromixing time is evaluated by using Eq. 4.20 (see pag. 43.)

[6] In this part of the work only converged simulations were considered. Notice that simulations that after 100,000 iterations did not satisfy convergence criteria are indicated in Tab. 6.4 with *.

The exponent calculated by fitting experimental data is 1.2, whereas both the relations used results in an exponent of 2.5, CFD simulations with standard wall function (std) 1.8, with non-equilibrium wall function (non-eq) 2.1, and with the two-layer zonal model 3.0.

The results show that the experimental data are closer to relation (B) (see Eq. 6.40) and both are in quite good agreement with CFD predictions with standard wall function. However it should be mentioned that the experimental data does not give an average value on the entire volume of the reactor, but only in the region where reaction takes place. Moreover use of these relations (Eqs. 6.38 and 6.40) is questionable and can be considered only to define the order of magnitude of the property.

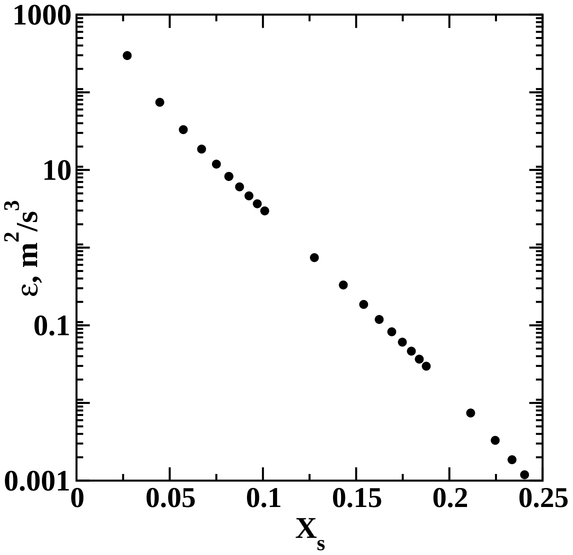

Figure 6.28: Relationship between turbulent dissipation rate.

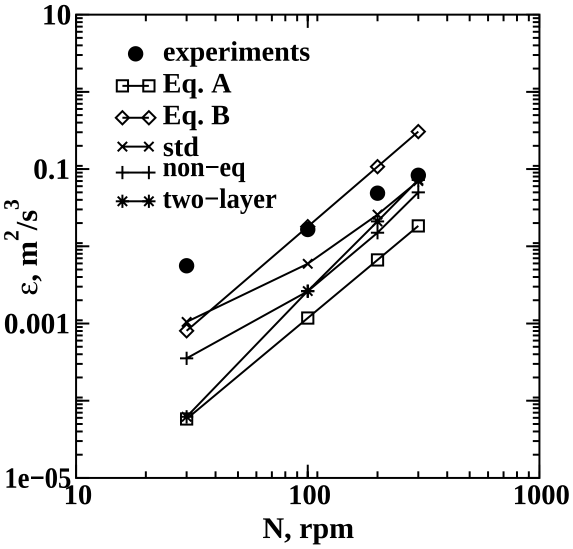

Figure 6.29: Comparison between the turbulent dissipation rate determined by experiments, by using Eq. A and Eq. B, and by CFD simulations with different near-wall treatments.

Model predictions and comparison with experimental data The results reported in the previous section (see pag. 105) showed that the flow field of the Taylor-Couette reactor can be modeled by using 2D simulations with RSM and standard wall functions. Moreover it was shown that the hypothesis of axial symmetry can be used also to model the scalar field. The reacting system will thus be modeled by using 2D simulations.

Before recalling the governing equation of the model and explaining the computational details of the simulations, let us consider again the parallel reaction scheme:

$$\begin{aligned} B+A &\rightarrow R, \\ C+A &\rightarrow S. \end{aligned} \tag{6.43}$$

In this case there are 5 reacting scalars with 2 reactions; in general for modeling this system one should solve 5 transport equations (one for each scalar.) However it can be shown that the reacting system can be written in terms of only 2 scalars in addition to the mixture fraction. In fact, this system of 5 scalar can be written in terms of 1 non reacting scalar (mixture fraction) and 2 reacting scalars (reaction progress variables.) A detailed explanation of this technique can be found in [30] and here we present the solution for parallel reactions. The relationships between mixture fraction (ξ) reaction progress variables (Y_1,Y_2) and concentrations are

$$\begin{aligned} \frac{c_A}{c_{Ao}} &= \xi - \xi_{s1}Y_1 - \xi_{s2}Y_2, \\ \frac{c_B}{c_{Bo}} &= 1 - \xi - (1-\xi_{s1})Y_1, \\ \frac{c_C}{c_{Co}} &= 1 - \xi - (1-\xi_{s2})Y_2, \\ \frac{c_R}{c_{Bo}} &= (1-\xi_{s1})Y_1, \\ \frac{c_S}{c_{Co}} &= (1-\xi_{s2})Y_2, \end{aligned} \tag{6.44}$$

where

$$\xi_{s1} = \frac{c_{Bo}}{c_{Ao}+c_{Bo}}, \tag{6.45}$$

and

$$\xi_{s2} = \frac{c_{Co}}{c_{Ao}+c_{Co}}. \tag{6.46}$$

The source terms for the reaction progress variables are:

$$S_{Y1} = \frac{R_1}{\gamma_1}, \tag{6.47}$$

and

$$S_{Y2} = \frac{R_2}{\gamma_2}, \tag{6.48}$$

where R_1 and R_2 are the source terms for reaction 1 and 2 and where

$$\gamma_1 = \frac{c_{Ao}c_{Bo}}{c_{Bo}+c_{Ao}}, \tag{6.49}$$

and

$$\gamma_2 = \frac{c_{Ao}c_{Co}}{c_{Co} + c_{Ao}}. \tag{6.50}$$

In the case in which the first reaction is considered infinitely fast, the first reaction progress variable ($Y_{1\infty}$) can be written in terms of Y_2 and ξ:

$$Y_{1\infty} = min\left(\frac{1-\xi}{1-\xi_{s1}}, \frac{\xi}{\xi_{s1}} - \frac{\xi_{s2}}{\xi_{s1}}Y_2\right), \tag{6.51}$$

that gives $c_B = 0$ where A is in excess and $c_A = 0$ where B is in excess. Thus this reactive system that originally was described by 5 transport equations can now be described by only 2 transport equations, one for the mixture fraction ξ and one for the reaction progress variable Y_2 whereas $Y_{1\infty}$ is directly computed from Eq. 6.51.

The final model is constituted by 4 transport equations: Eqs. 4.74 and 4.75 for the probabilities of Environment/mode 1 and 2 (p_1 and p_2)

$$\frac{\partial p_1}{\partial t} + \frac{\partial}{\partial x_i}(\langle u_i\rangle p_1) = \frac{\partial}{\partial x_i}\left(\Gamma_t \frac{\partial p_1}{\partial x_i}\right) + \gamma_s p_3 - \gamma p_1(1-p_1), \tag{6.52}$$

$$\frac{\partial p_2}{\partial t} + \frac{\partial}{\partial x_i}(\langle u_i\rangle p_2) = \frac{\partial}{\partial x_i}\left(\Gamma_t \frac{\partial p_2}{\partial x_i}\right) + \gamma_s p_3 - \gamma p_2(1-p_2), \tag{6.53}$$

and Eq. 4.76 for the weighted mixture fraction in Enviroment/mode 3 ($\langle s_\xi\rangle_3 = p_3\langle\xi\rangle_3$)

$$\begin{aligned}\frac{\partial\langle s_\xi\rangle_3}{\partial t} + \frac{\partial}{\partial x_i}(\langle u_i\rangle\langle s_\xi\rangle_3) = {} & \frac{\partial}{\partial x_i}\left(\Gamma_t \frac{\partial\langle s_\xi\rangle_3}{\partial x_i}\right) - \gamma_s p_3(\langle\xi\rangle_1 + \langle\xi\rangle_2) \\ & +\gamma p_1(1-p_1)\langle\xi\rangle_1 + \gamma p_2(1-p_2)\langle\xi\rangle_2,\end{aligned} \tag{6.54}$$

and the following equation for the weighted reaction progress variable ($\langle s_{Y_2}\rangle_3 = p_3\langle Y_2\rangle_3$):

$$\frac{\partial\langle s_{Y_2}\rangle_3}{\partial t} + \frac{\partial}{\partial x_i}(\langle u_i\rangle\langle s_{Y_2}\rangle_3) = \frac{\partial}{\partial x_i}\left(\Gamma_t \frac{\partial\langle s_{Y_2}\rangle_3}{\partial x_i}\right) + \frac{p_3 R_2(\langle c_A\rangle_3, \langle c_C\rangle_3)}{\gamma_2} \tag{6.55}$$

where $R_2(\langle c_A\rangle_3, \langle c_C\rangle_3)$ is the local source term for the chemical reaction calculated with local concentrations in Environment/mode 3 that are defined in Eqs. 6.44 by replacing ξ with $\langle\xi\rangle_3$, $Y_{1\infty}$ with $\langle Y_{1\infty}\rangle_3$, and Y_2 with $\langle s_{Y_2}\rangle_3$. The problem is closed once a functional form for the chemical source term $R_2(\langle c_A\rangle_3, \langle c_C\rangle_3)$ is given. In literature (see [88],) the following kinetic expression is proposed:

$$R_2 = k[H^+]^2[I^-]^2[IO_3^-], \tag{6.56}$$

where k is a function of the ionic strength I that has been determined experimentally:

$$\begin{aligned} I &< 0.166M \quad \log_{10}(k) = 9.28105 - 3.664\sqrt{I} \\ I &> 0.166M \quad \log_{10}(k) = 8.383 - 1.5112\sqrt{I} + 0.23689I, \end{aligned} \tag{6.57}$$

and with our notation:

$$R_2 = k(c_A)^2(5/6c_C)^2(1/6c_C). \tag{6.58}$$

As a first step simulations were carried out for the ideal case of instantaneous injection. In this case an uniform grid was used (15 nodes in the radial direction and 206 in the axial direction for a total of 3090 nodes.) First the flow field was solved by using steady-state simulation and then time-dependent simulations, for the scalar field, were carried out. For

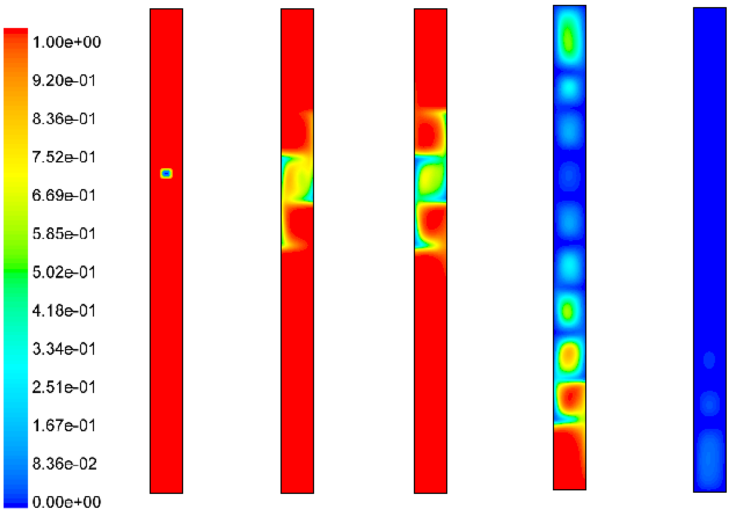

Figure 6.30: Contour plots of the volume fraction of Environment 2 (p_2) at different time steps (Left to right: $t_1 = 0$ s, $t_2 = 0.14$ s, $t_3 = 0.24$ s, $t_4 = 0.5$ s, $t_5 = 1$ s).

time-depedent simulations under-relaxation factors for p_1, p_2, $\langle s_\xi \rangle_3$ and $\langle s_{Y_2} \rangle_3$ were kept equal to one, whereas the time step was varied from 0.0001 seconds, in the beginning of the simulation, to 1 second at the end. The time step in the very beginning of the simulation has to be very small due to the fact that in the first period reaction rates are extremely high and the problem is numerically stiff. Due to the stiffness of the problem moreover all the simulations were carried out in double precision.

In this ideal case in the beginning of the simulation the reactor is filled with a mixture of B and C and A is present in a small spot around the injection point[7]. The portion of fluid containing the mixture of B and C is segregated from the portion of fluid containing A. Thus in the finite-mode PDF representation B and C form Environment 2 ($p_2 = 1$) whereas A forms Enviroment 1 ($p_1 = 1$). According to Eq. 6.44 the fluid that contains B and C has the local mixture fraction $\langle \xi \rangle_2 = 0$ whereas the fluid that contains A has the local mixture $\langle \xi \rangle_1 = 1$. As soon as mixing starts Environment 1 and 2 interact with each other and disappear to form Environment 3 which contains micromixed reactants. This is represented in Fig. 6.30, where the probability of mode 2 is reported. This means that in the beginning the PDF is represented by 2 delta functions centered at $\xi = 0$ (Environment/mode 2) and at $\xi = 1$ (Environment/mode 1). During mixing a third delta function appears and represents mixed reactants in Environment/mode 3.

In Fig. 6.31 the segregation index is reported for the case of instantaneous injection in FP1 for two rotational speeds of the inner cylinder. Fig. 6.31 confirms that the increase in the rotational speed of the inner cylinder causes a decrease in the segregation index: higher rotational speeds improve the mixing efficiency. Moreover in the figure the effect of the constant C_ϕ (see Eq. 4.19) is also reported. This constant defines the scalar variance

---

[7] The volume of this spot has to be the injected volume, and thus in this case is 4 ml.

dissipation rate:

$$\varepsilon_\xi = \frac{\langle \xi'^2 \rangle}{\tau_\phi}. \tag{6.59}$$

through the micromixing time (τ_ϕ.) As already mentioned several approaches have been proposed to evaluate this characteristic time (see pag. 43) such as the cascade model proposed by Baldyga or the spectral relaxation model proposed by Fox. However, these multi-scale models are based on the idea of fully developed turbulence spectra (high Reynolds numbers) and since in this reactor, especially near the injection zone, the spectra are probably not fully developed, the use of a simple large-scale motion dominated model, seems to be more reasonable:

$$\tau_\phi = \frac{2}{C_\phi}\frac{k}{\epsilon}, \tag{6.60}$$

where C_ϕ is the over mentioned numerical constant. It is also interesting to notice that this constant is related to the Damkoehler number (Da.) This number is defined as the ratio between the characteristic time for micromixing and the characteristic time of the chemical reaction. For homogeneous systems this number is constant, whereas for inhomogeneous systems is a function of position. For this reason it is interesting to carry out this sensitive analysis in respect of the constant C_ϕ; in fact, a variation of this constant results in an uniform change of the characteristic time ratio throughout the reactor, since

$$Da = \frac{\tau_\phi}{\tau_R} \propto \frac{1}{C_\phi}. \tag{6.61}$$

As it is possible to see model predictions are quite sensitive to the numerical value of C_ϕ. When C_ϕ increases the segregation index decreases and approximately when C_ϕ=6 an asymptote is reached. This value was shown to be the segregation index predicted by the model when micromixing is neglected[8].

In Fig. 6.31 the effect of micromixing is shown: given a particular flow field (and thus mixing in terms of convection and turbulent diffusion) the effect of mixing at the molecular level is to create local areas of segregation; the segregation slows down the first reaction, which is infinitely fast, and favors the second one.

The second case investigated is with injection in a finite time. In this case a 2D grid with finer resolution near the injection zone was used. The final grid was structured and with quadratic cells in all the computational domain except near the injection zone, where the grid was unstructured with triangular cells, for a total of 4778 cells. In this case the initial conditions for the computational domain inside the reactor are as follows:

$$p_1 = 0, \quad p_2 = 1, \quad \langle s_\xi \rangle_3 = \langle s_{Y_2} \rangle_3 = 0, \tag{6.62}$$

whereas at the inlet point:

$$p_1 = 1, \quad p_2 = 0, \quad \langle s_\xi \rangle_3 = \langle s_{Y_2} \rangle_3 = 0. \tag{6.63}$$

Thus the acid (A) is introduced through Environment 1 whereas the mixture of B and C is in Environment 2. The injection in this case is represented by a mass flow inlet surface.

---

[8] For testing the model in these conditions it is sufficient to set as initial conditions p_1=0 p_2=0 in every cell of the computational domain and then to set C_ϕ=0 and $\langle s_\xi \rangle_3$=0 except for the injection volume where $\langle s_\xi \rangle_3$=1.

During injection, A enters the reactor, and successively, due to micromixing, moves to Environment 3. In the same way, B and C move to Environment 3 where the reaction takes place.

In Fig. 6.32 contour plots of the volume fraction of Environment 2 at different time steps are reported. At the beginning of the simulation, the reactor is occupied by Environment 2 except at the injection point. As soon as Environment 1 enters into the reactor, Environment 2 starts to disappear due to mixing. After approximately one second, Environment 3 has completely taken the place of Environment 2, except near the injection zone, where Environment 3 will not be equal to one until the injection is finished. It is interesting to notice that Figs 6.30 and 6.32 are very similar but differs in a minute way because of the presence of the injector and of the injection.

The volume-averaged profiles of the volume fractions of Environments 1 and 2 for different injection velocities are reported in Figs. 6.33 and 6.34, respectively. From the figures, it is clear that the injection velocity has little effect on the temporal evolution of Environment 2, but has a strong effect on the temporal evolution of Environment 1. In fact, Fig. 6.33 shows that different injection velocities imply different injection times, and moreover the value of the volume fraction of Environment 1 during the injection increases with decreasing injection velocity. Note, however, that even at high injection velocities the volume fraction of Environment 1 remains very small.

From these observations, we can draw the following conclusions concerning mixing in this reactor. Within 1 second (see Figs. 6.32 and 6.33), large-scale gradients due to the initial conditions are eliminated. The reactor then operates in a steady-state regime until the injection is finished (see Fig. 6.33). During this period, the largest gradients (and hence micromixing) are concentrated in a small volume surrounding the injection point. At the end of the injection period, all gradients in mixture fraction are quickly eliminated and the system behaves like a perfectly mixed batch reactor.

In Fig. 6.35 the comparison between experimental and predicted segregation index for FP1 is reported. The agreement is satisfactory although for 100 rpm and for short injection time the model over predicts the segregation index. This can be caused by the fact that the flow field predictions in these operating conditions are not as good as at 300 rpm. Moreover for very long injection time ($t > 200$ s) the predicted segregation index decreases, meaning that the 2D model is not able to reproduce the asymptotic behavior.

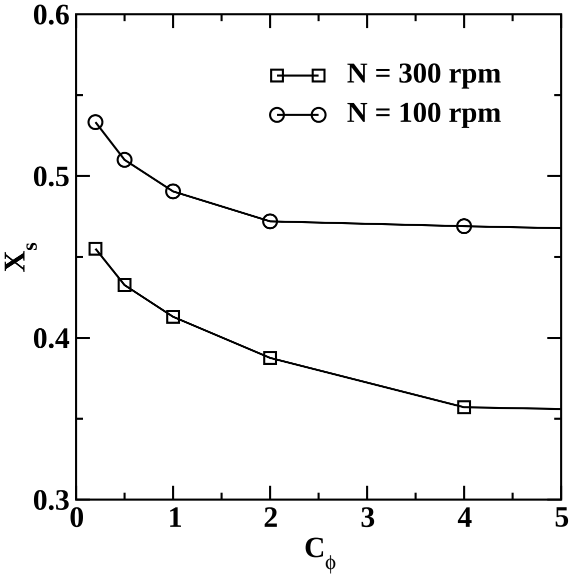

Figure 6.31: Segregation index in the case of istantaneous injection in FP1 for two rotational speeds of the inner cylinder.

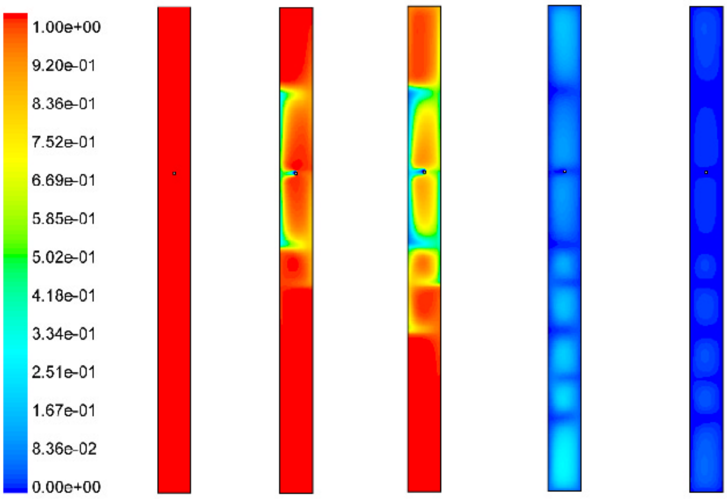

Figure 6.32: Contour plots of the volume fraction of Environment 2 (p_2) at different time steps (Left to right: $t_1 = 0$ s, $t_2 = 0.14$ s, $t_3 = 0.24$ s, $t_4 = 0.5$ s, $t_5 = 1$ s).

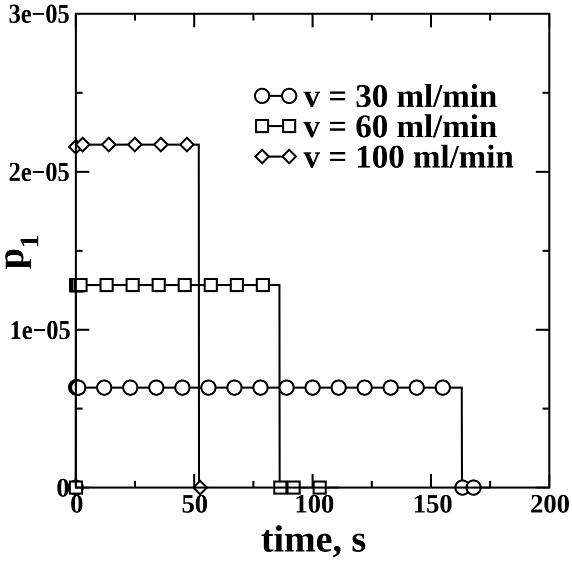

Figure 6.33: Volume-averaged volume fraction of Environments 1 for three different injection velocities (N = 500 rpm).

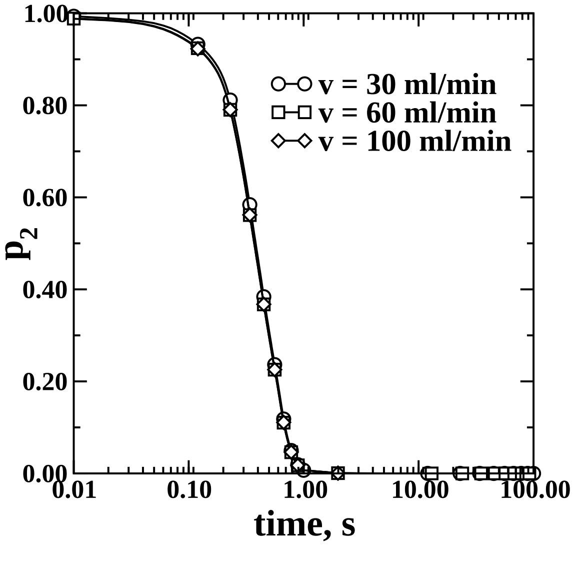

Figure 6.34: Volume-averaged volume fraction of Environments 2 for three different injection velocities (N = 500 rpm).

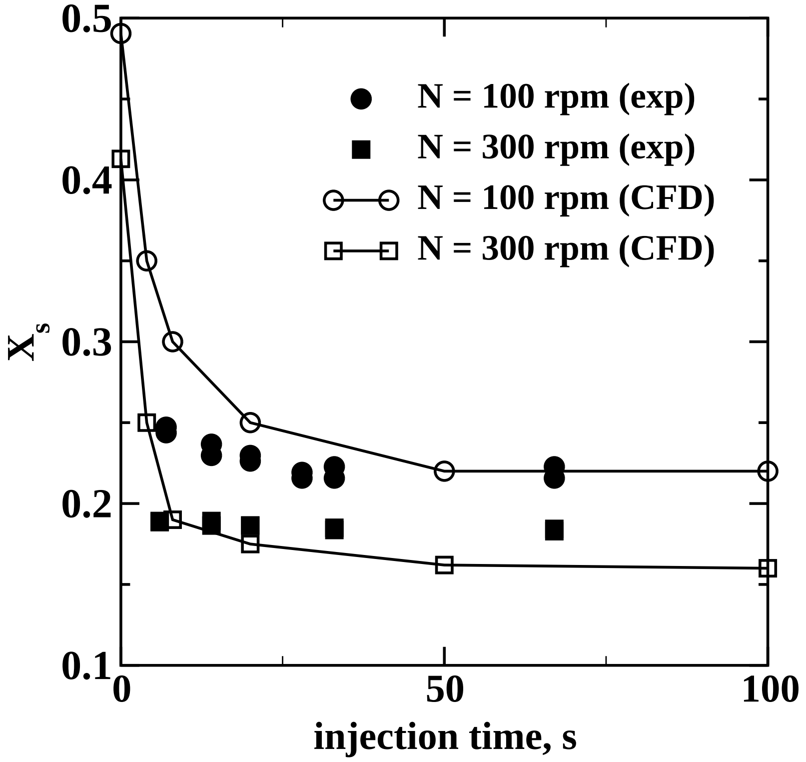

Figure 6.35: Comparsion between experimental and predicted segregation index for FP1.

6.3.2 Precipitation reaction in the Taylor-Couette reactor

Precipitation model Let us consider the application of the model to the precipitation of barium sulfate in the Taylor-Couette reactor. For simplicity all the transport equations will be recalled. After the solution of the flow field, the scalar field is solved by solving the transport equations for p_1, p_2, $\langle s_\xi \rangle_3$ and $\langle s_Y \rangle_3$

$$\frac{\partial p_1}{\partial t} + \frac{\partial}{\partial x_i}(\langle u_i \rangle p_1) = \frac{\partial}{\partial x_i}\left(\Gamma_t \frac{\partial p_1}{\partial x_i}\right) + \gamma_s p_3 - \gamma p_1(1-p_1), \tag{6.64}$$

$$\frac{\partial p_2}{\partial t} + \frac{\partial}{\partial x_i}(\langle u_i \rangle p_2) = \frac{\partial}{\partial x_i}\left(\Gamma_t \frac{\partial p_2}{\partial x_i}\right) + \gamma_s p_3 - \gamma p_2(1-p_2), \tag{6.65}$$

$$\begin{aligned}\frac{\partial \langle s_\xi \rangle_3}{\partial t} + \frac{\partial}{\partial x_i}(\langle u_i \rangle \langle s_\xi \rangle_3) = & \frac{\partial}{\partial x_i}\left(\Gamma_t \frac{\partial \langle s_\xi \rangle_3}{\partial x_i}\right) - \gamma_s p_3(\langle \xi \rangle_1 + \langle \xi \rangle_2) \\ & + \gamma p_1(1-p_1)\langle \xi \rangle_1 + \gamma p_2(1-p_2)\langle \xi \rangle_2, \end{aligned} \tag{6.66}$$

$$\frac{\partial \langle s_Y \rangle_3}{\partial t} + \frac{\partial}{\partial x_i}(\langle u_i \rangle \langle s_Y \rangle_3) = \frac{\partial}{\partial x_i}\left(\Gamma_t \frac{\partial \langle s_Y \rangle_3}{\partial x_i}\right) + \frac{p_3 S(\langle c_A \rangle_3, \langle c_B \rangle_3)}{\xi_s c_{Ao}} \tag{6.67}$$

where as usual $S(\langle c_A \rangle_3, \langle c_B \rangle_3)$ is the source term for the chemical reaction, and $\langle c_A \rangle_3$ and $\langle c_B \rangle_3$ are calculated from

$$\frac{c_A}{c_{Ao}} = \xi - \xi_s Y, \qquad \frac{c_B}{c_{Bo}} = (1-\xi) - (1-\xi_s)Y, \tag{6.68}$$

using $\langle \xi \rangle_3 = \langle s_\xi \rangle_3 / p_3$ and $\langle Y \rangle_3 = \langle s_Y \rangle_3 / p_3$. We recall here that γ and γ_s are computed from Eqs. 4.84 and 4.83.

Since reaction and particle formation occur only in mode 3 the population balance has to be solved only for this mode. The population balance was solved by using the standard moments method (SMM). In the case of size-independent growth rate, the final set of equations for the first five moments is as follows

$$\begin{aligned}\frac{\partial \langle s_{m_k} \rangle_3}{\partial t} + \frac{\partial}{\partial x_i}(\langle u_i \rangle \langle s_{m_k} \rangle_3) = & \frac{\partial}{\partial x_i}\left(\Gamma_t \frac{\partial \langle s_{m_k} \rangle_3}{\partial x_i}\right) + (0)^k p_3 J(\langle c_A \rangle_3, \langle c_B \rangle_3) \\ & + kG(\langle c_A \rangle_3, \langle c_B \rangle_3)\langle s_{m_{k-1}} \rangle_3 + p_3(\overline{B_k} - \overline{D_k}), \end{aligned} \tag{6.69}$$

with $k = 0, ..., 4$, and where $J(\langle c_A \rangle_3, \langle c_B \rangle_3)$ is the nucleation rate in mode 3, $\langle s_{m_k} \rangle_3$ is the weighted k^{th} moment and $\overline{B_k}$ is

$$\overline{B_k} = \frac{\beta_0}{2}\int_0^\infty \langle n(\lambda) \rangle_3 \int_0^\infty (u^3 + \lambda^3)^{k/3} \langle n(u) \rangle_3 du d\lambda, \tag{6.70}$$

where $u^3 = L^3 - \lambda^3$, and $\overline{D_k}$ is

$$\overline{D_k} = \beta_0 \int_0^\infty \langle n(L) \rangle_3 L^k \int_0^\infty \langle n(\lambda) \rangle_3 d\lambda dL, \tag{6.71}$$

where $\langle n(L) \rangle_3$ is the local particle number density function in mode 3, and the aggregation kernel is assumed to be constant [$\beta(L, \lambda) \approx \beta_0$]. The problem is closed if $\overline{B_k}$ and $\overline{D_k}$ are expressed in terms of the moments of the CSD. As explained in [94] in the case of constant kernel, and under some simplifications $\overline{B_k}$ and $\overline{D_k}$ become:

$$\overline{B_k} = \beta_0 b_k \langle m_0 \rangle_3 \langle m_k \rangle_3, \tag{6.72}$$

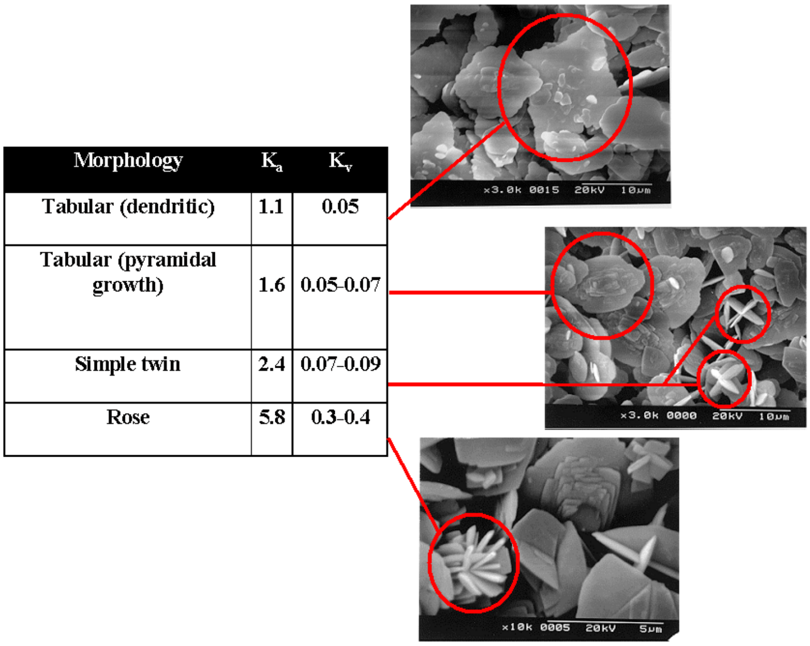

Morphology	K_a	K_v
Tabular (dendritic)	**1.1**	**0.05**
Tabular (pyramidal growth)	**1.6**	**0.05-0.07**
Simple twin	**2.4**	**0.07-0.09**
Rose	**5.8**	**0.3-0.4**

Figure 6.36: Crystal morphologies and corresponding shape factors for barium sulfate precipitation in a Taylor-Couette reactor.

$$\overline{D_k} = \beta_0 \langle m_0 \rangle_3 \langle m_k \rangle_3, \tag{6.73}$$

where $\langle m_k \rangle_3$ is the local kth moment $[\langle m_k \rangle_3 = \langle s_{m_k} \rangle_3 / p_3]$ and b_k are found by solving Eq. 6.70. Notice that $b_0 = 1/2$ and $b_3 = 1$ are derived from the exact solution of the integral in Eq. 6.70 whereas $b_1 = 2/3$, $b_2 = 5/6$ and $b_4 = 7/6$ are derived by replacing $(u^3 + \lambda^3)^{k/3}$ with its Taylor series.

The chemical source term is written as follows

$$p_3 S(\langle c_A \rangle_3, \langle c_B \rangle_3) = \frac{\rho 3 k_v \langle s_{m_2} \rangle_3}{2M} G(\langle c_A \rangle_3, \langle c_B \rangle_3). \tag{6.74}$$

where k_v is the volume shape factor that has been defined at pag. 16. As concerns nucleation and growth rates Eq. 1.11 and Eq. 1.24 were used.

In a previous work [26] the effect of operating conditions in a continuous Taylor-Couette reactor on barium sulfate morphology was investigated, and shape factors were calculated for the different morphologies observed. In Fig. 6.36 a summary of the results of this work is presented. These experimental values were used in a second study [95] to investigate the effect of this numerical parameter on the final predictions of the precipitation model, and finally an average value was used[9] ($k_v = 0.06$.)

The initial conditions used in this case are slightly different from the previous ones and are summarized below:

$$p_1 = 0, \quad p_2 = 1, \quad \langle s_\xi \rangle_3 = \langle s_{Y_2} \rangle_3 = \langle s_{m_k} \rangle_3 = 0, \tag{6.75}$$

---

[9] In this first case the crystals were considered as equidimensional objects. Thus in this case $K_v = k_v$ and $K_a = k_a$ and L_{43}=d_{43} since ϕ_c=1 (see Eqs. 1.44-1.45-1.46.)

whereas at the inlet point:

$$p_1 = 1, \quad p_2 = 0, \quad \langle s_\xi \rangle_3 = \langle s_{Y_2} \rangle_3 = \langle s_{m_k} \rangle_3 = 0. \tag{6.76}$$

Also in this case reactant A (barium chloride) is introduced through mode 1 from the injection but $\langle \xi \rangle_1 = 1$, and similarly reactant B (sodium sulfate) is already present in the reactor in mode 2 where $\langle \xi \rangle_2 = 0$. However the details concerning the computational procedure are identical to the previous one (see pag. 116.)

Effect of operating conditions The effect of the operating conditions on supersaturation (S), total particle number density (m_0) and mean crystal size (d_{43}) have been studied. The reported values of these variables are volume-averaged values over all the reactor. In the case of precipitation, the interpretation of the results is often difficult and controversial because of the many phenomena involved [i.e., mixing at various scales (macro-, meso- and micro-mixing), nucleation and growth]. Moreover, the effect of varying a single parameter can be different depending on the controlling process. For example, an increase in the intensity of mixing can reduce the volume-average intensity of segregation of the reactant favoring nucleation, or reduce the local peak of supersaturation disfavoring nucleation.

Effect of Rotation Speed. The effect of the rotational speed of the impeller on the crystal size has been analyzed by several authors, and different results and conclusions have been found. Kim and Tarbell [96] found a maximum of the mean crystal size versus the stirrer speed, while Phillips et al. [5] and Fitchett and Tarbell [97] found a monotonic increase. Differently from what is observed in the continuous apparatus [98], in the semi-batch Taylor-Couette reactor both the model and the experimental data show a decrease of the mean crystal size when plotted against the rotational speed of the internal cylinder (Fig. 6.37). This effect could be caused by enhanced macromixing, which reduces the degree of segregation of the reactants and favors nucleation. The final effect is to produce a slightly higher number of particles, but with a lower dimension.

In Fig. 6.38 a plot of the solid concentration against the speed of the internal cylinder is reported. The figure shows that the rotational speed does not significantly affect the final solid concentration. In fact, given that the experiments were sufficiently long for the reactants to completely react, this result was included only to show that the overall mass balance was satisfied. The same behavior for the final solids concentration has been found for all other parameters, except for the initial nominal supersaturation as will be explained below.

Effect of Injection Velocity. In Fig. 6.39 the calculated volume-averaged supersaturation evolutions are reported for three injection velocities. The discontinuity in the derivative of the profile shown by the plots occurs at the end of the injection period. From the figure it is clear that increasing the injection velocity results in a higher peak of supersaturation. However, the supersaturation subsequently decreases more rapidly due to crystal growth. Overall, the supersaturation is kept at a higher time-averaged value with low injection velocity and this effect causes the formation of a higher number of particles (Fig. 6.40) with a smaller dimension (Fig. 6.41) under these conditions. A comparison with the experimental data for the volume-averaged mean crystal size at the end of the reaction is reported in Fig. 6.42, showing good agreement.

Effect of reactant concentration. The time evolution of the volume-averaged supersaturation for three different initial nominal supersaturation ratios are reported in Fig. 6.43. From the figure it is clear that by increasing this ratio, the peak of the supersaturation is also increased. It has to be highlighted that for the highest initial supersaturation ratio after the peak, the reaction starts to remove the reactants, but after a while the injection of fresh reactants makes the profile rise again. This is caused by the large number of particles, created by the high supersaturation, that grow rapidly due to the enhanced growth rate, and remove the reactants. After this period the fresh reactants are almost completely segregated in different vortices in the bottom and in the top of the reactor (see Fig. 6.44), and it is necessary to wait for the end of the injection in order to have a further decrease of the concentration.

We saw earlier that during the injection period the reactor operates in a steady-state regime where the mixture fraction is slightly larger at the top of the reactor than at the bottom. Due to the nonlinear nature of the nucleation rate, at high supersaturation this small macroscale gradient is amplified in the reactant concentrations, leading to the macroscale segregation seen in Fig. 6.44. Such large-scale, reaction-induced segregation could not be predicted without resorting to CFD.

The comparison with the experimental data is reported in Fig. 6.45 for different initial nominal supersaturation ratios. Under these conditions an increase in S_o accelerates crystal growth more than nucleation, because the heterogeneous nucleation order (1.775) is smaller than the overall growth order (2.1). For higher S_o the homogeneous nucleation order (15) becomes very high and a further increase would cause more crystals of smaller size. From Fig. 6.45 it is possible to see that both model and experiments show an increase in the mean crystal size with increasing S_o. However the model over-predicts the rate of increase, because of the strong segregation in the system due to the vortices, that causes poor macromixing. This result, once again, shows the importance of an accurate knowledge of the flow field, in order to predict its effect on the final CSD.

Effect of reactant concentration ratio. The effect of the reactant concentration ratio has been studied for two different values of the initial nominal supersaturation ratio [$\log(S_o) =$ 4 and 6]. The results are reported in Fig. 6.46 and the model predictions for $\log(S_o) = 4$ are compared with experimental data. In this case the reactant concentration ratio α is the volume average of the mean mixture fraction $\langle\xi\rangle$ at the end of the injection period; in fact, it represents the final volume fraction of fluid injected into the reactor. In order to maintain a 1:1 stoichiometric ratio, decreasing α results in a higher concentration of the reactant over a shorter injection time at the same flow rate. This results in a significant increase of the local supersaturation near the injection point. Depending on the initial nominal supersaturation, this local increase can favor nucleation or growth.

At low values of the initial nominal supersaturation ratio [$\log(S_o) = 4$], the local value of the supersaturation is not high enough to induce homogeneous nucleation, and this results in a smaller number of crystals with larger dimension. However, when the initial nominal supersaturation ratio is increased to 10^6, the local value of the supersaturation leads to homogeneous nucleation and a higher number of particles with lower dimension are produced. Furthermore, a decrease in the mean crystal size is observed in the simulations for concentration ratios lower than 0.01 for $\log(S_o) = 4$, and 0.03 for $\log(S_o) = 6$. In the first case, only when the concentration ratio is lower than 0.01 is the local value of the supersaturation high enough to favor nucleation over growth. In the second case, this condition is satisfied for concentration ratios less than 0.1. The fact that the mean crystal size starts to decrease with a decreasing concentration ratio at lower values of this parameter is due to the segregation of the fresh reactants as explained above (Fig. 6.44). Only when the concentration ratio is small enough to have a short injection time, will the introduction of the reactant be faster than the growth process, so that during the injection the high local supersaturation favors nucleation.

The results show that the precipitation reaction is strongly influenced by the local value of supersaturation at high reactant concentrations. Mixing at various scales has been found to be the controlling phenomenon and in particular the vortical structure of the flow in the Taylor-Couette reactor favors the role of macromixing.

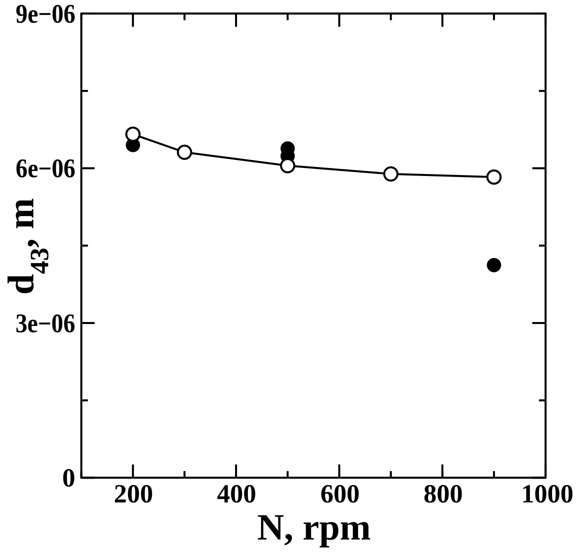

Figure 6.37: Final mean crystal size versus speed of the internal cylinder (v = 60 ml/min, $\alpha = 0.1$, $\log(S_o) = 4$). Open symbols: CFD prediction. Filled symbols: experimental data.

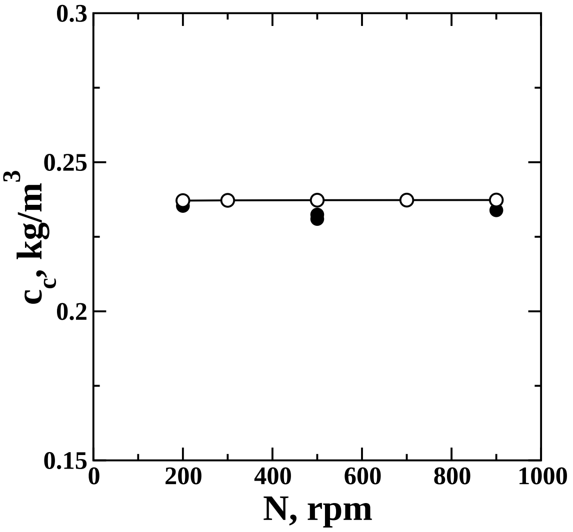

Figure 6.38: Final solid concentration versus speed of the internal cylinder (v = 60 ml/min, $\alpha = 0.1$, $\log(S_o) = 4$). Open symbols: CFD prediction. Filled symbols: experimental data.

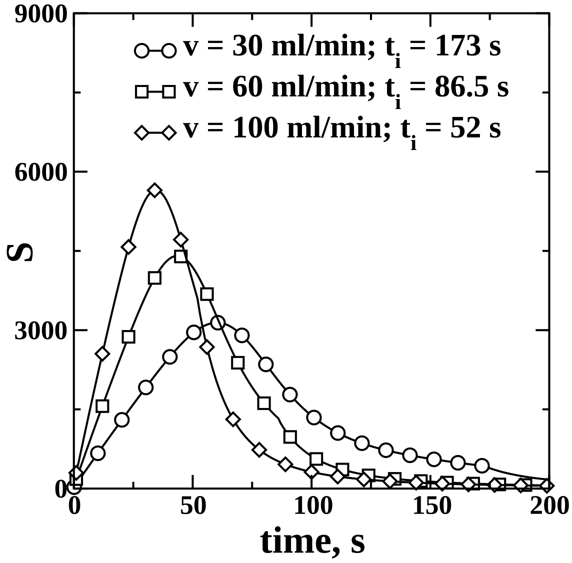

Figure 6.39: Volume-averaged supersaturation versus time for three injection velocities ($N = 500$ rpm, $\alpha = 0.1$, $\log(S_o) = 4$).

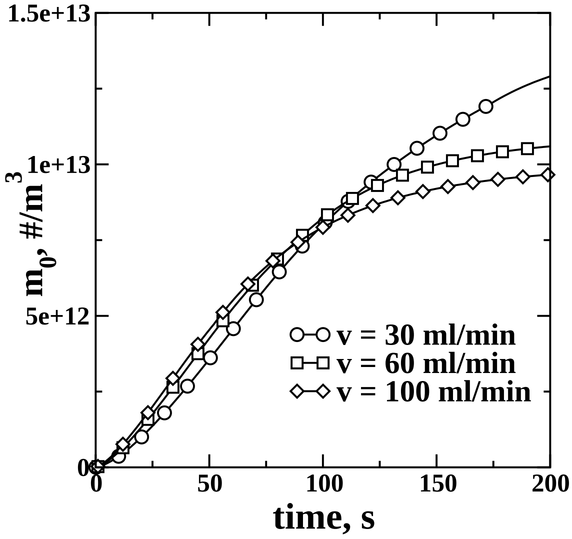

Figure 6.40: Volume-average total particle number density versus time for three injection velocities ($N = 500$ rpm, $\alpha = 0.1$, $\log(S_o) = 4$).

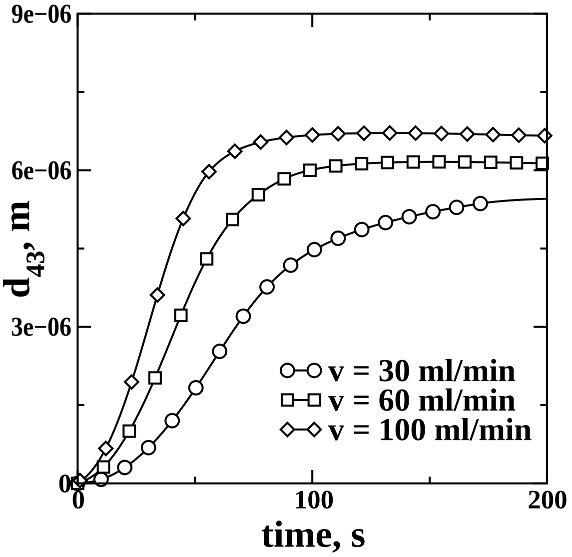

Figure 6.41: Volume-averaged mean crystal size versus time for three injection velocities ($N = 500$ rpm, $\alpha = 0.1$, $\log(S_o) = 4$).

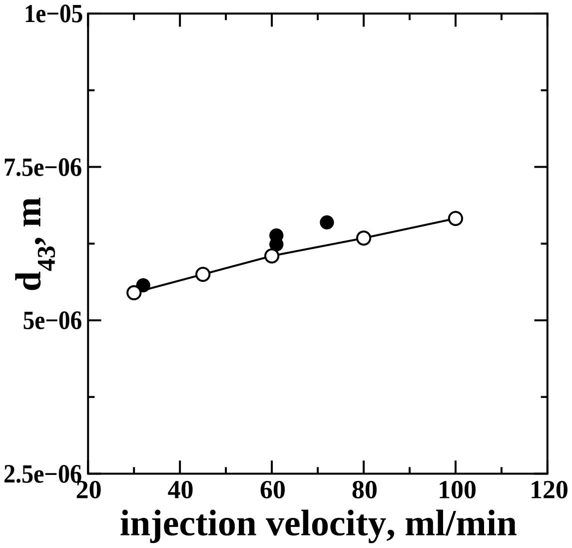

Figure 6.42: Final mean crystal size versus injection velocity ($N = 500$ rpm, $\alpha = 0.1$, $\log(S_o) = 4$). Open symbols: CFD prediction. Filled symbols: experimental data.

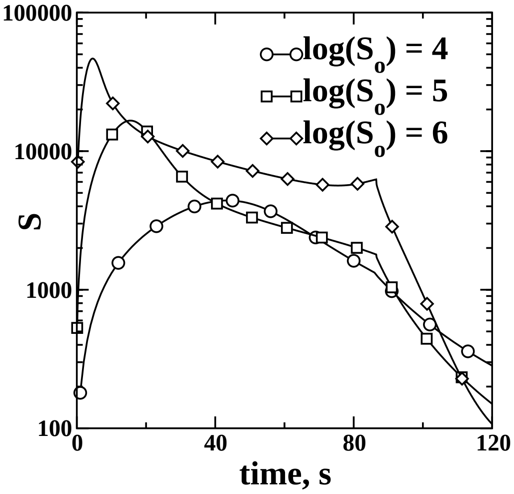

Figure 6.43: Volume-averaged supersaturation profiles versus time for three initial nominal supersaturation ratios (v = 60 ml/min, $\alpha = 0.1$, N = 500 rpm).

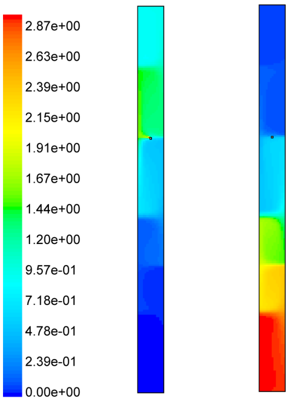

Figure 6.44: Contour plots of reactant concentrations in Environment 3 at the end of the injection period (v = 60 ml/min, $\alpha = 0.1$, N = 500 rpm, t = 86.5 sec). Left: $\langle c_A \rangle_3$, mol/m^3. Right: $\langle c_B \rangle_3$, mol/m^3.

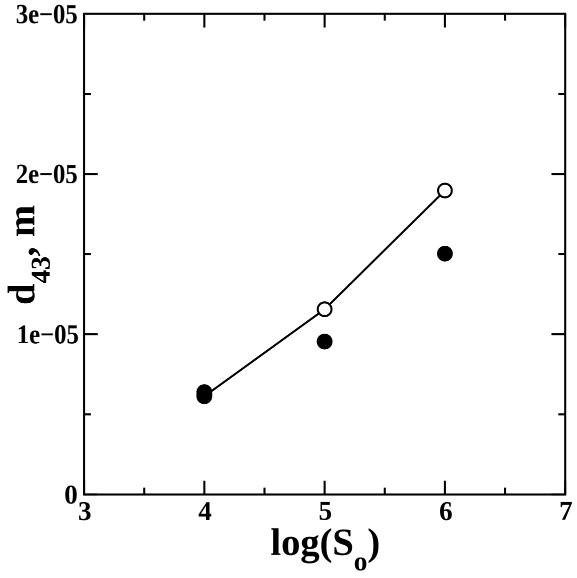

Figure 6.45: Comparison with experimental data for the final mean crystal size versus the initial nominal supersaturation ratio (v = 60 ml/min, $\alpha = 0.1$, N = 500 rpm). Open symbols: CFD prediction. Filled symbols: experimental data.

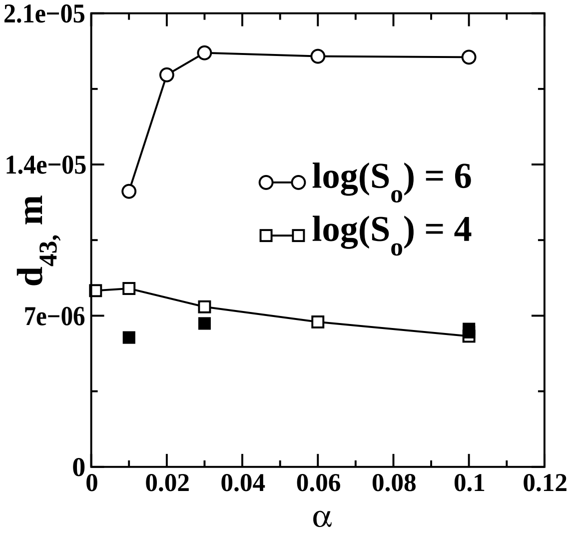

Figure 6.46: Final mean crystal size versus reactant concentration ratio for two different initial supersaturation ratios (N = 500 rpm, v = 60 ml/min). Open symbols: CFD predictions. Filled symbols: experimental data.

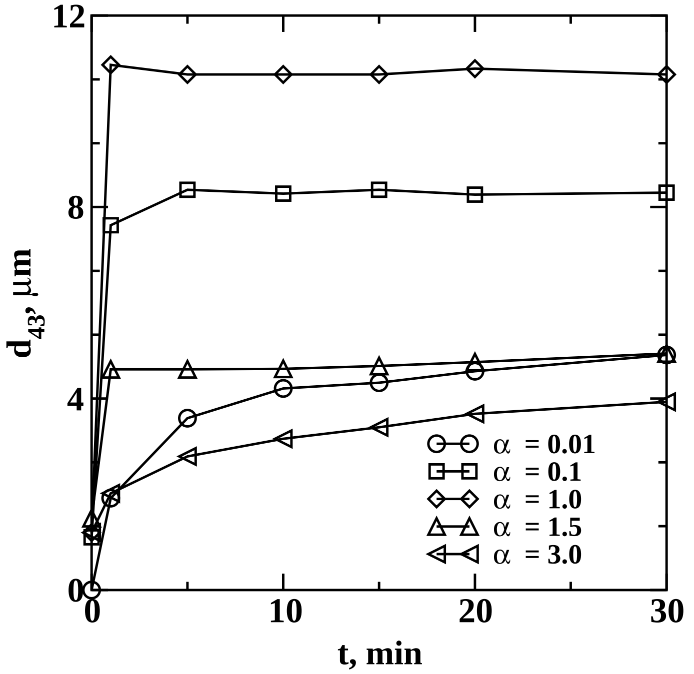

Figure 6.47: Time evolution of mean crystal size (d_{43}) in sampled suspensions as a function of the concentration ratio (α). $BaCl_2$ fed in the nozzle, c_{Ao}=34 mol/m^3. The first point represents the tubular reactor outlet.

6.3.3 Precipitation in the tubular reactor

Experimental results The effect of the concentration ratio ($\alpha = \frac{c_{Bo}}{c_{Ao}}$) at several conditions (see Tab. 5.2 at pag. 74) on CSD and crystal morphology was investigated in the tubular reactor. As a first thing the variation with time of the mean crystal size in the suspension sampled at the reactor outlet is investigated, to evidence the grade of completeness of the reaction, and get information on the amount of crystals formed. In Fig 6.47 the mean crystal size evolution versus time for several values of α in case 1 ($BaCl_2$ in the nozzle) is reported. Notice that as explained before $\alpha = 0.01$ correspond to a final reactant concentration ratio after complete mixing without reaction equal to 1 (i.e., reaction stoichiometry), whereas for greater values of α the reactant fed in the annular region is in excess. As the concentration of the reactant fed in the nozzle is kept constant for each series, increasing α the local reactant concentrations increase but the final solid concentration, after complete reaction, is constant. At low values of α, nucleation and growth are quite slow; after sampling, crystals continue to growth and well formed crystals are produced (see Fig. 6.48a). Increasing α up to 1.0, growth becomes diffusion-controlled, and in fact dendritic crystals are obtained (see Figs. 6.48b and 6.48c). Notice that in this condition crystals are stable after about 1 minute, meaning with this that the precipitate does not show any further growth. Moreover when α is in the range between 0.01-1.0 an increase in this parameter causes an increase in the final mean crystal size after 30 minutes, whereas for values of α greater than 1 the mean crystal size after 30 minutes decreases. This is due to the fact that, given the same final solid concentration after complete reaction, for low concentrations an increase in α favors growth in respect with nucleation, whereas at higher concentrations nucleation moves into the homogeneous region, and an increase in α has an opposite influence. For the highest value (α=3) the mean crystal size is the smallest, but crystals are not stable and the mean crystal size is slowly increasing. Since in this condition the reaction is very fast and, due to homogeneous nucleation, the total particle number density is very high, this further increase can be attributed to aggregation. Crystal morphology is sensibly different (see Fig. 6.48d) and seems to be originated by aggregation and subsequent recrystallization. In Fig. 6.49 the CSDs for three values of α at the reactor outlet and after 30 minutes are reported. As it possible to see for α=0.1 and 1.5 CSDs are monomodal both at the reactor outlet and after 30 minutes, whereas for α=3 the CSD presents more peaks. In this last case both CSD and crystal morphology indicate aggregation.

In Fig. 6.50 mean crystal size evolution with time for case 2 (Na_2SO_4 in the nozzle) is reported. The results present some similarities but also some differences with the previous case. For low α values, reaction is not complete but in this case the maximum of the mean crystal size is not anymore for $\alpha = 1$ but for $\alpha = 0.01$. This result shows that the transition to homogeneous nucleation occurs at lower concentrations and that a modification in the nucleation mechanism occurs. Increasing α the mean crystal size decreases and then increases again, but small differences are detected for higher values of α. However except for α=0.01 in all the other cases the mean crystal size is more stable after sampling. In Fig. 6.51 the CSDs for different α are reported and as it is possible to see CSDs at reactor outlet and after 30 minutes are more similar. Moreover, generally in case 2 the final mean crystal size after 30 minutes was always lower than in case 1. This can be explained in terms of ion adsorption.

Suspended particles interact depending on the balance between attractive and repulsive forces. An useful indication on the dispersion stability is given by the value of the point

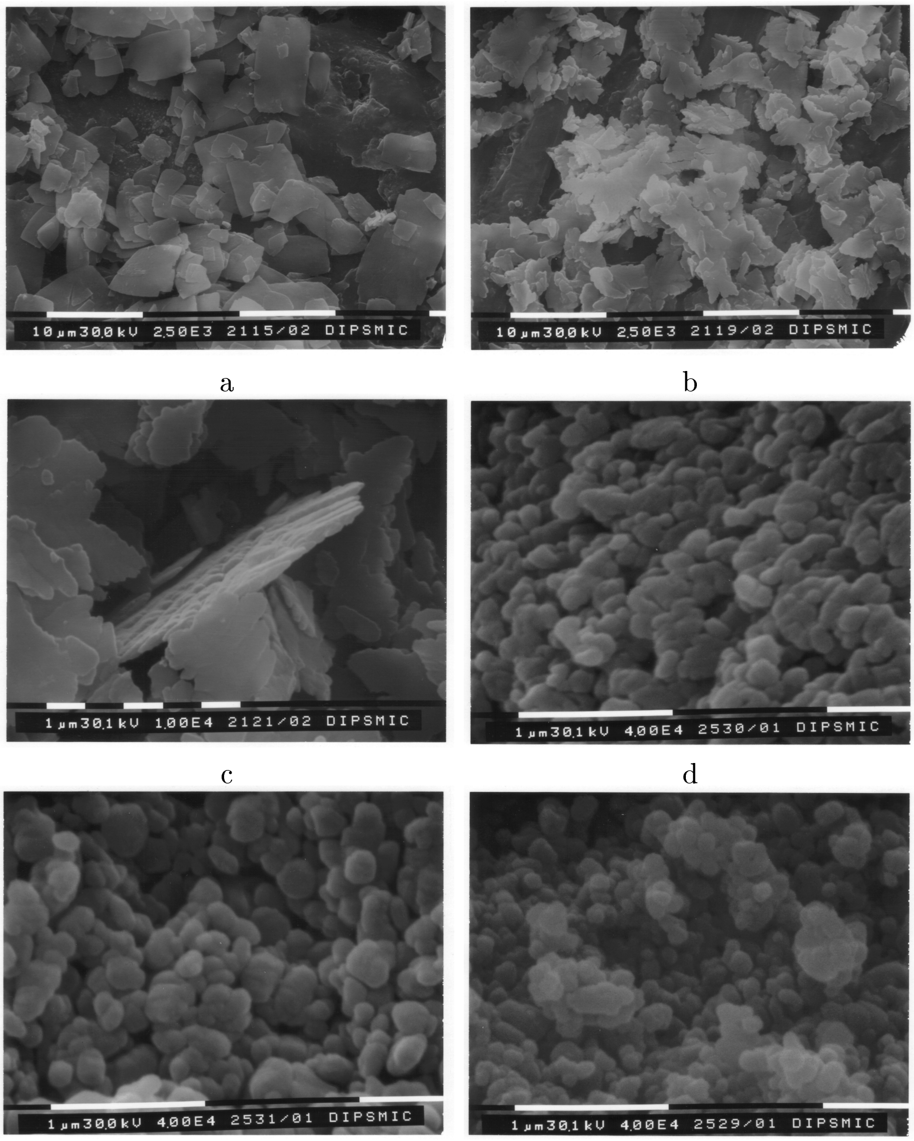

a b

c d

e f

Figure 6.48: Crystal morphologies: (a) tabular crystals ($BaCl_2$ in the jet $c_{Ao} = 34$ mol/m^3 $\alpha = 0.1$); (b) dendritic crystals ($BaCl_2$ in the jet $c_{Ao} = 34$ mol/m^3 $\alpha = 1.0$); (c) particular of a dendritic crystal (same condition of b); (d) round-shaped crystals ($BaCl_2$ in the jet $c_{Ao} = 34$ mol/m^3 $\alpha = 3.0$); (e) round-shaped crystals (Na_2SO_4 in the jet $c_{Ao} = 34$ mol/m^3 and $\alpha = 3.0$); (f) round-shaped crystals ($BaCl_2$ in the jet $c_{Ao} = 341$ mol/m^3 and $\alpha = 0.1$).

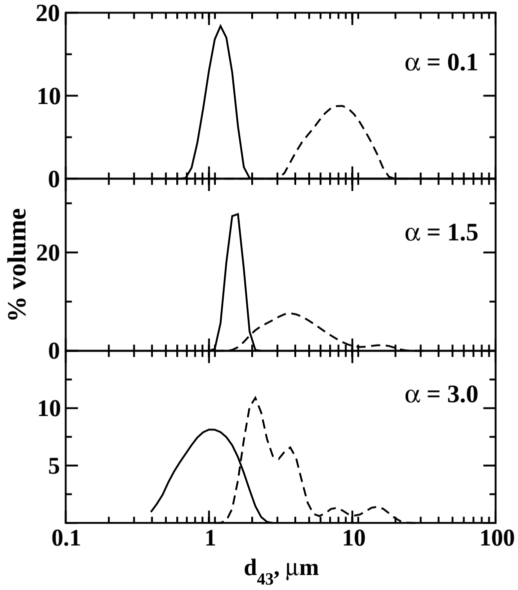

Figure 6.49: CSDs for several values of α in condition 1 at the reactor outlet (solid lines) and after 30 minutes of gentle stirring (dashed lines).

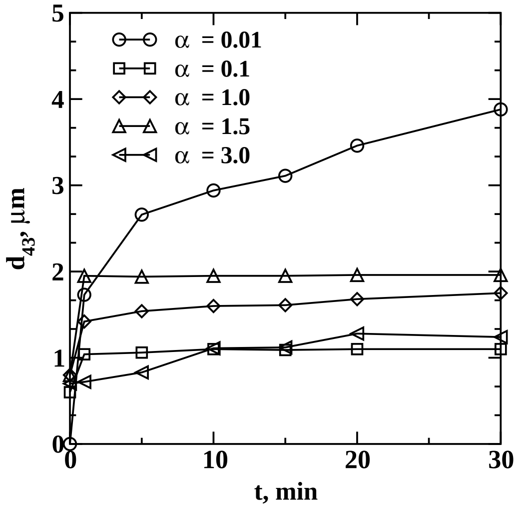

Figure 6.50: Time evolution of mean crystal size (d_{43}) in sampled suspensions as a function of the concentration ratio (α). Na_2SO_4 fed in the nozzle, c_{Ao}=34 mol/m^3. The first point represents the tubular reactor outlet.

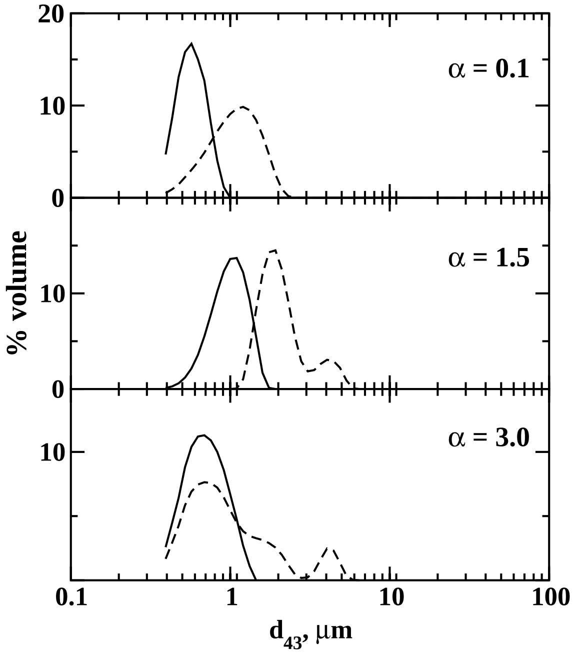

Figure 6.51: CSDs for several values of α in condition 2 at the reactor outlet (solid lines) and after 30 minutes of gentle stirring (dashed lines).

of zero charge (PZC), that is the ion concentration at which the surface charge is zero. When the surface charge is null, crystals have an higher tendency to aggregate and the system in unstable. For barium sulfate this value, in terms of pBa is 6.7, and since

$$pk_s = pBa + pSO_4 = 10, \tag{6.77}$$

it means that this situation is established when there is an excess of sulfate ion (case 1). It can be inferred that in this case, in the early stages of nucleation, due to high local values of total particle number density and strong instability, nuclei have a high tendency to aggregate resulting in a reduced nucleation rate. In case 2, nuclei are more stable and then once formed grow producing crystals; Crystal morphology in this case for α=3 is reported in Fig. 6.48e. As it is possible to see the structure is very similar to the one obtained in case 1 with the same α. However aggregates seem to be constituted by less particles as a proof of the reduced tendency to aggregate.

Results of experiments at high concentration (case 3) are reported in Fig. 6.52. As it is possible to see, in this case except for $\alpha = 0.01$, reaction was always complete at the reactor outlet. After sampling crystals were found to be quite stable although some small changes in the CSDs were detected. As it is possible to see in Fig. 6.53 for all values of α the CSDs maintain the same shape, although generally the first peak decreases and the second one (or ones) increases. This is a proof of the high tendency of the precipitate to aggregate also for longer time (30 min). It should be highlighted that in this case also at the reactor outlet CSDs had more than one peak, meaning that aggregation started to occur inside the reactor although the short residence time.

In Fig. 6.48f the crystal morphology for α=0.1 is shown. As it is possible to see crystals are spherical aggregates formed by spherical monomers. The formation of these round-shaped crystals has been obtained in the past only by using additives. Results from

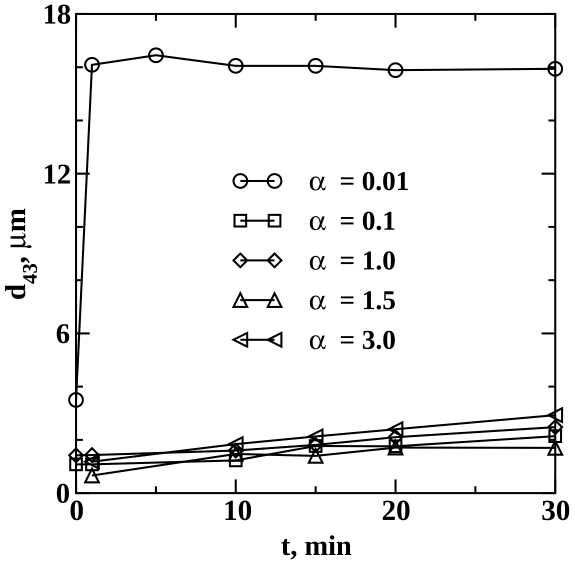

Figure 6.52: Time evolution of mean crystal size (d_{43}) in sampled suspensions as a function of the concentration ratio (α). $BaCl_2$ fed in the nozzle, c_{Ao}=341 mol/m^3. The first point represents the tubular reactor outlet.

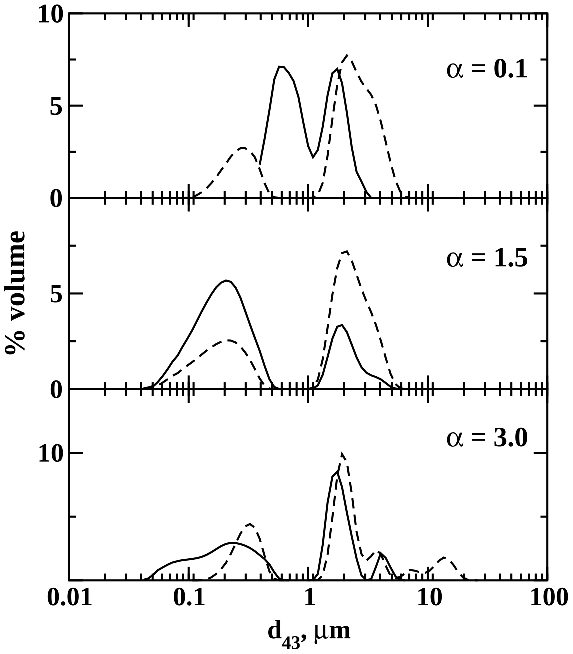

Figure 6.53: CSDs for several values of α in condition 3 at the reactor outlet (solid lines) and after 30 minutes of gentle stirring (dashed lines).

these studies are very interesting and can be useful in understanding the role of ion excess on crystal growth. For example, Archibald et al. [99] studied the effect of additives on barium sulfate morphology finding that the presence of an additive can favor or unfavor the growth of some specific crystal faces. Besides stable faces they found also some rounded faces composed of a variety of facets presenting corrugation sizes approaching the ionic dimensions. In their study they inferred that the degree of supersaturation and the ionic strength of the solution play an important role in determining the presence of charged domains on crystal surface that may help in explaining the rapid growth of this rounded faces. Yokota et al. [100] investigated the formation and the structure of round-shaped crystals of barium sulfate in the presence of additives. Their main conclusion is that additive ions may adsorb onto particular faces of a crystal and retard the growth of these faces whilst there is no influence on other surfaces.

Comparison with the model Simulations were carried out by using a commercial CFD code (Fluent 5.2). The real 3D geometry was modeled under the hypothesis of axialsymmetry (see Fig. 6.54.) Different grids were tested in order to find a grid-independent solution, and the final grid was with 131 nodes in the axial direction and 35 nodes in the radial direction. The standard $k-\varepsilon$ model with standard wall functions was used. The micromixing model and the population balance were introduced via user- defined functions.

The complete model is constituted by a set of nine transport equations, in which the convection and the turbulent diffusion are modeled by the CFD code, and a source term must be specified for each scalar[10]. After solving the flow field, once mean velocities and turbulence quantities were known, mixing properties were determined by solving the transport equations for p_1, p_2 and $\langle s_\xi \rangle_3$ according to Eqs. 4.74-4.75-4.76. Then reaction and particle formation were solved for mode 3, by solving the transport equations for the reaction progress variable $[\langle s_Y \rangle_3]$, and for the moments of the CSD $[\langle s_{m_k} \rangle_3$ with $k = 0, ..., 4]$ according to Eqs 6.55 and 6.69.

Two inlet streams were defined into the computational domain. For the first one (inner stream) p_1=1 and p_2=0, whereas for the second one (annular region) p_1=0 and p_2=1. All the other variables were set equal to zero in the two inlet streams. For the flow field default under-relaxation factors were used, whereas for user-defined scalars variable factors, depending on the stiffness of the problem, were used. Generally for low reactant concentrations unitary factors were used, whereas increasing concentrations under-relaxation factors were reduced down to 0.6.

In Fig. 6.54 plots of p_1 (top) and p_2 (bottom) are shown; p_1=1 in one inlet stream and p_2=1 in the other, and as soon as the two streams mix together modes 1 and 2 start to disappear, and then p_1 and p_2 go to zero, whereas p_3 becomes equal to one. Micromixing influences the reaction in zones of the computational domain where p_3 is lower than unity, resulting in local concentrations different from weighted concentrations. The mixture fraction variance is greater than zero when p_1 or p_2 or p_3 are not equal to unity, and it is generated by mean local gradients, (i.e., mixing zone between the two streams), and dissipated by molecular mixing, whose rate is proportional to ε/k and to a constant ($C_\phi = 1$, see Eqs. 6.60 and 6.59.)

Simulations were carried out by using different kinetic expressions in order to compare model predictions with experimental data. Different shape factors were used; for

---

[10] for details see pag. 98.

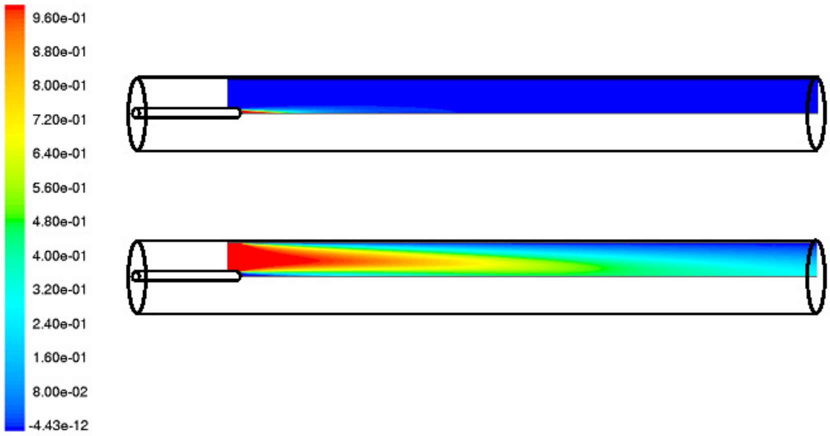

Figure 6.54: Contour plot of p_1 (top) and p_2 (bottom) near the injection point.

simulations at low concentration (experimental conditions 1 and 2) an average value was used ($k_v = 5, k_a = 30,\ \phi_c = 3$) whereas at high concentrations (experimental condition 3) crystals were considered as spheres ($k_v = \pi/6, k_a = \pi,\ \phi_c = 1$).

In the first part of the work kinetic expressions were chosen as follows: Eq. 1.11 for nucleation rate and Eq. 1.18 for growth rate. By using Eq. 1.18 the for growth rate the mass transfer coefficient (k_d) should be evaluated by using Eq. 1.23 leading to a size-dependent growth rate. However this is not possible since the standard moment method (SMM) is used to solve the population balance and thus k_d has to be considered as a pseudo-constant parameter. In a previous work [10] the effect of this parameter on model predictions is discussed. Eventually it was found a best-fit value $k_d = 10^{-6}$ (m/s)/(mol/m^3), and hereinafter all results refer to this specific value.

In Fig. 6.55 model predictions at the reactor outlet (averaged value along the radial direction) are presented. In the top of the figure the mean crystal size predicted by the model is compared with experimental data; as mentioned before the model is not able to give different predictions for condition 1 and 2. However both experimental data and model predictions show a shallow maximum for α=1.5.

When using kinetic expressions with activity coefficients (Eq. 1.17 for nucleation rate and Eq. 1.19 for growth rate,) the model is able to give different predictions for conditions 1 and 2. In Fig. 6.56 the comparison between experimental data and model predictions, at the reactor outlet and after 30 minutes is reported, for condition 1 and 2. As it is possible to see, in both conditions the agreement is not satisfactory. In fact, introduction of activity coefficient does not improve the quality of prediction in terms of the ion excess effect. However, the use of activity coefficients seems to be questionable, since this kind of treatment is usually used for determining equilibrium conditions and not for kinetic expressions that are expressed in terms of concentrations. For these reasons hereinafter kinetic expressions without activity coefficients are used.

In the bottom of Fig 6.55 the total particle number density is presented. For this variable experimental data at the reactor outlet are not available, but the total number density of crystal formed when the reaction is complete at t=30 min, can be derived from the CSDs measured. In fact, knowledge of the CSD and the final solid concentration suffice in determining the final total particle number density. This experimental data can be compared with model predictions by extending the precipitation model also to the second part of the experiment. Assuming that mixing is important only in the first part, by using a simple well-mixed approach, it is possible to model the reaction course until it is complete.

In Fig. 6.57 results from case 1 and 2 are compared with model predictions. As it is possible to observe, experimental data are very dispersed. This is due to the fact that this property is not directly measured but is derived from the CSD, and any uncertainty is amplified by the third power; in addition very small particles are not measured by the particle size analyzer. Also for this property a big difference between case 1 and 2 was observed, and model predictions are closer to case 2. The simulation results confirm that at low values of α notably the reaction is not complete, but also the nucleation step in ongoing (compare m_0 at α=0.01 in Figs. 6.55 and 6.57).

Moreover, model predictions can be compared with experimental mean crystal size obtained at different instants in the second part of the experiment. This comparison is very interesting since given a fixed concentration of the limiting reactant, and thus of the maximum final solid concentration, until reaction is not complete particles might have similar sizes and assume different sizes only when reaction proceeds. The comparison is reported in Fig. 6.58. As mentioned before the mean crystal size in case 2 is always lower than in case 1 and model predictions stand between the two series of experimental data, but are closer to case 2.

The results presented in Figs. 6.57 and 6.58 clearly show that the kinetic expressions used in this work are able to give good agreement in terms of the order of magnitude, but however there still exists a lack of information concerning this non-symmetric effect of the ion excess. Moreover, comparison of model predictions with and without the micromixing model showed that in these operating conditions micromixing has a small effect, and then macro- and meso- mixing play the major role in determining the final CSD.

In Fig. 6.59 model predictions at the reactor outlet are compared with experimental data in case 3. In the top the mean crystal size is compared with the model with and without aggregation. In this case only aggregation with constant kernel is considered (Eq. 1.27). Comparison shows that in these operating conditions if aggregation is neglected the mean crystal size is sensibly underestimated, for α greater than 0.1. It is useful to compare the mean crystal size predicted by the model without aggregation and the CSDs presented in Fig. 6.53. From this analysis it is possible to observe that the model is able to predict the size of the monomers, but only including aggregation the model is able to predict the size of the agglomerates. However the mean crystal size of agglomerates is still higher than model predictions. This could be caused by the fact that turbulent aggregation is not considered. In fact, it has been shown that also for particles smaller than the Kolmogorov scale turbulent aggregation might be important. Evaluation of the Pe number (see Eq. 1.33) showed that when L_{43} falls in the range between 10^{-7} m and 10^{-6} m Pe is approximately included in the range 0.001-100, meaning that both contributions (Brownian and turbulent) should be taken into account. However this can be done only if a more accurate approach for the population balance is used.

In the bottom of Fig. 6.59 the total particle number density is reported. Model predictions without aggregation, show an increase of m_0 increasing concentration, whereas including aggregation the final m_0 is reduced by particle-particle interactions. Also in this case the total particle number density derived from experimental CSD for t=30 min is compared with model predictions with and without aggregation (see Fig. 6.60); again nucleation is still ongoing at the reactor outlet for α=0.01 (compare Figs. 6.59 and 6.60). Although the dispersion of the experimental data, it is interesting to notice that the effect of aggregation is to reduce m_0 resulting in a better agreement.

Differently from cases 1 and 2, in these operating conditions also micromixing is very important; in fact, due to high reactant concentrations, precipitation is very fast and is confined in a small region near the injection where p_3 is lower than one. As a matter of fact, in case 3 neglecting micromixing causes an error of 30-50 % on the mean crystal size and of 150-200 % on the total particle number density.

As a conclusion it is possible to say that experimental results show that ion excess has a strong influence on the final CSD and it can be explained in terms of the preferential absorption of the ion in excess, whereas the role of activity coefficients seem to be questionable [10]. This finding is in agreement with other works [7, 4], and it shows the need of a systematic kinetic study on the effect of ion excess on nucleation and growth rate, in a wider range of concentration.

Moreover it has been shown that increasing concentration, aggregation and simultaneous growth from solution take place. This causes the formation of very stable aggregates that can be defined as agglomerates. Comparison with model predictions show in general good agreement. The role of the micromixing model has been shown to be critical especially for higher concentrations.

Moreover in the case of high aggregation rate also turbulent aggregation should be taken into account. This involves the use of non-constant kernels that can be handled by using more sophisticated population balance treatments (i.e., DPB or QMOM).

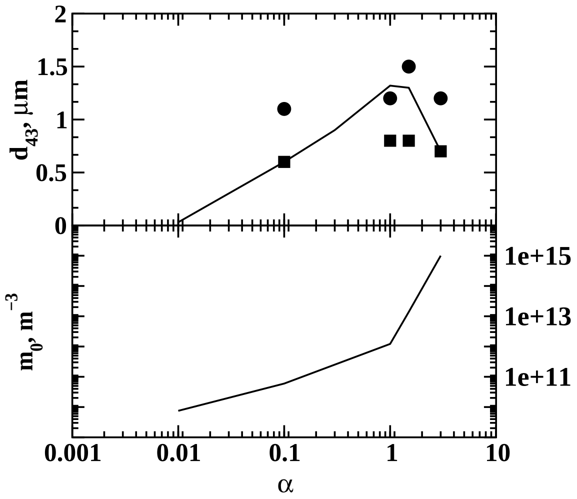

Figure 6.55: Top: mean crystal size versus α at the reactor outlet; bottom: total particle number density versus α at the reactor outlet; circles: experimental data in condition 1; squares: experimental data in condition 2; solid line: model predictions.

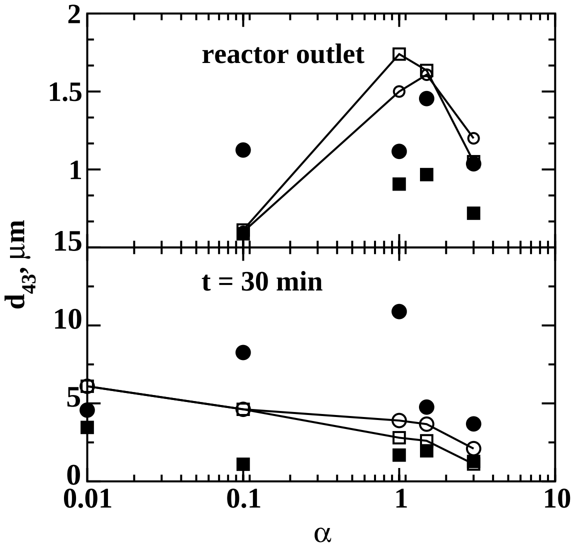

Figure 6.56: Top: mean crystal size versus α at reactor outlet; bottom: mean crystal size versus α after 30 minutes; filled circles: experimental data in condition 1; filled squares: experimental data in condition 2; open circles: model predictions with activity coefficient in condition 1; open squares: model predictions with activity coefficient in condition 2.

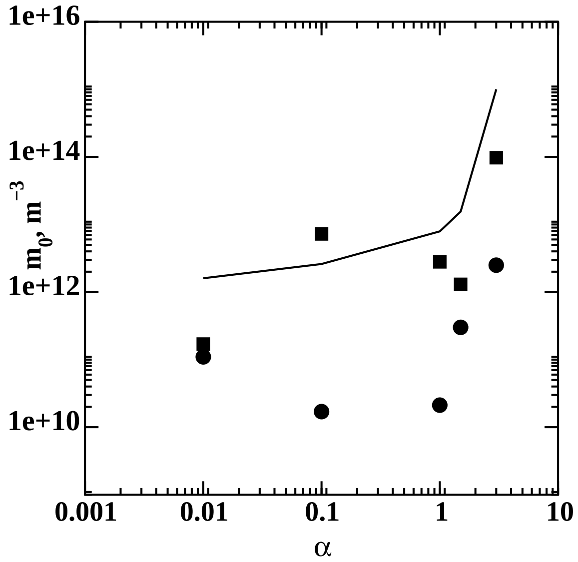

Figure 6.57: Total particle number density versus α for t = 30 min (complete reaction); filled symbols experimental data in condition 1 (circle) and in condition 2 (square); solid line: model predictions.

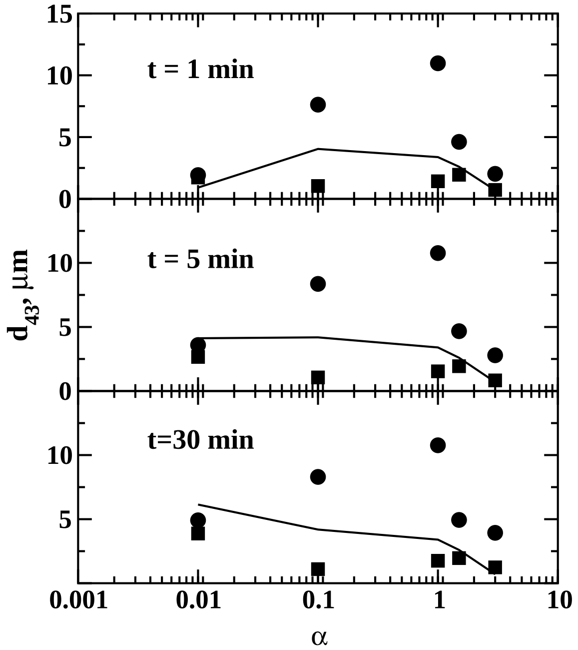

Figure 6.58: Mean crystal size versus α at different instants; filled symbols experimental data in condition 1 (circle) and in condition 2 (square); solid line: model predictions.

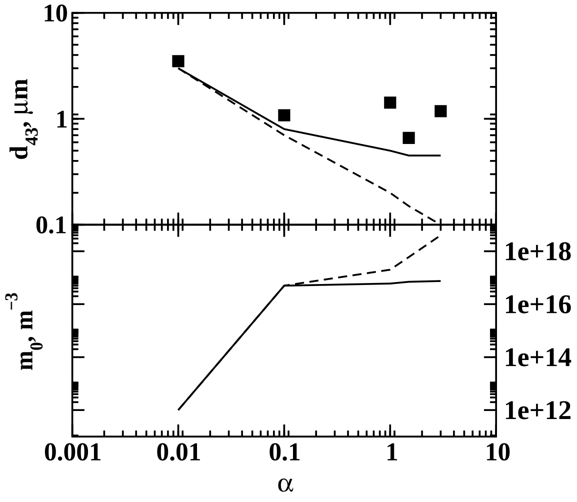

Figure 6.59: Top: mean crystal size versus α; bottom: total number density versus α; squares: experimental data in condition 3; solid line: model predictions; dashed line: model predictions neglecting aggregation.

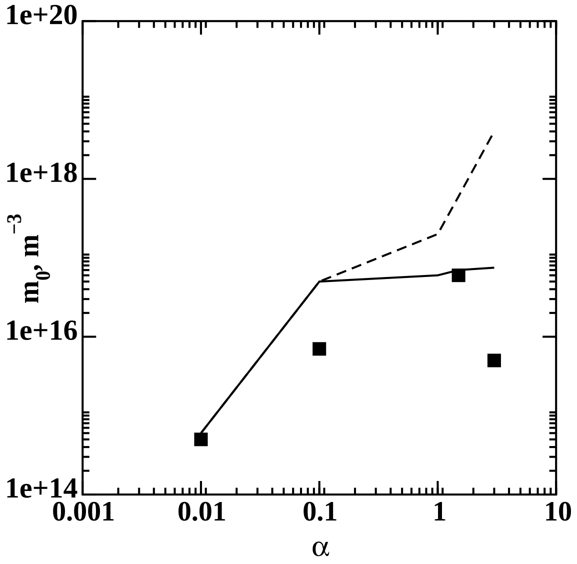

Figure 6.60: Total particle number density versus α for t = 30 min (complete reaction); square: number density derived from experimental data in condition 3; solid line: model predictions; dashed line: model predictions neglecting aggregation.

6.4 Comparison with the full PDF model

Precipitation in the tubular reactor in conditions 1 and 2 has been modeled also with the full PDF model and results were compared to those presented in the previous section. Also in this case the flow field was modeled by using the $k-\varepsilon$ model [37] in FLUENT (v. 5.2) and standard wall functions were used for the wall boundary layer. The grid for the flow field simulation was 131 nodes in the axial direction and 35 nodes in the radial direction. This grid included the annular region before the injection zone (x_o=168 mm with 20 nodes) in order to correctly predict the velocity profile in the inlet zone. This region was not considered in the full PDF simulation because no reaction occurs. Thus the final grid for the full PDF simulation had 111 nodes in the axial and 35 nodes in the radial direction.

Concerning the full PDF code, it was initialized by reading the axial and radial coordinates used in FLUENT and the steady-state solution of the flow field, including mean velocities (u_x and u_y), k, ε, mean pressure, and fluid density. A number of particles equal to $n_p n_{cells}$ where n_p=100, were positioned in the computational domain and the particle's flow properties were fixed by linear interpolation depending on its location. Particles were initialized at the inlet and were moved according to the velocity vector and the turbulent diffusivity assigned to them. Then particles interact with each other due to micro-mixing where the local mean values are derived by taking the ensemble average of scalar in each cell. (For details see [102].) The changes in scalar composition due to chemical reaction, nucleation and crystal growth, are calculated for each particle by direct integration using a routine based on a fourth-order Runge-Kutta method. Notice that kinetic expressions, shape factors are identical to those used in the finite-mode PDF simulation (see pag. 138.)

In Figs. 6.61 and 6.62 reactant concentrations (c_A, c_B) obtained with the full PDF code are reported. As it is possible to see, reactant A is fed in the small tube whereas reactant B is fed in the annular region. Due to turbulent diffusion, reactants mix together and react. Reactant B is in strong excess, and thus its concentration remains almost constant, whereas reactant A disappears, first because of mixing and later because of chemical reaction. The plot of nucleation rate (see Fig. 6.63) shows a peak near the injection point, which is due to very high supersaturation in this region. The nucleation rate reaches very high values in this region, and then decreases rapidly. The plot of the mean crystal size (L_{43}) is shown in Fig. 6.64. As it is possible to observe, the mean crystal size increases, until the final value is reached. It has to be highlighted that the wavelike fluctuations in the scalar fields are caused by statistical errors which can be improved by using more notional particles per cell or by averaging over several time steps.

In order to compare results provided by different models that are based on different methods, it is useful to compare mixture fraction and intensity of segregation profiles in different sections of the reactor. The mixture fraction is a non-reacting scalar and thus its mean value [$\langle\xi\rangle$] and its variance [$\langle\xi'^2\rangle$] are affected only by convection and turbulent diffusion. The intensity of segregation I_s is defined as follows:

$$I_s = \frac{\langle\xi'^2\rangle}{\langle\xi\rangle(1-\langle\xi\rangle)} \tag{6.78}$$

and is an index of the degree of mixing, in fact it is equal to one when the system is perfectly segregated and equal to zero when the system is perfectly micromixed. In Figs. 6.65-6.67 the mean mixture fraction and the intensity of segregation versus the radial direction at several axial positions [$(x-x_o)/D$] are reported. Comparison is made between time-averaged full PDF model predictions and FM-PDF model predictions, and as it is possible to observe predictions are quite similar.

Concerning the reacting scalars, contour plots of mean reactant concentrations, nucleation rate and mean crystal size look similar but differences were detected. For example, the FM-PDF model seems to under predict the nucleation rate (as compared to the full PDF results) and thus the final particle number density. The value of the total number density is extremely sensitive to numerics because of the strong non-linearity of the nucleation rate. However, as mentioned before, by testing different grids the solution was shown to be grid independent. Likewise, by using different discretization schemes, the approach used was shown to be adequate to handle the stiffness of the problem. In Fig. 6.68 the total particle number density along the reactor axis is reported for c_{Ao}=34.101 mol/m^3 and α=1. The peak of m_0 after the injection zone predicted by all models is initially very high, but decreases sharply. The comparison of the mean crystal sizes (see Fig. 6.69) highlights that without any closure this property is sensibly underestimated. Notice that full PDF predictions presented in the last two figures are time-averaged values.

In Fig. 6.70 model predictions for the three models are compared with experimental data, and as it is possible to see, overall agreement is quite good, but in general for these operating conditions the effect of micromixing is small, as already explained in the previous section. At higher concentrations the effect of micromixing is greater, but aggregation begins to play an important role and then all models definitively under predict the mean crystal size. The comparison of full and finite-mode PDF predictions at higher concentrations (i.e., conditions 3) will be possible only using a more accurate model for the population balance (i.e., Quadrature Method of Moment.)

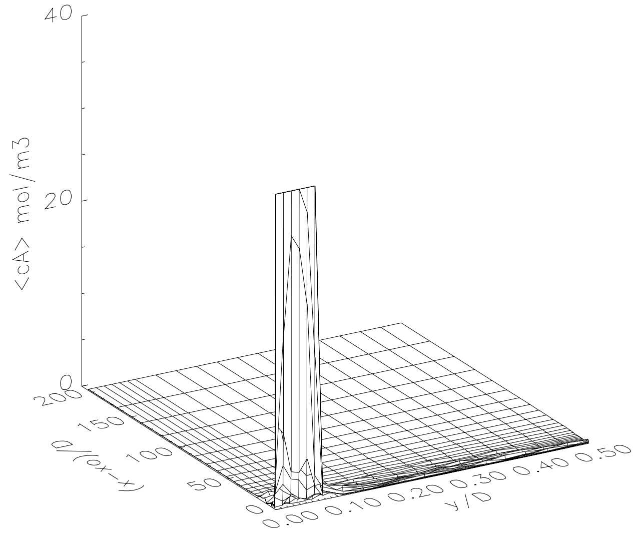

Figure 6.61: Full PDF prediction of concentration of reactant A (c_{Ao}=34.101 mol/m^3, α=1)

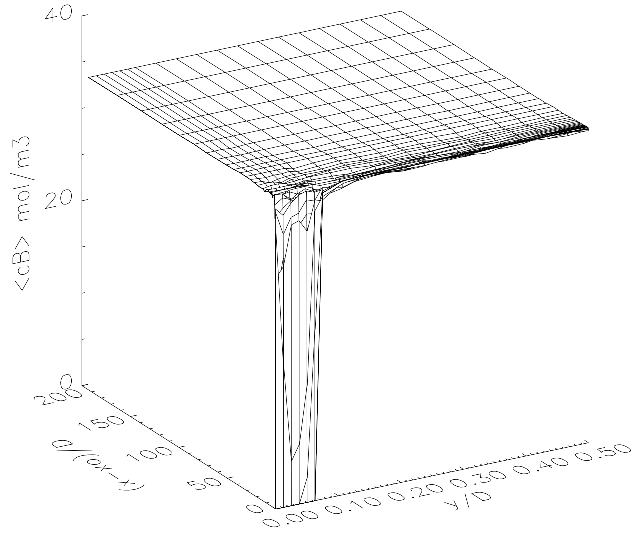

Figure 6.62: Full PDF prediction of concentration of reactant B (c_{Ao}=34.101 mol/m^3, α=1)

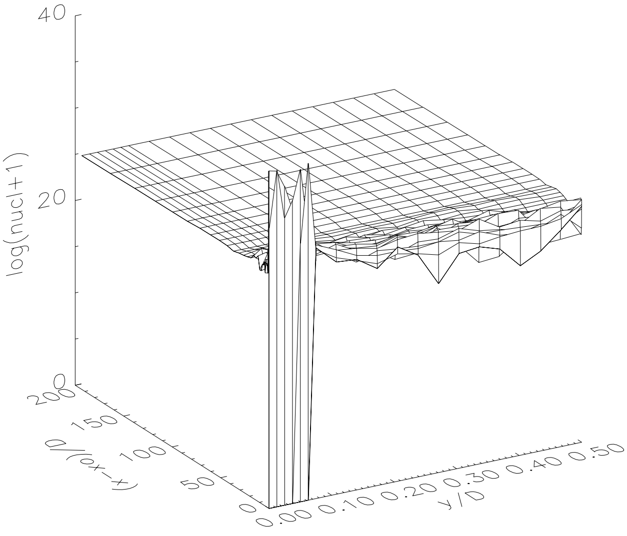

Figure 6.63: Full PDF prediction of nucleation rate (c_{Ao}=34.101 mol/m^3, α=1)

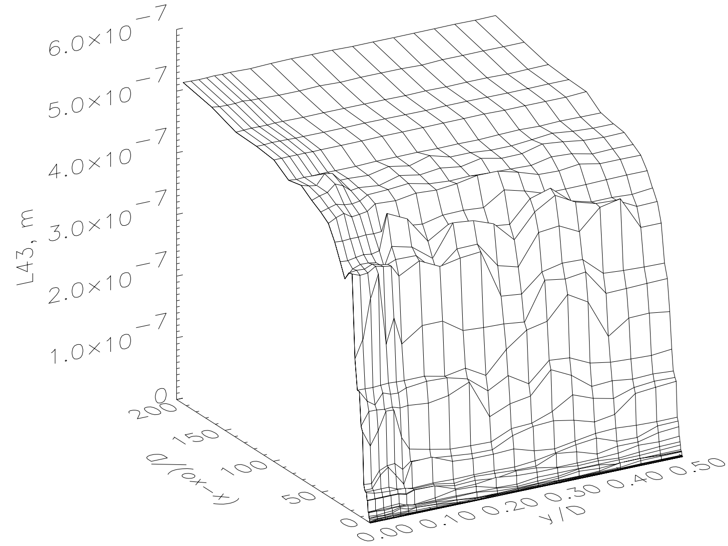

Figure 6.64: Full PDF prediction of mean crystal size (c_{Ao}=34.101 mol/m^3, α=1)

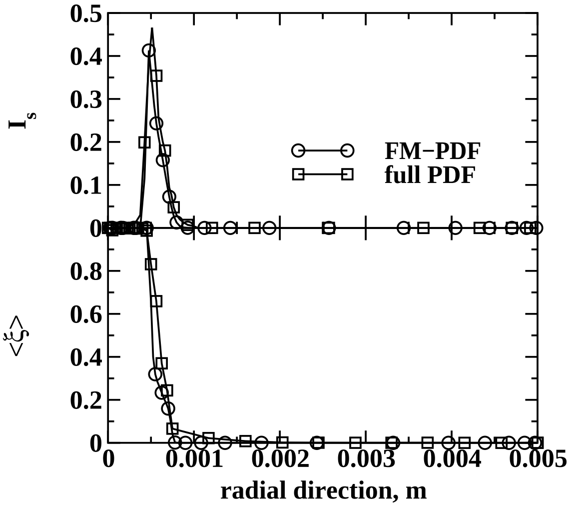

Figure 6.65: Comparison between the two PDF approaches for the mean mixture fraction $\langle \xi \rangle$ and the intensity of segregation I_s at $(x - x_o)/D$=0.0

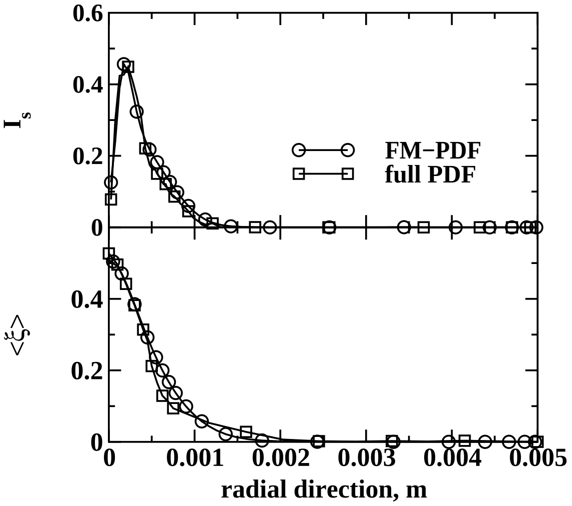

Figure 6.66: Comparison between the two PDF approaches for the mean mixture fraction $\langle \xi \rangle$ and the intensity of segregation I_s at $(x - x_o)/D$=1.0

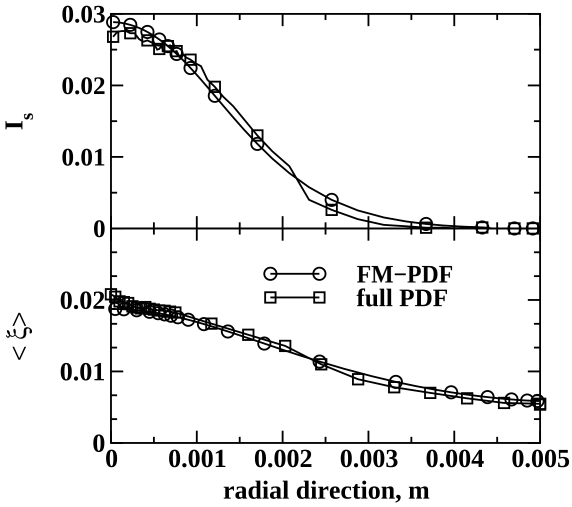

Figure 6.67: Comparison between the two PDF approaches for the mean mixture fraction $\langle \xi \rangle$ and the intensity of segregation I_s at $(x - x_o)/D$=10.0

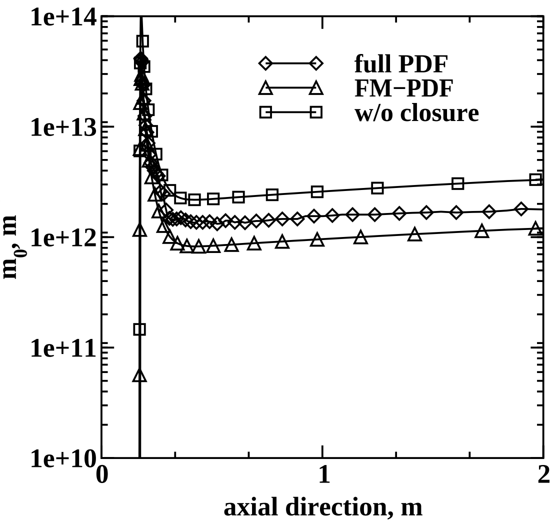

Figure 6.68: Comparison between model predictions for total number density along the centerline (c_{Ao}=34.101 mol/m^3, α=1)

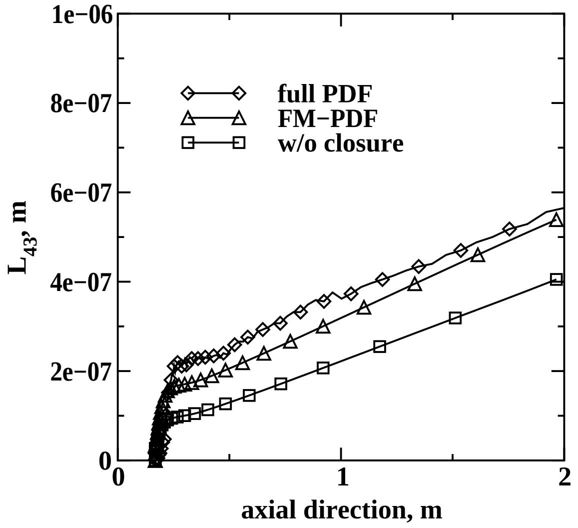

Figure 6.69: Comparison between model predictions for mean crystal size along the centerline (c_{Ao}=34.101 mol/m^3, α=1)

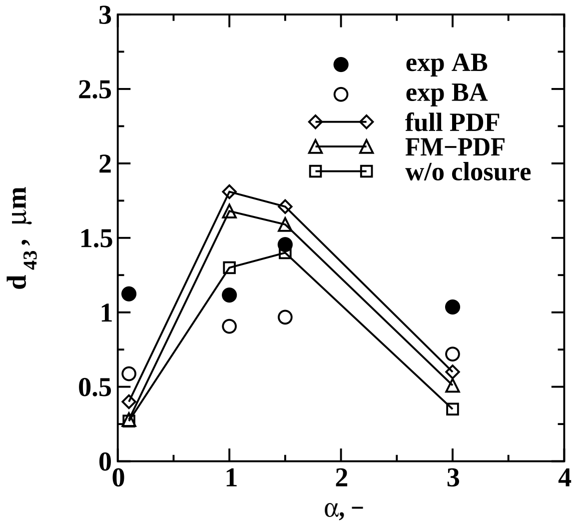

Figure 6.70: Comparison between model predictions and experimental mean crystal size (c_{Ao}=34.101 mol/m^3, $k_d = 10^{-6}$ (m/s)(m^3/mol))

Conclusions

Barium sulfate precipitation in turbulent liquid flows has been investigated and experimental data have been compared with model predictions. Moreover the presented model has been also compared with predictions obtained by using more sophisticated models (full PDF). It is thus possible to conclude that:

1. CFD is now a mature and well known tool for modeling chemical reactors; CFD predictions for flow and turbulent field in the Taylor-Couette reactor showed good agreement with experimental data; however an ad-hoc experimental validation is always recommended, when dealing with unusual problems, allowing the use of such a technique with much more confidence
2. comparison with experimental data and full PDF predictions showed that the finite-mode PDF model can be conveniently used for modeling fast reactions in turbulent liquid media, in fact with a small computational effort it is able to describe mixing at all scales with good accuracy
3. the Quadrature Method of Moment was shown to be a promising approach for population balance description; however further validation is needed
4. barium sulfate kinetics were found not be sufficiently known; especially the effect of ion excess is still not completely understood, and use of activity coefficients was shown to be questionable and inefficient.

These conclusions also define the future steps of this work:

1. concerning flow field predictions results showed good agreement but also some limitations were found; in fact the Reynolds-averged Navier-Stokes (RANS) equation approach was not able to reproduce some flow instabilities even when used for 3D simulations; this might be overcome by using Large Eddy Simulation (LES) nowadays available in commercial CFD code
2. the finite-mode PDF model might be also used for modeling turbulent reacting flows which present strong coupling between flow and scalar field (e.g. combustion), avoiding the use of two codes (one for the flow field and another for the scalar field) and overcoming the so-called two way coupling approach; however application of this appraoch for non-passive scalar needs further validation
3. use of the Quadrature Method of Moments requires further validation through comparison with more accurate models (i.e., Monte Carlo simulation) and experimental data
4. a new kinetic study of barium sulfate precipitation might be useful in order to find more reliable kinetic expressions.

Notation

a particle area, m^2

A Hamaker constant, J

B birth rate due to aggregation, m−4 s−1

c_A reactant A concentration, mol m−3

c_B reactant B concentration, mol m−3

c_{A0} inlet reactant A concentration, mol m−3

c_{B0} inlet reactant B concentration, mol m−3

c_{Ba} barium concentration, mol m−3

c_{SO4} sulfate concentration, mol m−3

C_μ constant appearing in turbulent viscosity definition

C_ϕ micromixing constant

d annular gap, m

d_{43} mean crystal size, m

d_f fractal dimension

D death rate due to aggregation, m−4 s−1

Da Damkoehler number

D_{ij} structure function, m^2 s^{-2}

D_{LL} longitudinal structure function, m^2 s^{-2}

D_{NN} transverse structure function, m^2 s^{-2}

E Engulfment parameter, s^{-1}

$E(\kappa)$ energy-spectrum function

$E_\phi(\kappa)$ scalar energy-spectrum

f friction factor

f_u one-point one-time velocity PDF

f_ϕ one-point one-time joint-composition PDF

f_ξ one-point one-time mixture fraction PDF

$f_{\xi,Y}$ one-point one-time joint mixture fraction and reaction progress variable PDF

$f_{\xi|Y}$ one-point one-time conditional PDF

G growth rate, m s^{-1}

$\Delta G(L)$ change of free energy during nucleation, J

I ionic strength, mol m^{-3}

I_s intensity of segregation

I_{agg} intensity of aggregation

k turbulent kinetic energy, m^2 s^{-2}

k_a area shape factor

k_B Boltzmann constant, J K^{-1}

k_d mass tranfer coefficient in growth rate expression, m^4 s^{-1} mol^{-1}

$\hat{k}_d$ mass tranfer coefficient, m s^{-1}

k_v volume shape factor

K_a real area shape factor

K_v real volume shape factor

J nucleation rate, m^{-3}s^{-1}

L particle size, m

L_i abscissas of the quadrature approximation

L_{11} longitudinal integral scale, m

L_{22} transverse integral scale, m

L_u turbulent integral length-scale, m

L_ϕ integral length-scale for scalar field, m

L_{43} characteristic mean crystal size, m

m_k kth moments of the CSD

M barium sulfate molecular weight, kg mol^{-1}

N rotational speed of the inner cylinder, rpm

$N(L)$ number denisty function, m^{-4}

N_c number of classes adopted in the CM

N_e number of modes (or environment) in the finite-mode PDF approximation

N_q number of nodes in the quadrature approximation

p fluid pressure, N m^{-2}

p_i probability of mode i

Pe Peclet number

r_1 radius of the inner cylinder, m

r_2 radius of the outer cylinder, m

R_ϕ autocorrelation function for scalar field

R_{ij} autocorrelation function, m^2 s^{-2}

R_{LL} longitudinal autocorrelation function, m^2 s^{-2}

R_{NN} transverse autocorrelation function, m^2 s^{-2}

Re_c critical Reynolds number

Re_L microscale Reynolds number

Re_p Reynolds number for microparticles

Re_r rotational Reynolds number

Re_y wall-distance-based Reynolds number

S supersaturatio ratio

$S_\alpha(\boldsymbol{\phi})$ chemical source term, mol m^{-3} s^{-1}

Sc Schimdt number

$\langle s_\xi \rangle_i$ weighted mixture fraction in mode i

Ta Taylor number

Ta_c critical Taylor number

u_i velocity in the i direction, m s^{-1}

u_i Kolmogorov microscale, m s^{-1}

v particle volume, m^3

V_R reactor volume, m^3

w_i weight of the quadrature approximation

W colloid stability ratio

X_s segregation index

Y reaction progress variable

Greek letter

alpha collision efficiency

beta aggregation kernel, m^{3}s^{-1}

γ micromixing rate, s^{-1}

γ_s spurious dissipation rate, s^{-1}

$\gamma_\pm$ activity coefficient

Γ_α molecular diffusivity of scalar α, m^2 s^{-1}

Γ_t turbulent diffusivity, m^2 s^{-1}

$\dot{\gamma}$ shear stress, s^{-1}

ϵ turbulent dissipation rate, $\mathrm{m}^2\ \mathrm{s}^{-3}$

ϵ_{ij} dissipation rate tensor, $\mathrm{m}^2\ \mathrm{s}^{-3}$

ϵ_ϕ scalar dissipation rate, $\mathrm{mol}^2\ \mathrm{m}^{-6}\ \mathrm{s}^{-1}$

κ wavenumber, m^{-1}

λ_B Batchelor microscale, m

λ_f longitudinal Taylor microscale, m

λ_g transverse Taylor microscale, m

λ_ϕ scalar Taylor microscale, m

λ_k Kolmogorov microscale, m

μ viscosity, kg $\mathrm{m}^{-1}\mathrm{s}^{-1}$

μ_t turbulent viscosity, kg $\mathrm{m}^{-1}\mathrm{s}^{-1}$

ν kinematic viscosity, $\mathrm{m}^2\ \mathrm{s}^{-1}$

ξ mixture fraction

ξ_s stochiometric mixture fraction

$\langle\xi\rangle_i$ local mixture fraction in mode i

ρ crystal density, kg m^{-3}

$\rho(L)$ fractal density, kg m^{-3}

σ_s selectivity of S

σ_1 inertial-convective contribution to scalar variance

σ_2 viscous-convective contribution to scalar variance

σ_3 viscous-diffusive contribution to scalar variance

τ_u turbulent integral time scale, s

τ_k Kolmogorov microscale, s

τ_ϕ mixing time, s

$\boldsymbol{\phi}$ composition vector, mol m^{-3}

ϕ_α concentration of scalar α, mol m^{-3}

ϕ_c mean crystal size factor

Φ_{ij} velocity-spectrum tensor

Φ_ϕ scalar energy spectrum

Ω_1 angular velocity of the inner cylinder, rad s^{-1}

Operators

$\langle\ \ \rangle$ Reynolds average

$'$ fluctuation

Abbrevation

CFD Computational fluid dynamics

CM Classes method

CSD Crystal size distribution

DPB Discretized population balance

FTF Fully turbulent flow

LCF Laminar Couette flow

LDA Laser doppler anenometry

LIF Laser induced fluorescence

LTVF Laminar Taylor Vortex flow

Non-eq non-equilibrium wall function

PDF Probability density function

QMOM Quadrature method of moments

QPWVF Quasi-periodic wavy vortex flow

RANS Reynolds-averaged Navier-Stokes

RNG Renormalization Group Theory

RSM Reynolds stress model

SMM Standard moments method

SPWVF Single-periodic wavy vortex flow

Std standard wall function

Two-eq Two-equation model

Bibliography

[1] Dirksen, J.A., and T.A. Ring, "Fundamentals of crystallization: kinetic effects on particle size distributions and morphology," *Chem. Eng. Sci.*, **46**, 2389 (1991).

[2] Nielsen, A.E., *Kinetics of precipitation,* Pergamon Press, London (1964).

[3] Baldyga, J., W. Podgorska, and R. Pohorecki, "Mixing-precipitation model with application to double feed semibatch precipitation," *Chem. Eng. Sci.*, **50**, 1281 (1995).

[4] Wong, D.C.Y., Z. Jaworski, and A.W. Nienow, "Effect of ion excess on particle size and morphology during barium sulphate precipitation: an experimental study," *Chem. Eng. Sci.*, **56**, 1 (2001).

[5] Phillips, R., S. Rohani, and J. Baldyga, "Micromixing in a single-feed semi-batch precipitation process," *AIChE J.*, **45**, 82 (1999).

[6] Aoun, M., E. Plasari, R. David, and J. Villermaux, "A simultaneous determination of nucleation and growth rates from batch spontaneous precipitation," *Chem. Eng. Sci.*, **54**, 1161 (1999).

[7] Aoun, M., E. Plasari, R. David, and J. Villermaux, "Are barium sulphate kinetics sufficiently known for testing precipitation reactor models?," *Chem. Eng. Sci.*, **51**, 2449 (1996).

[8] Wei, H., and J. Garside, "Application of CFD modelling to precipitation systems," *Chem. Eng. Res. Des.*, **70A**, 219 (1997).

[9] Bromley, L.A., "Thermodynamic properties of strong electrolytes aqueous solutions," *AIChE J.*, **19**, 313 (1973).

[10] Marchisio, D.L., R.O. Fox, A.A. Barresi, M. Garbero, and G. Baldi, "On the simulation of turbulent precipitation in a tubular reactor Via Computational Fluid Dynamics," *Chem. Eng. Res. Des.*, in press (2001).

[11] Nielsen, A.E., "Electrolyte crystal growth mechanisms," *J. Crystal Growth*, **67**, 289 (1984).

[12] Nielsen, A.E., and J.M. Toft, "Electrolyte crystal growth kinetics," *J. Crystal Growth*, **67**, 278 (1984).

[13] Armenante, P.M., and D.J. Kirwan, "Mass transfer coefficient to microparticles in agitated systems," *Chem. Eng. Sci.*, **44**, 2781 (1989).

[14] Nagata, S., *Mixing-principles and applications,* Cap. 6, pag. 268. Kodansha LTD, Tokyo (1975).

[15] Elimelech, M., J. Gregory, X. Jia, and R.A. Williams, *Particle deposition and aggregation,* Butterworth-Heinemann, Wouburn, MA (1995).

[16] Smoluchowsky, M.Z., "Versuch einer mathematischen Theorie der Koagulationskinetic Kolloider Losunger," *Z. Phys. Chem.*, **92**, 129 (1917).

[17] Saffman, P.G., and J.S. Turner, "On the collision of drops in turbulent clouds," *J. Fluid Mech.*, **1**, 16 (1956).

[18] Adachi, Y., M.A. Cohen Stuart, and R. Fokkink, "Kinetics of turbulent coagulation studied by means of end-over-end rotation," *J. Coll. Inter. Sci.*, **165**, 310 (1994)

[19] Tontrup, C., F. Gruy, and M. Cournil, "Turbulent aggregation of titania in water," *J. Coll. Inter. Sci.*, **229**, 511 (2000).

[20] Vanni, M., and G. Baldi, "Coagulation efficiency of colloidal particles in shear flow," *Adv. Coll. Inter. Sci.*, in press (2001).

[21] Liklema, J. *Fundamentals of interface and colloid science.* Academic Press, San Diego (1991).

[22] Kearney, M.M., "Engineered fractals enhance process applications," *Chem. Eng. Prog.*, **96**, 61 (2000).

[23] Sonntag, R.C., and W.B. Russel, "Structure and breakup of flocs subjected to fluid stresses. I. Shear Experimentens," *J. Colloid Interface Sci.*, **113**, 339 (1986).

[24] Torres, F.E., W.B. Russel, and W.R. Schowalter, "Simulation of coagulation in viscous flows," *J. Colloid Interface Sci.*, **145**, 51 (1991).

[25] Vanni, M., "Creeping flow over spherical permeable aggregates," *Chem. Eng. Sci.*, **55**, 685 (2000).

[26] Pagliolico, S., D. Marchisio, and A.A. Barresi, "Influence of operating conditions on $BaSO_4$ crystal size and morphology in a continuous couette precipitator," *J. Therm. Anal. Cal.*, **56**, 1423 (1999).

[27] Randolph, A.D., and M.A. Larson, *Theory of particulate processes*, 1st ed., Academic Press, San Diego (1971).

[28] Hinze, J.O., *Turbulent flow*, 1st ed., John Wiley & Sons, New York (1959).

[29] Pope, S., *Turbulent flows*, 1st ed., Cambridge University Press, Cambridge (2000).

[30] Fox, R.O., *Turbulent reacting flows* , Cambridge University Press, to appear (2001).

[31] Frisch, U., *Turbulence*, 1st ed., Cambridge University Press, Cambridge (1995).

[32] Tennekes, H., and J.L. Lumley, *A first course in turbulence*, 2th Ed., MIT Press, Cambridge MA (1989).

[33] Baldyga, J., and J.R. Bourne, "Principles of micromixing," In:*Encyclopedia of Fluid Mechanics*, Ed. N.P. Cheremisinoff, Gulf Publishing Company, Houston (1986).

[34] Baldyga, J., and J.R. Bourne, *Turbulent mixing and chemical reactions*, Jhon Wiley & Sons, New York (1999).

[35] Valerio, S., M. Vanni, A.A. Barresi, and G. Baldi, "Engineering modelling of turbulent flows in chemical engineering applications," *Trends Chem. Eng.*, **5**, 1 (1998).

[36] Launder, B.E., and D.B. Spalding, "Lectures in mathematical models of turbulence," Academic Press, London (1972).

[37] Fluent Inc., "Fluent 5 user guide," Fluent Inc., Lebanon, NH, USA (1998).

[38] Corrsin, S., "The isotropic turbulent mixer: Part II. Arbitrary Schimdt number," *AIChE J.*, **10**, 870 (1964).

[39] Baldyga, J., "Turbulent mixture model with application to homogeneous, instantaenous chemical reactions," *Chem. Eng. Sci.*, **44**, 1175 (1989).

[40] Fox, R.O., "The spectral relaxation model of the scalar dissipation rate in homogeneous turbulence," *Phys. Fluid*, **7**, 1082 (1995).

[41] Fox, R.O., "The lagrangian spectral relaxation model of the scalar dissipation rate in homogeneous turbulence," *Phys. Fluid*, **9**, 2364 (1997).

[42] Fox, R.O., "The lagrangian spectral relaxation model for differential diffusion in homogeneous turbulence," *Phys. Fluid*, **11**, 1550 (1999).

[43] Valerio, S., M. Vanni, and A.A. Barresi, "Contribution of different turbulent scales to mixing and reaction between unpremixed reactants," *Chem. Eng. Sci.*, **49**, 5159 (1994).

[44] Kruis, F.E., and L. Falk, "Mixing and reaction in a tubular jet reactor: a comparison ot experiments with a model based on a prescribed PDF," *Chem. Eng. Sci.*, **51**, 2439 (1996).

[45] Toor, H.L., "Turbulent mixing of two species with and without chemical reaction," *Ind. Eng. Chem. Fundam.*, **8**, 655 (1969).

[46] Spalding, D.B., "Mixing and chemical reaction in steady confined turbulent flames," *Proc. 13th Symposium on Combustion* (The Combustion Institute), 649 (1970).

[47] Valerio, S., M. Pipino, M. Vanni, and A.A. Barresi, "Experimental and numerical investigation of turbulent reactive flow in a tubular reactor," *I.Chem.E. Symp. Ser.*, **136**, 219 (1994).

[48] Pope, S., "Pdf methods for turbulent reacting flows," *Prog. Energy Combust. Sci.* , **11**, 119 (1985).

[49] Costa, P., and C. Trevissoi, "Some kinetics and thermodynamics features of reactions between partially segregated fluids," *Chem. Eng. Sci.*, **27**, 653 (1972).

[50] Costa, P., and C. Trevissoi, "Reactions with non-linear kinetics in partially segregated fluids," *Chem. Eng. Sci.*, **27**, 2041 (1972).

[51] Dopazo, C., "Probability density function approach for turbulent axisymmetric heated jet. Centerline evolution," *Phys. Fluids*, **18**, 397 (1975).

[52] Baldyga, J., and J.R. Bourne, "Comparison of the engulfment and the interaction-with-the-mean micromixing models," *Chem. Eng. J.*, **45**, 25 (1990).

[53] Baldyga, J., "A closure model for homogeneous chemical reactions," *Chem. Eng. Sci.*, **49**, 1985 (1994).

[54] Fox, R.O., "On the relationship between Lagrangian micromixing models and computational fluid dynamics," *Chem. Eng. Process*, **37**, 521 (1998).

[55] Marchisio, D.L., A.A. Barresi, and R.O. Fox, "Simulation of turbulent precipitation in a semi-batch Taylor-Couette reactor using CFD," *AIChE J.*, **47**, 664 (2001).

[56] Piton, D., R.O. Fox, and B. Marcant, "Simulation of fine particle formation by precipitation using computational fluid dynamics," *Canadian J. Chem. Eng.*, **78**, 983 (2000).

[57] Fox, R.O., "Computational methods for turbulent reacting flows in the chemical process industry," *Revue de l'Institute Francais du Petrole*, **51**, 215 (1996).

[58] Rhodes, R.P., "A probability density function for turbulent flows in turbulent mixing in nonreactive and reactive flows," (Ed. S.N.B. Murphy), Plenum, New York, 235 (1975).

[59] Li, K.T., and H.L. Toor, "Chemical indicators as mixing probes. A possible way to measure micromixing simply," *Ind. Eng. Chem. Fundam.*, **25**, 719 (1986).

[60] Hulburt, H.M., and S. Katz, "Some problems in particle technology," *Chem. Eng. Sci.*, **19**, 555 (1964).

[61] Kumar, S., and D. Ramkrishna, "On the solution of population balance equations by discretization-I. A fixed point technique," *Chem. Eng. Sci.*, **51**, 1311 (1996).

[62] Kumar, S., and D. Ramkrishna, "On the solution of population balance equations by discretization-II. A moving point technique," *Chem. Eng. Sci.*, **51**, 1333 (1996).

[63] Vanni, M., "Discretized procedure for the breakage equation," *AIChE J.*, **45**, 916 (1999).

[64] Marchal, P., R. David, J.P. Klein, and J. Villermaux, "Crystallization and precipitation engineering-I. An efficient method for solving population balance in crystalizzation with agglomeration," *Chem. Eng. Sci.*, **43**, 56 (1988).

[65] Muhr, H., R. David, and J. Villermaux, "Crystallization and precipitation engineering-VI. Solving population balance in the case of the precipitation of silver bromide crystals with high primary nucleation rates by using first order upwind differentation," *Chem. Eng. Sci.*, **51**, 309 (1996).

[66] Litster, J.D., D.J. Smit, and M.J. Hounslow, "Adjustable discretized population balance for growth and aggregation," *AIChE J.*, **41**, 591 (1995).

[67] Hounslow, M.J., R.L. Ryall, and V.R. Marshall, “A discretized population balance for nucleation, growth, and aggregation,” *AIChE J.*, **34**, 1821 (1988).

[68] Smith, M., and T. Matsoukas, “Constant-number Monte Carlo simulation of population balances,” *Chem. Eng. Sci.*, **53**, 1777 (1998).

[69] Ramkrishna, D., “The status of population balances,” *Rev. Chem. Eng.*, **3**, 49 (1985).

[70] Vanni, M., “Approximate population balance equations for aggregation-breakage processes,” *J. Colloid Interface Sci.*, **221**, 143 (2000).

[71] Ramkrishna, D., *Population balances: theory and applications to particulate systems in engineering.* New York: Academic Press (2000).

[72] McGraw, R., “Description of aerosol dynamics by the quadrature method of moments,” *Aerosol Sci. Tech.*, **27**, 255 (1997).

[73] Gordon, R.G., “Error bounds in equilibrium statistical mechanics,” *J. Math. Phys.*, **9**, 655 (1968).

[74] Valerio S., P. Baile, M. Fenoglio, M. Vanni, and A.A. Barresi, “Validation of turbulent transport models in confined jets with spectrophotometric determination of local concentration profiles,” *Proc. of the 2nd Italian Conf. on Chem. and Proc. Eng.*, 15-17 May, Florence, Italy, 39-47 (1995).

[75] Fournier, M.C., L. Falk, and J. Villermaux, “A new parallel competing reaction system for assessing micromixing efficiency. Experimental approach, *Chem. Eng. Sci.*, **51**, 5035 (1996).

[76] Taylor, G.I., “Stability of a viscous liquid contained between two rotating cylinders,” *Phil. Trans. Roy. Soc. A*, **223**, 289 (1923).

[77] Kataoka, K., “Taylor vorticies and instabilities in circular Couette flows,” In N.P. Cheremisinoff (Ed.), *Encyclopedia of Fluid Mechanics*, (Vol. 1, pp. 237-273). Houston: Gulf Publishing (1985).

[78] Davey, A., “The growth of toroidal vortices in flow between rotating cylinders,” *J. Fluid Mech.*, **14**, 336 (1962).

[79] Krueger, E.R., A. Gross, and R.C. Di Prima, “On the relative importance of Taylor-vortex and non-axisymmetric modes in flow between cylinders,” *J. Fluid Mech.*, **24**, 521 (1966).

[80] Davey, A., R.C. Di Prima, and J.T. Stuart, “On the instability of Taylor vortices,” *J. Fluid Mech.*, **31**, 17 (1968).

[81] Wereley, S.T., and R.M. Lueptow, “Spatio-temporal character of non-wavy and wavy Taylor-Couette flow,” *J. Fluid Mech.*, **364**, 59 (1998).

[82] Ohmura, N., K. Kataoka, T. Mizumoto, M. Nagata, and T. Matsumuoto, “Effect of vortex cell structure on bifurcation properties in a Taylor vortex flow system,” *Chem. Eng. Sci.*, **52**, 1757 (1997).

[83] Smith, G.P., and A.A. Townsend, "Turbulent Couette flow between concentric cylinders at large Taylor numbers," *J. Fluid Mech.*, **123**, 187 (1982).

[84] Doherty, M.F., and J.M. Ottino, "Chaos in deterministic systems: strange attractors, turbulence, and applications in chemical engineering," *Chem. Eng. Sci.*, **43**, 139 (1998).

[85] Riganti, R., "Biforcation and chaos," (in Italian), Torino, Editrice Universitaria Levrotto & Bella (2000).

[86] Buzug, Th., K. Pawelzik, J. von Stamm, and G. Pfister, "Mutual information and global strange attractors in Taylor-Couette flow," *Physica D*, **72**, 343 (1994).

[87] Buzug, Th., J. von Stamm, and G. Pfister "Fractal dimensions of strange attractors obtained from the Taylor-Couette experiment," *Physica A*, **191**, 559 (1992).

[88] Guichardon, P., and L. Falk, "Characterization of micromixing efficiency by the iodide-iodate reaction system. Part I: experimental procedure," *Chem. Eng. Sci.*, **55**, 4233 (2000).

[89] Baldyga, J., and W. Orciuch, "Closure problem for precipitation in inhomogeneous turbulence," *Chem. Eng. Res. Dev.*, **75A**, 160 (1997).

[90] Villermaux, J., L. Falk, "Generalized mixing model for initial contacting of reactive fluids," *Chem. Eng. Sci.*, **49**, 5127 (1994).

[91] Gelbard, F., and J. H. Seinfield, "Numerical solution of dynamic equation for particulate systems," *J. Comput. Physics,* **28**, 357 (1978).

[92] Ilievski, D., and M.J. Hounslow, "Agglomeration during precipitation: II. Mechanism deduction from tracer data," *AIChE J.*, **41**, 525 (1995).

[93] Chaer, E., P. Guichardon, L. Falk, and E. Plasari, "Determination of local energy dissipation rates in impinging jets by a chemical reaction method," *Chem. Eng. J.*, **72**, 125 (1999).

[94] Marchisio, D.L., R.O. Fox, A.A. Barresi, and G. Baldi, "A CFD approach to study the local importance of aggregation in precipitation," *Proc. of the 7th International Conf. on Multiphase Flow in Ind. Plants,* Bologna, Italy, 13-15 September, 373 (2000).

[95] Marchisio, D.L., A.A. Barresi, G. Baldi, and R. O. Fox, "Comparison of different modelling approaches to turbulent precipitation," *Proceeding 10th European Conference on Mixing*, (H. E. A. Van den Akker, Ed.), Delft, The Netherlands, July 2-5, 79 (2000).

[96] Kim, W. S., and J. M. Tarbell, "Micromixing effects on barium sulphate precipitation in a MSMPR reactor," *Chem. Eng. Comm.*, **146**, 33 (1996).

[97] Fitchett, D. E. and J. M. Tarbell, "Effect of mixing on the precipitation of barium sulphate in an MSMPR reactor," *AIChE J.*, **36**, 511 (1990).

[98] Barresi, A. A., D. Marchisio, and G. Baldi, "On the role of micro- and mesomixing in a continuous Couette-Type precipitator," *Chem. Eng. Sci.*, **54**, 2339 (1999).

[99] Archibald, D.D., B.P. Gaber, J.D. Hopwood, S. Mann, and T. Boland "Atomic force microscopy of synthetic barite microcrystals," *J. of Crystal Growth*, **172**, 231 (1997).

[100] Yokota, M., E. Oikawa, J. Yamanaka, A. Sato, and N. Kubota, "Formation and structure of rounded-shaped crystals of barium sulfate," *Chem. Eng. Sci.*, **55**, 4379 (2000).

[101] Marchisio, D.L., R.O. Fox, A.A. Barresi, and G. Baldi, "On the Comparison Between Presumed and Full PDF methods for Turbulent Precipitation," *Ind. Eng. Chem. Res.*, to appear (2001).

[102] Tsai, K.; R.O. Fox, "PDF simulation of turbulent series-parallel reaction in an axisymmetric reactor," *Chem. Eng. Sci., 49*, 5141 (1994).